Advanced numerical framework to simulate Incremental Forming Processes

Thesis submitted to the University of Liège and University of Aveiro
for the degree of 'Docteur en Sciences de l'Ingénieur'
and 'Doutor em Engenharia Mecânica'
by José Ilídio Velosa de Sena

July 2015

Author

José Ilídio Velosa de Sena

Email from University of Aveiro: sena.ilidio@ua.pt
Email from University of Liège: jsena@student.ulg.ac.be

Supervisors at University of Liège

Docteur Anne Marie Habraken
Research Director of F.N.R.S., ArGEnCo department, University of Liège
Email: anne.habraken@ulg.ac.be

Professor Laurent Duchêne
Assistant Professor, ArGEnCo department, University of Liège
Email: l.duchene@ulg.ac.be

Address
MS²Fdivision, ArGEnCo Department, Université de Liège,
Chemin des Chevreuils 1,
4000 Liège, Belgium

Supervisors at University of Aveiro

Professor Ricardo José Alves de Sousa
Auxiliar Professor, University of Aveiro, Portugal
Email: rsousa@ua.pt

Professor Robertt Angelo Fontes Valente
Auxiliar Professor, University of Aveiro, Portugal
Email: robertt@ua.pt

Address
GRIDS Research Group, TEMA Research Unity,
Department of Mechanical Engineering,
Campus Universitário de Santiago, University of Aveiro,
3810 Aveiro, Portugal

PhD Scholarship granted by Fundação para a Ciência e Tecnologia (FCT) under SFRH/BD/71269/2010

Apoio financeiro da FCT e do FSE no âmbito do III Quadro Comunitário de Apoio.

Jury members

President

Prof. João de Lemos Pinto
Full Professor, University of Aveiro, Portugal

Prof. Marta Cristina Cardoso de Oliveira
Auxiliar Professor of the Faculty of Sciences and Technology, University of Coimbra, Portugal

Prof. Renato Natal Jorge
Associate Professor of the Faculty of Engineering, University of Porto, Portugal

Prof. Luis Filipe Menezes
Full Professor of the Faculty of Sciences and Technology, University of Coimbra, Portugal

Dr. Anne Marie Habraken, Supervisor of the thesis
Research Director of F.N.R.S., ArGEnCo department, University of Liège, Belgium

Prof. Ricardo José Alves de Sousa, Supervisor of the thesis
Auxiliar Professor, University of Aveiro, Portugal

Acknowledgements

Em primeiro lugar, ao Professor Doutor Ricardo José Alves de Sousa, orientador principal, o meu reconhecimento e privilégio pela oportunidade de realizar o doutoramento, sua constante boa disposição, disponibilidade, orientação, amizade, otimismo e exigência científica ao longo da preparação do trabalho, o meu sincero muito obrigado.

To Research Director of F.N.R.S, Doctor Anne Marie Habraken, supervisor at University of Liège, my appreciation for the opportunity of developing part of my research work at the University of Liège. As well as the fruitful scientific discussions in order to finish this thesis successfully.

Ao Professor Doutor Robertt Angelo Fontes Valente, co-orientador, o meu obrigado pela amizade, boa disposição, disponibilidade, otimismo, rigor científico e conselhos relevantes dados ao longo da realização do trabalho.

To Professor Laurent Duchêne, co-supervisor at University of Liège, for his availability and scientific support during my stays in Liège. All the scientific discussions and ideas to identify and solve issues for the success of the numerical simulations.

To all LAGAMINE group members, for the sympathy and tasty cakes of the team meetings. In particular, to Amine BenBettaieb, Carlos Guzman and Kalipha Marmi for their friendship and scientific discussions. Also, the assistance provided at my first stay in Liège by Cédric Lequesne about technical and scientific knowledge of in-house code LAGAMINE.

To all the people which I shared social meetings with funny moments during all my stays in Liège, a special thanks.

To EURAXESS mobility centre for foreign PhD students at University of Liège for all the mobility support and stays in Liège.

Ao Tiago Almeida, José Sousa e ao Ricardo bastos, pela ajuda e colaboração na execução dos procedimentos experimentais, nomeadamente dos ensaios, produção e medições experimentais.

A todos os membros do GRIDS, obrigado pelo modo caloroso como fui recebido no grupo contribuindo para a minha imediata integração, pelo bom ambiente, espírito de grupo e convívio proporcionado. Em particular, agradeço aos colegas de gabinete ao longo destes anos pela camaradagem, boa disposição e discussões científicas proporcionadas.

À Fundação para a ciência e Tecnologia (FCT), por todo o apoio financeiro concebido através da bolsa de doutoramento SFRH/BD/71269/2010.

À minha família, pelo constante apoio sempre acreditando no meu potencial ao longo do meu percurso de vida. Em particular, aos meus Pais, o reconhecimento por todo o esforço, apoio e incentivo incondicional dado durante o meu percurso académico bem como em todas as etapas da minha vida, o meu maior agradecimento.

Finalmente, a todos e a cada um, que contribuíram diretamente ou indiretamente na concretização deste trabalho, a minha gratidão e reconhecimento. A todos, muito obrigado.

Keywords Incremental sheet forming; Single point incremental forming; Numerical simulation; Adaptative remeshing; Finite Element Method (FEM); Plastic deformation.

Abstract

The framework of the present work supports the numerical analysis of the Single Point Incremental Forming (SPIF) process resorting to a numerical tool based on adaptive remeshing procedure based on the FEM. Mainly, this analysis concerns the computation time reduction from the implicit scheme and the adaptation of a solid-shell finite element type chosen, in particular the Reduced Enhanced Solid Shell (RESS). The main focus of its choice was given to the element formulation due to its distinct feature based on arbitrary number of integration points through the thickness direction. As well as the use of only one Enhanced Assumed Strain (EAS) mode. Additionally, the advantages include the use of full constitutive laws and automatic consideration of double-sided contact, once it contains eighth physical nodes.

Initially, a comprehensive literature review of the Incremental Sheet Forming (ISF) processes was performed. This review is focused on original contributions regarding recent developments, explanations for the increased formability and on the state of the art in finite elements simulations of SPIF. Following, a description of the numerical formulation behind the numerical tools used throughout this research is presented, summarizing non-linear mechanics topics related with finite element in-house code named LAGAMINE, the elements formulation and constitutive laws.

The main purpose of the present work is given to the application of an adaptive remeshing method combined with a solid-shell finite element type in order to improve the computational efficiency using the implicit scheme. The adaptive remeshing strategy is based on the dynamic refinement of the mesh locally in the tool vicinity and following its motion. This request is needed due to the necessity of very refined meshes to simulate accurately the SPIF simulations. An initially mesh refinement solution requires huge computation time and coarse mesh leads to an inconsistent results due to contact issues. Doing so, the adaptive remeshing avoids the initially refinement and subsequently the CPU time can be reduced.

The numerical tests carried out are based on benchmark proposals and experiments purposely performed in University of Aveiro, Department of Mechanical engineering, resorting to an innovative prototype SPIF machine. As well, all simulations performed were validated resorting to experimental measurements in order to assess the level of accuracy between the numerical prediction and the experimental measurements. In general, the accuracy and computational efficiency of the results are achieved.

Contents

List of Figures

List of Tables

Nomenclature

List of Symbols (Scalars and tensors)

Chapter 1

Δz	Vertical step down
ϕ	Wall angle value
K	Strength coefficient
n	Strain hardening coefficient
r_n	Lankford coefficient
A	Elongation percentage (%)
h	Scallop height
σ	Stress
ε	Strain

Chapter 2

Fx; Fy; Fz	Force components
ϕ	Wall angle value
ε_{Major} ; ε_1	True strain in major in-plane direction
ε_{Minor} ; ε_2	True strain in minor in-plane direction
Δz	Vertical step down
k	Relative jet diameter
t	Sheet thickness
d_{WJ}	Water jet diameter
p_W	Water pressure

h_{SO}	Water jet distance
d	Diameter of the contour
R_{imp}	Imposed displacement radius
L	Distance between the centre of the tool and a limit contact area
θ	Angle between the tool contact point and the limit contact area L

Chapter 3

V	Generic Volume
S	Generic surface area
S_D	Dirichlet (essential) boundary conditions
S_N	Neumann (Natural) boundary conditions
$\mathbf{b}$	Body forces
$\boldsymbol{\nabla}$	Gradient operator
$\mathbf{t}$	Surface tractions forces per unit area
$\mathbf{n}$	Normal vector to the contact surface
$\mathbf{u}$	Displacement
$\boldsymbol{\sigma}$	Cauchy stress tensor
W	Work
δ	Infinitesimal operator for iterative variations
$\mathbf{e}$	Infinitesimal strain tensor; Linear strain
$\boldsymbol{\omega}$	Anti-symmetric part, the spin
X	Global Cartesian coordinate system
$\mathbf{x}$	Coordinate position
P	Material point
$\mathbf{u}^S$	Displacement acting on the surface
$\mathbf{S}$	2nd Piola-kirchhoff stress tensor

$\mathbf{E}$	Green-Lagrange strain tensor
ρ	Density
$\mathbf{F}$	Deformation gradient
$\frac{\partial \mathrm{u}}{\partial \mathrm{x}}$	Partial derivative
$\mathbf{R}$	Rotation matrix
$\mathbf{U}$	Right symmetric stretch matrix
$\mathbf{V}$	Left symmetric stretch matrix
$\mathbf{C}$	Right Cauchy-Green strain tensor; Stress-strain law
$\mathbf{b}^*$	Left Cauchy-Green strain tensor
$\mathbf{I}$	Identity matrix
$\boldsymbol{\eta}$	Nonlinear strain
t	Time (instant); Traction force component
$\mathbf{P}$	Nodal external forces
$\mathbf{r}$	Residual load vector
$\mathbf{K}$	Stiffness matrix
$\mathbf{f}$	Internal forces
$\mathbf{N}$	Shape function
$\mathbf{x}_k = (x, y, z)$	Position vector of node k
$\mathbf{B}$	Strain-displacement matrix
$\mathbf{d}$	Degrees of freedom
$(\xi,\ \eta,\ \zeta)$	Natural coordinates
$\mathbf{u} = (x, y, z)$	Displacement field
$\mathbf{J}$	Jacobian matrix
$\mathbf{v}_i$	Tangential directions of natural coordinates
$\mathbf{Q}$	Rotation

$\mathbf{L}$	Velocity gradient
$\dot{\mathbf{F}}$	Time derivative of deformation gradient
$\mathbf{\Omega}$	Rotation rate tensor
$\mathbf{D}$	Rate of deformation tensor, symmetric part of the velocity gradient tensor
$\mathbf{W}$	Spin rate tensor, anti-symmetric part of the velocity gradient tensor
$\boldsymbol{\sigma}^{\mathrm{J}}$	Jaumann objective stress rate of the Cauchy stress tensor
$\boldsymbol{\sigma}_9$	Stress tensor in 9×9 array composed by sub-blocks of $\boldsymbol{\sigma}_3$
$\boldsymbol{\sigma}_3$	Stress tenor in 3×3 array form
σ_{ij}	Stress components
$\boldsymbol{\varepsilon}$	Generic strain tensor
Φ	Yield function
$\overline{\sigma}$	Equivalent stress
σ_{y}	Yield stress
$\mathbf{C}_{\mathrm{T}}$	Tangent constitutive tensor
$\mathbf{C}^{\mathrm{e}}$	Elastic constitutive tensor
Δ	Finite operator for incremental variations
$\mathrm{r}_0; \mathrm{r}_{45}; \mathrm{r}_{90}$	Lankford coefficients
σ_{y0}	Initial Yield stress
$\overline{\varepsilon}^{\mathrm{p}}$	Effective plastic strain
$\boldsymbol{\alpha}$	Back-stress tensor
$A; C$	Voce-law parameters
$K; n$	Swift hardening parameters
Q	Plastic potential
λ	Plastic multiplier
$\boldsymbol{\sigma}^{\mathrm{TR}}$	Trial elastic stress
$\mathbf{a}$	Strain rate (flux) vector

θ	Parameter ranging from 0 (forward Euler) to 1 (backward Euler)
Ω^j	Body domain
ϕ^i	The solution of the equilibrium state
$\mathbf{C}_{\mathrm{C}}$	Contact matrix
d_{C}	Contact distance between two bodies
e_i	Local axis frame component
f_{C}	Contact yield function
p	Contact pressure
σ_{n}	Normal component of an applied force per unit area
φ	Contact type
τ_i	Shear component
μ	Friction coefficient
$\mathrm{K_p}$; K_τ	Penalty coefficients
Π	Potential energy
$\mathbf{E}_\alpha$	Enhanced strain field
$\psi = \left(\xi, \eta, \zeta\right)$	Natural coordinate system
α	Internal variables field of the EAS method
$\mathbf{f}_\alpha$	Force vector of enhanced part
$\mathbf{r}^i$	Local orthonormal frame
$\mathbf{T}_0$	Convective transformation tensor
W	Strain energy
$\mathbf{K}^{uu}$	Displacement-based stiffness matrix
$\mathbf{K}^{\alpha\alpha}$	EAS-based stiffness matrix
$\mathbf{K}^{u\alpha}$; $\mathbf{K}^{\alpha u}$	Coupled EAS-displacement-based stiffness matrices

Chapter 4

D	Shortest distance between the spherical tool centre and the element nodes
L	Longest diagonal of an element
R	Radius of the tool
α	Vicinity size coefficient (user parameter)
n	Number of nodes per edge (user parameter)
p	New node index
ξ	Local coordinate
$\mathbf{x}_{\mathrm{P}}$	Global coordinates of the new node between node $\mathbf{x}_{\mathrm{A}}$ and $\mathbf{x}_{\mathrm{B}}$
$\mathbf{x}_{\mathrm{A}}$	Global coordinates of the node A
$\mathbf{x}_{\mathrm{B}}$	Global coordinates of the node B
$\mathbf{Z}_{\mathrm{J}}$	Weighted-average value
$\mathbf{Z}_{\mathrm{K}}$; $\mathbf{Z}_{\mathrm{P}}$	Variables known values from old Gauss points
d	Highest length of the new element
D	Highest length of the mesh
R_{KJ} ; R_{PJ}	Distance between integration points
P; K	Integration point index
J	New integration point index
C; N	Threshold values
$\mathrm{R}_{\mathrm{max}}$	Maximum radius of influence
$\mathrm{R}_{\mathrm{min}}$	Minimum radius of influence
d_{max}	Maximum distance between $\mathbf{X}_{\mathrm{V}}$ and $\mathbf{X}_{\mathrm{C}}$ (user parameter)
$\mathbf{X}_i$	Positions of the four nodes in the coarse element plane
$\mathbf{X}_{\mathrm{V}}$	Virtual position of the new node in the coarse element plane
$\mathbf{X}_{\mathrm{C}}$	Current position of the new node
l; c	New node position within the cell

H	Interpolation function
$\mathbf{q}$	Degrees of freedom of a new node
$\mathbf{q}_{\mathrm{f}}$	Degrees of freedom of a free new node (unconstrained node)
$\mathbf{q}_{\mathrm{s}}$	Degrees of freedom of a slave new node (constrained node)
$\mathbf{N}$	Matrix containing the interpolation functions for each constrained DOF
N	Interpolation function
$\mathbf{I}$	Identity matrix
$\mathbf{A}$	Matrix composed with interpolation functions of constrained DOF
$\mathbf{K}$	Stiffness matrix
$\mathbf{f}$	Equilibrium forces vector
$\tilde{\mathbf{q}}$	Virtual degrees of freedom
$\mathbf{K}_{\mathrm{f}}$	Stiffness matrix of the unconstrained degrees of freedom
E	Young modulus
ν	Poisson ratio
$K; n;\ \varepsilon_0$	Swift hardening parameters

Chapter 5 and Appendix B

E	Young modulus
ν	Poisson ratio
$K; n;\ \varepsilon_0$	Swift hardening parameters
α	Vicinity size coefficient (user parameter)
$d_{\max}$	Maximum distance between $\mathbf{X}_{\mathrm{V}}$ and $\mathbf{X}_{\mathrm{C}}$ (user parameter)
n	Number of nodes per edge (user parameter)
$\mathrm{K_P};\ \mathrm{K}_\tau$	Penalty coefficients
μ	Friction
$\mathrm{F_Z}$	Axial force (z direction)

σ_0	Initial Yield stress
N	Number of points
Num.	Numerical value
Exp.	Experimental value
F_{Z_S}	Analytical axial force
R_m	Tensile strength
t	Sheet thickness
d_t	Tool diameter
Δh	Scallop height
Ø	Wall angle value
$\Delta\theta$	Empirical correction
C_X ; X_{sat}	Back-stress components
σ_{ij}	Stress components
ε^p_{eq}	Equivalent plastic strain
σ_{eq}	Equivalent stress

List of Indices

Chapter 3

${}^{t+\Delta t}_{t}\square$	Variable value between states (t) and ($t+\Delta t$)
${}^{t}_{0}\square$	Variable value between states (0) and (t)
${}^{t}\square$	Variable value evaluated at state (t)
${}^{0}\square$	Stands for initial value (Reference state) or evaluated at the point (0)
${}^{t+\Delta t}\square$	Variable evaluated at state ($t+\Delta t$)

$\square^{\mathrm{H}}$	Hourglass (stabilization) counterpart of a variable
$\square^{\mathrm{e}}$	Stands for elastic
$\square^{\mathrm{p}}$	Stands for plastic
$\square_{\mathrm{int}}$	Stands for internal
$\square_{\mathrm{ext}}$	Stands for external
$\square^{\mathrm{u}+\alpha}$	Displacement and enhanced based variable (condensed)
$\square_{i}$	Coordinate axis; Current increment number *(i)*
$\square_{\mathrm{u}}$	Displacement-based variable
$\square_{\alpha}$	Enhanced-based variable
$\square^{e}$	Variable in a finite element domain
$\square_{\mathrm{C}}$	Contact variable; Current position
$\square_{\mathrm{NL}}$	Nonlinear part including geometrically nonlinear variable
$\square_{\mathrm{L}}$	Linear part
$\square_{i}^{j}$	Coordinate axis *(i)* and current node number *(j)*
$\square_{j}$	Current node number
$\square^{i}$	Indicates the body
$\square_{(i-1)}$	Previous increment
$\square^{(k)}$	Current iteration number *(k)*
$\square^{(k-1)}$	Previous iteration
$\square^{\mathrm{sym}}$	Symmetric part of a tensor
$\square^{\mathrm{asy}}$	Anti-symmetric part of a tensor
$\square_{\mathrm{f}}$	Unconstrained freedom degree

$\square_{\mathrm{S}}$	Constrained freedom degree
$\square_{\mathrm{V}}$	Virtual position
$\dot{\square}$	Time derivative (rate) of a variable
$\widetilde{\square}$	Enhanced assumed strain variable
$\square^{\mathrm{T}}$	Transpose of a matrix
$\square_{ij}; \square_{mn}$	Tensor components

List of Abbreviations

3D	-	Three-dimensional
AA	-	Aluminium Alloy
AISF	-	Asymmetric Incremental Sheet Forming
BC	-	Boundary Condition
BUT	-	Bending-Under-Tension
CAD	-	Computer Aided Design
CAM	-	Computer Aided Manufacturing
CBT	-	Continuous Bending under Tension
CNC	-	Computer Numerical Control
CPU	-	Central Processing Unit
CSLVG	-	Constant Symmetric Local Velocity Gradient
DIC	-	Digital Image Correlation
DOF	-	Degree Of Freedom
DSIF	-	Double Sided Incremental Forming
FEM	-	Finite Element Method
FFLD	-	Fracture Forming Limit Diagram
FLC	-	Forming Limit Curve
FLD	-	Forming Limit Diagram
GA	-	Genetic Algorithm
GP	-	Gauss Point

ID	-	Identity
ISF	-	Incremental Sheet Forming
KUL	-	Catholic University of Leuven (Katholieke Universiteit Leuven)
MK	-	Marciniak-Kuczynski
NR	-	Newton-Raphson method
ORB	-	Oblique Roller Ball
PDE	-	Partial Differential Equations
PVW	-	Principle of Virtual Work
RD	-	Refinement/Derefinement; Radial Direction
RESS	-	Reduced Enhanced Solid-Shell
rpm	-	Rotation per minute
RSM	-	Response Surface Methodology
SPIF	-	Single Point Incremental Forming
SQP	-	Sequential Quadratic Programming
STL	-	Standard Template Library
TD	-	Transverse Direction
TL	-	Total Lagrangian
TPIF	-	Two Point Incremental Forming
TTS	-	Through-Thickness-Shear
UL	-	Updated Lagrangian
UTS	-	Ultimate Tensile Strength
VHW	-	Fraeijs de Veubeke-Hu-Washizu
VRB	-	Vertical Roller Ball
WJ	-	Water Jet

Chapter 1

Introduction

Sheet metal forming is a widely used and well-developed manufacturing process nowadays. Finished products have good quality, are geometrically accurate and parts are ready to be used. Additionally, it is used for large batches which amortize the tools cost, producing large quantities of components during a short time interval. However, the possibility to use conventional stamping processes to build low production of batches or personalized prototypes is naturally very expensive.
In R&D processes, prototype manufacturing is an important step in product development. Consequently, it is important to shorten the product's life-cycle and costs in its initial development. As a result, the Incremental Sheet Forming (ISF) technology appears as a new possibility to decrease the cost problem in small volume production. It introduces the use of metallic sheet for small batches production in an economic way without the need of expensive or dedicated tools. In fact, the study and development of this process have been growing over the last years.
The next sections in the current chapter will describe the ISF process and its variants. The thesis guidelines and main objectives are also presented.

1.1 Incremental Sheet Forming (ISF)

The designation of "incremental forming" covers several techniques with common features. This initial section will focus on the generality of the process as well as on its definition. The following explanation will describe the similarities between different alternatives of Incremental Sheet Forming (ISF).

The conventional spinning and shear spinning are forming processes closely related to ISF, but there are some fundamental differences. In general, with the

spinning concept the workpiece is clamped to a rotating mandrel while the spinning tool movement deforms it by means of several increments (Emmens *et al.*, 2010). This process is appropriate for axisymmetric products only. In the conventional spinning the component is formed through a series of extensive strokes with a forming tool. Shear spinning is similar, however the basic distinction is the fact that the tool is in permanent contact with the workpiece (Jeswiet *et al.*, 2005). Other consideration which distinguishes both variants of spinning is the final sheet thickness. In conventional spinning the final thickness is kept constant while in shear spinning the thickness is considerably reduced due to stretching mechanisms (Wong *et al.*, 2003; Emmens *et al.*, 2010). The final produced component using the spinning method is always axisymmetric and the mould in the rotating mandrel determines the final shape.

Since the 20th century until nowadays, many patents and developments have been performed on the ISF topic. The interest has been growing due to its advantageous applications, focused on the flexibility offered by the process. Nevertheless, the preliminary idea of ISF with a single tool was firstly mentioned in the patent of Leszak (Leszak, 1967). The real approximation to the well-known current ISF was reviewed by Mason in 1978 (Emmens *et al.*, 2010) for application on small batches of customized parts. The concept proposes the use of a single spherical tool with numerical control in three axes. The use of this method was possible with the advance of technology, more specifically with the appearance of numerical control machines. Later, the work of Mason was continued in Japan and it gave rise to new patents (Emmens *et al.*, 2010).

The ISF processes evolved more intensively since the 90's and new variants were developed and patented (Emmens *et al.*, 2010). In the literature, ISF processes are referenced as belonging to a group called Asymmetric Incremental Sheet Forming (AISF).

The AISF concept can include different configurations (Jeswiet *et al.*, 2005), as shown Figure 1.1. Its variants allow producing complex sheet components by CNC drive system of a simple tool, with or without the combined use of simple dies. The main common aspect in these variants is the use of a hemispherical forming tool in constant contact with the workpiece. The sheet is also clamped at its edges using a blank holder (Figure 1.1). During forming, the tool travels along the workpiece, following a specific trajectory determined by the user.

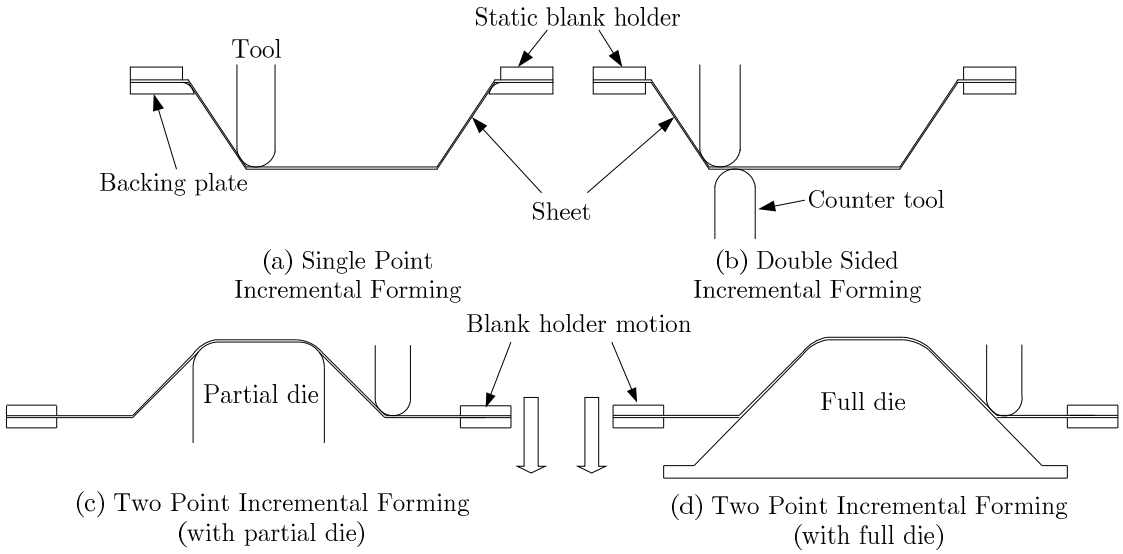

Figure 1.1: Asymmetric incremental sheet forming variants.

The Single Point Incremental Forming (SPIF) (Figure 1.1.a) variant can be considered as the real dieless forming technology as envisioned by Leszak (1967). The backing plate is used to create an angle transition near the clamped region. Within the AISF process group classification, the SPIF method is also called "negative forming" (Park and Kim, 2003). In SPIF process, the external surface does not contact with any mould or support.

The Two Point Incremental Forming (TPIF), also referred as "positive incremental forming", was first presented by Matsura in 1993 (Echrif and Hrairi, 2011). Its basic designation is due to the simultaneous contact between two points with both sheet surfaces. The pressure applied between the forming tool and the mould deforms the internal and external surfaces. The TPIF method can be divided in two categories: using a partial die (Figure 1.1.c) or using a full die (Figure 1.1.d) (Attanasio *et al.*, 2008). The partial die (c) is used as a static support to create strength support, influencing the final geometry accuracy. The TPIF with full die (d) uses a mould with the final component shape, located at the opposite surface of the metallic sheet. The mould is normally made using a cheap disposable material, which can be either a negative or a positive die (Reddy and Cao, 2014; Crowson, and Walker, 2015). This technique reduces the springback effect and increases geometrical accuracy (Attanasio *et al.*, 2006 and Callegari *et al.*, 2006). The blank holder device has a vertical displacement through guided columns during the forming process.

The incremental forming with counter tool (see Figure 1.1.b) is named as Double-Sided Incremental Forming (DSIF). It is a variant of TPIF process with an

addition of a second forming tool on the opposite surface, independently controlled, instead of a full or partial die. This particularity provides further flexibility to the process and reduces many limitations associated to the remaining variants. Another particularity is the fact that it does not use any backing plate. The main use given to this variant is to the production of highly complex parts (Jeswiet *et al.*, 2005; Malhotra *et al.*, 2012a; Ndip-Agbor *et al.*, 2015).

The purpose of this section was to introduce a brief description on the ISF process variants. A detailed review on technical developments in the last years can be found in the work of Emmens *et al.* (2010), Nimbalkar *et al.* (2013), Reddy and Cao (2014) and, recently, by Crowson, and Walker, 2015. In the present work, particular attention is devoted to the Single Point Incremental Forming (SPIF) variant (Figure 1.1.a) and the next section presents a more detailed description concerning this variant.

1.2 Single Point Incremental Sheet Forming (SPIF)

The SPIF concept represents a breakpoint with traditional forming processes. The classic press-stamping process generally deforms the sheet metal in only one stroke (even if multiple steps can occur). The sheet is forced by a punch against a mould, stretching the blank to the desired shape, while the edges are restrained by a blank holder, allowing however some sliding. In the SPIF process, on the other hand, the sheet is gradually deformed by a localized force. In any case, the external surface does not contact with any die or support. The final part is obtained by a toolpath strategy according to the desired final shape. Schematically, Figure 1.2 illustrates the SPIF process setup.

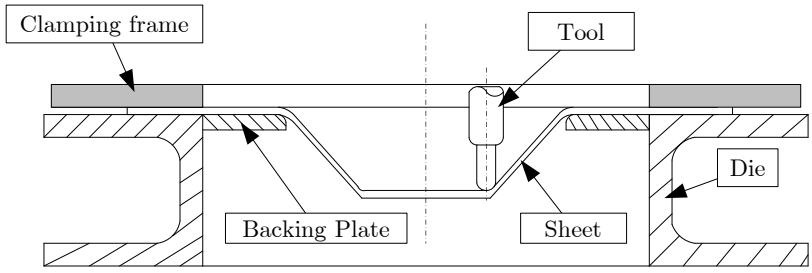

Figure 1.2: Single Point Incremental Forming (SPIF) setup (Sena *et al.*, 2011).

The sheet is previously clamped along its edges using a clamping frame (blank holder). A backing plate is necessary to provide an angle change at clamped region and decrease the springback effect during the forming progress. Springback phenomena can also be reduced using a compensatory algorithm (Allwood *et al.*, 2010). The tool is guided through a numerical control system, which defines the toolpath according to the desired final shape. The toolpath can be controlled by using a CAD/CAM software, where a change in the final shape can be fast and inexpensive. The pre-programmed contour combines the continuous contact of the tool along the sheet surface with successive small downward displacements. After each vertical increment, a new contour starts in the next horizontal plane. The component is constructed layer by layer (Figure 1.3.a). However, using a spiral toolpath (Figure 1.3.b) the tool gradually moves down and completes the downward movement equal to the incremental depth every time the tool completes 360° motion along the spiral. Figure 1.3 exhibits different toolpath strategies to perform a conical shape.

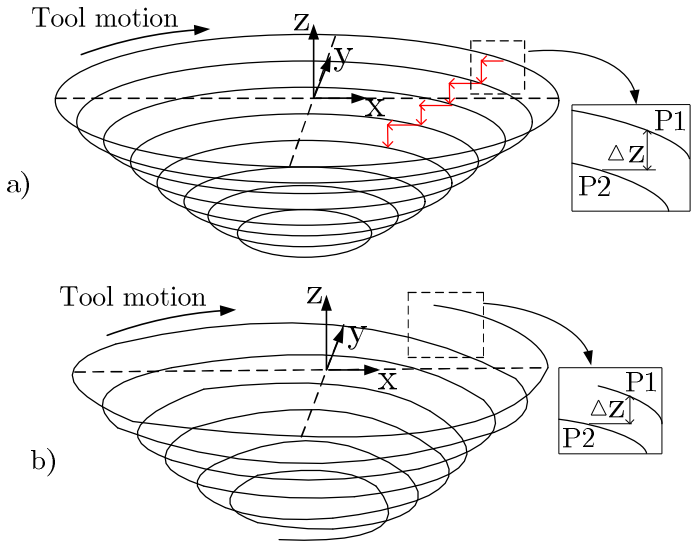

Figure 1.3: Contour a) and spiral b) toolpaths.

In general, the main practical setup of the SPIF method consists in the following steps: first, the final product is modelled by a CAD (Computer Aided Design) software, which allows creating a neutral file selected by the user. Next, the neutral file is exported to a CAM (Computer Aided Manufacturing) package. The first step for CAM package is to check the CAD file to visualise potential errors and then the toolpath is created (Jeswiet *et al.*, 2005). Next, the sheet is rigidly fixed on the frame, and the forming tool is controlled with a three-axis CNC

(Computer Numerical Control) software machine. Afterwards, during the process, the forming tool is in permanent contact with the sheet surface and moves vertically in each contour. Finally, the spherical tool repeats all these operations until the end of the toolpath, to obtain the final product.

Jeswiet *et al.* (2005) and (Hirt *et al.*, 2006) summarize the SPIF process advantages and limitations. The advantages are:

- the component can be directly formed from the CAD software;
- the process can be used in rapid prototyping to produce small number of parts in sheet metal and in polymers;
- it does not require expensive tools, i.e., punch and die. However, a backing plate can be necessary to create an angle change near the clamped region;
- a conventional CNC milling machine can be adopted for this process;
- the component sizes are limited to the machine table size;
- the operation is quiet and relatively without noise;
- the nature of the process involves deformation mechanisms that increase the material formability;
- the changes on the component design can be rapidly accommodated changing the CAM file.

The limitations are:

- a large forming time compared with the conventional stamping process;
- process limited to small production batches or prototypes;
- it is mandatory the use of multistage forming for steep wall angles, increasing the manufacturing time;
- some springback can occur after unclamping the component;
- lower geometric accuracy, particularly near the convex radii and bending edges areas.

A number of authors have studied the final product in order to analyse the influence of several parameters involved in the SPIF process. In summary, the following forming parameters are important in SPIF: the geometry of the forming tool, the sheet material, the sheet thickness, the toolpath, the stepdown increment size, the forming speeds (rotation and relative motion) and lubrication (Kim and Park, 2002; Kopac and Kampus, 2005; Cerro *et al.*, 2006; Duflou *et al.*, 2007b; Durante *et al.*, 2009; Ambrogio *et al.*, 2010b). Just a few studies from literature on the SPIF parameters influence are presented below.

1.2.1 Forming tool

Typically in SPIF process the tool tip is spherical and ensures a continuous contact point across the metal sheet surface. The relevant variables to the forming tool are its dimension, material and shape. This variable combination affects the time production, the surface quality and the geometry limitation of the final component.

In most applications, the spherical tip is solid and made out of steel. However, to reduce friction and increase tool lifetime can be used other options, such as, surface coating or a free rotating ball tool tip. The application of a polymeric material on the tool tip is used to avoid chemistry reactions or to improve surface quality. There is a wide range of tool diameters, from 4 mm, until a large spherical diameter as 100 mm. The spherical tool diameter values usually are between 4 mm to 15 mm (Jeswiet *et al.*, 2005). Therefore, the optimum tool depends of the product shape, the type of material and the depth at which the spherical tool will work.

The diameter depends also on component dimension and the negative slope (concave shape) of the wall angle. In the wall angle of the component (α) there is a point from which the tool diameter contact is maximum (Figure 1.4). This instant occurs when the contact point is tangent to the spherical surface. Figure 1.4 illustrates the tangential wall limit with a spherical tool.

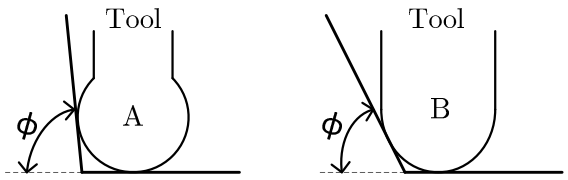

Figure 1.4: Wall contact with the forming tool.

To achieve a piece with a steep wall angle, it is necessary to select a forming tool with larger diameter than the sphere body support. The objective is to avoid contact between the sheet wall and the sphere support, as presented in Figure 1.4.A. The body support of the hemispherical head is used to mount the tool on the CNC milling machine shaft. Figure 1.4.B presents a tool configuration used to build a part with a small slope wall. Experiments have demonstrated that smaller diameter tools allow higher metal sheet formability than the use of tools with large diameter (Kim and Park, 2002; Jeswiet *et al.*, 2005; Bhattacharya *et al.*, 2011).

Ham and Jeswiet (2006) have studied the influence of the spherical diameter on the maximum wall slope angle. The research work demonstrated a significant increase on the maximum wall angle when tools with smaller diameters are used. The high formability with small diameter tools is a consequence of the force concentration and strains on a small area. The factor restricting the use of a small diameter is the tool resistance under bending fatigue effect.

1.2.2 Material and sheet thickness

The material and the sheet thickness may limit the forming process forces. The forming force involved is the result of the sheet characteristics, its material and its geometry.

Fratini *et al.* (2004) have investigated the influence of material proprieties on the formability. The tensile test was used for each selected material to determine its parameters. The material parameters were the following ones: strength coefficient (K), strain hardening coefficient[1] (n), Lankford coefficient (r_n), ultimate tensile strength (UTS) and the elongation percentage ($A\%$). From their SPIF experiments, for each material and using statistical analysis, they determined the influence of the above cited material proprieties. Their analysis concluded that the interaction between the strength coefficient (K) and strain hardening coefficients (n) had the highest influence on formability. Generally, higher hardening coefficients will provide higher formability.

Ham and Jeswiet (2006) have performed a research about the influence of the sheet thickness on the maximum wall angle and showed that increasing the thickness contributes to increase the wall angle. The maximum wall angle defines an indicator of formability. In this work, the interaction between the increasing thickness and the tool size decrease was analysed. The research showed a significant improvement in the wall angle when the tool diameter decreases and the sheet thickness increases.

[1] Stress (σ) strain (ε) curve expressed by an equation such as $\sigma = K\varepsilon^n$.

1.2.3 Forming speed

The tool rotation speed and the travel velocity over the sheet surface influence the sliding friction and the frictional heating at the tool/sheet interface. The process time and the final surface quality of the part are the final results which evaluate process performance. The tool relative motion over the sheet is directly proportional to the heat generated by friction. Increasing the speed improves the material formability due to the heating. However, there are negative effects, like higher speed rate, generates higher surface roughness, increases the tool wear and the lubricant film disappears faster. The high rotational velocity increases the probability to develop marks on the sheet surface (Jeswiet *et al.*, 2005; Ambrogio *et al.*, 2010b; Hamilton and Jeswiet, 2010).

1.2.4 Toolpath and vertical increment

Many experimental studies have been performed to find an optimum toolpath which gives the best results in terms of surface quality. The toolpath and the vertical increment are defined together on the CAM package. These parameters have direct impact on the dimensional accuracy, surface finish, formability, thickness variation and processing time. A number of researchers have discussed their effects and different conclusions were found.

Ham and Jeswiet (2006) have used the forming maximum angle to measure the material formability of AA3003. In their work, they have analysed the influence of the vertical step in the maximum wall angle and it was concluded that there is no significant effect on the final wall angle. Hence, it was shown that the vertical increment has an insignificant influence on the formability.

Many attempts have been performed to analyse various toolpath strategies, such as contour, spiral, radial and multiple-stages. The most common toolpaths are contours or spirals (Figure 1.3) with increasing depth, following the shape profile of the final product.

Attanasio and collaborators (Attanasio *et al.*, 2006; Attanasio *et al.*, 2008) have performed two different toolpaths. In the first experiment the tool followed a series of consecutive contours using a constant vertical step (ΔZ), Figure 1.5.a. With this strategy, the sheet is marked at the transition point between consecutive toolpath contours. The surface quality is poor when the vertical step has a high value. The second toolpath type tested an experiment with constant "scallop

height" (h), Figure 1.5.b. The tool follows a series of consecutive contours with a variable vertical step (ΔZ) in order to keep a constant value of scallop height (h). This strategy avoids the marked transition points and improves the final surface quality.

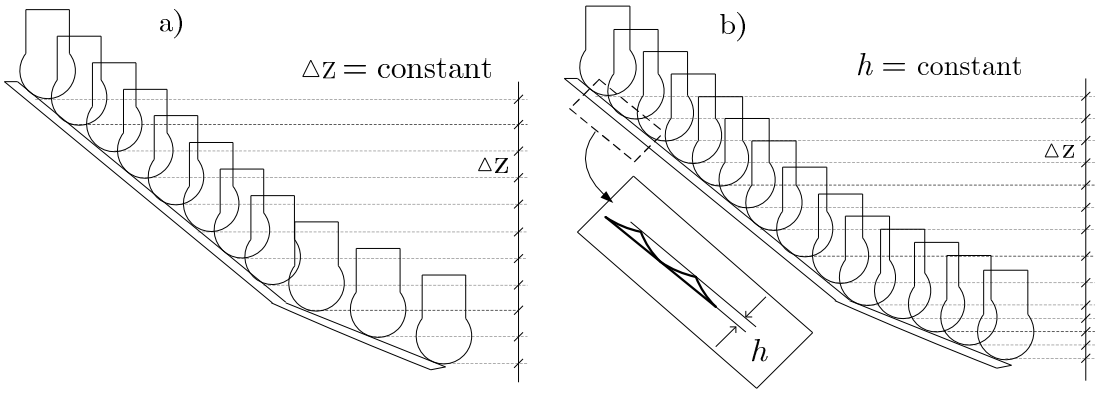

Figure 1.5: Schematic representation of a) constant vertical incremental (ΔZ) and b) constant scallop height (h).

The vertical step size tends to be related with the wall angle and roughness at the sheet surface. A small step size requires more process time to form the component but the surface quality improves. These experimental tests demonstrated how relevant is the toolpath with a variable step depth (depending on the part geometry). In particular, a correct value of the maximum step depth (ΔZ) and the scallop height (h) must be chosen in order to obtain good results in terms of surface quality, geometric accuracy and thickness of a final component.

1.2.5 Lubrication

The necessity of lubrication is related to the temperature generated at the tool/sheet interface, surface roughness and the forming tool wear (Kopac and Kampus, 2005; Azevedo *et al.*, 2015). The products obtained using the SPIF process are normally functional at its finished shape and, in this sense, the state of the surface is a significant subject. For that reason, the use of lubricants is common.

Kim and Park (2002) have tested two different types of tools, a tool with a free rotation ball at the tool tip and a standard tool with hemispherical tip. Both tools were tested with and without lubrication, which was grease. The authors have observed for the same conditions that the tool with rolling ball on the tip achieves

higher formability than the tool with standard tip. Additionally, the results showed that using a standard hemispheric tip without lubrication, it provided occurrence of scratches over the sheet. Finally, using a tool with a free ball on the tip without lubrication was considered the most ideal solution to increase formability. The friction between tool/sheet interfaces increases the tool pressure, lowering the stress state in the sheet. For this reason, damage is delayed and formability increases. A controlled friction at the tool/sheet interface helps to improve the formability. However, if friction increases significantly, it could result in fracture.

1.3 Machinery used in SPIF

Equipment intended for SPIF covers different topologies of machines used in the industry and in academic research. The execution of SPIF process presents essential aspects: it uses a simple spherical tip to build different shapes and the main process feature is the numerical control of the tool axis. The axis control depends of the degrees of freedom (DOF) available on the machine. There are different equipments to produce a component using the SPIF method, such as adopting a CNC milling machine, a robotic arm or a purposely built machine.

The most common applications to perform SPIF experiments has been carried out using an adapted CNC milling machine. Their advantages are the easy upgrade to work as SPIF machine, easily found in industry, considerable stiffness and large productivity rate. On the other hand, it offers a limited number of DOF (Jeswiet *et al.*, 2005). For instance, this choice is the one of Shim and Park (2001), Filice *et al.* (2002), Jeswiet et al. (2002), Fratini *et al.* (2004), Ceretti *et al.* (2004), Ambrogio *et al.* (2005; 2010a; b), Kopac and Kampus (2005), Araghi *et al.* (2009), Dejardin *et al.* (2010), just to mention some research groups.

Similarly, the industrial robotic arm appears as an alternative for many authors, such as Schafer and Schraft, 2005; Duflou *et al.*, 2005; Meier *et al.*, 2005; Lamminen *et al.*, 2005, as summarized by Callegari *et al.*, 2006. They have implemented this solution due to the flexibility given by the available six axes. It allows the tool positioning at different angles relatively to the sheet surface and gives the possibility to combine multiple steps with a single tool. The robotic arm has a large working volume and fast operation. The major drawbacks are the low

stiffness and a very low maximum force, which leads to a less accurate tool position, especially under high loading conditions (Jeswiet *et al.*, 2005).

Nowadays, purposely built machines for SPIF process are commercially available, such as the one developed by the Amino Corporation (Amino *et al.* 2002). However, a number of academic research groups have developed their own machine to perform the SPIF process. As examples, the machine from Julian Allwood's group at University of Cambridge (Allwood *et al.* 2005) and the innovative prototype machine called SPIF-A at University of Aveiro (Alves de Sousa *et al.*, 2014). This last referred SPIF machine introduced a Stewart platform (Yau, 2001) adaptation, allowing six independent degrees of freedom. Figure 1.6 exhibits the innovative prototype machine developed at University of Aveiro based on Stewart platform purposely adopted for SPIF.

Figure 1.6: Prototype machine for SPIF from University of Aveiro.

Among these different equipment options, the use of CAD/CAM software is the common feature between them to obtain a toolpath. The CAD model of a component is converted into a neutral file (STL) containing the geometric information. Afterward, the CAD model is sliced into horizontal layers through the CAM software and converted into a toolpath. Figure 1.7 exhibits the standard strategy to build a toolpath.

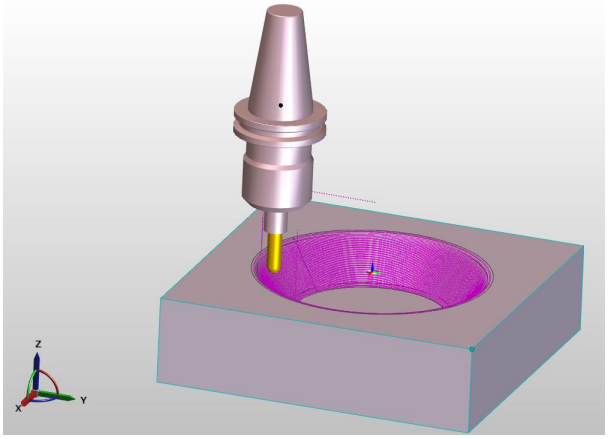

Figure 1.7: Standard strategy to build a toolpath for SPIF.

A brief overview of the SPIF process has been given based on the available literature. In this context, previous sections introduced a general understanding of SPIF process which will be the focus of the present work study. Section 1.4 presents the thesis scope and motivation, while Section 1.5 summarizes its contents.

1.4 Motivation and Scope

Many issues appear when simulating the SPIF process by the Finite Element Method (FEM). As always, a compromise between accuracy and CPU efficiency is necessary. Accuracy from the results of numerical simulations, specially related to the prediction of the forming forces, is important since it contributes to the protection of the tool and the machinery used in the process.

The present work aims to give a relevant contribution to the state-of-the-art and knowledge level of the SPIF process, from both academic and industrial standpoints, thus increasing the process feasibility in the numerical simulation field. In this topic, since the tool/sheet contact status changes continuously and only a small area is plastically deformed at each time increment, common methodologies resorting Finite Element Method (FEM) codes lose efficiency. The time increments become small and consequently the simulations take huge CPU time.

The work will focus on the numerical simulation performance based on the FEM, in order to reduce the high computational time of SPIF simulation. The main task includes the implementation of the Finite Element technology, with new elements such as those related to solid-shell finite element formulations and

remeshing algorithms. Solid-shell finite elements allow the automatic consideration of thickness variations taking into account 3D stress analysis. The use of different constitutive laws cover applications with distinct materials, such as aluminium and steel alloys, to assess the numerical accuracy.

An improved numerical simulation within the SPIF framework combined with accurate material modelling can be seen as the final objective. Benchmark proposals are used as case-studies to evaluate the numerical simulation predictions compared with experimental measurements.

1.5 Main objectives

The framework of this thesis is the numerical simulation of asymmetric and axisymmetric component shapes incrementally made using SPIF process based on FEM supported by experimental validation. The numerical simulations include the adaptive remeshing method combined with a hexahedral finite element, more properly the use of the RESS (Reduced Enhanced Solid-Shell). More details on this solid-shell element can be found in the series of works from Alves de Sousa *et al.* (2005; 2006; 2007). The choice of a solid-shell formulation to simulate sheet metal forming operations is also based on the possibility to use a general 3D constitutive law behaviour, while classical shell finite elements are implicitly based on plane stress/strain assumptions. Additionally, thickness variations and double-sided contact conditions are easily and automatically considered with solid-shell finite elements.

The main goals aim the implementation of the RESS finite element, especially designed for sheet metal forming, in the in-house FEM code named LAGAMINE (Cescotto and Grober, 1985). The extension of the adaptive remeshing technique, currently available in LAGAMINE code for a shell element (Lequesne *et al.*, 2008), to use it with the mentioned solid-shell element. These features are not available in common commercial FEM codes. Implicit analysis is used to perform the numerical simulations. It is worth noting that no previous work has been carried out using remeshing strategies with hexahedral elements on SPIF, which makes this work innovative.

1.6 Reading structure

The present dissertation is divided into six chapters.

The current chapter, Chapter 1 (*Introduction*), provides a summarized review on the field of Incremental Sheet Forming (ISF) and its variants. The process concept is introduced and practical aspects are described for each variant. A detailed description is given on the SPIF process. The main research topics are here defined along with the research objectives.

The second chapter (*State of the art: A review*) presents an updated literature review of the state of the art of SPIF process. It aims a review based on the experimental developments and an in-depth lecture in the numerical simulation analysis. The results presented are from recently published works.

The third chapter (*Topics in nonlinear formulation*) gives a brief review on nonlinear continuum mechanics. It presents also a description concerning the software used in the numerical simulations. The implicit scheme is the choice performed in the numerical simulation analysis. The theoretical aspects of a Reduced Enhanced Solid Shell (RESS) finite element, and alternative formulations that can be implemented, are referred.

The fourth chapter (*Remeshing for SPIF:* Description) describes the adaptive remeshing technique and presents its application combined with the solid-shell finite element. The line test benchmark is used to demonstrate the advantages, comparing results with and without remeshing use.

The fifth chapter (*Numerical tests*) focuses on the demonstrative case studies of SPIF process. The main objectives are to achieve accurate and fast numerical simulation results of SPIF.

Finally, the sixth chapter (*Conclusion*) ends the research work with the final considerations, including perspectives for future research works.

Chapter 2

State of the art: A review

Single point incremental forming (SPIF) is an emerging technique within sheet metal prototyping and small batch production, as previously outlined. Research interest has grown over the last years, both experimentally and numerically. According to the current state of the art review, it can cover a range of relevant topics presented in distinct sections below.
The present literature review deals with the state of the art on the experimental and numerical developments of SPIF process. In Section 2.1, the overview is focused on experimental studies. The literature review gives, in Section 2.2, more emphasis to research developments on numerical simulations, with the aim of providing a better understanding of the process and its peculiarities. Finally in Section 2.3, an overview is presented on the deformation mechanisms suggested in literature.

2.1 Experimental research and developments

In the last years, the SPIF process was intensively investigated and experimental evolutions allowed achieving accuracies at industrial level. The following experimental development overview includes the process optimization and the understanding of its physical characteristics, which influence the forming process.

2.1.1 Influence of SPIF parameters on the axial force

A number of researchers have performed experimental analysis on the forming forces by forming simple shapes using SPIF process, such as, Jeswiet *et al.* (2005), Jeswiet and Szekeres (2005), Duflou *et al.* (2007b), Filice *et al.* (2006); Ambrogio *et al.* (2007); Aerens *et al.* (2009); Henrard *et al.* (2010), just to mention a few. Globally, they have claimed that the forming forces increase with the tool diameter, the wall angle, the incremental step size and the sheet thickness.

Duflou *et al.* (2007b) have studied the influence of four main process parameters on the forming forces required to form a sheet metal part using SPIF. These were the tool diameter, the vertical step size, the steepness of the wall angle and the thickness of the sheet metal. The experiments were carried out using a 3-axis CNC milling machine. The investigated materials were different aluminium alloys, 3003-O and 3103-O, with different thickness values. The selected shapes for the experimental analysis were the pyramidal and conical shapes. The total forming force obtained for a pyramid shape was in the same order of force magnitudes to form a cone shape with identical process parameters. However, the individual analysis of each force components (Fx, Fy, Fz) exhibited different patterns. According to the results, increasing the vertical step size, tool diameter, wall angle or sheet thickness, the forces increased. Among these parameters and exploring their limits, the vertical step size revealed more significant effect. The combination of tool diameter in function of vertical step size revealed a linear fit approximation of forces. The relation found between sheet thickness and wall angle provided an accurate analytical approximation of force trends through a quadratic fit. From experimental measurements the force curves for wall angles above 60^{o} revealed a considerable force decrease after reaching an evident peak value. The noticeable decreasing of force can be considered a failure indicator explained due to the occurrence of localized necking. Figure 2.1 schematically represents the force peak and force valley profile occurrence for large wall angle shapes.

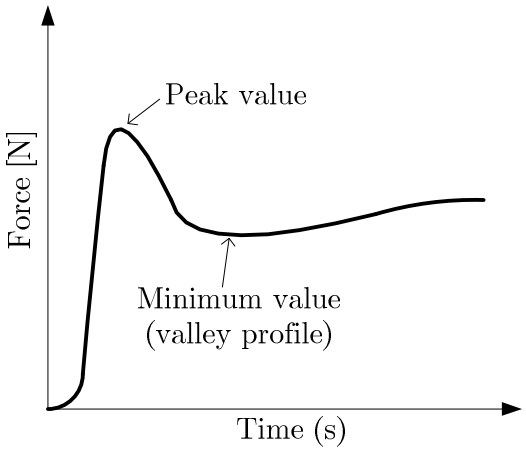

Figure 2.1: Variation of force curve for large wall angle values.

According to these authors, usually the peak value occurs in components with wall angles near the failure. After reaching the minimum force level, slowly it increases again. The thickness has decreased when the force decreased, and the minimum thickness value corresponds to the minimum force level. Several cone shapes were built with high wall angles above its critical value and some specimens failed. However, when the shapes around the critical wall angle value fractured, and their forming were repeated, some shapes were formed without fracture of the sheet. These results can be explained by localised material defects and/or small variation of the sheet thickness. The failure prediction can be supported observing the fast decrease of force. The pattern of the force curve between the peak and the minimum force can be used as a failure indicator.

Petek *et al.* (2009b) have experimentally analysed different process parameters, which affect the magnitude of forming forces and deformation. The analysed parameters were the wall angle, the tool rotation, the vertical step size, the tool diameter and the lubrication. Simple conical shapes were used and the material chosen was steel DC05 with 1 mm of thickness. The experiments are carried out for different wall angles. It was established that the maximum achievable wall angle in forming of the cone shape, before the crack occurrence, was 70°. At the wall angle of 71° the fracture already occurred. The deformation was measured using the graphometric analysis based on the size and directions of the major and minor strains. Circular grids are printed on the specimens before the forming process to evaluate the local deformation. After deformation, the grid circles were distorted into ellipses and the strains are measured in radial direction (major strain) and perpendicular to radial direction (minor strain) for each ellipse

along radial direction of the shape. Figure 2.2 exhibits the measurement directions of the circular grids.

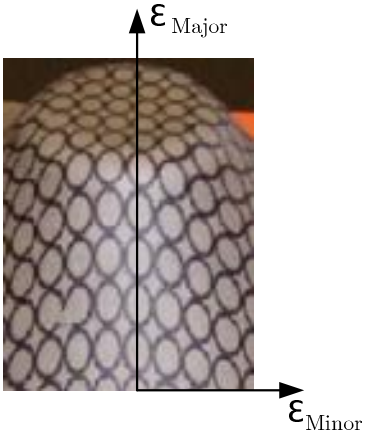

Figure 2.2: Grid circles distorted into ellipses and measurements orientation (Ambrogio *et al.*, 2008).

A significant difference was observed for wall angle values higher than 50°, a prominent axial force peak appeared, as similarly exhibited in Figure 2.1. This peak value could be noticed in the region where the fracture occurred at the maximum wall angle. In general, the experimental results of forces increase when the wall angle increases. Increasing the tool diameter and the vertical step size caused larger forces and deformations. The tool spindle rotation and the lubrication did not affect the force but they have strongly influenced the final quality of the component surface.

The obtained results from Duflou *et al.* (2007b) and Petek *et al.* (2009b) for different materials described a similar behaviour in terms of force curve profile. However, for aluminium the evident force peak appears in shapes with wall angles higher than 40° while for shapes with DC05 steel it occurred in wall angles higher than 50°.

Bagudanch *et al.* (2013) have studied the influence of several SPIF process parameters on forming forces. The parameters analysed were the tool diameter, the vertical step size and the spindle speed. The experiments were carried out on adopted 3-axis CNC milling machine. The material tested was stainless steel AISI304 with a sheet thickness of 0.8 mm. The experimental results demonstrate that the maximum axial force increases in function of tool diameter, due to the increase of contact zone between the tool and the sheet when higher tool diameters are used. Similarly, the increase of the vertical step size also provided an increase of the maximum force. Increasing the vertical step size, more material has to be pushed down in order to be deformed. On the other hand, increasing the tool

diameter could reduce the forming time and consequently higher vertical step size could be employed without compromising the surface finishing. The increase of the maximum forming force is not a desirable effect, it can be a limiting factor for the machinery used in the manufacturing process. Concerning the spindle speed influence, it decreases the maximum force value for higher spindle speeds, which can be explained due to the variation of the friction. In addition, the authors mentioned the effect of the spindle speed as being significant and it is not considered in the equation of Aerens *et al.* (2009) described in Section 2.1.2. However, a significant decrease of the temperature was observed when the tool rotates freely, but more force was needed to produce a given component. The control of the spindle speed mainly ensures the safe machinery operation and allows its application on hard materials. It generates heat and increases the formability of the material.

Riadh *et al.* (2013) have proposed an optimization procedure based on finite element analysis, experiments, Response Surface Methodology (RSM) and Genetic Algorithms (GA) method. In this work, the main objective is to minimize the thinning rate and maximum load force, analysing some SPIF process parameters. The steps of optimization procedure included the response surface method to establish the mathematical models that represent the relationship between design factors and the objective functions. The GA is used to find the optimum solutions from the RSM. The sheet metal used in the numerical simulation of a conical shape was AA3003-O. A Box-Behnken experimental design was used to determine the effect of process parameters chosen on the considered response methodology. According to the results, the parameters with more significant influence in maximum tool load and sheet thinning were the initial thickness and the wall angle slope respectively. Concerning the tool diameter parameter, it showed more effect in the maximum tool load than in the sheet thinning. The sheet thinning exhibited more sensitivity to the vertical step size than to the tool diameter.

Table 2.1 summarizes the influence of major process parameters on the axial force analysed by several authors chosen from literature review. Analogous analysis focused on the SPIF process parameters have been carried out by other authors, such as previously outlined in Section 1.2.

Table 2.1: Influence of SPIF process parameters on the axial force.

Paper	Shape	Material	Process parameters	Observation on axial force behaviour
Duflou *et al.* (2007b)	Cone	AA3003-O AA3103-O	Vertical step size increase	Increase
			Tool diameter increase	
			Sheet thickness increase	
	Pyramid		Wall angle slope increase	
			Wall angle slope $> 40^{o}$	Increase / visible peak value
			Lubrication	No significant influence
			Without Lubrication	Premature failure occurrence
Petek *et al.* (2009b)	Cone	DC05	Wall angle slope increase	Increase
			Tool diameter increase	
			Vertical step size increase	
			Wall angle slope $> 50^{o}$	Increase / visible peak value
			Tool rotation	Fix tool > Free tool > 40 rpm
				No significant influence
			Wall angle slope $> 70^{o}$	Crack occurrence
			Lubrication	No significant influence

Bagudanch *et al.* (2013)	Conical frustum	Stainless steel AISI304	Tool diameter increase	Increase
			Vertical step size increase	
			Tool rotation	Free > 1000 rpm
Riadh *et al.* (2013)	Cone	AA3003-O	Wall angle slope	Sheet thickness > Wall angle slope
			Sheet thickness	
			Tool diameter	Tool diameter > Vertical step size
			Vertical step size	

2.1.2 Force prediction

Aerens *et al.* (2009) have established an analytical formulae allowing a prediction of force components during SPIF process. This study has been based on a large set of systematic experiments and on numerical simulation results by the Finite Element Method (FEM). It leaded to analytical formulae to compute the three main components of the force for five selected materials (AA3003, AA5754, DC01, AISI304, 65Cr2) in function of the working conditions (sheet thickness, wall angle, tool diameter, and vertical step). The analytical equations for the force components are partially obtained using regression techniques based on the physics of the process and Finite Element simulations. These equations are used to compute the axial and tangential components of forming force. For conical shapes, during the toolpath, the in-plane forces result from tangential and radial components. Preliminary, experiments were carried out to identify the relation between each parameter (sheet thickness, wall angle, tool diameter, and step down) and the three components of the force. Afterwards, the regression equations are obtained from the relation between the parameters and each selected material. The Finite Element simulations are performed to study the contact areas near the forming tool for different wall angles. Three scales of mesh models are used, 40° pie section called "global model" and two rectangular parts of the mesh with different sizes, mentioned as "large submodel" and "small submodel". This strategy allowed the study of contact area between the tool and the sheet, and the distribution of the contact pressure, which demonstrated an acceptable precision. Furthermore, a general model has been deduced, allowing an analytical value approximation of force for any material, based on knowledge of the tensile strength.

The analytical equation developed for axial forming force prediction of SPIF of Aerens *et al.* (2009) was compared with experimental results of SPIF under different working conditions selected by Pérez-Santiago *et al.* (2011). The formulae of Aerens *et al.* (2009) was applied to estimate the axial forming force of conical and pyramidal shapes with variable and constant wall angle slopes. For each selected case, they have presented the analytical force prediction and its error compared to the experimental measurements and FEM simulations. It was verified that the proposed analytical formula has been adequate for constant wall angle slopes but limited to predict the forming force of variable wall angle geometries. The FEM simulation predicted acceptable forming force for aluminium alloys. However, they have mentioned that more detailed constitutive modelling and characterization tests are necessary for other materials. Finally, the authors have claimed that the FEM models are the best choice to predict forming forces of variable wall angle components.

2.1.3 Twist phenomena

Twist, an undesirable deformation phenomenon occurring in ISF, was firstly observed by Matsubara (2001) during experiments performed using Two Point Incremental Forming (TPIF) process. It was found to be caused by uncontrolled rotation of the workpiece around the axial support structure as a result of tangential forces exercised on the workpiece by the tool. Similarly, Jadhav (2004) have explained twist effect in SPIF as being the result of tangential forces, which induced in-plane shear into the workpiece. Figure 2.3 exhibits twist phenomenon observed in different components shapes.

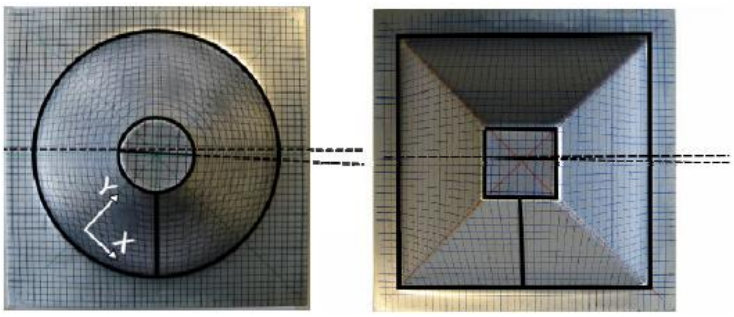

Figure 2.3: Twist effect observed for cone and pyramid shapes (Vanhove et al., 2010).

Duflou *et al.* (2010) and Vanhove *et al.* (2010) have observed the twist effect in SPIF of pyramid and cone shapes using unidirectional toolpaths, as presented in Figure 2.3. They have quantified twist in terms of angle by drawing appropriate lines (radial lines in case of cone) before forming and measuring their deviations after forming. They classified the twist in two categories: the conventional one, which occurred at low wall angles, and the reverse one, occurring at high angles or near formability limits. At low wall angles, conventional twist occurred in toolpath direction until a wall angle of approximately 40° for an AA3103 with 1.5 mm of thickness. This can be explained by the reduction of wall thickness and approximately constant tangential force in function of the wall angle, as observed by Aerens *et al.* (2009). At high wall angles for pyramidal component, an asymmetric strain distribution, asymmetric thickness and force distribution became noticeable. Then, twist effect started to decrease in tool motion direction and reversing its effect into opposite direction. They also reported that the geometrical features, for instance, ribs and corners have significant influence on the twist. However, the authors found that the twist was independent of tool diameter, rotation speed of the tool, and tool feed rate. While with an increased vertical step size between contours a higher rate of twist was observed. Summarizing, the twist along tool motion direction increased with wall angle until a certain value, and then this tendency is reversed for further increase of wall angle.

Later, Asghar *et al.* (2012) have carried out experimental and numerical analysis to study the effect of SPIF process parameters on twist. Their work was based on the study of twist in conical components. The authors concluded that the twist increased with the increase of incremental depth. However, they claimed that twist effect increases with the decreases of tool diameter and sheet thickness, while previous authors did not verified the effect of these parameters. Feed rate effects showed insignificant influence. The numerical predictions obtained good agreement with experimental results.

2.1.4 Forming tool developments

The majority of research works are focused on the use of a standard hemispherical tool to incrementally form the sheet into a final shape. Interesting alternative applications to replace the rigid tool have been explored, including the use of different typologies of roller ball tip, laser irradiation and water jet. Hereafter works found in literature are presented using these different forming tools.

a) Free rotation ball tip

Shim and Park (2001) have developed a forming tool containing a freely rotating ball on the tool tip. Its main advantages are lower forming load, lower friction and, as a result, better surface finish. The authors used the tool with free-ball tip to characterize the formability of AA1050 sheet in the forming of various shapes: triangle, square, pentagon, hexagon, octagon, circle and square with round corners. The analysis of these shapes were performed until crack occurrence. The major and minor strains of deformed grids were measured around cracks. Finite Element analysis was performed to understand the deformation of SPIF and compared with the experimental results. Their research results confirmed that the deformation is limited to the vicinity of the contact area of the tool. In general, from the results all the shapes, except the circle, confirmed that near equi-biaxial stretching occurred at the corner, while near plane-strain stretching occurred along straight side. The circular shape developed a much larger minor strain than any other shape. The crack has frequently happened at the corners due to its higher deformation than in straight side. The forming limit curve exhibited a singular forming behaviour, it appeared to be a straight line with a negative slope in the positive region of the minor strain (see Figure 2.8).

b) Comparison of Oblique Roller Ball and Vertical Roller Ball

Lu *et al.* (2014) have investigated a newly developed Oblique Roller Ball (ORB) tool. In order to examine the efficiency of the developed ORB tool, a series of tests have been carried out to access the final surface quality, formability and deformation behaviour. Different topologies of forming tools were experimentally compared, including the conventional rigid tool (a), the Vertical Roller Ball (VRB) tool (b) and the ORB tool (c). Figure 2.4 exhibits all tools experimentally tested.

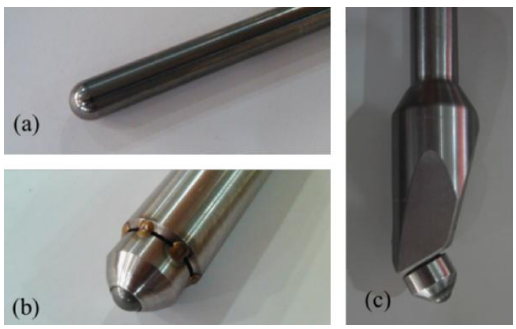

Figure 2.4: Different topologies of forming tools tested, (a) standard hemispherical rigid tool, (b) VRB and (c) ORB (Lu et al., 2014).

Concerning the material sheet, different aluminium alloys were used. The experimental results were explained based on the stress state analysis assuming an analytical membrane model approach similar to Silva *et al.* (2008). The tests were performed using a rigid tool with lubricant, VRB and ORB tools, both without lubricant. The experimental results revealed better final surface quality and lower friction condition with using roller-ball tools than a rigid tool. The friction reduction was more apparent when the pressure between the tool and sheet surface was increased to a specific level. The surfaces processed by ORB tool showed low roughness values, while those processed with a rigid tool have obtained the maximum roughness values. Comparing the VRB and ORB tools, it was found similar roughness values without significant difference. The frictional effect on SPIF formability was evaluated using the rigid and the ORB tools. The deformation behaviour suggests that friction between the tool and the sheet was the main factor which caused the Through-Thickness-Shear (TTS). Experimental results using the rigid tool showed stretching occurrence along the radial direction and larger TTS along the tool motion direction than using the ORB tool. The fracture depth of parts produced by using the rigid tool tip occurred at lower depths than using the ORB tool. Concerning the analytical approach, it was assumed that the increase of TTS results has two contrary effects. Firstly, the yielding of the sheet metal around contact zone increases deformation stability without necking occurrence. Secondly, increasing the stress triaxiality decreases the formability. In addition, the friction affected the surface roughness. The sheet surface exhibited scratches processed by the rigid tool. These scratches probably have reduced the formability of the sheet. However, it was difficult to assess quantitatively the influence of the final surface quality on the overall formability. This study considered TTS as a secondary effect and the source of the increased formability was largely due to Bending Under Tension (BUT) or other deformation mechanisms. Generally, the ORB tool demonstrated its advantages: it reduced the friction between the tool and the sheet surface, it decreased the forming load, increased the formability and improved the final surface quality even without lubricants. However, no matter what tool was used, the roughness of the formed part surface increased in comparison with the initial surface. The ORB tool has shown its advantages due to its use in a 3-axis CNC milling machine. As this machine has a limited number of degrees of freedom, its combination with the ORB tool, facilitates the forming of wall angles.

c) Laser forming process coupled with SPIF

Laser Forming Process is based on thermal effect induced on the sheet by laser irradiation.

Duflou *et al.* (2007a) have introduced the laser device in the SPIF process. The objective of its use was to heat locally the metal sheet on the opposite sheet surface of the tool application. The effectiveness of local dynamic heating was aimed to improve the material formability, dimensional accuracy and reduce the forces involved in the process. The local heating increased the material ductility reducing the most important parameters of material, i.e., the yield stress and the hardening coefficient locally. In the vicinity of the local heating area the material parameters have the initial values, which are high, ensuring a low springback effect increasing the final dimensional accuracy. Furthermore, it was demonstrated that the formability of different materials can be significantly extended. The elastic deformation during unclamping allowed concluding that appropriate settings of the local heating and cooling parameters leads to reduced residual stress levels. The localised heating was ensured by a good synchronization between the heat source (laser) and the forming tool. The power source and the laser diameter are the monitored parameters to ensure that the heating is limited to the contact area between the tool and sheet.

d) Water jet as a tool

In Water Jet forming (WJ) the forming tool is replaced by a water jet. The advantages found are: more flexibility, better surface integrity, less tooling requirements, lower equipment costs, less environmental impact and contact conditions. On the other hand, WJ is less accurate, consumes more energy and takes more time than other forming tool adopted (Jurisevic *et al.*, 2005).

Jurisevic *et al.* (2005) have introduced high-speed WJ as a tool for dieless ISF variants. For a better process characterization, the relative jet diameter (k) was introduced, which was defined as the ratio between the WJ diameter (d_{WJ}) and the sheet thickness (t). Relevant process parameters were identified and technological windows were phenomenological predicted, showing that WJ can be applied as an alternative solution of SPIF. Accordingly, two technological windows (operation regions) were defined by the water pressure (p_{W}) and the relative jet diameter (k), while a last process parameter was defined by the WJ distance (h_{SO}). Figure 2.5

represents schematically both technological windows used for WJ process adopted for SPIF.

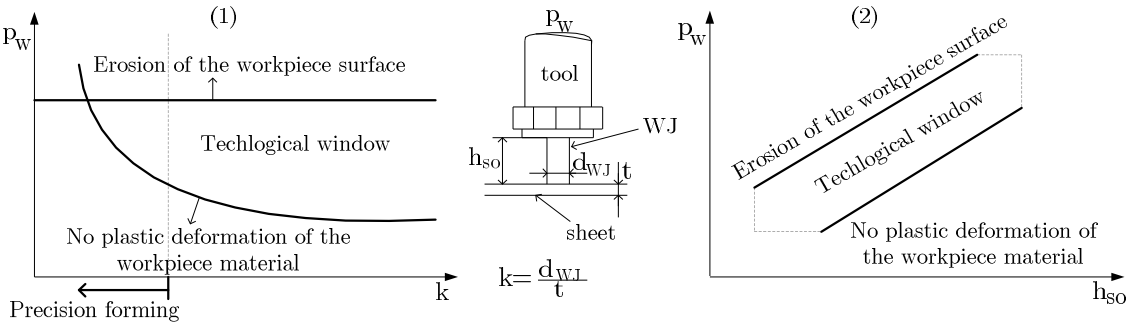

Figure 2.5: Technological windows of WJ process.

In all cases, a quantitative interpretation was performed through experiments. A first technological window (1) was limited on the top by the surface pressure at which erosion starts. In the bottom it was limited by the force of the WJ needed to induce plastic deformation into the blank of a given thickness (t). Both limit lines are dependent of the material and consequently, technological windows have to be found separately for each workpiece material. A second technological window (2) can also be defined according to the water pressure (p_W) and the distance between the forming WJ and the workpiece (h_{SO}). Similarly, the technological window was defined as a function of the water pressure and the relative jet diameter. It can be observed that it was limited due to erosion, which takes place at higher water pressures and smaller distances. On the other hand, if the water pressure is too low and the distance is too high no plastic deformation occurs. The operation region of the process depends on the sheet material.

Petek *et al.* (2009a) have also analysed WJ process. Their work aimed the study of the most influential parameters which affect the WJ and classical SPIF process. Experimental work was based on the forming of a simple pyramidal shape in aluminium sheet with 0.23 mm of thickness. It was observed that the two processes were complementary according to the optimal range of horizontal step and wall angle. From the experimental research carried out it could be concluded that, rigid tool was more appropriate in cases of bigger wall angles [44° to 60°] and smaller horizontal steps [0.2 mm to 0.8 mm]. The maximum wall angle obtained with rigid tool using the horizontal step size of 0.2 mm was 60°. Appling WJ, it was better at larger horizontal steps [0.8 mm to 1.6 mm] and smaller wall angles [22° to 26°]. The controlling principle is the main difference between both forming tools. The main process parameter using rigid tool was the definition of the loads acting

on the work sheet surface. Using WJ the main parameters were the water pressure (p_W) and the distance (h_{SO}), which define the loads on the work sheet surface. They have concluded that the rigid tool enables higher process accuracy and shorter machining time than the WJ application.

Besides these few descriptions of tooling used in SPIF process found in the literature review, the most widely used option continues to be a solid hemispherical rigid tool. Its main advantages are to keep the SPIF process simple and cheap.

2.1.5 Tool trajectory

Currently, the solutions available involve the process enhancement, already described in sections 1.3 and 2.1.4, as well as toolpath optimization strategies. In this sense, these solutions have been proposed in order to enhance SPIF performance at industrial level. In terms of toolpath strategy, it concerns the manufacture of products with high quality and accuracy, which are fundamental topics on which the interest of research groups are focused. According to the literature review, there are different proposals regarding the toolpath modification: real time toolpath optimization (Meier *et al.*, 2009; Rauch *et al.*, 2009), iterative toolpath correction (Fu *et al.*, 2013; Hirt *et al.*, 2004; Ndip-Agbor *et al.*, 2015) and automatic toolpath generation methods, based on the behaviour of individual features, known as Feature-assisted Single Point Incremental Forming (FSPIF) (Verbert, 2010) and their interactions (Behera *et al.*, 2014).

Most of the researchers have used machining toolpaths available in commercial Computer Aided Manufacturing (CAM) packages for SPIF. Some efforts were made to specifically generate toolpaths for incremental forming from STL files. Typically, the toolpath generation is defined by a fixed or variable vertical pitch size (Δz) between consecutive separated contours (see Figure 1.3a). This is also the most common technique used. Mainly, the disadvantages are scratches left at the transition points between each contour, giving origin to force peaks experimentally observed. Many authors have tested techniques to avoid the vertical step down at each contour and optimize the contours.

Blaga *et al.* (2011) have investigated the influence of spiral and contour toolpaths on strain distribution, relative thinning and forces in SPIF. The material chosen to produce parts was DC04 steel, with 0.7 mm thicknesses. They have observed homogeneous strain distribution and lower strain values with spiral

toolpath than using other toolpath. The forces were also more homogeneous with spiral toolpath without local peaks and valleys (see Figure 2.1).

Azaouzi and Lebaal (2012) have optimised spiral toolpath using FEM combined with Response Surface Method (RMS) and Sequential Quadratic Programming (SQP) algorithm. Their objective was to reduce the manufacturing time and homogenize thickness distribution of an asymmetric part. The proposed strategy provided an optimal toolpath after 27 FEM calculations and the new trajectory length was reduced by 60 % in comparison to initial toolpath. The optimal solution has provided an improvement around 7 % of the sheet thickness distribution, due to the decrease of reaction forces. However, in order to find the shortest toolpath, the accuracy and the final surface quality of the component were deteriorated.

2.2 Numerical simulation developments

Nowadays, metal forming FEM simulation has been intensively used in R&D processes to better predict the structural behaviour during any component forming and its final geometry.

Numerical simulation of SPIF process can be very demanding and time consuming, mainly due to high nonlinearities: small contact area constantly changing between the tool and the sheet surface, as well as the nonlinear material behaviour combined with non-monotonic strain paths (Eyckens *et al.*, 2007).

An accurate estimation from the numerical simulation results, specially related to the prediction of the forces during the forming process, is important as it contributes to the safe use of the hardware. Also, the forming forces prediction is particularly important in the case of using adapted machinery not designed for the SPIF process. For instance, the CNC milling machine adopted which does not support high axial forces. In the following, a review of numerical studies about different aspects of the simulation, found in the literature is presented.

2.2.1 Integration algorithms: Explicit and Implicit

The FEM is an approximation technique which computes the solution of algebraic equation systems, based on equilibrium equations, which depend on the problem type which can be static or dynamic. The integration of these equations over time can be based on two different integration schemes: explicit or implicit. Both solution procedures are commonly available in commercial FEM codes, having been investigated for SPIF process simulation in the literature.

The explicit integration is a dynamic approach which gives the equation system solution without request of an iterative procedure. The algorithm scheme uses a diagonalzed mass matrix and the final force balance is not checked. The differences between the internal and external forces are used to calculate the nodal acceleration, velocity and the displacement. For this integration scheme to be computationally efficient, the mass matrix has to be easily inverted. This situation happens if the mass matrix is diagonal. However, if out of diagonal terms exist, it is necessary to use a mathematic strategy to artificially transform the mass matrix into a diagonal matrix. The nodal positions at the end of the step are extrapolated using the initial nodal position and acceleration field. The equilibrium is never completely satisfied. This method is conditionally stable, which means that there is no check of unbalanced forces and the solution converges as long as the increment size is smaller than the critical value. The most important advantage of the dynamic explicit scheme is the fact that it is not necessary to check the unbalanced forces due to no convergence control. Consequently, the computational efficiency increases, the memory requirement and the programming complexity are lower than with the static implicit scheme. However, the disadvantages are: the explicit time integration solution converges if the mass matrix is diagonal and the simulation performance depends of the number of elements in the mesh. It is claimed that the error introduced by the diagonalized mass matrix can be compensated by the type of integration scheme of the element. This approach can leads to an inconsistent computation of stress and springback (Tekkaya, 2000).

In the implicit approach, the static equilibrium of the algebraic equations is satisfied at the unknown final configuration of a time increment. This method enables a full static solution of the deformation problem with convergence control. Implicit method can also be applied for dynamic loading, however this case is not discussed. Theoretically the increment sizes can be very large, but they can be limited due to the contact conditions. The Finite Element equation solution in

implicit integration scheme involves an iterative procedure to achieve the convergence criterion at each increment. This iterative procedure is based on the Newton-Raphson method. It is the most used method in static FEM programming to perform the iterative procedure on equilibrium equations and where the inertia is not included. The major advantage of the implicit method is its unconditional stability: It can provide a correct solution independently of the time step/increment. The size of the increment used in the implicit method is larger than the increment size in the explicit method. The increment size is limited by the accuracy requirement and robustness of the Newton-Raphson procedure.

After this brief introduction of the main integration time schemes, it is presented below SPIF simulations carried out by several researchers using both mentioned integration schemes.

Bambach *et al.* (2007) have carried out FEM analysis of SPIF process with ABAQUS/Explicit, for optimizing the toolpath. Those authors compared the values of sheet thickness and geometry accuracy with the experimental results, along a radial section of a conical shapes. The blank was modelled with shell finite elements and five analyses with varying friction coefficients, from 0.0 to 0.5 on the contact surface between tool and sheet. As a result, the authors have shown that no considerable influence on the prediction of geometry and thickness was found, regarding the five different values of friction coefficients chosen. Resorting to an explicit scheme combined with mass-scaling (with a time step of 10^{-5} s), the results did not considerably deteriorate. However, the calculation time increased from 30 minutes to more than three hours. A direct comparison of the predicted thickness using the explicit and implicit analyses demonstrated that the maximum difference between both schemes occurred at the vertical pitch. This observation was due to the high kinetic energy transmitted through the tool during the sudden change from the in-plane movement to the vertical increment (Bambach *et al.*, 2007). The obtained force also had a deviation when this vertical displacement was performed. To avoid the vertical pitch influence, the helical toolpath was tested. The tool forces obtained by the explicit scheme were in good agreement with previous results computed by implicit scheme.

Yamashita *et al.* (2008) have used the dynamic explicit finite element code LS-DYNA to perform a quadrangular pyramid with variations in its height. Several types of toolpaths were tested in order to find their effect on the deformation behaviour. The thickness strain distribution and the force acting during the tool travel were evaluated. According to the results, the density of the sheet material

and the travelling speed of the tool cause inertial effect on deformation. They were pre-examined and optimised to determine the computational condition to use in the simulations in LS-DYNA, to reduce the computational time. The conclusion was that numerical simulations using explicit scheme might be used for the toolpath optimization of the SPIF process.

Henrard (2008) has developed a strategy to perform SPIF simulations with dynamic explicit integration time scheme with an in-house code called LAGAMINE (Cescotto and Grober, 1985). The simulations were applied to a line test benchmark, and the mesh model was built with the COQJ4 shell element (Jetteur and Cescotto, 1991; Li, 1995). Initially, the line test simulation was run without mass-scaling and using different diagonal mass matrices. However, the results were not satisfactory due to poor shape accuracy when compared with implicit strategies. The mass-scaling value increased the largest stable time step and speeds up the simulation. The computation time with a mass-scaling factor of 10^4 was around 50% of the computation time of the implicit scheme. However, a mass-scaling factor of 10^3 guarantees the stability but the CPU time does not decrease and the use of dynamic explicit strategy introduces inertia terms into the equilibrium equations. The choice of the mass-scaling factor affects the compromise between accuracy and the computation time. The explicit strategy was shown to be more unstable than the implicit approach. This instability of the explicit scheme is due to the mesh sensitivity in terms of aspect ratio of the elements, between the thickness and the length of the elements.

2.2.2 Finite element types

Bambach and Hirt (2005) have tested the performance of different Finite Element types available in ABAQUS software package. The finite elements used were all types of solid elements available and a shell element named S4R. The difference between all brick elements are the choice of anti-hourglass and anti-shear-locking modes. The finite element S4R is a shell element with reduced integration. More details of the finite elements chosen can be found in the user manuals of ABAQUS elements library (ABAQUS 6.5). The numerical simulations were performed varying the elements types on the benchmark part, which consisted into an axisymmetric cup made of 1.5 mm DC04 steel. The toolpath consisted into five circles with a vertical step of 5 mm, which described a cone opening from the centre of the toolpath with a d=0 mm at z=0 mm to d=115 mm at z=-25 mm.

Figure 2.6 exhibits schematically an alternative toolpath for a vertical wall angle cone.

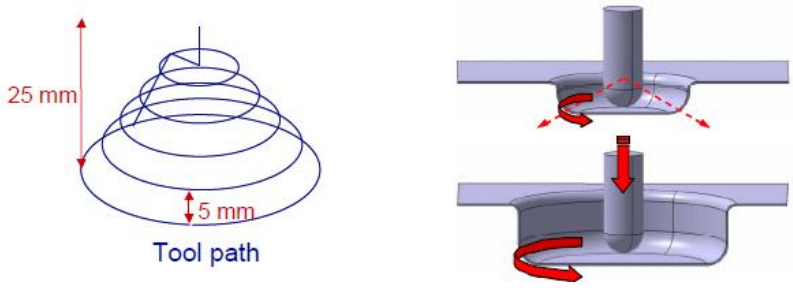

Figure 2.6: Schematic representation of an alternative toolpath (Bambach and Hirt, 2005).

The number of elements used in the in-plane mesh discretisation was kept constant for all simulations performed with different element formulations. For solid elements meshes, only two layers in the sheet thickness direction were used which is a minimum for modelling the bending state present in SPIF. With such a choice it is without surprise that the results showed that the finite element with the best results in terms of shape accuracy were the simulations performed using shell element S4R (plane stress). Besides, it presented the fastest CPU time within the tested solid elements, the reduced integrated solids with an hourglass control and based on enhanced assumed strains exhibited the best overall performance in terms of shape accuracy and CPU time. In general, the solid element results showed a considerable increase of computational costs. The poor performance obtained using brick elements was probably due to the use of only two elements over the sheet thickness, which created inaccurate bending stiffness.

Sena *et al.* (2011) have validated the results coming from numerical simulations of SPIF process using the reduced enhanced solid-shell (RESS) formulation (Alves de Sousa *et al.*, 2007), and compared it with results from solid finite elements available in ABAQUS software (ABAQUS, 2005). In this preliminary work, isotropic hardening and implicit analysis were considered. The experimental results were used as reference to assess the effectiveness of several finite element formulations: the RESS formulation and a set of hexahedral finite element options, namely C3D8 (full integration), C3D8R (reduced integration) and C3D8I (full integration with incompatible deformation modes) available in ABAQUS. From the user point of view the main differences between ABAQUS solid elements and the RESS element was the possibility to vary the number of integration points through the sheet thickness, in the latter formulation. For ABAQUS solid elements, the number of layers through the thickness direction must

be increased in order to have more than one (C3D8R) or two (C3D8/C3D8I) integration points per layer in this direction. With the RESS formulation, on the other hand, the number of integration points can be unlimitedly increased within a single layer. Concerning the role of the finite elements adopted here, it was concluded that reduced integrated solid element (four layers through the thickness were adopted) has significant error when simulating the SPIF process (Sena *et al.*, 2011).

Henrard *et al.* (2010) have analysed the factors which influenced the accuracy of Finite Element simulation in the prediction of the tool force during the SPIF process. This work analysed the influence of three factors: the finite element type, the constitutive law and the identification of the material parameters. However, in the current section it is discussed only the influence of the finite element type. Afterward, in Section 2.2.3 it is described the influence of the constitutive law in the simulations performed in this work. The authors have compared two finite elements codes: the in-house research code LAGAMINE and ABAQUS/Standard (implicit integration scheme) software. The finite elements used were: the solid finite element called BW3D with one integration point and hourglass control (Wang and Wagoner, 2004; Duchêne, *et al.*, 2007) and a shell element called COQJ4, 3D quadrilateral finite element of four nodes. All of these elements are from LAGAMINE in-house code. The sheet mesh in ABAQUS was modelled using the reduced integration solid element C3D8R distributed in three layers. The tool was modelled as a rigid body and the friction coefficient used was equal to 0.05 for all simulations. The tool rotation was not imposed in all numerical simulations and the experimental toolpath was simulated. Two cone shapes were analysed with different wall angles, 20^{o} and 60^{o}. These cases were chosen due to the observations of Eyckens *et al.* (2008) underlying by experiments the different strain distributions present (presence or not of through thickness shear). In order to identify material parameters, the line test benchmark from the work of Bouffioux *et al.* (2008a) was chosen due to the similar stress and strain states occurrence during SPIF process. The line test exhibited a localised strain gradient and through thickness shear which do not occurred in classic tests (tensile test, the monotonic and cyclic shear test). The accurate material data parameters were obtained through the inverse method procedure using the classics tests and the first step of line test corresponding to indentation. The simulations performed using LAGAMINE with a shell element with five integration points in thickness direction provided a slightly better modelling of bending behaviour occurring than the simulations performed

using three layers of solid elements. However, the Through Thickness Shear (TTS) cannot be taken into account in shell element. This fact results in problems to accurately simulate both 20° and 60° cones for shell element. The numerical simulations performed with a solid element named C3D8R from ABAQUS software, provided a solution for the shear locking problem. However, the rank-deficiency of the stiffness matrix leaded to hourglass phenomenon occurrence. The authors concluded that the choice of the material parameters cannot be made separately from the element type, as "artificially modified material parameters" can hide the element inability to model some mechanism as TTS.

2.2.3 Constitutive laws

Bambach and Hirt (2005) have tested two different hardening laws in simulations of a cylindrical component described in Section 2.2.2. The authors have used isotropic and mixed (isotropic/kinematic) hardening laws, in order to verify its results sensitivity. Results obtained with the mixed hardening law presented a more accurate prediction than using a simple isotropic hardening law. As mentioned in Section 2.2.2, the toolpath used a very large vertical step increment. Decreasing its size, the effects of the cyclic loading with mixed hardening law would be even larger. The use of an advanced constitutive law was recommended due to the cyclic toolpath. However, it depends on the material sensitivity to Bauchinger effect. Consequently, a complex law requires a large number of parameters which can be difficult to identify. The accuracy of the material parameter set has a huge influence on the numerical results.

He *et al.* (2005) have studied several aspects associated with FEM simulation choices as well as the material and process parameters of the SPIF process. The comparison between the simulation results and the experimental measurements was based on a 50° wall angle cone shape analysis. Two FEM codes, named LAGAMINE in-house code and ABAQUS, were used in this comparison study. They have suggested that the difference between both codes in terms of force predicted can be explained due to the effect of too stiff behaviour of the solid element selected and too high penalty coefficient used in the LAGAMINE contact model. Besides, both friction coefficients tested showed no significant influence on the cone shape or on the reaction force. Regarding the numerical results using Hill 48 and von Mises yield criteria, clearly almost no difference appeared when the anisotropic yield criterion were applied. As the outside edges along the perimeter of

the sheet mesh are clamped, the deformation of the material in plane directions were strongly constrained, which could explain this result.

Bouffioux *et al.* (2008 a; b; 2010) have used a specific inverse method for adjusting the material parameters with the experimental measurements. The main concept consisted in FEM simulations of simple tests involving the SPIF specificities. The inverse method was coupled to an in-house code named LAGAMINE in order to fit the material data and the material used was AA3103-O. Firstly, a set of material parameters were adjusted by inverse method using classical tests, tensile, monotonic shear and cyclic shear tests. The Swift hardening law was coupled with a Hill yield locus. The material parameters found with classical tests were tested using a line test benchmark. The results obtained exhibited a gap between the predicted and experimental forces. A new identification procedure adjusted the material data using both, tensile test and an indent test corresponding to the first step of the line test. The results of the line test simulations, using two different kinematic hardening models, showed an acceptable good correlation between the predicted and measured tool force, especially for the first two steps of the line test. From the comparison between LAGAMINE in-house code and implicit scheme of ABAQUS software, they demonstrated that the material parameters identified depended on the stiffness of the solid element. Also the number of solid elements in thickness direction influenced the results. Both codes presented similar levels of force prediction for tensile test and line test. However, the authors claimed that the identification method of material data was far from being trivial. The use of the classical methods by a combination of tensile and cyclic shear tests to identify material data for SPIF process seems not adapted.

Eyckens *et al.* (2010) have analysed numerically SPIF process based on different finite elements to model the sheet. Different plastic behaviours are considered, isotropic and anisotropic yield criteria combined with either isotropic or kinematic hardening. The simulations using the shell element (COQJ4) are performed with LAGAMINE in-house code. The solid finite elements meshes are modelled in ABAQUS software (ABAQUS 6.5) using a reduced integration solid element (C3D8R). These meshes are modelled using three elements through the sheet thickness. The experimental geometry was a truncated cone of AA3103-O. All the simulations were carried out using static implicit scheme. Regarding the effects of the adopted constitutive behaviour in the shell model, it predicted almost identical results for the different strain components using von Mises or Hill yield criteria. The hardening law, Swift or Armstrong-Frederic, leaded to a low difference

in strains. However, in all cases, the authors have mentioned this fact as being a forming process displacement-controlled, which means the strains are independent of the adopted material behaviour. In terms of forming force prediction, the dependence on the type of hardening law is more pronounced than the choice of yield criterion.

Henrard *et al.* (2010) have analysed the influence of plastic behaviour on the accuracy of force prediction by FEM simulations. These comparisons include the use of Swift and Voce hardening laws, isotropic or kinematic hardening models, isotropic von Mises and anisotropic Hill yield criteria. Also, different types of finite elements were used in this study, as described in Section 2.2.2. The material used was AA3003-O. The simulation analysis was based on two cone shapes with different wall angles, 20° and 60° and corresponding submodels from the centre zone of the 40° pie-model. The simulations and experiments carried out showed different material flow for 20° and 60° cones, resulting in different stress and strain states. In the 20° cone, both finite elements types provided a similar accuracy of axial force prediction when using the material model taking into account both isotropic and kinematic hardening. For the 60◦ cone, a submodel with a more refined mesh showed more accurate force prediction and the shear dependency of the mesh density. This large wall angle cone demonstrated that a saturating hardening law of Voce is essential for accurate force prediction. A less significant improvement in force prediction was obtained when taking into account kinematic hardening. Globally, the highest accuracy was reached using solid elements combined with a fine mesh, which used the isotropic yield locus of von Mises and the mixed isotropic–kinematic hardening model of Voce–Ziegler. The identification procedure based on the work of Bouffioux *et al.* (2008 a; b) proved that the choice of the material parameters set cannot be made separately from the element type. Moreover, in the forming force predictions, the dependence on the type of hardening law was more pronounced than the choice of yield criterion.

2.2.4 Interaction between tool and sheet

Eyckens *et al.* (2008) and Eyckens (2010) have used ABAQUS/Standard implicit for FEM simulation of SPIF. The authors performed Finite Element analysis of three different mesh model scales for each of the four cone shapes with different wall angles, 20° and 60°, using AA3003-O sheet. The first sheet mesh scale is referred as the global model (GL) modelling only a sheet section of 40° and using

a relative coarse mesh with 3 layers of elements through thickness. The second large Sub-model (S1) considered only a small section from the central region of GL, also using 3 layers of elements. Finally, the small sub-model (S2) is located at the centre of S1 sub-model, and consisted in 5 layers of elements. All scales were modelled with a reduced integration brick element named C3D8R from ABAQUS package. The material was considered isotropic described by Swift hardening law in combination with the isotropic von Mises yield criterion. The simulated contact pressure area between the tool and the sheet exhibited similar oscillations as the force components. Both sub-models practically showed identical results, while the GL model presented considerably high values of contact pressure. It can be argued that the coarse mesh of this model results in an over prediction of the contact area. The distribution of the contact pressure observed under different working conditions revealed that the contact can generally be divided into two parts. Firstly, the contact with the cone wall is well approximated as a line contact at larger wall angles, while it diminished at small wall angles. Secondly, the contact on the cone bottom appeared to be "sickle-shaped". This can be attributed to the presence of a contact groove in the sheet material, formed during the previous contour of the tool. It makes an important contribution to the overall contact, even when the wall angle was large as 60°. At very low wall angles, such as 20°, it was responsible for the radial components of the forming forces to become nearly zero or even negative, which means that the tool was pushed outwards instead of in the direction of the cone centre. The sub modelling strategy improved the modelling of the plastic deformation zone in the SPIF simulation. However, the authors mentioned that the constitutive model of the sheet was too simple to accurately predict the forming force components, the quality of the forming force predictions was improved through the use of finer meshes.

Delamézière *et al.* (2011) have developed a simplified approach modelling to simulate the contact between the tool and the sheet in order to reduce the CPU time of SPIF simulation. This work was continued later by Ben Ayed *et al.* (2014). In this model, the contact/friction with the rigid tools was replaced by imposed nodal displacements and it was used a geometrical assumption for the successive local deformed shapes. An algorithm was developed to find the nodes supposed to be in contact with the tool and to estimate their imposed displacements during a tool displacement increment. This was done by taking into account the geometry of the sheet at the beginning of that increment and according to the geometric assumptions. The simplified approach procedure is composed of three main steps:

the determination of the nodes in contact with the tool, definition of the nodes direction and management of different toolpath increments. To determine the nodes on the tool contact area to impose the displacements, it was proposed to limit the tool contact area. If all the nodes in the interpenetration zone are considered in contact the sheet deformed cannot be in conformity with experiments. In this case, a parameter named "imposed displacement radius" (R_{imp}) was proposed to limit the contact area and it depends on distance L. The value of the distance L from the tool centre was based on several benchmark tests, this distance was limited to 5 times the tool radius. Then R_{imp} can be determined as a function of the position of the tool centre, radius and a user parameter called θ. Figure 2.7 schematically shows the geometric assumption of the parameters L and R_{imp}.

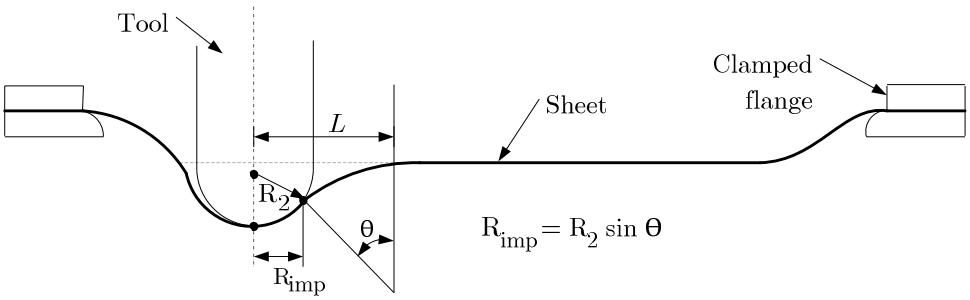

Figure 2.7: Geometrical assumption, parameter L limited to 5x times the tool radius.

Numerical results were compared with experimental data of pyramidal and square box benchmarks. The material used was AA1050 and the isotropic hardening behaviour was modelled by Swift law. The numerical results were obtained using the commercial finite element code ABAQUS, in order to validate the simplified approach. The simplified contact algorithm was assessed with different sizes of vertical steps down chosen by the user. The thickness distribution, compared with experimental result was globally acceptable and the CPU time was significantly reduced when compared with a classical simulation performed in ABAQUS implicit.

The local plastic deformation characteristic of the SPIF process simulation requires a fine meshing discretization due to the contact interface between tool and sheet modelling. However, refining entire part with a fine mesh would increase tremendously the CPU time. In order to overcome this issue alternative numerical strategies appeared, such as adaptive re-meshing or domain decomposition methods for saving computation time. These approaches have been implemented to speed up implicit integration scheme simulations.

2.2.5 Domain decomposition methods

Sebastiani *et al.* (2007) have applied a decoupling algorithm to reduce computing time in Finite Element analysis of incremental sheet forming (ISF) processes. The decoupling algorithm consists into divide a Finite Element model discretization in an elastic and an elastoplastic deformation zones. These two separated systems are alternately solved resorting to an algorithm which results in a partial model providing boundary conditions for the other system. The decoupled simulation involves several subsequent simulations which dependent on each other. The boundary condition includes degrees of freedom and a number of elastic elements representing the elastic reaction of the remaining structure. The mentioned elastic elements were modelled as spring elements constants based on the reaction forces and displacements of the boundary nodes. Several strategies of elastic boundary conditions at the boundary of the plastic forming zone were also investigated in order to predict the spring constants. The implementation of this decoupling method for enhancing the calculation performance notably reduced the system size. However, all approximations are still subject to a severe amplification of initial errors once the entire elastoplastic region is decoupled.

Hadoush and van den Boogaard (2009; 2012) have proposed a substructuring method to reduce the computation time of SPIF simulations using implicit integration scheme. This proposal consisted into dividing the Finite Element mesh in regions with different computation treatments. The hypothesis is that plastic deformation is localised and restricted to the tool vicinity, while elastic deformation region is considered in the rest of the sheet mesh due to a low geometrical nonlinearity. The strong nonlinearity requires the use of the standard Newton method, but it was not efficient to use in large elastic deformation part. Using a relatively less expensive iterative procedure, as the modified Newton method, reduces the cost of the tangent stiffness matrix and the internal force vector update at iteration level. The difference between Newton method and the modified Newton method is the treatment of the tangent stiffness matrix (Zienkiewicz and Taylor, 2005). To reduce the computation time, different domain approaches are applied for the treatment of each mesh zones.

The two domain approach divides the mesh into two zones. In the first part containing the strong nonlinearity on the vicinity of the tool, the Newton method is applied. In the other sheet mesh zone considered elastically deformed, the modified

Newton method or the pseudo-linear approach is applied incrementally. At the beginning of each increment, the stiffness matrix and internal force vector are calculated as nonlinear, including the material and the geometrical nonlinearities of the previous increment.

Later, Hadoush (2010) have extended the basic idea of the two domain method to three domain approach. The new region added in this approach was the split of the pseudo-linear treatment of the elastic deformation zone into two parts. The first and second zones are similarly performed as two domain approach and the third zone was assumed as being multi-incremental in pseudo-linear domain instead of one increment. In terms of performance, the three domain approach achieved the best speed factor for standard Newton-Rapson of 1.63 and, consequently, less CPU time. However, the authors mentioned that the size of the plastic region has to be carefully selected for an accurate modelling of SPIF simulation.

2.2.6 Adaptive refinement strategies

Lequesne *et al.* (2008) have modelled the SPIF process using LAGAMINE. In order to decrease the simulation time of SPIF simulation combined with an implicit integration scheme, a new method using adaptive remeshing procedure was developed. The sheet mesh was modelled with 4-node shell element implemented in the code, called COQJ4. The contact surface uses the node connectivity of the shell finite element combined with classical penalty method (Habraken and Cescotto, 1998). The spherical tool was modelled as a rigid body. As the present thesis deals with the extension of this method from shell to solid-shell elements, its detailed description is given in Chapter 4. The validation of adaptive remeshing in SPIF process for shell elements was performed using a line test simulation from the work of Bouffioux *et al.* (2008a).

Hadoush and van den Boogaard (2008) have proposed an implementation of a mesh Refinement/Derefinement (RD) approach to reduce the computing time of SPIF process simulation. The RD approach consists in a refined mesh in the vicinity of the tool since there is a small contact area between the tool and the sheet metal, while the rest of the sheet was described by a coarse mesh. During the process simulation, the mesh connectivity is continuously changing, because of the tool motion. This approach was implemented in an in-house implicit Finite Element package. The finite element type used was a triangular shell element and each coarse element was divided in four new refined equal elements when it is in the tool

neighbourhood. The mesh can only be refined once during the refinement procedure. The main goal of this approach was to keep the number of elements as low as possible during the simulation. The numerical simulation was applied to the forming process of a pyramid with 45° of wall slope. The state variables, when the new refined elements are generated, are transferred from the old coarse element to the new smaller elements. To conclude, the RD approach reduced the computing time compared to no refinement case by approximately 50%. The predicted equivalent plastic strain with this approach showed a good agreement with the reference model.

The main differences between the remeshing procedure of Lequesne *et al.* (2008) and the one proposed by Hadoush and van den Boogaard (2008) are the mesh compatibility, the finite elements type used and the refinement/derefinement criterion. In this last approach, the refinement criterion is fulfilled if the geometrical error exceeds an indicator value. It measures the variation of the geometry within the blank. This variation was based on a set of tangent axes determined for each element. The variation of these sets of tangents from each element to its neighbourhood elements indicates the geometry variation. A nodal averaging technique was used to quantify this variation. The derefinement occurs if the variation within the group of refined elements decreases and is less than a user input value. Consequently, the coarse element is reactivated. Additionally, their refinement/derefinement technique allows preserving the mesh compatibility between refined and coarse elements due to the usage of a triangular shell element.

Suresh and Regalla (2014) have studied the effects of finite element size and an adaptive remeshing technique in numerical simulations. Such effects were analysed on the plastic strain, punch force and deformed shape accuracy. The simulations were performed using the explicit dynamic finite element code LS-DYNA. Its adaptive remeshing procedure has two types of indicators/criteria based on angle change and thickness change. In case of angle indicator, the angle between the in-plane and out of plane is measured, and if it is higher than a value chosen by the user, the mesh is refined. In case of thickness indicator, the mesh is refined if the thickness of the blank reaches the specified value chosen by the user. The mesh refinement was set to a maximum number of 3 levels during a refinement procedure. The sheet mesh was discretised using Belytschko-Tsay shell element with two integration points in thickness direction. The effect of four different meshes were tested with element edge length of 1 mm, 2 mm, 4 mm (coarse mesh) and 4 mm combined with an adaptive remeshing method. The effects on plastic

strain, punch force and deformed cross-section shape using adaptive remeshing were similar as the fine mesh with element edge length of 1 mm. While the force prediction using element edge length of 2 mm presented slightly deviation. The strain distribution of the coarse mesh results showed higher deviation than the other mesh topologies. The estimation of force and deformed shape using coarse mesh have shown a higher deviation than the results obtained with edge lengths of 1 mm and 2 mm. Additionally, the force prediction with a coarse mesh presented a lower force level and larger force peaks than fine mesh. The computational time was reduced by 50% applying adaptive remeshing technique.

Giraud-Moreau *et al.* (2013) have analysed SPIF using a remeshing method based on refinement and coarsening strategies in order to decrease the time simulation. The numerical results were calculated with the dynamic explicit solver of ABAQUS software coupled with the remeshing method. The finite element used to mesh the sheet was S4R shell element with 4 nodes and reduced integration. The validation of the numerical results have been carried out through the comparison of geometrical profile and thickness profile. The comparison was based on the experimental measurements of a 45° wall angle cone in AA1050 sheet. Only the shell elements close to the tool could be refined. The coarsening strategy was applied to the elements when the tool moves away from these elements. The remeshing criteria were based on the geometrical and physical error estimators. The geometrical estimator measures the maximum angular gap between the normal to the element and the normal to its vertices. If the angular gap is greater than a limit value, the element is curved and it is considered close to the tool. The physical criterion is used to refine the mesh with respect of the physical field distribution, the equivalent plastic strain. The refinement was defined by the distance between the curved element and the spherical tool. If this distance is less than a limit value, then the element must be refined in a uniform subdivision into four new elements. To preserve the mesh compatibility, the refined elements on the vicinity of the coarse elements are divided into three or four triangular elements. The mesh can be refined more than once during a refinement procedure, which is contrary to the strategies proposed by Hadoush *et al.* (2008) and Lequesne *et al.* (2008). The coarsening method is the reverse operation of the refinement technique. It can only be applied to refined elements. Globally, a good agreement has been observed between numerical and experimental results showing the efficiency of the proposed method.

Bambach (2014) has introduced an approach based on dynamic explicit Finite Element simulation analysis of ISF combining adaptive remeshing and subcycling methods, in order to reduce the computing time. This proposal allows the decrease of the CPU time by different ways: increasing the tool velocity or applying mass-scaling, use of parallel computation, reduction of the number of elements by adaptive remeshing and additionally, integration of the elements with different time steps through subcycling. The simulations were modelled with shell element with reduced integration (S4R). Concerning the adaptive remeshing, three methods of h-, p- and r-adaptivity are feasible: h-adaptivity refers to subdividing elements into smaller ones; p-adaptivity is based on increasing the polynomial order of the shape functions and r-adaptivity refers to relocating the mesh nodes according to gradients in the solution. From these three possibilities h-adaptivity is the most common strategy adopted by many authors that used adaptive remeshing in SPIF simulations, such as previously described. The subcycling is applied to the coarse elements integrated with a larger time step than the refined elements in the deformation region. The numerical simulations carried out with only adaptive remeshing reduced 28.8% of the time needed for a globally refined mesh. Applying adaptive remeshing combined with subcycling with a factor of 2 reduced the CPU time to 24.8% and to 12% for a factor of 10. This combination of adaptive remeshing with subcycling demonstrated tremendous reduction of CPU time. However, at large subcycling factors, the error in von Mises stress increases, it exceeds 10% for a subcycling factor of 4 and reaches 25% for a very large factor of 10. For a subcycling factor of 8.3 in combination with adaptive remeshing, the stress results are poor.

2.3 Formability and SPIF mechanisms

In the literature review is claimed that formability on the SPIF process is higher than in conventional sheet forming process. In conventional stamping operations, the metallic sheet is considered subjected to an in-plane and bending deformation with, occurrence of necking. However, the deformation mechanisms on SPIF process are still a questionable subject among different metal forming research groups.

The limit of sheet metal forming processes is defined as the maximum deformation level achieved before fracture. The most common procedure to determine the forming limit of sheet metal forming can be named as Forming Limit Diagram (FLD) also known as a Forming Limit Curve (FLC). It consists into plotting the major principal strain and minor principal strain showing the safe and the failure zones. These curves are experimentally established, providing the values of major and minor principal strains, for various loading patterns, such as, equi-biaxial, biaxial, plane strain and uniaxial. Figure 2.8 exhibits a schematic comparison between the FLC of conventional forming (stamping/deep drawing) and SPIF.

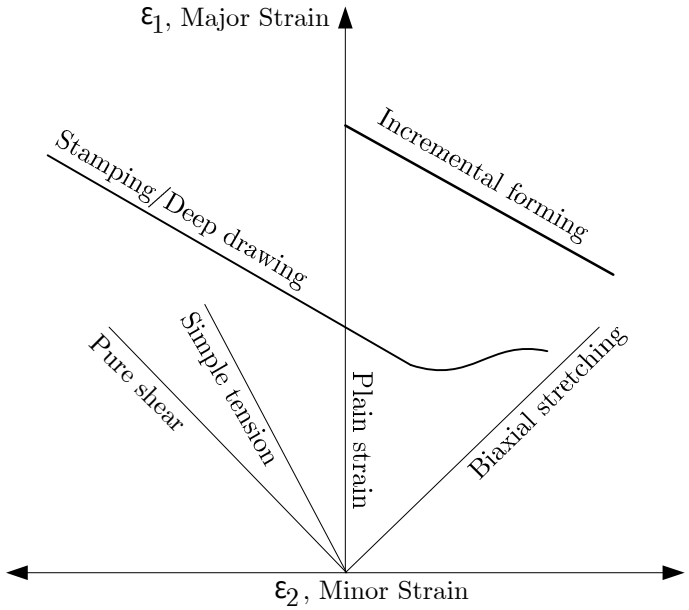

Figure 2.8: Schematic representation of FLC in SPIF against conventional forming.

The SPIF FLC is generally a straight line with a negative slope in the positive region of minor strain, whereas the conventional stamping is presented in both regions of minor strain, as shown in Figure 2.8. In the literature, several studies of SPIF parameters concerning their influence on the formability can be found. For the effects of tool type, tool size, vertical pitch size, feed rate, friction at the contact interface of tool/sheet surface and plane-anisotropy of sheet. Kim and Park (2002) have summarised the effects of different parameters on the formability of AA1050 sheet. The use of freely rotating ball tool tip enhances the formability and reduces the friction at the tool/sheet interface. The formability decreases when increasing the tool diameter and vertical increment, and the best formability is

obtained with a tool of 10 mm. Due to plane-anisotropy, the formability differs according to the direction of the tool motion.

Formability in SPIF process can be analysed using the maximum forming wall angle as being an indicator. It can be the first step to know the formability limits of the material. For instance, Ham and Jeswiet (2006) have analysed several SPIF parameters and their combined influence on the maximum wall slope angle. Similarly, Malwad and Nandedkar (2014) have performed experiments to study the combined influence of wall angle, step size and tool diameter on formability. The formability analysis of AA8011 was performed using conical shapes with different wall angles, at 55°, 65° and 75°. Afterwards, a multistage test with continuous variation of wall angle from 35° to 90° was carried out to assess the maximum forming wall angle achieved in function of depth. From their experimental work, it was observed that the thickness reduction was possible at large wall angle, but uniform thickness distribution along the wall was found for angles smaller than 65°. Concerning the wall angle, when it was increased, the occurrence of stretching was more significant than shearing. For smaller wall angles the deformation mainly occurred by shearing. Using constant wall angle shapes, the cone forming achieved the target final depth without fracture occurrence. However, using multistage (variable wall angle) tests the fracture occurred earlier than using constant wall angle shapes.

Many authors have tried to present analytical, experimental and numerical analysis to understand and validate the peculiarities of deformation mechanisms which occurred in the SPIF process. Localised deformation was attributed as an essential characteristic of SPIF process and different mechanisms were proposed as being the local stabilizers before occurrence of fracture.

Emmens and van den Boogaard (2009) have presented a literature review of mechanisms that have been suggested to explain the enhanced formability in ISF processes. In their review, several mechanisms were mentioned: contact stress, bending-under-tension, stretching, shear, cyclic straining, necking stabilization and hydrostatic pressure. The mechanism explanations were based on theoretical considerations and some of them have been experimentally validated (Martins *et al.*, 2008; Silva *et al.*, 2008). They claimed that the identification of a single mechanism occurrence in ISF cannot be imposed or generalised as being the main mechanism. Recently, Nimbalkar and Nandedkar (2013) have updated the review of deformation mechanisms in ISF and included the membrane analysis and noodle theory. Besides the mechanisms mentioned previously, other researchers have

proposed the forming mechanism as being a combination of in-plane deformation, Through-Thickness Shear (TTS) and stretch instead of shear. In the following sections, the main mechanisms found in the literature review are described in detail.

2.3.1 Analytical analyses

Martins *et al.* (2008) and Silva *et al.* (2008) have presented an analytical model of SPIF based on the experimental observation of contact interaction between forming tool and sheet surface. A similar examination was performed for material failure at the transition regions between the inclined wall and the corner radius of the shape. Their analytical membrane theory model proposes the fundaments of the process and it was explained through experimental and numerical results.

Martins *et al.* (2008) have presented a theoretical model based on membrane analysis with bi-directional in-plane contact friction focused on the deformation modes commonly found in SPIF. It was explained by experimental and numerical results available in the literature. The formability limits of the process are analysed by combining the proposed membrane analysis with ductile damage mechanics. The analytical model approach was only focused on three modes of deformation: a) the flat surfaces under plane strain stretching conditions; b) rotational symmetric surfaces under plane stretching conditions; and c) corners under bi-axial stretching conditions. These modes were considered in order to explain the high formability of the process. The explanation of the increased formability of SPIF was compared with conventional stamping operations through the Fracture Forming Limit Diagram (FFLD) based on the onset of fracture instead of FLD based on the onset of necking. The evolution of thickness with depth along two meridional cross sections revealed that plastic deformation takes place by uniform thinning until fracture. From their experimental observations, the authors claimed that there is no evidence of necking before the failure occurrence in the component. The crack propagates under tensile meridional stresses acting under stretching modes of deformation.

Silva *et al.* (2008) have provided a reviewed theoretical model for rotational symmetric SPIF, which was employed under membrane model analysis considering bi-directional in-plane contact friction forces. The main purpose of their analysis was the understanding of state of stress and strain in the localized deformation and the material fracture initiation during SPIF process. A schematic representation of

the shell element details the acting stresses in the meridional, circumferential and in thickness directions. The contact stress was introduced in this model by stretching of the sheet around the punch radius. The contact stress in SPIF occurred due to the bending of the sheet around the punch. It can be assumed that the stress increased with increasing sheet thickness and decreasing punch radius. This would mean that the formability also increased in agreement with general observations. Fracture in SPIF was claimed as being happened by meridional tensile stress and not by in-plane shearing stress.

Fang *et al.* (2014) have developed an analytical approach for SPIF process to describe the localised deformation mechanism. In their work, they assumed a plane strain condition in the analytical model, which is only the material deformation in the plane perpendicular to the tool motion direction. The localised deformation region was divided into sub deformation regions: the first one, the contact area between the tool and the sheet, and the second one, the wall of the formed part on the neighbourhood of the first region. In each one, the state of stress and strain was analysed through the thickness direction to include the bending effect. In addition, the stretching effects were also considered by calculating the thickness strain and, finally, the strain hardening was assessed. In order to validate the theoretical study, simulations and experiments of a cone shape were performed. The results confirmed the accuracy of the analytical model using both Finite Element simulation and experiments. The experimental validation was performed by measuring the circumferential and meridional strain variations, the growth of crack and morphological analysis of the fractured region. The measured meridional strain was larger than the circumferential strain, which confirmed the plane strain assumption used in the analytical modelling. The analytical evaluation revealed that the deformation occurred not only in the contact zone, but also in the inclined wall in the vicinity of the contact zone. The deformation in the non-contact area may affect the geometrical accuracy. Finally, the results also suggested that the fracture tends to appear at the transitional zone between the contact area and formed wall. In addition, the authors mentioned a model limitation: the plane strain assumption in the theoretical analysis validation would be validated only for axisymmetric components.

2.3.2 Combination of stretch, bending and shear

Emmens and van den Boogaard (2009) have mentioned in their review that simple shear is responsible for the lack of necking appearance, as no tensile force is applied in the plane of the sheet. An additional shear stress decreases the yield stress in tension. It was observed as occurring in ISF as referred in Emmens and van den Boogaard (2007). Figure 2.9 exhibits the lateral cut section view of different deformation modes: bending, stretching and shearing in the orientation of the original vertical cross-sections (XZ plane).

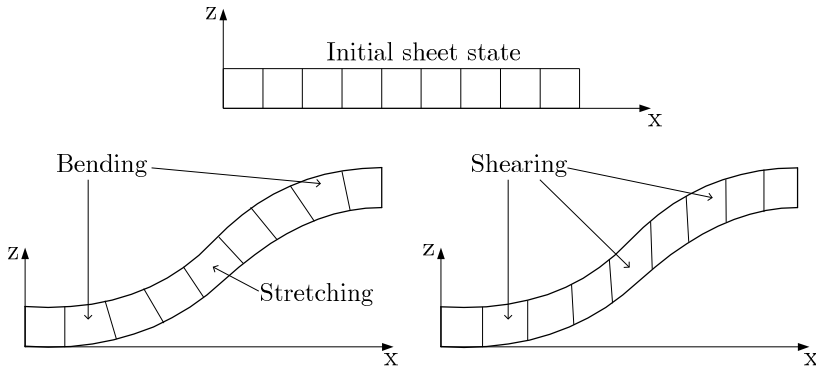

Figure 2.9: Difference between forming by stretch (left) and forming by shear (right).

In forming by stretching, the initial section lines normal to the surface of the sheet material remain perpendicular to the surface, while in forming by shear they keep their original orientation.

Jackson and Allwood (2009) have experimentally examined the deformation mechanisms of two variants of ISF: TPIF and SPIF, and compared them for a forming process of an identical geometry. In addition, a second aim was to evaluate the accuracy of the sine law prediction of wall thickness, and relate the measured thickness to the deformation mechanisms. The strain distribution through the thickness of the sheet was measured for the cooper C101 sheet formed into a truncated cone with a wall angle of 30^{o} shaped using each forming method. A sheet thickness of 3.1-3.3 mm was used to allow a longitudinal gridline printing along the cross-section to indicate the variation of strains through the thickness. Their observation analysis brought three significant results. In both SPIF and TPIF the deformation was a combination of stretching and shear that increased on successive contours. Shear was the most significant strain component in the tool direction, it was a result of friction between the tool and workpiece. Also, shear occurred perpendicularly to the tool direction in both SPIF and TPIF, it was more significant in SPIF resulting in piling up of the material at the centre of the plate.

Finally, the deformation mechanism was inherently different for SPIF and TPIF, they both differ from a pure shear mechanism. High stretching and shear perpendicular to the tool direction provided differences between the sine law prediction and measured wall thickness for both SPIF and TPIF. It was due to the radial displacement of the material. The conventional forming process exhibited no stretching occurrences anywhere along the cross-section. This was due to the material sliding under the blank holder minimizing stretching. Whereas, the localised stretching occurred under the tool indentation in both ISF processes, due to the material draw-in from the sheet borders restricted by the rigid clamping.

In order to validate their observations, the authors performed an evaluation of their experimental results by comparing them with other typical ISF experiments. The comparison includes main similarities from results of previous experiments of different researchers. It was important due to the material, sheet thickness and geometry used in their experiments. Concerning the unusual choice of material and sheet thickness used in the experiments, they resulted in strains that have some differences to more typical ISF experiments. However, some similarities were found and some results can be transferable to typical ISF experiments. Specifically, the through-thickness shear is assumed greater for the copper plate than thinner sheets, but, it has a similar evolution in strains in successive contours in experiments using thinner sheets.

Malhotra *et al.* (2012b) have developed a fracture model combined with Finite Element analysis in order to predict the occurrence of fracture in SPIF using two conical shapes. Experiments were performed to validate the predictions from Finite Element analysis in terms of forming forces, thinning and fracture depths. It was reported that fracture in SPIF was controlled by both local bending and shear. Local stretching and bending of sheet on the tool vicinity originated higher plastic strain on the outside surface of the sheet increasing damage as compared to the inner surface. Additionally, the deformation mechanism in SPIF was compared to conventional forming process using the deformation history obtained from Finite Element analysis. The shear effect in SPIF delayed damage accumulation while high local bending of the sheet around the tool caused greater damage accumulation in SPIF than in conventional forming. These facts explain the increased formability in SPIF in comparison to conventional forming. It was claimed that both through-the-thickness shear and local bending of the sheet around the tool play a role in fracture in SPIF process.

2.3.3 Through Thickness Shear (TTS)

Eyckens (2010) has discussed the occurrence of Through-Thickness Shear (TTS) in SPIF. The author demonstrated TTS, also known as out-of-plane shear, through numerical and experimental supports. Firstly, resorting to FEM by modelling the sheet with solid finite elements which provided a suitable validation. Secondly, direct experimental measurement based on the deformation of small holes drilled in the sheet (Eyckens *et al.*, 2009b). Finally, the third method, also an experimental validation was performed based on the crystallographic deformation texture (Eyckens *et al.*, 2011).

Eyckens *et al.* (2009a) have extended the Marciniak–Kuczynski (MK) forming limit model in order to predict the localised necking in sheet metal forming operations in which TTS occurs. The FLD of a purely plastic, isotropic hardening material with von Mises yield locus was discussed, for monotonic deformation paths that include TTS. Formability increases based on TTS was explained through a detailed study of some selected deformation modes. The case study showed that the presence of TTS in the plane is related to the critical groove direction in MK model. TTS allowed a change of strain mode resulting in a delayed of necking.

Eyckens *et al.* (2009b) have carried out experimental measurements of the TTS. The direct experimental measurement method of the total TTS was proposed based on the deformation of small drilled holes. From this method, statistically non-zero TTS angles were measured for a low carbon steel sheet (DC01), subjected to different levels of deformation. The experiments have showed the existence of TTS in SPIF in cone shapes with different wall angles, from 40° to 67°. The formability prediction was presented using a MK type of forming limit model (Eyckens *et al.*, 2009a) which can take into account the TTS. The observed TTS along the cone wall differed from the one that would follow a pure shear mechanism in SPIF and it increased in magnitude with increasing wall angles. However, the TTS in the circumferential direction of the cone showed an insignificant dependency of the wall angle. From the MK model applied to a 65° wall angle cone, the TTS measurements used to study the localised necking demonstrated that the presence of TTS can indeed delay the onset of localised necking in SPIF. This observation present TTS as one the factors of very high formability during SPIF process.

Eyckens *et al.* (2011) have extended the MK model, taking into account TTS for generalised anisotropic material sheets. It was a continuation of previous

work from Eyckens *et al.* (2009a). The extension aimed the prediction of the onset of localised necking during forming and compared to a proposed alternative approach of Allwood and Shouler (2009). The combination of TTS with anisotropic plastic behaviour was not included in the MK model framework leading to two additional issues. Firstly, the local material frame from the work of Montleau *et al.* (2008) was included and the rotation of anisotropic properties was considered during shearing. Secondly, to describe anisotropic yielding for strain modes which have non-zero TTS components, the Facet method was used (Van Houtte *et al.*, 2009). From the textures of an aluminium alloy AA3103 sheet and a sheet of low carbon steel DC01, the Facet plastic potential was obtained through virtual tests of the Taylor–Bishop–Hill multilevel model. It revealed out-of-plane anisotropy which cannot be obtained using experimental tests. It was seen that the anisotropic yield state including TTS influenced the formability prediction for monotonic strain paths. For the aluminium texture, formability with anisotropy taken into account was higher compared to the one associated to isotropic von Mises yield locus, however this was not verified for the low carbon steel texture. The sheet orientation had a small influence on the improvement effects of TTS on the forming limit. Formability predictions were seen to be greatly affected by the direction of applied TTS in the major in-plane strain direction. This last result was in contrast to the results obtained with the model of Allwood and Shouler (2009) which predicts no effect of the direction of TTS on formability.

2.3.4 Bending Under Tension (BUT)

Emmens and van den Boogaard (2009) have described the Bending-Under-Tension (BUT) as being the simultaneous bending and stretching of a sheet. The force needed to stretch the material is dependent on both quantity of bending and a quantity of stretching. In general, the BUT has a dynamic effect occurring when actually the material is moving around the cylindrical punch while at the same time it is bent and stretched. The simultaneous bending and stretching caused a non-uniform stress over the thickness. The comparison of its occurrence in ISF operation is difficult to directly establish. However, it is obvious that the material is being bent near the tool and being stretched at least in some directions. The BUT mechanism is proposed as an additional stabilizing effect. This effect leads to a proportionally increasing of sheet thickness and decreasing punch radius.

The Continuous Bending under Tension (CBT) test has an analogous feature as a common tensile test. However, during the tensile procedure, a set of three rolls are continuously moving up and down along the specimen repeatedly bending and unbending as in a three-point bending test. Emmens and van den Boogaard (2008) have analysed in detail the CBT. Particularly, experimental conditions have been studied: speed and bending angle. Several materials specimens are used, which were aluminium alloys and low carbon steel.

Emmens and van den Boogaard (2009) have showed that CBT test was suitable for studying BUT as a mechanism in ISF, but the conditions should be changed to ensure a small bending radius. The experimental conditions, pulling speed and depth setting, have a significant effect on the final results, notably on the maximum level of stretch. At a fixed geometry, there is an optimal pulling speed for obtaining maximum uniform straining. Pulling at low speeds, the formability was reduced due to the increased number of bending-unbending cycles. The CBT test was performed with different materials showing different levels of formability. This means that, besides the deformation stability, there is a material effect at the same time. From these test results the highest reported uniform strain achieved corresponds to an elongation of 430% obtained for mild steel, DC04. On the other hand, the general performance of aluminium was found to be much worse than that of steel. Summarising, the results demonstrated the hypothesis that the material actually bent required a lower stretching force. The authors have concluded that the CBT was a critical factor affecting the localised deformation and the formability of ISF (Emmens and van den Boogaard, 2008).

2.3.5 Cyclic strain effect

During SPIF operation, the forming tool has a contact with a material point several times. Each path causes bending and unbending with possible strain reversal, so the material is subjected to cyclic straining. However, this cyclic effect should not be confused with the BUT. It involves repetitive bending but not necessarily cyclic and presents inhomogeneous stress distribution in the thickness direction. The stabilizing effect of cyclic loading, involves cyclic straining but not necessarily bending and the stress distribution over the thickness may be homogeneous. In a practical situation, these mechanisms will be hard to separate, but their effects are fundamentally different (Emmens and van den Boogaard, 2009).

Eyckens *et al.* (2007, 2010) have showed the non-monotonic strain path of the material submitted to SPIF process, playing a role in the high formability, compared to the monotonic loading in the traditional FLC. They have analysed the deformation history retrieved from a Finite Element simulation of a 50° wall angle cone shape formed by SPIF using AA3003-O. The finite element simulation revealed complex deformations occurring during the SPIF process. To illustrate this, three elements along the thickness direction were selected in the centre of the inclined wall mesh. The strain paths consisted into a number of serrations. The physical meaning of the serrated strain paths was understood by a closer analysis of deformation during a single contour of the tool. The simulation showed that the final deformation at the cone wall was approximated by a plane strain deformation with elongation along the local radial direction, and this final deformation was reached incrementally by the forming tool. Along the direction of the tool motion, the sheet was repeatedly bent in one way by the moving tool, bent in the other way, and unbent. The usage of different constitutive models in this analysis showed that mixed hardening contributed to the delay of the onset of necking in SPIF process. Afterwards, the strain paths at three finite elements in thickness direction are used as input into a MK forming limit model. The large difference in the predicted forming limits obtained from the different layers indicated that an interaction between these layers should be taken into account for more accurate forming limit predictions of sheets subjected to SPIF.

2.4 General remarks

In general, the present chapter describes and summarizes the main subjects chosen from the state-of-art review of SPIF process. The main developments on experimental and numerical fields were presented in order to be a basis in further analysis performed in this research field.

The experimental work description of different authors provide analyses that can be obtained and compared with FEM simulation predictions, such as the force prediction and twist occurrence. Tests showed that twist effect can not only be observed in rotational geometries, but it was also presented in non-rotational structures, for instance, pyramidal parts. Concerning the experimental parameters of SPIF and different toolpaths, they are mentioned due to their effects in the

process formability. As demonstrated in the work of Wu *et al.* (2012), they have numerically analysed the influence of different toolpaths on formability by FEM coupled with damage model.

In terms of FEM simulation review, the state-of-art includes the computational aspects that must be taken into consideration. The SPIF process is commonly simulated to predict the tool force, the final geometry of a component and occasionally to predict rupture. The results obtained are based on user options: integration scheme, type of element, friction conditions between the tool and the sheet, hardening law and Boundary Conditions (BC).

The simulation of SPIF process is a demanding task, due to its long computation time to model with implicit or explicit FEM codes, as previously outlined. Several authors have claimed the dynamic explicit scheme as being faster than the static implicit analysis. On the other hand, many authors reported problems associated to the dynamic explicit analysis, as described in Section 2.2.1. In this work, the chosen FEM code and its integration scheme are based on previous efficient results from Henrard (2008), resorting to the static implicit approach.

Generally, these choices are effective to predict the final shape but regarding the tool force prediction, it provides an overestimated value. A number of authors have studied the ability of FEM to correctly predict the tool force during SPIF process. From the literature review is evident that the shell finite element type is the most widely used for SPIF simulation, as shown in Table 2.2. On the other hand, the material behaviour through the sheet thickness is neglected. Besides, as established by Eykens *et al.* (2011) to model TTS, the material behaviour through sheet thickness has a relevant importance. Moreover, Belchior *et al.* (2013; 2014) have presented a mixed mesh model as a solution, combining the advantages of shell elements and solid elements.

Many other authors have analysed the influence of Finite Element type coupled with different hardening laws. The calibration of the hardening law parameters play an influent rule on the force level, as shown through a series of works from Bouffioux *et al.* (2008a, 2008b and 2010). Similarly, Eykens *et al.* (2010) and Henrard *et al.* (2010) analysed different hardening laws. Both authors have obtained similar observations regarding the simulation performed in ABAQUS using the same solid element of reduced integration (C3DR). In addition, both described the force prediction as being improved using a refined mesh submodel. Later, Sena *et al.* (2011) have performed SPIF simulations using the solid elements

available in ABAQUS software in order to assess the force prediction. From the comparison analysis, the reduced integration solid element (C3D8R) revealed to be not suitable for SPIF simulation due to its overestimation of tool force. In this sense, the observation of Eykens *et al.* 2010 and Henrard *et al.* (2010) cannot be associated only to a behaviour law, but also the hexahedral finite element chosen for SPIF simulation. In addition, the authors used several layer of finite elements in thickness direction which leads to well-known locking pathologies.

Table 2.2 summarises a number of authors chosen from literature that have used different integration schemes combined with different types of finite elements.

Table 2.2: Authors that used different integration schemes combined with types of finite elements.

Explicit		**Implicit**		
Shell	**Solid**	**Shell**	**Solid**	**Solid-Shell**
Cerro *et al.* (2006); Bambach and Hirt (2007); Henrard (2008); Azaouzi and Lebaal (2012); Dejardin *et al.* (2010); Robert *et al.* (2012); Shanmuganatan and Senthil Kumar (2012); Cui *et al.* (2013); Mirnia *et al.*, 2014 Bambach (2014);	Malhotra *et al.* (2012b); Mohammadi *et al.* (2014); Ndip-Agbor *et al.* (2015);	Henrard (2008); Lequesne *et al.* (2008) Hadoush and Boogaard (2009); Eyckens *et al.* (2010); Henrard *et al.* (2010); Bouffioux *et al.* (2011); Arfa *et al.* (2012); Guzmán *et al.* (2012); Li *et al.* (2012);	Flores *et al.* (2007); Aerens *et al.* (2009); Eyckens *et al.* (2010); Henrard *et al.* (2010); Essa and Hartley (2010);	Sena *et al.* (2011); Duchêne *et al.* (2013); Seong *et al.* (2014); Sena *et al.* (2015);

The choice of RESS formulation can help to decrease the computational cost, given the special integration scheme employed, and that is the reason of its selection in the present work. The addition of Enhanced Assumed Strain (EAS) modes, as appearing in RESS formulation, was shown to improve the overall

quality of the results (Sena *et al.*, 2011). A plausible explanation is that the bending-dominated deformation mechanism appearing during the forming process is better described using enhanced strain-based formulations.

The optimal material behaviour model according to the results from the aluminium alloy considered in many studies presented in Section 2.2.3, is mainly isotropic hardening, as in this case the effect of the cyclic effect is low.

The application of remeshing procedure confirmed a significant CPU time reduction and provided an acceptable result accuracy as clearly claimed by different authors that used different FEM codes. Hence, the use of a remeshing technique has an enormous advantage and provides an answer to the request of performing faster SPIF simulations.

As a last topic on the numerical standpoint, the Boundary Conditions (BC) applied to the simulation, such as, symmetric conditions and clamping edges can also lead to an artificial stiffening of the model. Bouffioux *et al.* (2007) have remarked the force overestimation due to stationary BC. To avoid this overestimation the clamping system has been modelled by springs distributed along the sheet edges. In addition, Henrard *et al.* (2010) and Bouffioux *et al.* (2010) have used boundary conditions based on a link between displacements at both edges of a pie model in order to minimize the effect of missing material. The main purpose is due to the tendency of the sheet to twist which cannot be predicted using symmetric BC.

The deformation modes in SPIF has been subject of controversy in the metal forming community. The increased formability of SPIF has been demonstrated as significantly higher compared with conventional sheet metal forming processes, such as stamping and deep drawing. Different explanations of forming limits of SPIF were presented in this review. These mechanisms are still not fully understood, although several mechanisms have been proposed in the literature review. Many authors claimed that the deformation occurs by stretching instead of shearing while others claimed the opposite. From experimental observation, the formability is limited by fracture without evidences of necking occurrence (Malhotra *et al.*, 2012b). Although the increase of formability can also be due to a large amount of TTS or, instead, due to serrated strain paths from cyclic plastic deformation and local plastic deformation.

Chapter 3

Topics in Nonlinear Formulation

In the present chapter the fundamental topics on nonlinear computational mechanics are summarized, particularly the kinematics of continuum bodies as well as strain and stress measures.
A Lagrangian formulation is chosen regarding the Finite Element code adopted to perform the numerical analysis in the following chapters. The following sections focus on the major points of general solid mechanics and their application by the Finite Element Method (FEM).

3.1 Principle of Virtual Work

The Finite Element Method (FEM) is established in terms of a weak form of differential equations. The weak form is a re-formulation of the original Partial Differential Equations (PDE), also called a variational equation. This method actually does not solve the so-called strong form of the differential equation (Fish and Belytschko, 2007), it purely solves its integral over the volume or domain, the so-called weak form of the differential equation. The weak formulation is the basic requirement for the application of approximation methods. In this sense, there are three integral principle approaches commonly used: principle of virtual work, principle of the minimum of total potential and principle of virtual force.

In order to develop the concept of stress, it is necessary to study the action of generic forces on a given body. Considering a generic three-dimensional deformable body defined by a volume V, with boundary S and in static equilibrium, a schematic representation can be given as shown in Figure 3.1. Also, assume that the body is under the action of external body forces $\mathbf{b}_i$ and tractions $\mathbf{t}$ (per unit

area) acting on the boundary, with $\mathbf{n}$ as the normal vector to the contact surface. The volume domain V is limited by boundaries divided into S_{D} and S_{N}. The boundary S_{D} is associated to prescribed displacements, representing the Dirichlet (essential) boundary conditions, such as supports ($\mathbf{u}_1$) or applied displacements. Prescribed surface tractions $\mathbf{t}$ are applied on S_{N}, defining the Neumann (Natural) boundary conditions.

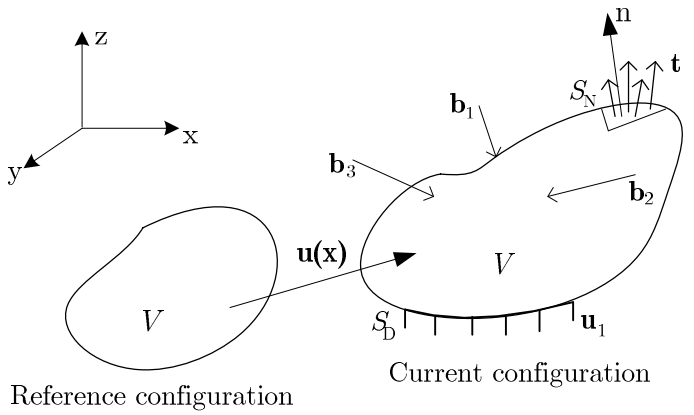

Figure 3.1: General three-dimensional body and Dirichlet and Neumann boundary conditions.

The equilibrium equation of a deformable body can be given as (Bathe, 1996; Bonet and Wood, 2008; Teixeira-Dias, *et al.*, 2010)

$$\mathrm{div}(\boldsymbol{\sigma}) + \mathbf{b} = 0\,, \tag{3.1}$$

where div(.) is the divergence operator. In order to obtain the weak form of Equation 3.1, it is multiplied by an arbitrary virtual displacement, $\delta\mathbf{u}$, consistent with the given boundary conditions S_{D}, and integrated over the volume, V

$$\int_V \delta\mathbf{u}\big[\mathrm{div}(\boldsymbol{\sigma}) + \mathbf{b}\big]\mathrm{d}\,V = 0\,. \tag{3.2}$$

The divergence (Gauss' theorem) of the vector $\delta\mathbf{u}\cdot\boldsymbol{\sigma}$ is defined as

$$\begin{aligned} \mathrm{div}(\delta\mathbf{u}\cdot\boldsymbol{\sigma}) &= \delta\mathbf{u}\cdot\mathrm{div}(\boldsymbol{\sigma}) + \nabla(\delta\mathbf{u}):\boldsymbol{\sigma}\,, \\ \delta\mathbf{u}\cdot\mathrm{div}(\boldsymbol{\sigma}) &= \mathrm{div}(\delta\mathbf{u}\cdot\boldsymbol{\sigma}) \text{ - } \nabla(\delta\mathbf{u}):\boldsymbol{\sigma}\,. \end{aligned} \tag{3.3}$$

where $\nabla(.)$ is the gradient operator. Decomposing Equation 3.2 and replacing Equation 3.3, in direct tensorial form gives

$$-\int_V \nabla(\delta\mathbf{u}):\boldsymbol{\sigma}\,\mathrm{d}\,V + \int_V \mathrm{div}(\delta\mathbf{u}\cdot\boldsymbol{\sigma})\mathrm{d}\,V + \int_V \delta\mathbf{u}\cdot\mathbf{b}\,\mathrm{d}\,V = 0\,, \tag{3.4}$$

Furthermore, the Gauss theorem for the divergence of a first order tensor, applied to the volume integral gives

$$\int_V \mathrm{div}(\delta\mathbf{u}\cdot\boldsymbol{\sigma})\mathrm{d}\,V = \int_S \delta\mathbf{u}\cdot\boldsymbol{\sigma}\cdot\mathbf{n}\,\mathrm{d}S = \int_S \delta\mathbf{u}\cdot\mathbf{t}\,\mathrm{d}S\,. \tag{3.5}$$

Taking into account that $S = S_{\mathrm{D}} \bigcup S_{\mathrm{N}}$ and $\delta\mathbf{u} = 0$ in S_{D}, Equation 3.4 can be rewritten as follows

$$-\int_V \nabla(\delta\mathbf{u}) : \boldsymbol{\sigma}\, \mathrm{d}\, V + \int_{S_{\mathrm{N}}} \delta\mathbf{u} \cdot \mathbf{t}\, \mathrm{d}S + \int_V \delta\mathbf{u} \cdot \mathbf{b}\, \mathrm{d}\, V = 0\,. \tag{3.6}$$

The strain measure is based on the gradient of the displacement vector, $\nabla\mathbf{u}$, which may be divided into a symmetric part ($\nabla^{(\mathrm{sym})}\mathbf{u}$) and an anti-symmetric part ($\nabla^{(\mathrm{asy})}\mathbf{u}$)

$$\nabla\mathbf{u} = \nabla^{(\mathrm{sym})}\mathbf{u} + \nabla^{(\mathrm{asy})}\mathbf{u}\,. \tag{3.7}$$

Based on this split, the symmetric part defines the strain

$$\nabla^{(\mathrm{sym})}\mathbf{u} = \frac{1}{2}\left(\nabla\mathbf{u} + \nabla\mathbf{u}^{\mathrm{T}}\right) = \mathbf{e}\,, \tag{3.8}$$

the anti-symmetric part defines the spin

$$\nabla^{(\mathrm{asy})}\mathbf{u} = \frac{1}{2}\left(\nabla\mathbf{u} - \nabla\mathbf{u}^{\mathrm{T}}\right) = \boldsymbol{\omega}\,. \tag{3.9}$$

Based on this decomposition, the Green-Lagrange strain tensor ($\mathbf{E}$) can be written in the following compact form

$$\mathbf{E} = \underbrace{\nabla^{(\mathrm{sym})}\mathbf{u}}_{\text{linear}} + \underbrace{\frac{1}{2}\left(\nabla\mathbf{u} \cdot \nabla\mathbf{u}^{\mathrm{T}}\right)}_{\text{nonlinear } (\nabla^{(\mathrm{asy})}\mathbf{u})}. \tag{3.10}$$

The first term in this equation is a linear part and the second term is nonlinear part of the displacement gradient, $\nabla\mathbf{u}$. The nonlinear term affects the strain tensor only when the gradient of the displacement field is large.

For a body that undergoes a displacement $\mathbf{u}(x)$ due to applied external forces, each material point displacement can be expressed through a virtual displacement, $\delta\mathbf{u}$, and the external forces generating virtual work, $\delta\mathrm{W}$. The virtual work for a set of virtual displacements, $\delta\mathbf{u}$, and its associated virtual strains, $\delta\mathbf{e}$, can also be expressed in indicial tensorial form as

$$\delta\mathrm{W} = \int_V \sigma_{ij}\delta\mathrm{e}_{ij}\mathrm{d}\, V - \int_V \mathrm{b}_i\,\delta\mathrm{u}_i\,\mathrm{d}\, V - \int_{S_{\mathrm{N}}} \mathrm{t}_i\,\delta\mathrm{u}_i\,\mathrm{d}S = 0\,. \tag{3.11}$$

This equation establishes the equilibrium of a deformable body and becomes the basis for the Finite Element discretisation. In a body in equilibrium, the internal virtual work must be equal to the external virtual work, as described through the condition of Equation 3.11. The virtual strains from the compatible virtual displacements define the internal virtual work, $\delta\mathrm{W}_{\mathrm{int}}$

$$\delta\mathrm{W}_{\mathrm{int}} = \int_V \sigma_{ij}\delta\mathrm{e}_{ij}\mathrm{d}\, V\,, \tag{3.12}$$

where σ_{ij} is the Cauchy stress. The quantity δe_{ij} is the infinitesimal strain tensor defined as

$$\delta e_{ij} = \frac{1}{2}\left(\frac{\partial \delta u_i}{\partial x_j} + \frac{\partial \delta u_j}{\partial x_i} \right). \tag{3.13}$$

where $\partial\delta\mathbf{u}$ is the virtual displacement related to the current coordinates $\mathbf{x}$. Equation 3.13 is based on the assumption that the displacements are small, wearing that the initial and final positions of a particle are practically equal. If the external loads $\mathbf{b}$ and $\mathbf{t}$ are applied at position $\mathbf{x}$, and this point undergoes a virtual displacement, $\delta\mathbf{u}(x)$, the total external virtual work, δW_{ext}, is

$$\delta W_{ext} = \int_V b_i \delta u_i \, dV + \int_{S_N} t_i \delta u_i \, dS \, . \tag{3.14}$$

Summarizing, the weak form of Equation 3.1, known as the Principle of Virtual Work (PVW), can also be rewritten taking into account the effect of concentrated forces, f_k, acting on the body as

$$\int_V \sigma_{ij} \delta e_{ij} \, dV = \int_V b_i \delta u_i \, dV + \int_{S_N} t_i \delta u_i \, dS \, . \tag{3.15}$$

Figure 3.2 exhibits the global relation between each component defined by the PVW.

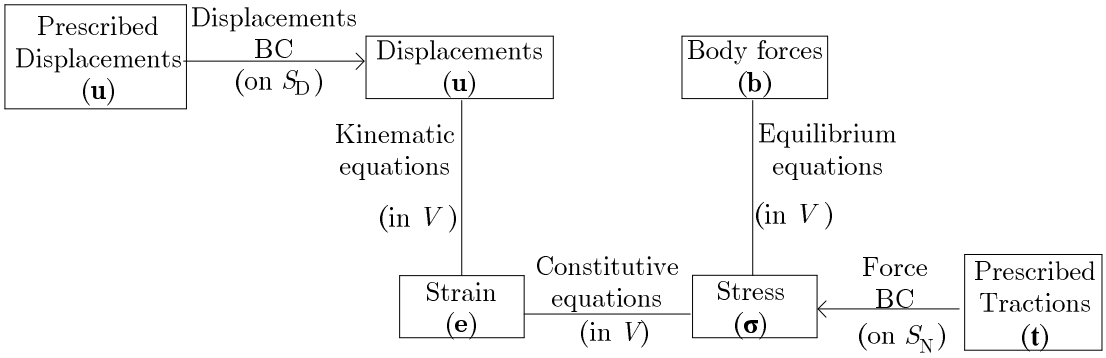

Figure 3.2: Connecting relations of fields in continuum mechanics.

3.2 Continuum Mechanics

Consider a deformed body that undergoes large displacements, large rotations and large strains as exhibited in Figure 3.3.

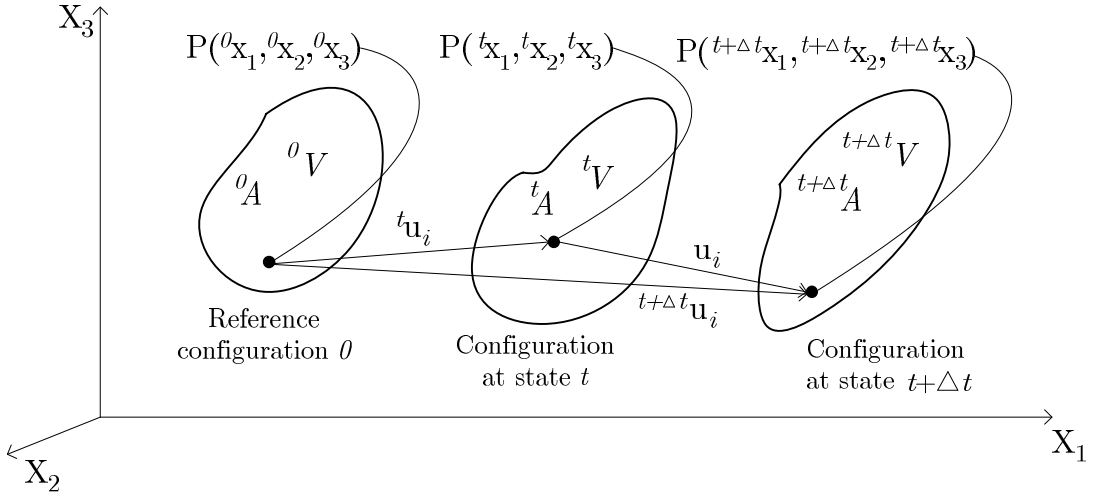

Figure 3.3: Position of a material point at different configurations.

A general application of virtual strain carries a subscript meaning that it is a strain referred to a time configuration. In static analysis, time is transformed into pseudo-time, which only assists to characterise the state of deformation. So, this subscript can appear as *t*, $t+\Delta t$ or *n*, *n+1*. According to Equation 3.12, PVW at configuration t can be expressed as

$$\int_{^tV} {}^t\sigma_{ij}\delta_t e_{ij}\,\mathrm{d}\,V = \int_{^tV} {}^t b_i \delta u_i \,\mathrm{d}\,V + \int_{^tS} {}^t t_i \delta u_i^S \,\mathrm{d}S \ . \tag{3.16}$$

The first part of the right-hand side of the equation corresponds to an integral over the volume of ${}^t\mathbf{b}$, and consists in the external applied forces at increment t, multiplied by the virtual displacement, $\delta\mathbf{u}$. The second part of the right-hand term is composed by the product of the external applied force per unit current area on surface, ${}^t\mathbf{t}$, with the virtual displacement $\delta\mathbf{u}^S$ acting on the surface. This product is integrated over the total area of the body. The ${}^tV$ and ${}^tS$ are volume and surface area, respectively, at configuration t.

Consider a particular material point P which has coordinates $\mathbf{x}_i$, corresponding to configurations, *0*, t and $t+\Delta t$ defined as the left upper superscript. The right subscript i is equal to 1, 2, 3, referring to the coordinate axis. Regarding this notation, the Cartesian axis remains stationary in which the body motion is measured and the distance unit along the axes, X_i, are the same for ${}^0\mathrm{x}_i$, ${}^t\mathrm{x}_i$ and

${}^{t+\Delta t}\mathrm{x}_i$. In the Lagrangian method, a particle position is measured in a referential coordinates system attached to a stationary observer. Hence, the particle motion is always measured in the global frame. The material point motion is described by the coordinates defined as (Bathe and Bolourchi, 1979)

$$ {}^{t}\mathbf{x} = {}^{0}\mathbf{x} + {}^{t}\mathbf{u} \ , \tag{3.17} $$

$$ {}^{t+\Delta t}\mathbf{x} = {}^{0}\mathbf{x} + {}^{t+\Delta t}\mathbf{u} \ . \tag{3.18} $$

The unknown increment of displacement from time t to $t+\Delta t$ is obtained as

$$ {}^{t+\Delta t}_{t}\mathbf{u} = {}^{t+\Delta t}\mathbf{u} - {}^{t}\mathbf{u} \ , \tag{3.19} $$

where ${}^{0}\mathbf{x}$ is the coordinates at reference configuration, ${}^{t+\Delta t}_{t}\mathbf{u}$ is the increment of displacement during Δt, ${}^{t}\mathbf{u}$ and ${}^{t+\Delta t}\mathbf{u}$ are the displacements at state t and $t+\Delta t$, respectively.

Applying the PVW at configuration $t+\Delta t$ and assuming that the solution from the state *0* to state t is known, the internal virtual work, ${}^{t+\Delta t}\delta\mathrm{W}_{\mathrm{int}}$, becomes

$$ {}^{t+\Delta t}\delta\mathrm{W}_{\mathrm{int}} = \int_{{}^{t+\Delta t}V} {}^{t+\Delta t}\sigma_{ij}\,\delta_{t+\Delta t}\mathrm{e}_{ij}\,\mathrm{d}\,V \ , \tag{3.20} $$

where the external virtual work, ${}^{t+\Delta t}\delta\mathrm{W}_{\mathrm{ext}}$ at increment $t+\Delta t$ is equal to

$$ {}^{t+\Delta t}\delta\mathrm{W}_{\mathrm{ext}} = \int_{{}^{t+\Delta t}V} {}^{t+\Delta t}\mathrm{b}_i\,\delta\mathrm{u}_i\,\mathrm{d}\,V + \int_{{}^{t+\Delta t}S} {}^{t+\Delta t}\mathrm{t}_i\,\delta\mathrm{u}_i\,\mathrm{d}S \ , \tag{3.21} $$

and the infinitesimal virtual strains, $\delta_{t+\Delta t}\mathrm{e}_{ij}$

$$ \delta_{t+\Delta t}\mathrm{e}_{ij} = \frac{1}{2}\left(\frac{\partial\delta\mathrm{u}_i}{\partial\,{}^{t+\Delta t}\mathrm{x}_j} + \frac{\partial\delta\mathrm{u}_j}{\partial\,{}^{t+\Delta t}\mathrm{x}_i} \right). \tag{3.22} $$

Extending the PVW from the infinitesimal displacement description to large deformation analysis and large displacements is quite similar. However, when the displacements are large, the initial and final coordinates of a particle are distinguished. This difference is due to the fact that coordinates ${}^{t+\Delta t}\mathbf{x}$ at current configuration, $t+\Delta t$, are unknown.

In order to use the PVW it is necessary to adapt it, as the integral of Equation 3.20 is computed over an unknown volume, ${}^{t+\Delta t}V$. As a result, the equation cannot be directly solved at current state, $t+\Delta t$, since it is not possible to integrate over an unknown volume. Accordingly, it is not possible to directly work with increments in the Cauchy stress, ${}^{t+\Delta t}\sigma_{ij}$, always referred to the current geometry. At this point, it is impossible to add a quantity that is referred to t into a quantity that is referred to $t+\Delta t$, due to the reference area, that has changed. Appropriate stress and strain measures are required, which leads to choose two

well-known quantities from literature: the 2nd Piola-kirchhoff stress tensor, ${}^{t}_{0}\mathbf{S}$ and its energy conjugate strain measure, that it the Green-Lagrange strain tensor, ${}^{t}_{0}\mathbf{E}$. The upper left subscript t means the configuration in which the strain or stress is measured, and the lower subscript 0 means the configuration to what the measure is referred. The 2nd Piola-kirchhoff stress tensor definition in indicial notation can be expressed as

$$ {}^{t}_{0}\mathrm{S}_{ij} = \frac{{}^{0}\rho}{{}^{t}\rho}\, {}^{0}_{t}\mathrm{F}_{im}\, {}^{t}\sigma_{mn}\, {}^{0}_{t}\mathrm{F}^{\mathrm{T}}_{nj}, \tag{3.23} $$

where ${}^{t}_{0}\mathrm{S}_{ij}$ is the force per unit of undeformed area in current configuration, t, referred to reference configuration, 0, with ij being the stress tensor components, $\frac{{}^{0}\rho}{{}^{t}\rho}$ is the mass density ratio, ${}^{t}\sigma_{mn}$ is the Cauchy stress, with (mn) ranging from 1 to 3, ${}^{0}_{t}\mathbf{F}^{-1}$ is the inverse deformation gradient and, similarly, i, j, m and n runs from 1 to 3. The Green-Lagrange strain tensor is defined as

$$ {}^{t}_{0}\mathrm{E}_{ij} = \frac{1}{2}\left({}^{t}_{0}\mathrm{u}_{i,j} + {}^{t}_{0}\mathrm{u}_{j,i} + {}^{t}_{0}\mathrm{u}_{k,i}\, {}^{t}_{0}\mathrm{u}_{k,j} \right), \tag{3.24} $$

where, ${}^{t}_{0}\mathrm{E}_{ij}$ is the strain in configuration t referred to configuration 0, with ij being the strain tensor components, and ${}^{t}_{0}\mathbf{u}$ is the displacement, that similarly i, j and k runs over all the possibilities from 1 to 3. The inverse deformation gradient, ${}^{0}_{t}\mathrm{F}^{-1}_{i,m}$, and displacement, ${}^{t}_{0}\mathrm{u}_{i,j}$, are defined as

$$ {}^{0}_{t}\mathrm{F}_{im} = \frac{\partial\, {}^{0}\mathrm{x}_{i}}{\partial\, {}^{t}\mathrm{x}_{m}}, \qquad {}^{t}_{0}\mathrm{u}_{i,j} = \frac{\partial\, {}^{t}\mathrm{u}_{i}}{\partial\, {}^{0}\mathrm{x}_{j}}. \tag{3.25} $$

The original coordinates, ${}^{0}\mathrm{x}_{i}$, are given and the coordinates ${}^{t}\mathrm{x}_{m}$ at configuration t, are assumed to be given. Notice that ${}^{t}\mathrm{x}_{m}$ is obtained through the sum of ${}^{0}\mathrm{x}_{i}$ with the displacement that has occurred, as shown by Equation 3.17.

Using the 2nd Piola-kirchhoff stress and its conjugate Green-Lagrange strain, the PVW can be rewritten as

$$ \int_{{}^{0}V} {}^{t}_{0}\mathrm{S}_{ij}\, \delta\, {}^{t}_{0}\mathrm{E}_{ij}\, \mathrm{d}\, V\,. \tag{3.26} $$

Due to the difficulty to deal with the integration of Cauchy stress at current configuration, t, the product on the right-hand side is integrated over the original volume of the body, ${}^{0}V$. This approach is used to obtain an approximation to the Cauchy stress, as in general incremental analysis, the volume at increment t is unknown. At increment t, it was calculated the volume up to t-Δt. This relation holds for the following configuration, t+Δt.

The stress and strain measures are related either to the undeformed or deformed volume. It depends on whether the internal virtual work is integrated over the original or the deformed geometry. Table 3.1 summarizes different energy conjugate pairs of stress-strain to represent the stress and strain measures.

Table 3.1: Work conjugacy of stress-strain pairs.

Strain	Stress	Symmetry	Volume	Orientation
Engineering Strain; True strain; Almansi strain	Cauchy (True stress)	Symmetric	Deformed	Spatial
Engineering Strain; Almansi strain	Kirchhoff	Symmetric	Original	Spatial
Deformation gradient	First Piola-Kirchhoff (Nominal Stress)	Non-Symmetric	Original	Mixed
Green-Lagrange strain	2nd Piola-Kirchhoff	Symmetric	Original	Material

In order to understand the properties of the 2nd Piola-kirchhoff stress tensor and the Green-Lagrange strain tensor, it is necessary to introduce the deformation gradient tensor (which already appear in Equation 3.23).

3.2.1. Deformation Gradient

The deformation gradient tensor, ${}^{t}_{0}\mathrm{F}_{ij}$, describes how a given point in the reference (or original state) *0*, maps into a following state, *t*. Its computation is fundamental in continuous mechanics and it is defined as

$$ {}^{t}_{0}\mathbf{F} = \frac{\partial^{t}\mathbf{x}}{\partial^{0}\mathbf{x}} \quad \text{or} \quad {}^{t}_{0}\mathbf{F} = \left({}_{0}\nabla^{t}\mathbf{x}^{\mathrm{T}} \right)^{\mathrm{T}}, \tag{3.27} $$

where ${}_{0}\boldsymbol{\nabla}^{t}$ is the gradient operator.

Regarding a known body, the motion from state *0* to *t*, and particularly at state *t*, the deformation gradient relates how the original configuration of a particular point will rotate and stretch to a current configuration, *t*. Its application is useful in Finite Element analysis. Besides those quantities described above, the calculation of the mass density ratio is also obtained. In other words, it is necessary to assess the mass density of the body, how it evolves through the space and time. For an infinitesimal volume $\mathrm{d}V$, the mass should be preserved in the space and time

$$ {}^{t}\rho\,{}^{t}\mathrm{d}V = {}^{0}\rho\,{}^{0}\mathrm{d}V\,, \tag{3.28} $$

where ρ is the mass density and $\mathrm{d}V$ is the differential volume. The following equation demonstrates how the differential volume changes from reference configuration, *0*, to current configuration, t

$$ {}^{t}\mathrm{d}V = \det({}^{t}_{0}\mathbf{F})\,{}^{0}\mathrm{d}V\,, \tag{3.29} $$

in which $\det({}^{t}_{0}\mathbf{F})$ is a measure of the change in volume. The relation between equations 3.28 and 3.29 gives

$$ {}^{0}\rho = {}^{t}\rho\,\det\left({}^{t}_{0}\mathbf{F}\right)\cdot \tag{3.30} $$

This equation shows how the mass density changes and provides the mass density ratio. The original orientation and length, $\mathrm{d}^{0}\mathrm{x}_{i}$, in reference configuration is defined as

$$ \mathrm{d}\,{}^{0}\mathbf{x}_{1} = \begin{bmatrix}1\\0\\0\end{bmatrix}\mathrm{d}\mathbf{s}_{1};\ \mathrm{d}\,{}^{0}\mathbf{x}_{2} = \begin{bmatrix}0\\1\\0\end{bmatrix}\mathrm{d}\mathbf{s}_{2};\quad \mathrm{d}\,{}^{0}\mathbf{x}_{3} = \begin{bmatrix}0\\0\\1\end{bmatrix}\mathrm{d}\mathbf{s}_{3}, \tag{3.31} $$

hence the original differential volume at original state is given as ${}^{0}\mathrm{d}V = \mathrm{d}\mathbf{s}_{1}\mathrm{d}\mathbf{s}_{2}\mathrm{d}\mathbf{s}_{3}$. However, recognising that

$$ \mathrm{d}\,{}^{t}\mathbf{x}_{i} = {}^{t}_{0}\mathbf{F}\,\mathrm{d}\,{}^{0}\mathbf{x}_{i}\ ;\quad i = 1,2,3\,, \tag{3.32} $$

and

$$ \begin{aligned} {}^{t}\mathrm{d}V &= \left(\mathrm{d}\,{}^{t}\mathbf{x}_{1}\times\mathrm{d}\,{}^{t}\mathbf{x}_{2}\right)\cdot\mathrm{d}\,{}^{t}\mathbf{x}_{3} \\ &= \det({}^{t}_{0}\mathbf{F})\,{}^{0}\mathrm{d}s_{1}\mathrm{d}s_{2}\mathrm{d}s_{3} \\ &= \det({}^{t}_{0}\mathbf{F})\,{}^{0}\mathrm{d}V \end{aligned}\quad . \tag{3.33} $$

in which this relation proves Equation 3.29.

The inverse of deformation gradient mathematically can be seen as

$$ {}^{0}_{t}\mathbf{F} = \left({}^{t}_{0}\mathbf{F}\right)^{-1}, \tag{3.34} $$

where

$$ \mathrm{d}\,{}^{0}\mathbf{x} = {}^{0}_{t}\mathbf{F}\ \mathrm{d}\,{}^{t}\mathbf{x}\,. \tag{3.35} $$

Replacing Equation 3.32 into Equation 3.35 leads to

$$ \begin{aligned} \mathrm{d}\,{}^{0}\mathbf{x} &= {}^{0}_{t}\mathbf{F}\left({}^{t}_{0}\mathbf{F}\,\mathrm{d}\,{}^{0}\mathbf{x}\right) \\ &= \left({}^{0}_{t}\mathbf{F}\,{}^{t}_{0}\mathbf{F}\right)\mathrm{d}\,{}^{0}\mathbf{x} \\ &= \mathbf{I}\,\mathrm{d}\,{}^{0}\mathbf{x} \end{aligned}\quad . \tag{3.36} $$

where $\mathbf{I}$ is the identity matrix.

3.2.2. Polar Decomposition

The deformation gradient tensor, **F**, describes the stretches (change of shape) and the rigid body rotation, but does not include information of possible rigid body translation, which enables the following calculation. This theorem demonstrates that a non-singular second-order tensor can always be decomposed into the product of an orthogonal rotation matrix, **R**, and a symmetric stretch matrix, **U**. Applying the polar decomposition theorem results

$$\mathbf{F} = \mathbf{RU} = \mathbf{VR}, \tag{3.37}$$

where **R** is the orthogonal rotation tensor, i.e. $\mathbf{R}^{\mathrm{T}}\mathbf{R} = \mathbf{I}$ with $\det(\mathbf{R}) = 1$, **U** and **V** are the symmetric right and left stretch matrices, respectively. Also, through the deformation gradient, **F**, it is possible to define the right, **C**, and left, $\mathbf{b}^{*}$, Cauchy-Green strain tensors

$$\mathbf{C} = \mathbf{F}^{\mathrm{T}}\mathbf{F}\,, \tag{3.38}$$

and

$$\mathbf{b}^{*} = \mathbf{F}\mathbf{F}^{\mathrm{T}}, \tag{3.39}$$

respectively. The deformation gradient can be symmetric or non-symmetric. Usually, it is a non-symmetric matrix, but it is a symmetric matrix if there is no rigid body rotation. Notice that being a non-symmetric matrix transposed, $\mathbf{F}^{\mathrm{T}}$, multiplied by itself, **F**, makes **C** a symmetric matrix. Replacing Equation 3.37 into Equation 3.38 gives

$$\mathbf{C} = \left(\mathbf{U}^{\mathrm{T}}\mathbf{R}^{\mathrm{T}}\right)\left(\mathbf{RU}\right) = \left(\mathbf{U}\right)^{2}. \tag{3.40}$$

Since ${}^{t}_{0}\mathbf{R}$ is orthogonal, it means that $\mathbf{R}^{\mathrm{T}}\mathbf{R} = \mathbf{I}$ and **C** is independent of the rotation.

The presence of a rigid body motion is vanished in analysis of large rotations and/or large deformations. The definition of the Green-Lagrange strain measure used through the right Cauchy-Green strain tensor can be written into an equivalent form as

$$\mathbf{E} = \frac{1}{2}\left(\mathbf{C} - \mathbf{I}\right), \tag{3.41}$$

This definition allows for an easy use of the deformation gradient. For instance, if a given body is subjected to a rigid body motion only, between states *0* and *t*, the deformation gradient results in **F**=**R** and leads to

$$\mathbf{C} = \mathbf{R}^{\mathrm{T}}\mathbf{R} = \mathbf{I}\,. \tag{3.42}$$

Replacing Equation 3.42 into Equation 3.41 gives

$$\mathbf{E} = \frac{1}{2}\left(\mathbf{R}^{\mathrm{T}}\mathbf{R} - \mathbf{I}\right) = \frac{1}{2}\left(\mathbf{I} - \mathbf{I}\right) = \mathbf{0}, \tag{3.43}$$

which proves that Equation 3.41 avoids the presence of rigid body motion. Another way to define the Green-Lagrange strain tensor is by replacing its terms by displacements, as previously shown in Equation 3.24.

Summarizing all these definitions, the 2nd Piola-kirchhoff stress tensor, ${}^{t}_{0}\mathbf{S}$, can be expressed by

$${}^{t}_{0}\mathbf{S} = \frac{{}^{0}\rho}{{}^{t}\rho}\,{}^{0}_{t}\mathbf{F}\;{}^{t}\boldsymbol{\sigma}\;{}^{0}_{t}\mathbf{F}^{\mathrm{T}} = \frac{{}^{0}\rho}{{}^{t}\rho}\,{}^{0}_{t}(\mathbf{RU})\;{}^{t}\boldsymbol{\sigma}\;{}^{0}_{t}(\mathbf{RU})^{\mathrm{T}}, \tag{3.44}$$

where ${}^{0}_{t}\mathbf{F}$ is the inverse of the deformation gradient matrix (see Equation 3.34). Concerning its properties: ${}^{t}_{0}\mathbf{S}$ is a symmetric tensor, invariant under a rigid-body motion (translations and/or rotation), hence ${}^{t}_{0}\mathbf{S}$ only changes when the material is deformed. The tensor ${}^{t}_{0}\mathbf{S}$ has no direct physical interpretation, however it is linked to the Cauchy stress, ${}^{t}\boldsymbol{\sigma}$, as

$${}^{t}\boldsymbol{\sigma} = \frac{{}^{t}\rho}{{}^{0}\rho}\,{}^{t}_{0}\mathbf{F}\,{}^{t}_{0}\mathbf{S}\,{}^{t}_{0}\mathbf{F}^{\mathrm{T}}. \tag{3.45}$$

Considering small strains (unidimensional) or small stretches (multidimensional), large displacements and arbitrary rotations, the stretch tensor $\mathbf{U}$ can be approximately given as $\mathbf{U} \approx \mathbf{I}$ and the determinant of deformation gradient turns $\frac{{}^{0}\rho}{{}^{t}\rho} = \det({}^{t}_{0}\mathbf{F}) = 1$. As well as the $2nd$ Piola-kirchhoff stress, ${}^{t}_{0}\mathrm{S}$, is approximately equal to the rotated Cauchy stress, ${}^{t}\boldsymbol{\sigma}$. For this reason, ${}^{t}_{0}\mathrm{S}$ can be linked to the stress-strain law or co-rotational stress (Doghri, 2000).

The PVW cannot be directly applied due to the unknown variable values, more specifically the increment of displacement value, $\mathbf{u}_i$. To linearize it, it is necessary to choose a reference configuration, giving rise to two distinct approaches: Total Lagrangian formulation (TL), if the original state of a body is used as reference configuration, and the Updated Lagrangian formulation (UL), if the last converged configuration is used as reference. As the in-house Finite Element code named LAGAMINE (Cescotto and Grober, 1985) based on UL formulation is chosen, the following sections describe its main formulation topics.

3.2.3. Updated Lagrangian

The Updated Lagrangian (UL) formulation uses the displacements, stresses and the strain measures referred to the immediately previous converged configuration of the body at state t. It means that this formulation deals with a integration over a known volume, ${}^{t}V$. The incremental solution of the PVW applied for the configuration $t+\Delta t$, using UL formulation gives the 2nd Piola-kirchhoff stress, ${}^{t+\Delta t}_{t}\mathrm{S}_{ij}$, as

$$\int_{{}^{t}V} {}^{t+\Delta t}_{t}\mathrm{S}_{ij}\delta\,{}^{t+\Delta t}_{t}\mathrm{E}_{ij}\mathrm{d}\,V = {}^{t+\Delta t}\delta\mathrm{W}_{\mathrm{ext}}\,, \tag{3.46}$$

and the equivalent for Cauchy stress, ${}^{t+\Delta t}\sigma_{ij}$ is written as

$$\int_{{}^{t+\Delta t}V} {}^{t+\Delta t}\sigma_{ij}\delta_{t+\Delta t}\mathrm{e}_{ij}\mathrm{d}\,V = {}^{t+\Delta t}\delta\mathrm{W}_{\mathrm{ext}}\,. \tag{3.47}$$

This equation expresses the equilibrium, compatibility and stress-strain law at state $t+\Delta t$. If the equilibrium is satisfied, it must hold for any virtual displacement that satisfies the displacement boundary condition. The virtual displacement, $\delta\,{}^{t+\Delta t}\mathrm{u}_i$, comes from the external virtual work term, ${}^{t+\Delta t}\delta\mathrm{W}_{\mathrm{ext}}$, and $\delta_{t+\Delta t}\mathrm{e}_{ij}$ is the corresponding virtual strain. The compatibility enters in the internal virtual work, left-hand side term, due to the calculation of stress from compatible displacement. The stress-strain law enters in the calculation of the stress, ${}^{t+\Delta t}\sigma_{ij}$, and applied at current state, $t+\Delta t$.

Considering the solution at state t known, the incremental stress and strain decompositions for the UL formulation can directly be represented for the following configuration, $t+\Delta t$, as shown

$${}^{t+\Delta t}_{t}\mathrm{S}_{ij} = {}^{t}\mathrm{S}_{ij} + \Delta_t\mathrm{S}_{ij} \approx {}^{t}\sigma_{ij} + \Delta_t\mathrm{S}_{ij}\,, \tag{3.48}$$

$${}^{t+\Delta t}_{t}\mathrm{E}_{ij} = \underbrace{{}^{t}\mathrm{E}_{ij}}_{=0} + \Delta_t\mathrm{E}_{ij} = \Delta_t\mathrm{E}_{ij} \;\Leftrightarrow\; {}^{t+\Delta t}_{t}\mathrm{E}_{ij} = \Delta_t\mathrm{E}_{ij}\,, \tag{3.49}$$

where ${}^{t}\mathrm{S}_{ij}$ and ${}^{t}\mathrm{E}_{ij}$ are known, and the increments of $\Delta_t\mathrm{S}_{ij}$ and $\Delta_t\mathrm{E}_{ij}$ are unknown, if a displacement increment is considered. The known stress, ${}^{t}\mathrm{S}_{ij}$, is equal to Cauchy stress, ${}^{t}\sigma_{ij}$, applying Equation 3.48. The quantity ${}^{t}\mathrm{E}_{ij}$ is equal to zero since only the increment of displacement from state t to state $t+\Delta t$ is used, remaining the unknown term, $\Delta_t\mathrm{E}_{ij}$. The last target configuration, once reached, becomes the next reference configuration. Strains and stresses are redefined as soon as the reference configuration is updated.

The total strain, ${}^{t+\Delta t}_{t}\mathrm{E}_{ij}$, at state $t+\Delta t$ referred to t is given as

$$ {}^{t+\Delta t}_{t}\mathrm{E}_{ij} = \Delta_t \mathrm{E}_{ij} = \frac{1}{2}\left({}^{t+\Delta t}_{t}\mathrm{u}_{i,j} + {}^{t+\Delta t}_{t}\mathrm{u}_{j,i} + {}^{t+\Delta t}_{t}\mathrm{u}_{k,i}\ {}^{t+\Delta t}_{t}\mathrm{u}_{k,j} \right), \tag{3.50} $$

where

$$ {}^{t+\Delta t}_{t}\mathrm{u}_{i,j} = \frac{\partial\left({}^{t+\Delta t}\mathrm{u}_i - {}^{t}\mathrm{u}_i \right)}{\partial\, {}^{t}\mathrm{x}_j} = \frac{\partial(\Delta \mathrm{u}_i)}{\partial\, {}^{t}\mathrm{x}_j} , \tag{3.51} $$

and $\Delta_t \mathrm{E}_{ij}$ can be decomposed as

$$ \Delta_t \mathrm{E}_{ij} = \underbrace{\frac{1}{2}\left({}_t\mathrm{u}_{i,j} + {}_t\mathrm{u}_{j,i} \right)}_{Linear} + \underbrace{\frac{1}{2}\, {}_t\mathrm{u}_{k,i}\, {}_t\mathrm{u}_{k,j}}_{Nonlinear} . \tag{3.52} $$

Hence from this decomposition $\Delta_t \mathrm{E}_{ij}$ and $\delta_t \mathrm{E}_{ij}$ are

$$ \Delta_t \mathrm{E}_{ij} = \Delta_t \mathrm{e}_{ij} + \Delta_t \eta_{ij} , \tag{3.53} $$

$$ \delta_t \mathrm{E}_{ij} = \delta_t \mathrm{e}_{ij} + \delta_t \eta_{ij} . \tag{3.54} $$

where $\Delta_t \mathrm{e}_{ij}$ and $\Delta_t \eta_{ij}$ are the linear and nonlinear increments, respectively, of the Green-Lagrange strain. Replacing directly equations 3.48 and 3.54 into the expression of PVW (Equation 3.46) and after manipulation, it becomes

$$ \int_{{}_tV} \Delta_t \mathrm{S}_{ij} \delta_t \mathrm{E}_{ij} \mathrm{d}\, V + \int_{{}_tV} {}^{t}\sigma_{ij} \delta_t \eta_{ij} \mathrm{d}\, V = {}^{t+\Delta t}\delta \mathrm{W}_{\mathrm{ext}} - \int_{{}_tV} {}^{t}\sigma_{ij} \delta_t \mathrm{e}_{ij} \mathrm{d}\, V . \tag{3.55} $$

where $\Delta_t \mathrm{S}_{ij}$ is the increment of stress, $\delta_t \mathrm{E}_{ij}$, is the variation of the increment Green-Lagrange strain, from t to $t+\Delta t$, and $\delta_t \eta_{ij}$ is the nonlinear strain increment corresponding to total Green-Lagrange strain increment. On the right hand side, ${}^{t+\Delta t}\delta \mathrm{W}_{\mathrm{ext}}$ is the external virtual work and $\delta_t \mathrm{e}_{ij}$ is the linear strain increment corresponding to total Green-Lagrange strain increment. Finally, ${}^{t}\sigma_{ij}$ is the total Cauchy stress corresponding to state *t*. Notice that on the left-hand side are the unknown displacement variation increments, $\delta \mathrm{u}_i$, and on the right-hand side are the known terms.

3.2.4. Finite Element Linearization

The PVW equation in general is a nonlinear function with the unknown displacement increments, u_i. An approximate solution in Finite Element analysis is obtained by linearizing Equation 3.55, i.e., all higher-order terms in u_i are neglected and only linear terms remain. In detail, the linearization of each term is verified in order to know if it contains the unknown displacement increments.

The term $\int_{{}_tV} {}^{t}\sigma_{ij} \delta_t \eta_{ij} \mathrm{d}\, V$ is linear in u_i:

- ${}^{t}\sigma_{ij}$ does not contain u_i (${}^{t}\sigma_{ij}$ is known quantity);
- $\delta_t \eta_{ij} = \frac{1}{2}\,{}_t u_{k,i}\delta_t u_{k,j} + \frac{1}{2}\delta_t u_{k,i}\,{}_t u_{k,j}$ is linear in u_i (unknown), where $\delta_t u_{k,j}$ and $\delta_t u_{k,i}$ are constants for a given variation.

The term $\int_{{}^{t}V} {}_t S_{ij}\delta_t E_{ij}\,dV$ contains linear and higher-order terms in u_i:

- ${}_t S_{ij}$ is a nonlinear function of ${}_t E_{ij}$;
- $\delta_t E_{ij} = \delta_t e_{ij} + \delta_t \eta_{ij}$ is a linear function of u_i.

Multiplying these terms gives ${}_t S_{ij}\delta_t E_{ij}$, which leads to an expression with higher-order terms in u_i. Its linearization has the objective to compute an approximation ${}_t S_{ij}$ as a linear function of u_i. The term $\delta_t E_{ij}$ contains only constants and linear terms in u_i. The term ${}_t S_{ij}$ can be written as Taylor series

$$\begin{aligned} {}_t S_{ij} &= \underbrace{\left.\frac{\partial\, {}_t S_{ij}}{\partial\, {}_t E_{rs}}\right|_t}_{known} \underbrace{{}_t E_{rs}}_{\substack{linear\ and \\ quadratic\ in\ u_i}} + \textit{higher order terms,} \\ &\approx \left.\frac{\partial\, {}_t S_{ij}}{\partial\, {}_t E_{rs}}\right|_t \Big(\underbrace{{}_t e_{rs}}_{linear\ in\ u_i} + \underbrace{{}_t \eta_{rs}}_{quadratic\ in\ u_i} \Big) \approx \underbrace{{}_t C_{ijrs}\,{}_t e_{rs}}_{linearized\ term}. \end{aligned} \tag{3.56}$$

where ${}_t C_{ijrs}$ is the stress-strain derivation law corresponding to the constitutive relation $\frac{\partial\, {}_t S_{ij}}{\partial\, {}_t E_{rs}}$. The higher order terms and ${}_t \eta_{rs}$ are neglected.

The stress-strain law basically relates the stress increment with the strain increment, ${}_t\mathbf{C}$. Substituting equations 3.54 and 3.56 into the term ${}_t S_{ij}\delta_t E_{ij}$, its linearization is directly obtained as shown

$$\begin{aligned} {}_t S_{ij}\delta_t E_{ij} &\approx {}_t C_{ijrs}\,{}_t e_{rs}(\delta_t e_{ij} + \delta_t \eta_{ij}) \\ &\approx \underbrace{{}_t C_{ijrs}\,{}_t e_{rs}\delta_t e_{ij}}_{Linear\ in\ u_i} + \underbrace{{}_t C_{ijrs}\,{}_t e_{rs}\delta_t \eta_{ij}}_{Quadratic\ in\ u_i} \\ &\approx \underbrace{{}_t C_{ijrs}\,{}_t e_{rs}\delta_t e_{ij}}_{Linearized\ result}. \end{aligned} \tag{3.57}$$

where $\delta_t e_{ij}$ does not contain u_i, it is constant, $\delta_t \eta_{ij}$ and ${}_t e_{rs}$ are linear in u_i, which turns the right-hand term quadratic in u_i, so it is neglected.

Summarizing, the final linearized Equation 3.57 is replaced into Equation 3.55 and it gives

$$\underbrace{\int_{{}^{t}V} {}^{t}\mathrm{C}_{ijrs}\, {}_{t}\mathrm{e}_{rs}\delta_{t}\mathrm{e}_{ij}\mathrm{d}\,V + \int_{{}^{t}V} {}^{t}\sigma_{ij}\delta_{t}\eta_{ij}\mathrm{d}\,V}_{\delta\mathbf{u}^{\mathrm{T}}\,{}^{t}\mathbf{K}\Delta\mathbf{u}}$$
$$= \underbrace{{}^{t+\Delta t}\delta\mathrm{W}_{\mathrm{ext}} - \int_{{}^{t}V} {}^{t}\sigma_{ij}\delta_{t}\mathrm{e}_{ij}\mathrm{d}\,V}_{\delta\mathbf{u}^{\mathrm{T}}\left({}^{t+\Delta t}\mathbf{P}-{}^{t}\mathbf{f}\right)}. \tag{3.58}$$

where ${}^{t}\mathbf{K}$ is the tangent stiffness matrix, which contains the material tensor, ${}_{t}\mathrm{C}_{ijrs}$, as well the current stress. The incremental displacement, $\Delta\mathbf{u}$, comes from a linear strain part, ${}_{t}\mathrm{e}_{rs}$, and from a nonlinear strain pair, $\delta_{t}\eta_{ij}$. The virtual displacement vector, $\delta\mathbf{u}^{\mathrm{T}}$, comes from $\delta_{t}\mathrm{e}_{ij}$ and also from $\delta_{t}\eta_{ij}$, which becomes equal to the identity matrix, $\delta\mathbf{u}^{\mathrm{T}} = \mathbf{I}$. The external virtual work, ${}^{t+\Delta t}\delta\mathrm{W}_{\mathrm{ext}}$, results into a vector of nodal external forces, ${}^{t+\Delta t}\mathbf{P}$, and the term ${}^{t}\sigma_{ij}\delta_{t}\mathrm{e}_{ij}$ results into the internal force vector, ${}^{t}\mathbf{f}$, corresponding to internal element stress. The calculation of ${}^{t}\mathbf{f}$ should be accurately achieved iteratively to provide the equilibrium with the external force vector, ${}^{t+\Delta t}\mathbf{P}$. This equilibrium is interpreted as an "out-of-balance" virtual work term. The stiffness matrix ${}^{t}\mathbf{K}$ is used to obtain in the incremental solution the appropriate incremental displacement, $\Delta\mathbf{u}$. An important assumption is

$$\int_{{}^{t}V} {}^{t}\sigma_{ij}\delta_{t}\mathrm{e}_{ij}\mathrm{d}\,V, \tag{3.59}$$

which it is the virtual work of the internal stresses at state t introduced within the equilibrium relation

$$\mathbf{K}\Delta\mathbf{u} = {}^{t+\Delta t}\delta\mathrm{W}_{\mathrm{ext}} - \int_{{}^{t}V} {}^{t}\sigma_{ij}\delta_{t}\mathrm{e}_{ij}\mathrm{d}\,V. \tag{3.60}$$

In general, Equation 3.58 is solved by an iterative solution procedure based on the UL formulation

$$\begin{aligned}&\int_{{}^{t}V} {}^{t}\mathrm{C}_{ijrs}\Delta_{t}\mathrm{e}_{rs}^{(k)}\delta_{t}\mathrm{e}_{ij}\mathrm{d}\,V + \int_{{}^{t}V} {}^{t}\sigma_{ij}\delta\Delta_{t}\eta_{ij}^{(k)}\mathrm{d}\,V \\ &= {}^{t+\Delta t}\delta\mathrm{W}_{\mathrm{ext}} - \int_{{}^{t+\Delta t}V^{(k-1)}} {}^{t+\Delta t}\sigma_{ij}^{(k-1)}\delta_{\,t+\Delta t}\mathrm{e}_{ij}^{(k-1)}\mathrm{d}\,V.\end{aligned} \tag{3.61}$$

which is the weak form obtained for the development of Finite Element approach. The discretization of Equation 3.61 using FEM can be written as follows

$${}^{t}\mathbf{K}\Delta\mathbf{u}^{(k)} = {}^{t+\Delta t}\mathbf{P} - {}^{t+\Delta t}\mathbf{f}^{(k-1)}, \quad \textit{(for } k = 1,2,3\ldots\textit{)} \tag{3.62}$$

where ${}^{t+\Delta t}\mathbf{f}^{(k-1)}$ is the internal force computed from current displacements, ${}^{t+\Delta t}\mathbf{u}_{i}^{(k-1)}$ and ${}^{t+\Delta t}\mathbf{P}$ is the nodal point vector that corresponds to the external applied forces. The initial condition is ${}^{t+\Delta t}\mathbf{f}^{(0)} = {}^{t}\mathbf{f}$ at k equal to 1 or generally the initial

solution for Newton-Raphson is always the last converged one. Analysing the term on the right-hand side of Equation 3.62, the nodal equilibrium is satisfied when

$$\mathbf{r} = {}^{t+\Delta t}\mathbf{P} - {}^{t+\Delta t}\mathbf{f}^{(k-1)} \approx 0 \quad . \tag{3.63}$$

which means that the equilibrium is achieved if the externally applied loads are approximately equal to nodal internal forces. The difference between them leads to a residual load vector, $\mathbf{r}$, used to compute the nodal displacement increment, $\Delta\mathbf{u}$. Subsequently, it is added to the nodal displacement from previous iteration (k-*1*) in order to obtain the updated nodal displacement, ${}^{t+\Delta t}\mathbf{u}$, at $t+\Delta t$

$${}^{t+\Delta t}\mathbf{u}^{(k)} = {}^{t+\Delta t}\mathbf{u}^{(k-1)} + \Delta\mathbf{u}^{(k)} \quad . \tag{3.64}$$

The initial condition for iterative procedure is ${}^{t+\Delta t}\mathbf{u}^{(0)} = {}^{t}\mathbf{u}$ at k equal to 1, which means that the initial solution for Newton-Raphson procedure is always the last converged one. The displacement update, ${}^{t+\Delta t}\mathbf{u}^{(k)}$, is performed at each iteration as

$$\begin{gathered} {}^{t+\Delta t}\mathbf{u}^{(k)} = {}^{t}\mathbf{u} + \sum_{j=1}^{k} \Delta\mathbf{u}^{(j)}. \\ (\text{for } k = 1, 2, 3...) \end{gathered} \tag{3.65}$$

The iterative procedure is repeated until the solution converges, i.e., when the equilibrium is satisfied, ${}^{t+\Delta t}\mathbf{P} - {}^{t+\Delta t}\mathbf{f}^{(k-1)} \approx 0$ and the correct configuration is achieved for the Finite Element mesh. By replacing the initial conditions in the iterative subscripts of equations 3.62 and 3.64, they are reduced to the previous state t

$${}^{t}\mathbf{K}\Delta\mathbf{u} = {}^{t+\Delta t}\mathbf{P} - {}^{t}\mathbf{f}\,, \quad {}^{t+\Delta t}\mathbf{u} \approx {}^{t}\mathbf{u} + \Delta\mathbf{u}\,. \tag{3.66}$$

3.3 Approximate Solution: Finite Element Discretization

Generalizing for a multidimensional example with any prescribed boundary condition value, S, and based on the Partial Differential Equation, the constitutive relation and boundary conditions are defined as follows (Teixeira-Dias, *et al.*, 2010)

$$\begin{cases} \sigma = \mathbf{C} : \mathbf{e} & \in V \\ t \cdot \mathbf{n} = \mathbf{t} & \in S_{\mathrm{N}} \\ \mathbf{u} = \overline{\mathbf{u}} & \in S_{\mathrm{D}} \end{cases} . \tag{3.67}$$

Reorganising Equation 3.6 in direct tensorial form gives

$$\int_V \nabla(\delta\mathbf{u}) : \boldsymbol{\sigma}\, \mathrm{d}\, V = \int_V \delta\mathbf{u}\cdot\mathbf{b}\, \mathrm{d}\, V + \int_{S_\mathrm{N}} \delta\mathbf{u}\cdot\mathbf{t}\, \mathrm{d}S\ , \tag{3.68}$$

and replacing the conditions expressed in Equation 3.67, one obtains

$$\int_V \nabla(\delta\mathbf{u}) : \mathbf{C} : \mathbf{e}\, \mathrm{d}\, V = \int_V \delta\mathbf{u}\cdot\mathbf{b}\, \mathrm{d}\, V + \int_{S_\mathrm{N}} \delta\mathbf{u}\cdot\mathbf{t}\, \mathrm{d}S\ , \tag{3.69}$$

On the other hand, regarding the strain-displacement relation defined in Equation 3.8, and replacing it into the previous equation, it gives

$$\int_V \nabla(\delta\mathbf{u}) : \mathbf{C} : \nabla(\delta\mathbf{u})\, \mathrm{d}\, V = \int_V \delta\mathbf{u}\cdot\mathbf{b}\, \mathrm{d}\, V + \int_{S_\mathrm{N}} \delta\mathbf{u}\cdot\mathbf{t}\, \mathrm{d}S\ . \tag{3.70}$$

Resorting to the weak formulation, the unknown trial function, $\mathbf{u}(\mathrm{x},\mathrm{y},\mathrm{z})$, is approximated as follows

$$\mathbf{u}(x,y,z) = \mathbf{N}(\mathrm{x},\mathrm{y},\mathrm{z})\mathbf{d}\ , \tag{3.71}$$

where $\mathbf{N}(\mathrm{x},\mathrm{y},\mathrm{z})$ is the shape functions matrix used to interpolate the displacement and $\mathbf{d}$ is the degrees of freedom vector. The trial function describes a possible candidate shape of the approximate solution and must satisfy the essential boundary conditions. The equilibrium resolution of Equation 3.70 requires its discretization, i.e. the division of the domain in elements. Similarly, for each element, subscript e, the candidate function is approximated by shape functions

$$\mathbf{u}^e(x,y,z) = \mathbf{N}^e(\mathrm{x},\mathrm{y},\mathrm{z})\mathbf{d}^e\ . \tag{3.72}$$

where $\mathbf{d}^e$ is given in terms of global nodal values for the element. Through Equation 3.8 we can obtain the following relation

$$\mathbf{e} = \nabla^{\mathrm{sym}}\mathbf{u} = \nabla^{\mathrm{sym}}(\mathbf{N}^e\mathbf{d}^e) = \mathbf{B}^e\mathbf{d}^e\ . \tag{3.73}$$

where $\mathbf{B}^e$ is the strain-displacement operator which contains the derivatives of the element shape functions and

$$\nabla\mathbf{N}^e(\mathrm{x},\mathrm{y},\mathrm{z}) = \begin{Bmatrix} \dfrac{\partial\mathbf{N}^e(\mathrm{x},\mathrm{y},\mathrm{z})}{\partial x} \\ \dfrac{\partial\mathbf{N}^e(\mathrm{x},\mathrm{y},\mathrm{z})}{\partial y} \\ \dfrac{\partial\mathbf{N}^e(\mathrm{x},\mathrm{y},\mathrm{z})}{\partial z} \end{Bmatrix} = \mathbf{B}^e(\mathrm{x},\mathrm{y},\mathrm{z})\,. \tag{3.74}$$

The $\mathbf{B}^e$ operator is applied for each node of a finite element and it will be presented in detail in further sections. As demonstrated in previous sections, the PVW expresses the equilibrium between the internal forces and external applied

forces. The virtual displacements and virtual strains can be obtained through the virtual displacements, $\delta\mathbf{d}^e$, as

$$\begin{aligned}\delta\mathbf{u}^e &= \mathbf{N}^e\delta\mathbf{d}^e \\ \delta\mathbf{e}^e &= \mathbf{B}^e\delta\mathbf{d}^e\end{aligned} \quad . \tag{3.75}$$

Substituting Equation 3.75 in each term of the PVW equation provides the internal force work of each element as

$$\delta \mathrm{W}_{\mathrm{int}} = (\delta\mathbf{d}^e)^{\mathrm{T}} \int_{V^e} \left(\mathbf{B}^e\right)^{\mathrm{T}} \boldsymbol{\sigma}\, \mathrm{d}\, V \,, \tag{3.76}$$

where transposed terms are used due to matrices calculation compatibility. Similarly, for the work of external forces of each element in domain V and on boundary S is given by

$$\delta \mathrm{W}_{\mathrm{ext}} = (\delta\mathbf{d}^e)^{\mathrm{T}} \int_{V^e} \left(\mathbf{N}^e\right)^{\mathrm{T}} \mathbf{b}\, \mathrm{d}\, V \,, \tag{3.77}$$

and

$$\delta \mathrm{W}_{\mathrm{ext}} = (\delta\mathbf{d}^e)^{\mathrm{T}} \int_{S_{\mathrm{N}}^e} \left(\mathbf{N}_{\mathrm{S}}^e\right)^{\mathrm{T}} \mathbf{t}\, \mathrm{d}S \,. \tag{3.78}$$

where S_{N}^e is the element boundary on the natural boundary. As the nodal virtual displacement, $\delta\mathbf{d}$, is independent of the spatial coordinates, it can be brought to outside of the integral. The equilibrium expressed by Equation 3.68 can be rewritten as

$$(\delta\mathbf{d}^e)^{\mathrm{T}} \int_{V^e} \left(\mathbf{B}^e\right)^{\mathrm{T}} \boldsymbol{\sigma}\, \mathrm{d}\, V = (\delta\mathbf{d}^e)^{\mathrm{T}} \left[\int_{V^e} \left(\mathbf{N}^e\right)^{\mathrm{T}} \mathbf{b}\, \mathrm{d}\, V + \int_{S_{\mathrm{N}}^e} \left(\mathbf{N}_{\mathrm{S}}^e\right)^{\mathrm{T}} \mathbf{t}\, \mathrm{d}S \right], \tag{3.79}$$

or, replacing Equation 3.73 into Equation 3.79, regarding the definition of $\boldsymbol{\sigma}$ expressed in Equation 3.67, it gives

$$(\delta\mathbf{d}^e)^{\mathrm{T}} \underbrace{\int_{V^e} \left(\mathbf{B}^e\right)^{\mathrm{T}} \mathbf{C}\mathbf{B}^e\, \mathrm{d}\, V}_{\mathbf{K}^e} \mathbf{d}^e = (\delta\mathbf{d}^e)^{\mathrm{T}} \underbrace{\left[\int_{V^e} \left(\mathbf{N}^e\right)^{\mathrm{T}} \mathbf{b}\, \mathrm{d}\, V + \int_{S_{\mathrm{N}}^e} \left(\mathbf{N}_{\mathrm{S}}^e\right)^{\mathrm{T}} \mathbf{t}\, \mathrm{d}S \right]}_{\mathbf{P}^e}. \tag{3.80}$$

Taking into account that the virtual displacement is an arbitrary quantity and always non-zero (with $\delta\mathbf{d}^e = 0$ in S_{D}^e), it is possible to avoid $\delta\mathbf{d}^e$ from both terms of Equation 3.80. The generalization leads to a global equation defined as

$$\mathbf{K}^e\mathbf{d}^e = \mathbf{P}^e. \tag{3.81}$$

The element stiffness matrix, $\mathbf{K}^e$, and the element external forces vector, $\mathbf{P}^e$, are defined in FEM application as follows

$$\mathbf{K}^e = \int_{V^e} \left(\mathbf{B}^e\right)^{\mathrm{T}} \mathbf{C}\mathbf{B}^e \,\mathrm{d}V\,, \tag{3.82}$$

$$\mathbf{P}^e = \underbrace{\int_{V^e} (\mathbf{N}^e)^{\mathrm{T}}\ \mathbf{b}\,\mathrm{d}V}_{\mathbf{P}^e_{\mathrm{V}}} + \underbrace{\int_{S^e_{\mathrm{N}}} (\mathbf{N}^e_{\mathrm{S}})^{\mathrm{T}}\mathbf{t}\,\mathrm{d}S}_{\mathbf{P}^e_{\mathrm{S}}}\,. \tag{3.83}$$

where $\mathbf{P}^e_{\mathrm{V}}$ and $\mathbf{P}^e_{\mathrm{S}}$ are the element external body and boundary force vectors, respectively. These integrals are calculated for each element and assembled to a global matrix. For linear problems the solution of Equation 3.81 usually is straightforward, it can be achieved in one single step without a costly load increments and iterative schemes.

In contrast, nonlinear problems that use implicit scheme need incremental and iterative procedures in order to correctly achieve the solution. Recovering Equation 3.62 and its corresponding terms described in Equation 3.58, the stiffness matrix, ${}^{t}\mathbf{K}$, can also be decomposed into linear and nonlinear terms as follows

$$({}^{t}\mathbf{K}_{\mathrm{L}} + {}^{t}\mathbf{K}_{\mathrm{NL}})\Delta\mathbf{u}^{(k)} = {}^{t+\Delta t}\mathbf{P} - {}^{t+\Delta t}\mathbf{f}^{(k-1)}\,, \tag{3.84}$$

where ${}^{t}\mathbf{K}_{\mathrm{L}}$ is the linear part of stiffness matrix and ${}^{t}\mathbf{K}_{\mathrm{NL}}$ is the stiffness component related with the nonlinear geometric of strain-displacement matrix. Individually, each term of Equation 3.84 can be obtained by (Bathe and Bolourchi, 1979)

$$\int_{{}^{t}V} {}^{t}C_{ijrs}\,{}_{t}e_{rs}\delta\,{}_{t}e_{ij}\,{}^{t}\mathrm{d}V \Leftrightarrow {}^{t}\mathbf{K}_{\mathrm{L}} = \int_{{}^{t}V} ({}^{t}\mathbf{B}_{\mathrm{L}})^{\mathrm{T}}\,{}_{t}\mathbf{C}\,{}^{t}\mathbf{B}_{\mathrm{L}}\,{}^{t}\mathrm{d}V\,, \tag{3.85}$$

$$\int_{{}^{t}V} {}^{t}\sigma_{ij}\delta\,{}_{t}\eta_{ij}\,{}^{t}\mathrm{d}V \ \Leftrightarrow\ {}^{t}\mathbf{K}_{\mathrm{NL}} = \int_{{}^{t}V} ({}^{t}\mathbf{B}_{\mathrm{NL}})^{\mathrm{T}}\,{}^{t}\boldsymbol{\sigma}\,{}^{t}\mathbf{B}_{\mathrm{NL}}\,{}^{t}\mathrm{d}V\,, \tag{3.86}$$

and finally

$$\int_{{}^{t}V} {}^{t}\sigma_{ij}\delta\,{}_{t}e_{ij}\,{}^{t}\mathrm{d}V \ \Leftrightarrow\ {}^{t}\mathbf{f} = \int_{{}^{t}V} ({}^{t}\mathbf{B}_{\mathrm{L}})^{\mathrm{T}}\,{}^{t}\boldsymbol{\sigma}\,{}^{t}\mathrm{d}V\,. \tag{3.87}$$

in which ${}^{t}\mathbf{B}_{\mathrm{L}}$ is the linear part of the strain-displacement operator, ${}^{t}\mathbf{B}_{\mathrm{NL}}$ is the strain-displacement part related with the nonlinear geometric and ${}^{t}\boldsymbol{\sigma}$ is the Cauchy stress vector at state *t*. The geometric nonlinearity is described in Section 3.6.1.

3.3.1. Isoparametric Space

The governing Finite Element equations developed from the general continuum mechanics equations presented in the previous sections are now discretised for an isoparametric space. The basic assumption is the approximation of displacements and coordinates at any point of the element using appropriate interpolation functions. They are attached to each node and, thus, correspond to

the degree of freedom (DOF) of the discrete system. The interpolation functions, $\mathbf{N}$, are the same for displacements and coordinates

$$\begin{aligned} \mathbf{u}_i^e &= \sum_{j=1}^{n} \mathbf{N}_j \mathbf{u}_i^j \\ \mathbf{x}_i^e &= \sum_{j=1}^{n} \mathbf{N}_j \mathbf{x}_i^j \end{aligned} \quad . \tag{3.88}$$

where $\mathbf{u}_i^e$ and $\mathbf{x}_i^e$ are the displacement and the coordinate of a generic element e from a discretised body (mesh) in the i direction, respectively. The $\mathbf{u}_i^j$ and $\mathbf{x}_i^j$ are the displacement and the coordinate of node j in the i direction, respectively, and $\mathbf{N}_j$ is the interpolation function of node j.

Standard FEM is based on local interpolation through shape functions that locally define polynomials within each element and being zero outside the considered element. The geometry description using shape functions are defined through a normalized natural coordinate system $O\xi\eta\zeta$, concerning a three-dimensional geometry. All points inside a Finite Element are contained in the domain $[-1,+1]\times[-1,+1]\times[-1,+1]$, and the natural coordinates $(\xi,\ \eta,\ \zeta)$ have their axis origin at the geometric centre of the element, as shown in Figure 3.4 (right). The trilinear hexahedral Finite Element of 8 nodes, is widely used in three-dimensional finite element analysis. Figure 3.4 schematically exhibits the representation of a general linear hexahedral element in the global and natural reference systems.

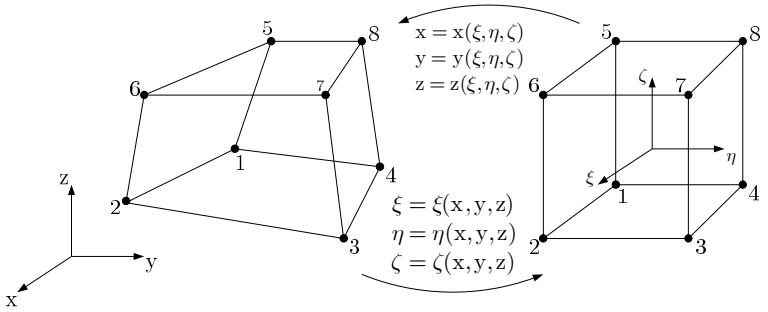

Figure 3.4: Linear 8 nodes hexahedral finite element in the global and local coordinate systems.

The use of natural coordinates system is suitable to construct the shape functions to perform the numerical integration, through the Gauss-Legendre quadrature scheme. The shape functions for a given node j, with j=1... n_{n}, of an isoparametric hexahedral element is defined as (Teixeira-Dias, *et al.*, 2010)

$$\mathbf{N}_j(\xi,\eta,\zeta) = \mathbf{N}_j(\xi)\mathbf{N}_j(\eta)\mathbf{N}_j(\zeta)\ , \tag{3.89}$$

where

$$\mathbf{N}_j(\xi) = \prod_{l=1, l\neq j}^{n_\xi} \frac{\xi - \xi_l}{\xi_j - \xi_l} \ , \tag{3.90}$$

$$\mathbf{N}_j(\eta) = \prod_{l=1, l\neq j}^{n_\eta} \frac{\eta - \eta_l}{\eta_j - \eta_l} \ , \tag{3.91}$$

$$\mathbf{N}_j(\zeta) = \prod_{l=1, l\neq j}^{n_\zeta} \frac{\zeta - \zeta_l}{\zeta_j - \zeta_l} \ , \tag{3.92}$$

in which n_ξ, n_η and n_ζ are the number of nodes in the ξ, η and ζ directions, respectively. The geometry of three-dimensional isoparametric elements, such as 8 nodes element of Figure 3.4, can be written relative to the coordinate system as

$$\mathbf{N}_j(\xi,\eta,\zeta) = \frac{1}{8}(1+\xi_j\boldsymbol{\xi})(1+\eta_j\boldsymbol{\eta})(1+\zeta_j\boldsymbol{\zeta}), \tag{3.93}$$

where ξ_j, η_j and ζ_j are the components of the following vectors, given as

$$\begin{aligned} \boldsymbol{\xi} &= \left\{\text{-1 1 1 -1 -1 1 1 -1}\right\}^T \\ \boldsymbol{\eta} &= \left\{\text{-1 -1 1 1 -1 -1 1 1}\right\}^T \\ \boldsymbol{\zeta} &= \left\{\text{-1 -1 -1 -1 1 1 1 1}\right\}^T \end{aligned} . \tag{3.94}$$

The shape function derivatives in global coordinates (x, y, z) can be determined using the inverse Jacobian matrix, $\mathbf{J}^{-1}$. The mapping relation between the global and natural coordinate systems is obtained as

$$\begin{Bmatrix} \dfrac{\partial N_j}{\partial x} \\ \dfrac{\partial N_j}{\partial y} \\ \dfrac{\partial N_j}{\partial z} \end{Bmatrix} = \mathbf{J}^{-1} \begin{Bmatrix} \dfrac{\partial N_j}{\partial \xi} \\ \dfrac{\partial N_j}{\partial \eta} \\ \dfrac{\partial N_j}{\partial \zeta} \end{Bmatrix} \ , \tag{3.95}$$

where the Jacobian matrix, $\mathbf{J}$, is given by

$$\mathbf{J} = \begin{bmatrix} \dfrac{\partial x}{\partial \xi} & \dfrac{\partial y}{\partial \xi} & \dfrac{\partial z}{\partial \xi} \\ \dfrac{\partial x}{\partial \eta} & \dfrac{\partial y}{\partial \eta} & \dfrac{\partial z}{\partial \eta} \\ \dfrac{\partial x}{\partial \zeta} & \dfrac{\partial y}{\partial \zeta} & \dfrac{\partial z}{\partial \zeta} \end{bmatrix} . \tag{3.96}$$

The Jacobian matrix can be rewritten using the isoparametric coordinate transformation, Equation 3.88, i.e. the shape functions in natural reference system and the Cartesian coordinates of each node $\mathbf{x}_j = (x_j, y_j, z_j)$ as

$$\begin{Bmatrix} x \\ y \\ z \end{Bmatrix} = \sum_{j=1}^{n_n} N_j(\xi,\eta,\zeta) \begin{Bmatrix} x_j \\ y_j \\ z_j \end{Bmatrix} \Leftrightarrow \mathbf{J} = \sum_{i=1}^{n_n} \begin{bmatrix} \frac{\partial N_j}{\partial \xi} x_j & \frac{\partial N_j}{\partial \xi} y_j & \frac{\partial N_j}{\partial \xi} z_j \\ \frac{\partial N_j}{\partial \eta} x_j & \frac{\partial N_j}{\partial \eta} y_j & \frac{\partial N_j}{\partial \eta} z_j \\ \frac{\partial N_j}{\partial \zeta} x_j & \frac{\partial N_j}{\partial \zeta} y_j & \frac{\partial N_j}{\partial \zeta} y_j \end{bmatrix} . \quad (3.97)$$

where n_n is the total number of nodes. The strain-displacement operator, $\mathbf{B}$, introduced in Equation 3.73, can be built using the derivatives of the shape functions with respect to global coordinates as

$$\mathbf{B} = \begin{bmatrix} \mathbf{B}_1 & \mathbf{B}_2 & \dots & \mathbf{B}_j & \dots & \mathbf{B}_{n_n} \end{bmatrix} , \quad (3.98)$$

with

$$\mathbf{B}_j = \underbrace{\begin{bmatrix} \frac{\partial N_j}{\partial x} & 0 & 0 \\ 0 & \frac{\partial N_j}{\partial y} & 0 \\ 0 & 0 & \frac{\partial N_j}{\partial z} \\ \frac{\partial N_j}{\partial y} & \frac{\partial N_j}{\partial x} & 0 \\ \frac{\partial N_j}{\partial z} & 0 & \frac{\partial N_j}{\partial x} \\ 0 & \frac{\partial N_j}{\partial z} & \frac{\partial N_j}{\partial y} \end{bmatrix}}_{For\ each\ node\ j} . \quad (3.99)$$

where j is the node number.

The elemental stiffness matrix, $\mathbf{K}^e$, from equations 3.82, 3.85 and 3.86 can also be alternatively calculated in the natural domain as

$$\begin{aligned} \mathbf{K}^e_{ij} &= \int_{-1}^{+1}\int_{-1}^{+1}\int_{-1}^{+1} \left(\mathbf{B}^e_i\right)^{\mathrm{T}} \mathbf{C}\, \mathbf{B}^e_j (\det \mathbf{J}^e)\, \mathrm{d}\xi \mathrm{d}\eta \mathrm{d}\zeta , \\ \mathbf{K}^e_{\mathrm{NL}ij} &= \int_{-1}^{+1}\int_{-1}^{+1}\int_{-1}^{+1} \left(\mathbf{B}^e_{\mathrm{NL}i}\right)^{\mathrm{T}} \boldsymbol{\sigma}\, \mathbf{B}^e_{\mathrm{NL}j} (\det \mathbf{J}^e)\, \mathrm{d}\xi \mathrm{d}\eta \mathrm{d}\zeta , \end{aligned} \quad (3.100)$$

in which i and j are submatrices subscripts for subsequent assemblage of stiffness matrix.

Generally, multi-dimensional integrals over product domains can be numerically evaluated using multiple summations. The stiffness matrix can also be approximated through its numerical integration using the Gauss-Legendre quadrature given as

$$\begin{aligned}\mathbf{K}_{ij}^{e} &\approx \sum_{r=1}^{n_r}\sum_{s=1}^{n_s}\sum_{z=1}^{n_z}\left(\left(\mathbf{B}_{i}^{e}\right)^{\mathrm{T}}\mathbf{C}\,\mathbf{B}_{j}^{e}\left|\mathbf{J}^{e}\right|\right)_{r,s,z} w_r w_s w_z \quad , \\ \mathbf{K}_{\mathrm{NL}ij}^{e} &\approx \sum_{r=1}^{n_r}\sum_{s=1}^{n_s}\sum_{z=1}^{n_z}\left(\left(\mathbf{B}_{\mathrm{NL}i}^{e}\right)^{\mathrm{T}}\boldsymbol{\sigma}\,\mathbf{B}_{\mathrm{NL}j}^{e}\left|\mathbf{J}^{e}\right|\right)_{r,s,z} w_r w_s w_z \quad ,\end{aligned} \tag{3.101}$$

where $\left|\mathbf{J}\right|$ is the jacobian determinant, n_r, n_s and n_z are the number of integration points in the $O\xi$, $O\eta$ and $O\zeta$ directions, respectively, and w_r, w_s and w_z are the corresponding weights.

Similarly for each term of Equation 3.83, the contribution of the external load $\mathbf{P}^e$ over whole body volume in the natural domain is given as

$$\mathbf{P}_{\mathrm{V}}^{e} = \int_{-1}^{+1}\int_{-1}^{+1}\int_{-1}^{+1}\left(\mathbf{N}\right)^{\mathrm{T}}\mathbf{b}(\det\mathbf{J}^{e})\,\mathrm{d}\xi\mathrm{d}\eta\mathrm{d}\zeta \;, \tag{3.102}$$

and its numerical integration gives

$$\mathbf{P}_{\mathrm{V}}^{e} = \sum_{r=1}^{n_r}\sum_{s=1}^{n_s}\sum_{z=1}^{n_z}\left(\mathbf{N}^{\mathrm{T}}\mathbf{b}\left|\mathbf{J}^{e}\right|\right)_{r,s,z} w_r w_s w_z \quad . \tag{3.103}$$

For traction forces which are applied on the face of the element, the normal vector of the face must be determined first. Doing so, the tangential directions of the natural axis ξ, η and ζ are required

$$\mathbf{v}_1 = \begin{Bmatrix}\dfrac{\partial x}{\partial\xi}\\ \dfrac{\partial y}{\partial\xi}\\ \dfrac{\partial z}{\partial\xi}\end{Bmatrix},\;\; \mathbf{v}_2 = \begin{Bmatrix}\dfrac{\partial x}{\partial\eta}\\ \dfrac{\partial y}{\partial\eta}\\ \dfrac{\partial z}{\partial\eta}\end{Bmatrix}, \mathbf{v}_3 = \begin{Bmatrix}\dfrac{\partial x}{\partial\zeta}\\ \dfrac{\partial y}{\partial\zeta}\\ \dfrac{\partial z}{\partial\zeta}\end{Bmatrix} \quad . \tag{3.104}$$

Comparing the tangential vectors with Equation 3.96, it can be seen that they correspond to the Jacobian matrix lines. The normal direction of the hexahedral element faces are calculated as

$$\mathbf{n}_1 = \frac{\mathrm{v}_2\times\mathrm{v}_3}{\left\|\mathrm{v}_2\times\mathrm{v}_3\right\|},\;\; \mathbf{n}_2 = \frac{\mathrm{v}_3\times\mathrm{v}_1}{\left\|\mathrm{v}_3\times\mathrm{v}_1\right\|},\;\; \mathbf{n}_3 = \mathrm{n}_1\times\mathrm{n}_2 \quad . \tag{3.105}$$

where the normal $\mathbf{n}_i$ is normal to the face where the load t_i is applied and the applied traction force $\mathbf{t}_i$ is determined as

$$\mathbf{t}_i = t_i\mathbf{n}_i \quad (\text{for } i=1,2,3), \tag{3.106}$$

The equivalent nodal forces can be calculated according to the perpendicular direction

$$\begin{aligned}\mathbf{f}^{e}_{S_{\mathrm{N}}k} &= \int_{-1}^{+1}\int_{-1}^{+1}\left(\mathbf{N}_k\right)^{\mathrm{T}}(\pm 1,\eta,\zeta)t_1\mathbf{n}_1 \mathrm{d}\eta\mathrm{d}\zeta \\ \mathbf{f}^{e}_{S_{\mathrm{N}}k} &= \int_{-1}^{+1}\int_{-1}^{+1}\left(\mathbf{N}_k\right)^{\mathrm{T}}(\xi,\pm 1,\zeta)t_2\mathbf{n}_2 \mathrm{d}\xi\mathrm{d}\zeta \quad . \\ \mathbf{f}^{e}_{S_{\mathrm{N}}k} &= \int_{-1}^{+1}\int_{-1}^{+1}\left(\mathbf{N}_k\right)^{\mathrm{T}}(\xi,\eta,\pm 1)t_3\mathbf{n}_3 \mathrm{d}\xi\mathrm{d}\eta\end{aligned} \tag{3.107}$$

where $\mathbf{f}^{e}_{S_{\mathrm{N}}k}$ is the correspondent nodal force of node k.

3.4 Incremental-Iterative Procedure

Generally, in Finite Element analysis the basic step to solve a set of nonlinear equations of equilibrium is a linearized approximation of a small increment of force and corresponding increment of displacement. Figure 3.5 schematically exhibited the incremental procedure to obtain an approximate solution.

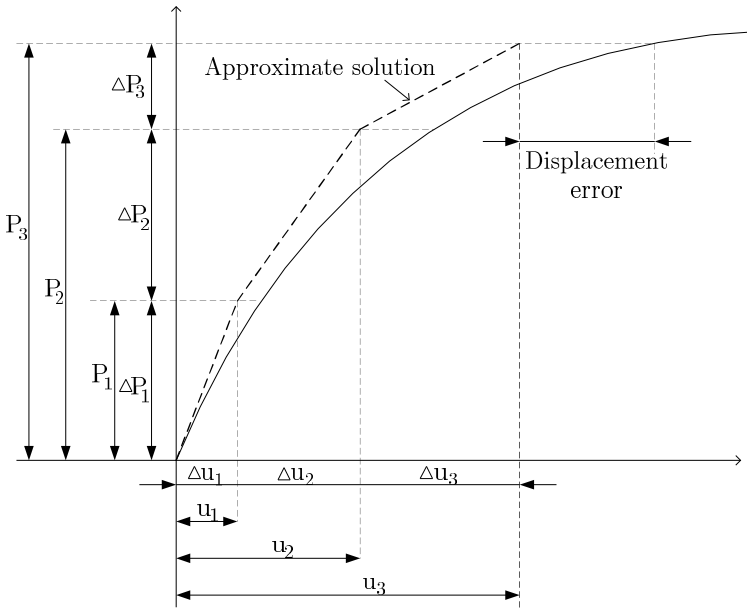

Figure 3.5: Incremental procedure.

The load is divided into a set of small increments, $\Delta\mathbf{P}_{(i)}$, and increments of displacements, $\Delta\mathbf{u}_{(i)}$, are calculated

$$\mathbf{K}_{(i\text{-}1)}\Delta\mathbf{u}_{(i)} = \Delta\mathbf{P}_{(i)}, \tag{3.108}$$

and an updated displacement, $\mathbf{u}_{(i)}$, is obtained as

$$\mathbf{u}_{(i)} = \mathbf{u}_{(i-1)} + \Delta\mathbf{u}_{(i)}\,. \tag{3.109}$$

where the subscript i refers to the increment number, $\mathbf{K}_{(i-1)}$ and $\mathbf{u}_{(i-1)}$ are the tangent stiffness matrix and the displacement from previous increment, respectively. This procedure shows the difference between exact solution and FEM prediction which are gradually cumulated, i.e. solution error. To reduce this error, large number of small incremental steps have to be done, but it makes the procedure inefficient and consequently time consuming. On the other hand, division of loading process into sufficiently small increments is necessary to model load path dependent behaviour of a structure. In these problems, incremental method is usually combined with an iterative method. The following sections describe two iterative procedures usually applied in static analysis through FEM.

3.4.1. Newton-Raphson

The Newton-Raphson method (NR) starts with the evaluation of the out-of-balance force vector, which it is the difference between the internal forces and the applied external loads. Then, the program performs a linear solution, using the out-of-balance force (residual), and checks for convergence. If convergence criteria are not satisfied, the unbalanced force vector is re-evaluated, the stiffness matrix is updated, and a new solution is obtained. This iterative procedure continues until the problem achieves the convergence (Zienkiewicz and Taylor, 2005). Figure 3.6 explains schematically the iterative method of Standard NR applied to an increment of **P**.

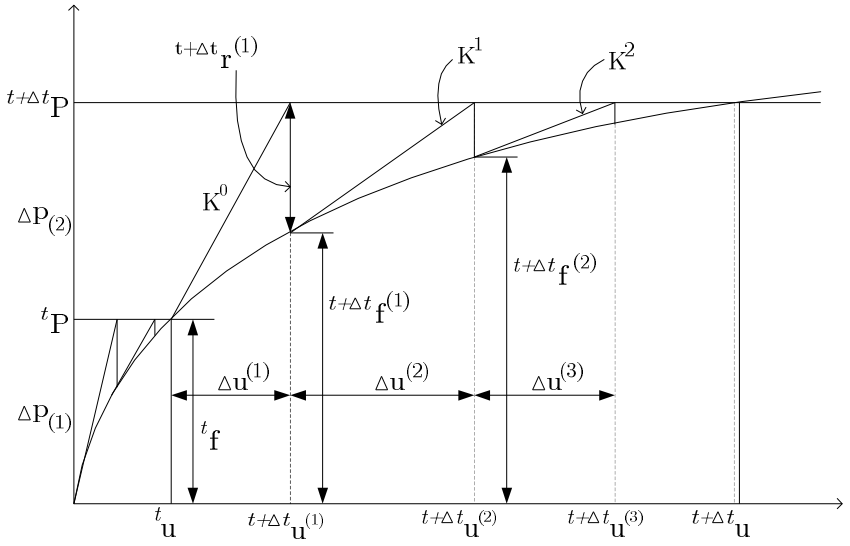

Figure 3.6: Standard Newton-Raphson method.

The first guess of nodal displacements for load $\mathbf{P}$ is calculated by solving the algebraic equations, assuming that the initial displacements $\mathbf{u}^{(t)}$ are known

$$\mathbf{K}^{(0)\,t+\Delta t}\mathbf{u}^{(1)} = {}^{t+\Delta t}\mathbf{P} - {}^{t}\mathbf{f}\,, \tag{3.110}$$

where

$$\mathbf{K}^{(0)} = \mathbf{K}({}^{t}\mathbf{u})\,, \tag{3.111}$$

in which $\mathbf{K}^{(0)}$ is tangent stiffness matrix calculated for initial corresponding displacements, ${}^{t}\mathbf{u}$. As the displacements ${}^{t+\Delta t}\mathbf{u}^{(1)}$ are most probably not accurate at the first trial solution the equilibrium equation is not satisfied

$${}^{t+\Delta t}\mathbf{P} \neq {}^{t+\Delta t}\mathbf{f}^{(1)}\left({}^{t+\Delta t}\mathbf{u}^{(1)}\right), \tag{3.112}$$

which means that there are unbalanced (or residual) nodal forces

$${}^{t+\Delta t}\mathbf{r}^{(1)} = {}^{t+\Delta t}\mathbf{P}^{(1)} - {}^{t+\Delta t}\mathbf{f}\left({}^{t+\Delta t}\mathbf{u}^{(1)}\right) \Leftrightarrow {}^{t+\Delta t}\mathbf{r}^{(1)} \neq 0\,. \tag{3.113}$$

Computing the new tangent stiffness matrix

$$\mathbf{K}^{(1)} = \mathbf{K}({}^{t+\Delta t}\mathbf{u}^{(1)})\,, \tag{3.114}$$

and solving a new set of algebraic equations

$$\mathbf{K}^{(1)}\Delta\mathbf{u}^{(2)} = {}^{t+\Delta t}\mathbf{r}^{(1)}\,, \tag{3.115}$$

lead to an improved solution obtained as

$${}^{t+\Delta t}\mathbf{u}^{(2)} = {}^{t+\Delta t}\mathbf{u}^{(1)} + \Delta\mathbf{u}^{(2)}\,, \tag{3.116}$$

If the equilibrium is not satisfied for this new trial solution

$${}^{t+\Delta t}\mathbf{r}^{(2)} = {}^{t+\Delta t}\mathbf{P} - {}^{t+\Delta t}\mathbf{f}({}^{t+\Delta t}\mathbf{u}^{(2)}) \neq \mathbf{0}\,. \tag{3.117}$$

the procedure is repeated until achievement of an accurate solution. This method is often combined with incremental method, in order to perform the Newton-Raphson procedure for each next load increments, $\Delta\mathbf{P}_{(i)}$.

Generally, the Standard NR iteration scheme finds the equilibrium for each load increment by

$${}^{t+\Delta t}\mathbf{K}^{(k-1)}\Delta\mathbf{u}^{(k)} = {}^{t+\Delta t}\mathbf{P}^{(k)} - {}^{t+\Delta t}\mathbf{f}^{(k-1)}\,. \tag{3.118}$$

After the manipulation of Equation 3.118, to compute the increment of displacement, $\Delta\mathbf{u}^{(k)}$, it is used to obtain the displacement given by

$${}^{t+\Delta t}\mathbf{u}^{(k)} = {}^{t+\Delta t}\mathbf{u}^{(k-1)} + \Delta\mathbf{u}^{(k)}\,, \tag{3.119}$$

with initial conditions

$$ {}^{t+\Delta t}\mathbf{u}^{(0)} = {}^{t}\mathbf{u} \;\;,\;\; {}^{t+\Delta t}\mathbf{K}^{(0)} = {}^{t}\mathbf{K}\,, {}^{t+\Delta t}\mathbf{f}^{(0)} = {}^{t}\mathbf{f}\,. \tag{3.120} $$

where k stands for iteration number. A new unbalanced force, ${}^{t+\Delta t}\mathbf{r}^{(k)}$, and a new increment of displacement, $\Delta\mathbf{u}^{(k+1)}$, are obtained for the next iteration. The iterative procedure continues until the residual force, ${}^{t+\Delta t}\mathbf{r}^{(k)}$, is smaller than a limited tolerance defined by the user.

3.4.2. Modified Newton-Raphson

As previously outlined, the Standard NR method provides the solution of equations at a given load level **P**. This is effective in many cases, but it is time demanding for large equations systems. Since, it may be computationally expensive to calculate the tangent stiffness matrix, **K**, an alternative is the Modified NR iterative scheme. It differs from standard Newton-Raphson algorithm in that the stiffness matrix is only updated occasionally. Figure 3.7 schematically exhibits the comparison of both procedures to iteratively compute the tangential stiffness matrix.

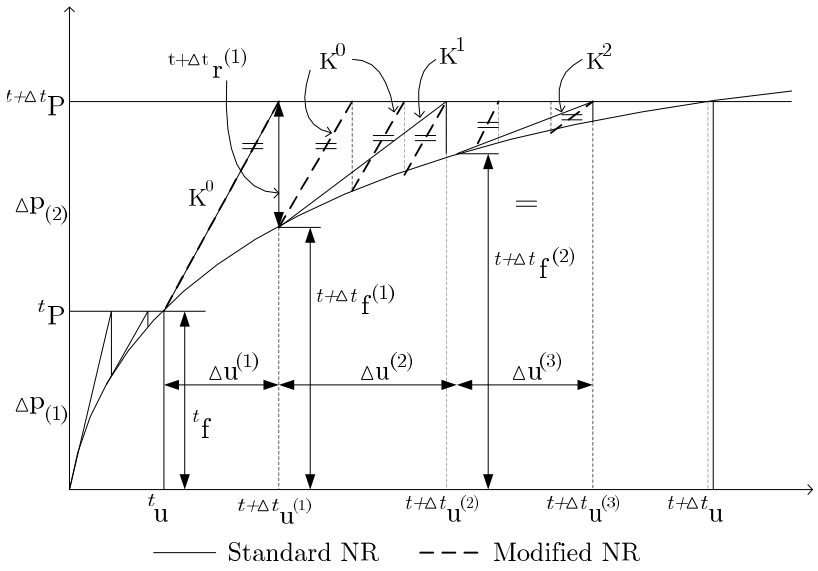

Figure 3.7: Modified Newton-Raphson method.

The nonlinear Equation 3.84 can be solved using the Modified NR method, schematically illustrated in Figure 3.7. The tangent stiffness matrix or slope of the force-displacement curve is updated only at the beginning of each load step/increment (Zienkiewicz and Taylor, 2005). In contrast, the standard Newton-Raphson method updates the tangent stiffness matrix at each iteration. It speeds up convergence but can lead to an increase of computation time.

The advantage of the Modified NR method is saving computer time, due to factorization of the tangent stiffness matrix performed only once for the load increment. However, a large number of iterations is needed, with no cost for the recalculation of the stiffness matrix and consequently decreasing the time.

3.5 Objective Stress Rate

The principle of objectivity ensures that the material behaviour should remain invariant quantities with respect to rigid body motion. This property is an important concept in solid mechanics, which means that the material constitutive relation should be independent of any rigid body motions. In literature it is also called the principle of material frame indifference. Hence, a constitutive equation describing the material behaviour must be invariant under the change of coordinate system, mutually rotating with respect to each other. The definition of objectivity for a scalar, vector and tensor is presented as follows

i) Scalar: $$\Psi^* = \Psi \,, \tag{3.121}$$

ii) Vector: $$\mathbf{j}^* = \mathbf{Q}\mathbf{j} \,, \tag{3.122}$$

iii) Second order tensor: $$\mathbf{J}^* = \mathbf{Q}\mathbf{J}\mathbf{Q}^{\mathrm{T}} \,, \tag{3.123}$$

where $\mathbf{Q}$ is a rotation.

The equilibrium is expressed using the updated Lagrangian formulation in LAGAMINE code, which means that the reference configuration evolves at each step/increment. Let us identify a step by its time at the beginning denoted as t_A and its time at the end as $t_B = t_A + \Delta t$, which characterize two configurations. The deformation gradient tensors at the beginning and at the end of the step are computed as (Alves de Sousa, 2006; Montleau *et al.*, 2008)

$$ {}^{t_A}\mathbf{F} = \frac{\partial^{t_A}\mathbf{x}}{\partial^{0}\mathbf{x}} \,, \quad {}^{t_B}\mathbf{F} = \frac{\partial^{t_B}\mathbf{x}}{\partial^{0}\mathbf{x}} \,, \tag{3.124}$$

in which the global incremental deformation gradient is given as follows

$$ {}^{t_B}\mathbf{F} = {}^{t_A}\mathbf{F}\,{}^{t_B}_{t_A}\mathbf{F} \;\Leftrightarrow\; {}^{t_B}_{t_A}\mathbf{F} = {}^{t_B}\mathbf{F}\left({}^{t_A}\mathbf{F}\right)^{-1} = \frac{\partial^{t_B}\mathbf{x}}{\partial^{t_A}\mathbf{x}} \,. \tag{3.125}$$

and considering the time derivative of Equation 3.124, it gives

$$\dot{\mathbf{F}} = \frac{\partial}{\partial t}\left(\frac{\partial^{t_B}\mathbf{x}}{\partial^{t_A}\mathbf{x}}\right) = \frac{\partial}{\partial^{t_A}\mathbf{x}}\underbrace{\left(\frac{\partial^{t_B}\mathbf{x}}{\partial t}\right)}_{\dot{\mathbf{x}}} = \frac{\partial\dot{\mathbf{x}}}{\partial^{t_A}\mathbf{x}} = \frac{\partial\dot{\mathbf{x}}}{\partial^{t_B}\mathbf{x}}\frac{\partial^{t_B}\mathbf{x}}{\partial^{t_A}\mathbf{x}} = \mathbf{LF} \Leftrightarrow \mathbf{L} = \frac{\partial\dot{\mathbf{x}}}{\partial^{t_B}\mathbf{x}} = \dot{\mathbf{F}}\mathbf{F}^{-1} \ , \quad (3.126)$$

From the previous equation comes the definition of the velocity gradient tensor

$${}^{t_A}\mathbf{L} = \frac{\partial^{t_A}\dot{\mathbf{x}}}{\partial^{t_A}\mathbf{x}} \ , \quad {}^{t_B}\mathbf{L} = \frac{\partial^{t_B}\dot{\mathbf{x}}}{\partial^{t_B}\mathbf{x}} \ , \quad (3.127)$$

and applying the polar decomposition theorem to Equation 3.127 leads to

$$\mathbf{L} = \dot{\mathbf{F}}\mathbf{F}^{-1} = (\mathbf{R}\dot{\mathbf{U}} + \dot{\mathbf{R}}\mathbf{U})\cdot\mathbf{U}^{-1}\mathbf{R}^{-1} = \underbrace{\dot{\mathbf{R}}\mathbf{R}^{\mathrm{T}}}_{\Omega} + \mathbf{R}\dot{\mathbf{U}}\mathbf{U}^{-1}\mathbf{R}^{\mathrm{T}}, \quad (3.128)$$

with

$$\mathbf{F}^{-1} = (\mathbf{RU})^{-1} = \mathbf{U}^{-1}\mathbf{R}^{-1} \quad \text{and} \quad \mathbf{R}^{-1} = \mathbf{R}^{\mathrm{T}} \text{ if } \mathbf{R}^{\mathrm{T}}\mathbf{R} = \mathbf{I}. \quad (3.129)$$

where $\boldsymbol{\Omega}$ is the rotation rate tensor which represents the rate of rigid body rotation at a given material point.

The velocity gradient tensor, $\mathbf{L}$, can be alternatively decomposed into symmetric, $\mathbf{D}$, and anti-symmetric, $\mathbf{W}$, terms

$$\mathbf{L} = \mathbf{D} + \mathbf{W}, \quad (3.130)$$

in which these terms are known as the rate of deformation tensor, $\mathbf{D}$, and spin rate tensor, $\mathbf{W}$, and after some manipulation using Equation 3.128 can be written as

$$\mathbf{D} = \frac{1}{2}(\mathbf{L} + \mathbf{L}^{\mathrm{T}}) = \mathbf{R}\left(\dot{\mathbf{U}}\mathbf{U}^{-1}\right)^{\mathrm{sym}}\mathbf{R}^{\mathrm{T}}, \quad (3.131)$$

and

$$\mathbf{W} = \frac{1}{2}(\mathbf{L} - \mathbf{L}^{\mathrm{T}}) = \dot{\mathbf{R}}\mathbf{R}^{\mathrm{T}} + \mathbf{R}\left(\dot{\mathbf{U}}\mathbf{U}^{-1}\right)^{\mathrm{asy}}\mathbf{R}^{\mathrm{T}}, \quad (3.132)$$

where the subscript (sym) and (asy) denote symmetric and anti-symmetric parts of the tensor, respectively. When the principal material lines of $\dot{\mathbf{U}}$ and $\mathbf{U}$ coincide and the product $\dot{\mathbf{U}}\mathbf{U}^{-1}$ is symmetric part, consequently $\mathbf{D}$ and $\mathbf{W}$ are simplified as

$$\mathbf{D} = \mathbf{R}\dot{\mathbf{U}}\mathbf{U}^{-1}\mathbf{R}^{\mathrm{T}} \ , \quad (3.133)$$

$$\mathbf{W} = \dot{\mathbf{R}}\mathbf{R}^{\mathrm{T}} \ . \quad (3.134)$$

Usually time derivatives of tensorial variables are not objective, as it is the case for the Cauchy stress, $\boldsymbol{\sigma}$. The incremental procedure requires the definition of a stress rate which must be objective, i.e. independent on rigid body rotation. In LAGAMINE code generally the Jaumann objective stress rate is adopted and it is introduced before the integration of the stress-strain constitutive relation. This objective derivative has the form

$$\boldsymbol{\sigma}^{\mathrm{J}} = \dot{\boldsymbol{\sigma}} - \boldsymbol{\Omega}\boldsymbol{\sigma} + \boldsymbol{\sigma}\boldsymbol{\Omega} = \dot{\boldsymbol{\sigma}} - \mathbf{W}\boldsymbol{\sigma} + \boldsymbol{\sigma}\mathbf{W} \,. \tag{3.135}$$

where $\dot{\boldsymbol{\sigma}}$ is the time derivative of the stress tensor and $\boldsymbol{\Omega}$ is a second order anti-symmetric spin. When the spin part $\boldsymbol{\Omega}$ is the anti-symmetric part $\mathbf{W}$ of the velocity gradient $\mathbf{L}$ ($\boldsymbol{\Omega} = \mathbf{W}$), the Jaumann derivative is used. In this case $\mathbf{W}$ is also called the rigid body spin. This tensor represents the rate of deformation of the principal axes of tensor $\mathbf{D}$ and the Jaumann stress rate is also defined, as shown in Equation 3.135.

In nonlinear FEM using the hypoelastic laws, the elastic strains are assumed small compared to plastic strains, the symmetric part of the velocity gradient, $\mathbf{L}$, is written in the form (a good assumption for sheet metal)

$$\mathbf{D} = \mathbf{D}^{\mathrm{e}} + \mathbf{D}^{\mathrm{p}} \,, \tag{3.136}$$

where the subscripts (e) and (p) are elastic and plastic parts, respectively. From the orthogonality character of the rotation tensor $\mathbf{R}$ expressed in Section 3.2.2, it is possible to rotate the strain rate $\mathbf{D}$

$$\mathbf{D}' = \mathbf{R}^{\mathrm{T}} \left(\mathbf{D}^{\mathrm{e}} + \mathbf{D}^{\mathrm{p}} \right) \mathbf{R} \,, \tag{3.137}$$

The computation of the incremental rotated strain, $\Delta\mathbf{e}'$, between configurations t_A and t_B is given by

$$\Delta\mathbf{e}' = \int_{t_A}^{t_B} \mathbf{D}' \, dt \,. \tag{3.138}$$

The method used to compute the rotation of the local frame in LAGAMINE code is named as Constant Symmetric Local Velocity Gradient (CSLVG) (Duchêne *et al.*, 2008; Montleau *et al.*, 2008). This assumption is considered in order to impose the strain path with constant velocity gradient, $\mathbf{L}$, on a step. According with Equation 3.128, the deformation gradient must satisfy an additional condition

$$\mathbf{L} = \dot{\mathbf{F}}(t) \left[\mathbf{F}(t) \right]^{-1} = \text{constant}, \qquad t \in [t_B, t_A] \,, \tag{3.139}$$

To apply the CSLVG method, first $\Delta\mathbf{F}$ is calculated by the following relation

$$\Delta\mathbf{F} = \exp\left[\mathbf{L}(\Delta t) \right], \tag{3.140}$$

where $\Delta t = t_B - t_A$ is the size of the time step and using the initial condition $\mathbf{F}(t_A) = \mathbf{F}_A$ the solution can be expressed as

$$\mathbf{F}(t_B) = \exp(\mathbf{L}(t_B - t_A))\mathbf{F}_A \,, \tag{3.141}$$

in which manipulating Equation 3.141, setting $\mathbf{F}(t_B) = \mathbf{F}_B$ and regarding Equation 3.125, it allows to find a constant value of velocity gradient

$$\mathbf{L}=\frac{1}{\Delta t}\ln(\mathbf{F}_{AB})\,, \tag{3.142}$$

where $\mathbf{F}_{AB}$ is in general non-symmetric. It is reduced to a rotation matrix and the logarithm of an orthogonal matrix is anti-symmetric. For each element, $\mathbf{F}_{AB}$ can be computed with respect to the interpolation functions of the element and making use of the isoparametric Jacobian matrix

$$\mathbf{F}_{AB}=\frac{\partial \mathbf{x}_B}{\partial \mathbf{x}_A}=\frac{\partial \mathbf{x}_B}{\partial \boldsymbol{\xi}}\frac{\partial \boldsymbol{\xi}}{\partial \mathbf{x}_A}=\mathbf{J}_B\mathbf{J}_A^{-1}\,. \tag{3.143}$$

From now, the velocity gradient is determined in the local reference frame. First, the deformation gradient tensor is expressed in the local reference system as

$$\mathbf{F}'=\mathbf{R}^{\mathrm{T}}\mathbf{F}\mathbf{R}_0\,. \tag{3.144}$$

with $\mathbf{R}$ is the current rotation matrix between the local and the global reference systems and $\mathbf{R}_0$ is the corresponding rotation matrix at the beginning of the procedure.

Similarly, the local velocity gradient can be obtained as

$$\mathbf{L}'=\frac{1}{\Delta t}\ln(\mathbf{F}'_{AB})\,. \tag{3.145}$$

This velocity gradient defined in the local frame is constant during the increment and, additionally, it is assumed to be symmetric. Consequently, $\mathbf{F}'_{AB}$ is also symmetric. The procedure applied to the local frame for Equation 3.125, doing so, the local incremental deformation gradient is

$$\mathbf{F}'_{AB}=\mathbf{F}'_B\left(\mathbf{F}'_A\right)^{-1}\,. \tag{3.146}$$

Substituting Equation 3.144 into Equation 3.146 allows developing the local incremental deformation as

$$\mathbf{F}'_{AB}=\mathbf{F}'_B\left(\mathbf{F}'_A\right)^{-1}=\left(\mathbf{R}_B^{\mathrm{T}}\mathbf{F}_B\mathbf{R}_0\right)\left(\mathbf{R}_0^{\mathrm{T}}\mathbf{F}_A^{-1}\mathbf{R}_A\right)=\mathbf{R}_B^{\mathrm{T}}\mathbf{F}_B\mathbf{F}_A^{-1}\mathbf{R}_A=\mathbf{R}_B^{\mathrm{T}}\mathbf{F}_{AB}\mathbf{R}_A\,. \tag{3.147}$$

From this equation, $\mathbf{F}^{*}_{AB}$ is defined as

$$\mathbf{F}^{*}_{AB}=\mathbf{F}_{AB}\mathbf{R}_A=\mathbf{R}_B\mathbf{F}'_{AB}\,, \tag{3.148}$$

Then, from Equation 3.148 replaced into Equation 3.145 and after its manipulation, as demonstrated in Montleau *et al.* (2008), the CSLVG can be written as

$$\mathbf{L}'=\frac{1}{2\Delta t}\ln\left((\mathbf{F}^{*}_{AB})^{\mathrm{T}}\mathbf{F}^{*}_{AB}\right)\,, \tag{3.149}$$

where the local velocity gradient, $\mathbf{L}'$, become symmetric.

In the case when the initial rotation is $\mathbf{R}_A = \mathbf{I}$, which means no rotation at the beginning of the step, Equation 3.148 leads to

$$\mathbf{F}^{*}_{AB} = \mathbf{F}_{AB}\mathbf{R}_A = \mathbf{F}_{AB} \quad \text{and} \quad \mathbf{F}^{*}_{AB} = \mathbf{F}_{AB} = \mathbf{R}_B\mathbf{F}'_{AB} \ . \tag{3.150}$$

The rotation at the end of the step, $\mathbf{R}_B$, is obtained by the right decomposition of $\mathbf{F}_{AB}$, with $\mathbf{U}_{AB} = \mathbf{U}_B$. Knowing that $\ln(x^y) = y\ln(x)$ and regarding equations 3.148 and 3.150 replaced into Equation 3.149, it can be rewritten as

$$\begin{aligned} \mathbf{L}' &= \frac{1}{2\Delta t}\ln\left((\mathbf{F}_{AB})^{\mathrm{T}}\mathbf{F}_{AB}\right) \\ &= \frac{1}{\Delta t}\ln\left(\mathbf{U}_{AB}\right) . \end{aligned} \tag{3.151}$$

The condition of $\mathbf{L}'$ being symmetric, means that it equals the local strain rate, $\mathbf{D}'$, applied to a uniaxial extension case, which satisfy Equation 3.138 and gives the increment of strain, $\Delta\mathbf{e}'$, in the local frame

$$\begin{aligned} &\mathbf{L}'\Delta t = \Delta\mathbf{e}' \Leftrightarrow \mathbf{D}'\Delta t = \Delta\mathbf{e}' , \\ &\Delta\mathbf{e}' = \int_{t_A}^{t_B}\mathbf{D}'\mathrm{d}t = \int_{t_A}^{t_B}(\dot{\mathbf{U}}\mathbf{U}^{-1})\mathrm{d}t = \ln(\mathbf{U}_{AB}) . \end{aligned} \tag{3.152}$$

As the integration of the constitutive law is performed in the local frame, the stress tensor from previous state, t_A, is rotated by the following relation

$$\boldsymbol{\sigma}'_A = \mathbf{R}_A^{\mathrm{T}}\boldsymbol{\sigma}_A\mathbf{R}_A \ , \tag{3.153}$$

then, it is integrated within the constitutive law giving the local stress tensor for state t_B

$$\boldsymbol{\sigma}'_B = \boldsymbol{\sigma}'_A + f(\boldsymbol{\sigma}'_A, \mathbf{L}', ...) \ , \tag{3.154}$$

and afterwards it is rotated back to the global frame

$$\boldsymbol{\sigma}_B = \mathbf{R}_B^{\mathrm{T}}\boldsymbol{\sigma}'_B\mathbf{R}_B \ . \tag{3.155}$$

where $\boldsymbol{\sigma}_B$ is the Cauchy stress tensor. The procedure from Equation 3.153 to Equation 3.155 is performed at the element level, for each integration point, also known as Gauss point (GP).

3.6 Nonlinearities

Nonlinear continuum mechanics involves large deformations described in terms of the material or spatial coordinates. Summarizing, the PVW has resulted in the emergence of a variety of stress-strain measures and the deformation gradient is the main component to describe the strain. After, the PWV was recognized as having nonlinear terms and they were consequently written in a linearized form, using Taylor's series. The linearization demanded the necessity of Newton-Raphson solution scheme involving the tangent stiffness matrix.

In structural analysis there are sources of nonlinearities which can arise from many effects, such as geometric, material and boundary conditions. The effect of large displacements on the overall geometric configuration of the structure leads to geometric nonlinearities. The material nonlinearities occurred due to nonlinear relation of stress-strain, described by a constitutive law behaviour. It can be described as nonlinear elastic, elastoplastic, viscoplastic or viscoelastic. The boundary nonlinearities include displacement conditions and the most frequent is contact between two bodies.

3.6.1. Geometric nonlinearity

The geometric nonlinearity occurrence is characterized by "large" displacements and/or rotations. The coupling nonlinear geometric strain-displacement matrix, $\mathbf{B}_{\mathrm{NL}}$, associated to classic finite element formulation from Equation 3.86, can be written according to UL formulation for three-dimensional case as (Alves de Sousa, 2006)

$$
{}^{t}\mathbf{B}_{\mathrm{NL}} = \left[\underbrace{\begin{matrix}
{}^{t}N_{j,x} & 0 & 0 \\
{}^{t}N_{j,y} & 0 & 0 \\
{}^{t}N_{j,z} & 0 & 0 \\
0 & {}^{t}N_{j,x} & 0 \\
0 & {}^{t}N_{j,y} & 0 \\
0 & {}^{t}N_{j,z} & 0 \\
0 & 0 & {}^{t}N_{j,x} \\
0 & 0 & {}^{t}N_{j,y} \\
0 & 0 & {}^{t}N_{j,z}
\end{matrix}}_{\text{node } j} \right] \text{, for } j = 1,8 \ , \tag{3.156}
$$

where ${}^{t}N_{j,i}$ are the derivatives of the shape function of node j with respect to direction i (x, y, z) at increment t. Finally, the 9×9 array, ${}^{t}\boldsymbol{\sigma}_9$, composed by sub-blocks of the stress tensor, ${}^{t}\boldsymbol{\sigma}_3$, written in 3×3 form, is evaluated at each integration point

$$ {}^{t}\boldsymbol{\sigma}_9 = \begin{bmatrix} {}^{t}\boldsymbol{\sigma}_3 & \mathbf{0} & \mathbf{0} \\ \mathbf{0} & {}^{t}\boldsymbol{\sigma}_3 & \mathbf{0} \\ \mathbf{0} & \mathbf{0} & {}^{t}\boldsymbol{\sigma}_3 \end{bmatrix} , \tag{3.157} $$

with

$$ {}^{t}\boldsymbol{\sigma}_3 = \begin{bmatrix} {}^{t}\sigma_{11} & {}^{t}\sigma_{12} & {}^{t}\sigma_{13} \\ {}^{t}\sigma_{21} & {}^{t}\sigma_{22} & {}^{t}\sigma_{23} \\ {}^{t}\sigma_{31} & {}^{t}\sigma_{32} & {}^{t}\sigma_{33} \end{bmatrix} \quad \text{and} \quad \mathbf{0} = \begin{bmatrix} 0 & 0 & 0 \\ 0 & 0 & 0 \\ 0 & 0 & 0 \end{bmatrix} . \tag{3.158} $$

3.6.2. Material nonlinearity

The problem that arises now is fundamental in computational mechanics, where not only equilibrium equations but also constitutive equations of the material must be satisfied. This means that at each increment/step, iteratively the procedure is performed until both equilibrium conditions and constitutive equations are simultaneously satisfied. The converged solution at the end of the load increment is then used at the start of new load increment.

The material behaviour studied is characterized by two domains, namely the elastic and elastoplastic ones. In the linear elastic behaviour domain, the mechanical response is described by an elastic law, where the stress is given from a measure of elastic deformation. Accordingly, the linear elastic Finite Element analysis is based on linear constitutive stress-strain equation defined as

$$ \boldsymbol{\sigma} = \mathbf{C}^{\mathrm{e}}\boldsymbol{\varepsilon} , \tag{3.159} $$

where the terms of the elastic material matrix $\mathbf{C}^{\mathrm{e}}$ are symmetric with its components expressed as function of the Young modulus and Poisson ratio. The linear elastic model is acceptable only within a limited range of stress, bounded by a yield criterion. The boundary is typically distinguished and characterized by the yield stress, σ_{y}, and the yield criterion which defines the transition from elastic to elastoplastic domain. Yield criteria describe the form and the size of the yield surface evolution, generally expressed as

$$\Phi = \overline{\sigma} - \sigma_y = 0 \ , \tag{3.160}$$

where $\boldsymbol{\sigma}_y$ is the yield stress and $\overline{\sigma}$ is the equivalent stress, which is function of the effective stress tensor. When the stress level exceeds the yield stress, an elastoplastic constitutive behaviour law governs the relationship between increments of stress and strain. The elastoplastic behaviour characterizes the physical irreversibility of the material due to the dissipation of energy. The Equation 3.160 is the yield criterion for a material point, it leads to the following stress states

- $\overline{\sigma} < \sigma_y$, elastic behaviour $(\Phi < 0)$;
- $\overline{\sigma} = \sigma_y$, elastoplastic behaviour $(\Phi = 0)$;
- $\overline{\sigma} > \sigma_y$, unphysical domain $(\Phi > 0)$, it only happens in mathematical iterations, during the algorithm procedure, used to integrate the constitutive equations.

Figure 3.8 schematically exhibits the concepts of elastic and elastoplastic domains for two-dimension plane stress conditions.

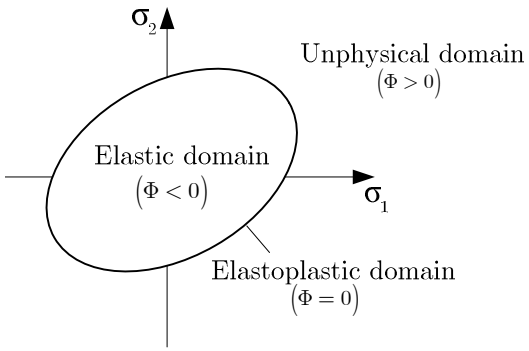

Figure 3.8: Schematic concept of yield surface.

In general, the constitutive equation is represented as

$$d\boldsymbol{\sigma} = \mathbf{C}_T d\boldsymbol{\varepsilon} \ . \tag{3.161}$$

where $\mathbf{C}_T$ is the tangent material matrix derived from stress tensor, according to the strain tensor. The total strain increment, $d\boldsymbol{\varepsilon}$, is additively decomposed into an elastic (recoverable), $d\boldsymbol{\varepsilon}^e$, and a plastic (irreversible), $d\boldsymbol{\varepsilon}^p$, part

$$d\boldsymbol{\varepsilon} = d\boldsymbol{\varepsilon}^e + d\boldsymbol{\varepsilon}^p \ , \tag{3.162}$$

From Equation 3.159 the elastic part is generally given by

$$d\boldsymbol{\varepsilon}^e = (\mathbf{C}^e)^{-1} d\boldsymbol{\sigma} \ . \tag{3.163}$$

where the inverse of the elastic matrix, $(\mathbf{C}^{e})^{-1}$, is performed in the pre-processor program of LAGAMINE code for each corresponding material subroutine.

In Finite Element analysis, the increments of $\Delta\boldsymbol{\varepsilon}$ and $\Delta\boldsymbol{\sigma}$ are computed at each integration (Gauss) point of a finite element of the mesh discretization

$$\Delta\boldsymbol{\sigma} = \mathbf{C}_{T}\Delta\boldsymbol{\varepsilon}\,. \tag{3.164}$$

hence it is necessary to integrate the mathematical law over the time increment

$$\Delta\boldsymbol{\sigma} = \int_{t}^{t+\Delta t} \mathrm{d}\boldsymbol{\sigma}\,. \tag{3.165}$$

From constitutive law and according to Equation 3.162, we have

$$\mathrm{d}\boldsymbol{\sigma} = \mathbf{C}_{T}\mathrm{d}\boldsymbol{\varepsilon}^{e} \;\Leftrightarrow\; \mathrm{d}\boldsymbol{\sigma} = \mathbf{C}_{T}(\mathrm{d}\boldsymbol{\varepsilon} - \mathrm{d}\boldsymbol{\varepsilon}^{p})\,. \tag{3.166}$$

The additive decomposition of the rate of deformation defined in Equation 3.136 is recovered. It deals with a hypoelastic formulation of the constitutive law. Considering previous developments, the extension of the small strain isotropic linear constitutive relation (Equation 3.163) to the objective stress rate is needed for finite strain elastoplasticity.

In order to calculate the plastic strain increment, ${}^{t+\Delta t}_{t}\boldsymbol{\varepsilon}^{p} = \Delta\boldsymbol{\varepsilon}^{p} = \mathrm{d}\boldsymbol{\varepsilon}^{p}$, there are three elastoplastic principles: the yield function, hardening law and plastic flow rule (Borst *et al.*, 2012). They are mathematical relations which describe the macroscopic behaviour of the material, known as phenomenological models.

a) Yield criterion

As previously mentioned, the main purpose of the yield criterion is to limit the elastic domain, mathematically expressed by the so-called yield surface or also named Haig-Westergaard space. From the state-of-art, the yield criteria can be described as isotropic or anisotropic.

A material is assumed isotropic when its properties are independent of the directions considered. Among all known isotropic criteria, the most widely used yield criterion to describe the plastic behaviour of isotropic materials, it is the von Mises yield function, expressed as

$$\Phi = \sqrt{\frac{1}{2}\left[\left(\sigma_{11}-\sigma_{22}\right)^{2} + \left(\sigma_{22}-\sigma_{33}\right)^{2} + \left(\sigma_{33}-\sigma_{11}\right)^{2}\right] + 3\left(\sigma_{12}^{2}+\sigma_{13}^{2}+\sigma_{23}^{2}\right)} - \sigma_{y}\,. \tag{3.167}$$

Its yield surface represents a cylinder of radius σ_{y} in the Haig-Westergaard space. The von Mises yield criterion is the one implemented within the material subroutines of LAGAMINE code.

Anisotropic yield surfaces takes into account the variation dependency of the yield stress on the loading direction. The criterion proposed by Hill (1948) is the most well-known used for anisotropic yield criterion to model the behaviour of orthotropic materials. This yield function is expressed as

$$\Phi = \sqrt{F\left(\sigma_{22}-\sigma_{33}\right)^2 + G\left(\sigma_{33}-\sigma_{11}\right)^2 + H\left(\sigma_{11}-\sigma_{22}\right)^2 + 2L\sigma_{12}^2 + 2M\sigma_{13}^2 + 2N\sigma_{23}^2} - \sigma_y. \quad (3.168)$$

where F, G, H, L, M, and N are six material parameters that characterize the material anisotropy. Each Hill parameter is computed based on the Lankford coefficients according to the following relations

$$r_0 = \frac{H}{G}, \quad r_{90} = \frac{H}{F}, \quad r_{45} = \frac{4N - F - G}{2\left(F+G\right)} . \quad (3.169)$$

with additional conditions: $H+G=2$ and $N=L=M$. In LAGAMINE code, the subroutine that concerns this anisotropic criterion can be reduced to von Mises's criterion when F=G=F=1 and L=M=N=3. Alternatively, this criterion can be written, using tensorial notation, as

$$\Phi = \sqrt{\boldsymbol{\sigma} : \mathbf{H} : \boldsymbol{\sigma}} - \sigma_y . \quad (3.170)$$

where **H** is a forth-order tensor, also known as anisotropy tensor, which represents the anisotropy of the material. Using Voigt's notation, it gives

$$\mathbf{H} = \begin{pmatrix} G+H & -H & -G & 0 & 0 & 0 \\ -H & H+F & -F & 0 & 0 & 0 \\ -G & -F & F+G & 0 & 0 & 0 \\ 0 & 0 & 0 & 2N & 0 & 0 \\ 0 & 0 & 0 & 0 & 2L & 0 \\ 0 & 0 & 0 & 0 & 0 & 2M \end{pmatrix}. \quad (3.171)$$

b) Hardening behaviour

The hardening phenomenon is a nonlinear behaviour occurring when the limit of the elastic domain is achieved and the plastic strain takes place during a forming process, with the progress of loading imposition. In the context of computational plasticity, hardening is defined as the evolution of the yield surface described by a hardening law. This evolution can induce expansion (isotropic), translation (kinematic), rotations or distortion (anisotropic) of the yield surface during the deformation. Figure 3.9 exhibits the schematic representation of each of hardening behaviour.

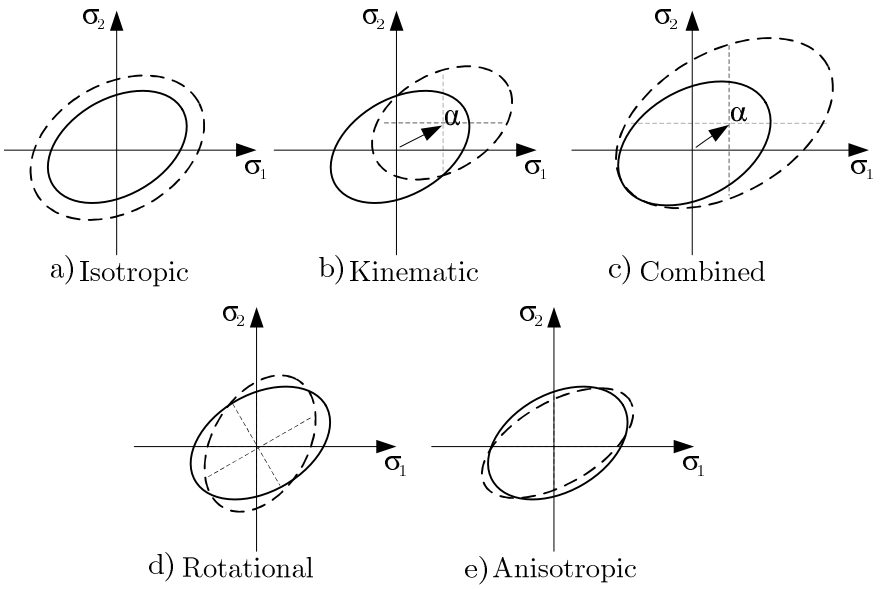

Figure 3.9: Evolution behaviour of the yield surface.

The most general hardening behaviours are isotropic, kinematic and the combined/mixed hardening, in which isotropic and kinematic hardening are simultaneously taken into account, as shown in Figure 3.9c. The anisotropic effect of the yield surface can occur combined with kinematic hardening behaviour.

The isotropic hardening model takes into account the isotropic expansion of the yield surface as shown in Figure 3.9a. The yield criterion defined in terms of a potential stress, depends on internal parameters describing the yield surface size evolution. Equation 3.160 can be expressed as

$$\Phi(\boldsymbol{\sigma}, \overline{\varepsilon}^{\mathrm{p}}) \ = \overline{\sigma}(\boldsymbol{\sigma}) - \boldsymbol{\sigma}_{\mathrm{y}}(\overline{\varepsilon}^{\mathrm{p}}) = 0 \ , \tag{3.172}$$

where $\boldsymbol{\sigma}$ is the stress tensor and $\overline{\varepsilon}^{\mathrm{p}}$ is the effective plastic strain, which is an internal variable of hardening.

The Bauschinger effect present in cyclic loading is expressed by the kinematic hardening introduced by Prager (1956). It is represented in Figure 3.9b, the yield surface translates in the stress space without change in its size, shape, or orientation. This translation mathematically is described through the back-stress evolution, redefining a new yield surface centre. Some other evolution laws for back-stress tensor can be found in the literature, such as Ziegler (1959), Armstrong and Frederick (1966) and Chaboche (1991), just are to mention a few. They are the ones available within LAGAMINE code. The yield criterion including kinematic hardening is given as

$$\Phi(\boldsymbol{\sigma}, \boldsymbol{\alpha}, \overline{\varepsilon}^{\mathrm{p}}) \ = \overline{\sigma}(\boldsymbol{\sigma} - \boldsymbol{\alpha}) - \boldsymbol{\sigma}_{\mathrm{y}}(\overline{\varepsilon}^{\mathrm{p}}) = 0 \ , \tag{3.173}$$

where $\boldsymbol{\alpha}$ is the back-stress tensor, which describes the displacement of the yield surface centre during plastic deformation. In case of representing Figure 3.9b, the value of yield stress, σ_y, remains constant ($\sigma_y = \sigma_{y0}$).

The hardening law describes the plastic behaviour of the material mathematically expressed in terms of yield stress, σ_y, in function of accumulated plastic strain, $\bar{\varepsilon}^p$. The most well-known hardening laws are: Linear, Hollomon (1945), Voce (1948), Swift (1952), Ludgwigson (1971) and Sung *et al.* (2010). In the present work the hardening laws used are Voce and Swift hardening laws. The Voce's equation is known for its flow stress saturation behaviour with linear decrease of the plastic slope, it is defined as

$$\sigma_y = \sigma_{y0} - A(1 - e^{-C\bar{\varepsilon}^p}), \tag{3.174}$$

where σ_{y0} is the initial yield stress, A and C are material parameters. On the other hand, in Swift's hardening law, the stress evolution is unbounded, it is expressed as

$$\sigma_y = K(\varepsilon_0 + \bar{\varepsilon}^p)^n, \tag{3.175}$$

where K, ε_0 and n are material parameters. These hardening laws generally are most widely employed in the description of the mechanical behaviour of aluminium and steel alloys, respectively.

Finally, the combined/mixed hardening, Figure 3.9c, describes the size and displacement of the yield surface according to Equation 3.173 together with a combination of Equation 3.174 or Equation 3.175 and a back-stress tensor definition.

c) Plastic flow rule

Generally, the flow rule determines the relation between the strain rate tensor and the stress tensor. The flow rule assumes that the plastic deformations are normal to a plastic potential of stress. This definition includes the associative and non-associative flow rules. The rate of plastic strain, $\dot{\varepsilon}^p_{ij}$, can be expressed by making use of the plastic potential function, Q

$$d\varepsilon^p_{ij} \equiv \dot{\varepsilon}^p_{ij} = \dot{\lambda}\frac{\partial Q}{\partial \sigma_{ij}} \quad , \quad \dot{\lambda} \geq 0 \ , \tag{3.176}$$

where $\dot{\lambda}$ is a proportional positive scalar factor named plastic multiplier, often referred to as the plastic consistency parameter.

The adoption of the associated flow rule to describe the behaviour of metallic materials is widely accepted. In this sense, the present work uses the associated flow rule, also referred as normality principle, i.e. the plastic potential coincides with the yield function, it is assumed that $Q = \Phi$. The associated plastic strain increment, ${}^{t+\Delta t}_{t}\boldsymbol{\varepsilon}^{\mathrm{p}} = \Delta\boldsymbol{\varepsilon}^{\mathrm{p}}$, can be obtained as

$$ {}^{t+\Delta t}_{t}\boldsymbol{\varepsilon}^{\mathrm{p}} = {}^{t+\Delta t}_{t}\overline{\boldsymbol{\varepsilon}}^{\mathrm{p}}\,\frac{\partial\Phi}{\partial\boldsymbol{\sigma}} \ . \tag{3.177} $$

where ${}^{t+\Delta t}_{t}\overline{\boldsymbol{\varepsilon}}^{\mathrm{p}} = \Delta\overline{\boldsymbol{\varepsilon}}^{\mathrm{p}}$ is the equivalent plastic strain increment, equivalent to the plastic multiplier, λ, in proportional loading if $\dfrac{\partial\Phi}{\partial\boldsymbol{\sigma}}$ is normalized (${}^{t+\Delta t}_{t}\overline{\boldsymbol{\varepsilon}}^{\mathrm{p}} = \lambda$).

d) Constitutive law integration

In order to numerically integrate the constitutive equations, commonly a predictor–corrector, also known as return mapping, strategy is applied. This procedure consists of two successive phases: an elastic prediction followed by a plastic corrector. The first attempt is assumed to be purely elastic (elastic predictor), which means that there is no plastic flow or internal variables evolution

$$ \Delta\boldsymbol{\sigma}^{\mathrm{TR}} = {}^{t+\Delta t}_{t}\boldsymbol{\sigma}^{\mathrm{TR}} = \mathbf{C}^{\mathrm{e}}\left({}^{t+\Delta t}\boldsymbol{\varepsilon} - {}^{t}\boldsymbol{\varepsilon}\right) , \tag{3.178} $$

$$ {}^{t+\Delta t}\boldsymbol{\sigma}^{\mathrm{TR}} = {}^{t}\boldsymbol{\sigma} + {}^{t+\Delta t}_{t}\boldsymbol{\sigma}^{\mathrm{TR}} \ . \tag{3.179} $$

If the trial relative stress state, ${}^{t+\Delta t}\boldsymbol{\sigma}^{\mathrm{TR}}$, is within the yield surface, $\Phi({}^{t+\Delta t}\boldsymbol{\sigma}^{\mathrm{TR}}) < 0$, this means that the first assumption is correct and the material point is effectively in elastic state. In this circumstance, there is no need to integrate the equations. Otherwise, if the elastic trial relative stress is outside of the yield surface, a corrector phase (plastic corrector) is required in order to project the stress on the yield surface

$$ {}^{t+\Delta t}\boldsymbol{\sigma} = {}^{t+\Delta t}\boldsymbol{\sigma}^{\mathrm{TR}} - \mathbf{C}^{\mathrm{e}}\left({}^{t+\Delta t}_{t}\boldsymbol{\varepsilon} - \lambda\mathbf{a}\right) . \tag{3.180} $$

with $\mathbf{a} = \dfrac{\partial\Phi}{\partial\boldsymbol{\sigma}}$.

Figure 3.10 exhibits the schematic interpretation of the predictor-corrector method.

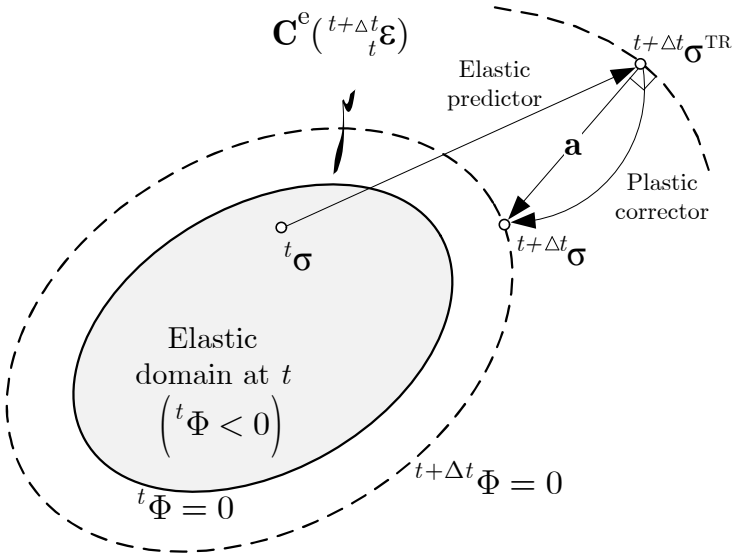

Figure 3.10: Generic representation of stress return mapping procedure.

According to Crisfield (1994) the strategy of elastic predictor and plastic corrector algorithms can be defined in three different approaches: sub-incremention technique, explicit method and implicit method. In each case, the aim is to update the stresses at a Gauss point level and the first step is to use an elastic relation to update the stresses, previously described.

The *sub-incremention* technique consists in dividing the increment of stress in equal sub-increments, performing the return correction for each one separately. Additionally, this method helps decreasing the gap between the predicted stress state after the plastic correction and the correct stress state on the yield surface.

The *explicit return* method, also known as belonging to the forward-Euler category, integrates the constitutive equations based on the variables at a known stress state. However, this algorithm does not directly lead to stresses that satisfy the yield criterion, usually it is coupled with the sub-incremention to improve the accuracy of the explicit procedure making it, incremental and iterative.

The *implicit integration* scheme is known as belonging to backward-Euler algorithm. The returning procedure is evaluated based on the final stress state which is unknown. This algorithm uses an iterative procedure to compute the state variables resorting to the Newton-Raphson method, described in Section 3.4. The radial return algorithm is a special form of the backward-Euler procedure.

Ortiz and Popov (1985) have defined these algorithms in two different groups: generalized trapezoidal rule and generalized midpoint rule. Both groups can lead to implicit and explicit integration schemes. For a particular case, considering von Mises criterion with associative plasticity and a linear isotropic hardening

behaviour, both rules give the same result. The major difference between both rules is related with flow tensor. In the trapezoidal rule algorithm it is assumed a linear combination between the flow tensor from previous increment, ${}^{t}\mathbf{a}$, (see Equation 3.180 for a definition) and the current flow tensor, ${}^{t+\Delta t}\mathbf{a}$, expressed as

$$ {}^{t+\Delta t}_{t}\boldsymbol{\varepsilon}^{\mathrm{p}} = \lambda\Big[\big(1-\theta\big)\,{}^{t}\mathbf{a} + \theta\;{}^{t+\Delta t}\mathbf{a}\Big], \tag{3.181} $$

Although, in the midpoint rule algorithm the flow tensor is obtained by interpolation at intermediate position, ${}^{t+\theta\Delta t}\mathbf{a}$, between the previous increment, ${}^{t}\mathbf{a}$, and the current increment, ${}^{t+\Delta t}\mathbf{a}$, given as follows

$$ {}^{t+\Delta t}_{t}\boldsymbol{\varepsilon}^{\mathrm{p}} = \lambda\;{}^{t+\theta\Delta t}\mathbf{a}\;. \tag{3.182} $$

where θ is a parameter ranging from 0 to 1. If θ is equal to 0 we obtain explicit (forward Euler) integration scheme. If θ is equal to 1 we obtain implicit (backward Euler) integration scheme.

In particular, if the value of parameter θ is 0.5 we have the generalized trapezoidal rule algorithm, the one available within the material subroutines of LAGAMINE code used in the present work to perform the numerical simulations.

e) Consistent elastoplastic tangent modulus tensor

The stress update is efficiently performed resorting to a return-mapping scheme as previously described. But, the stress state obtained would not achieve directly the equilibrium solution of the finite element discretization, for the reason that the strain is calculated at the corrector step. As a result, the tangent modulus tensor, also called the consistent tangent modulus tensor, is required at the end of each plastic corrector step. The integration scheme algorithm chosen should ensure the asymptotically quadratic convergence (Simo and Taylor, 1985).

Afterward, the stiffness matrix evaluation through nonlinear implicit finite element solver is obtained, at each integration point, for each finite element and regarding an incremental-iterative procedure, as similarly described in Section 3.4. For instance, in case of standard Newton-Raphson, the stiffness matrix update is performed at each iteration through the computation of the consistent elastoplastic tangent modulus. Then, the new nodal displacements vector is computed by solving the equilibrium Equation 3.118, from which the corrected nodal displacement incremental vector, Equation 3.119, is calculated.

3.6.3. Boundary Conditions: Contact Formulation

Nonlinearity of an analysis is not only geometric and material. It also includes quantities associated to boundaries, such as, constrained displacements, applied forces (surface tractions and/or body forces) and contact conditions. In particular, the present section is more focused on the description of contact with friction.

In order to describe the contact solving method for our case, the analysis is based on penalty method applied for general problems, such as, contact between a rigid tool body and a deformable metal sheet. Penalty method consists into an addition of a large value parameter, known as penalty coefficient, in the governing equations of equilibrium. This penalty parameter acts as a stiff spring between the contact surfaces. In theory, the penalty parameter tends to infinity. However, the resulting system of equations may become ill-conditioned if the penalty parameter is too large. Previous works have been done in order to develop an efficient contact finite element based on penalty method adapted for LAGAMINE code, such as Habraken and Cescotto (1998). Their work concern a contact element used in the numerical applications further in this work, a brief description and its basic theory description are given below.

Consider two bodies domains Ω^1 and Ω^2 with boundaries $\partial\Omega_C^1$ and $\partial\Omega_C^2$, as shown in Figure 3.11, which represents the contact between them.

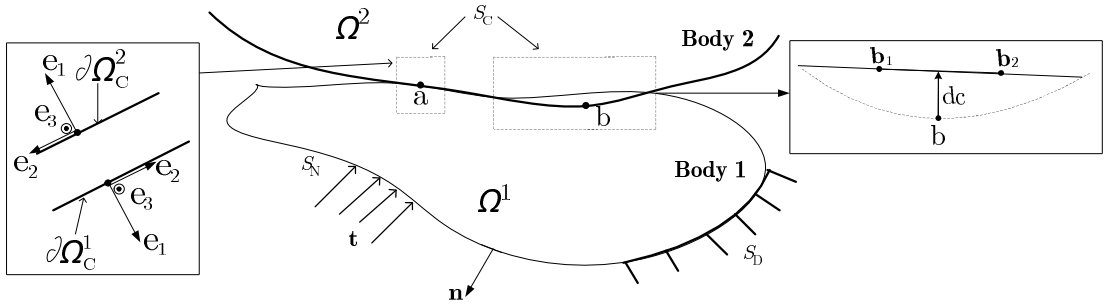

Figure 3.11: Schematic contact between two bodies.

The contact side of each body Ω^1 and Ω^2 can be discretised with contact isoparametric elements. They are compatible, sharing the same DOF and common nodes, with 8 node finite elements used to discretise the corresponding body.

In general, the contact principle is based on the sum of the PVW equation terms defined earlier, internal virtual work and external virtual work of forces

applied on S_{N}, balanced with the virtual work of the contact forces, W_{C}, acting on contact bodies, S_{C}, gives

$$\begin{aligned}\delta \mathrm{W}^{i}(\phi^{i},\ \delta\mathbf{u}^{i}) &= \int_{V}\mathbf{S}\ \delta\mathbf{E}^{i}\,\mathrm{d}\,V - \int_{V}\mathbf{b}^{i}\delta\mathbf{u}^{i}\,\mathrm{d}\,V - \int_{S_{\mathrm{N}}}\mathbf{t}^{i}\delta\mathbf{u}^{i}\,\mathrm{d}S_{\mathrm{N}} \\ -\delta \mathrm{W}_{\mathrm{C}}^{i}(\phi^{i},\ \delta\mathbf{u}^{i}) &= \int_{S_{\mathrm{C}}^{i}}\mathbf{t}_{c}^{i}\delta\mathbf{u}^{i}\,\mathrm{d}S_{\mathrm{C}}^{i}\ .\end{aligned} \tag{3.183}$$

where ϕ^{i} is the solution of the equilibrium state and the subscript i indicates each body. $\delta \mathrm{W}^{i}(\phi^{i},\delta\mathbf{u}^{i})$ is the sum of the internal virtual work and the virtual work of the applied forces for body i

$$\delta \mathrm{W}^{i}(\phi^{i},\delta\mathbf{u}^{i}) + \delta \mathrm{W}_{\mathrm{C}}^{i}(\phi^{i},\delta\mathbf{u}^{i}) = 0\ , \tag{3.184}$$

with

$$\delta \mathrm{W}_{\mathrm{C}}^{i}(\phi^{i},\delta\mathbf{u}^{i}) = -\int_{S_{\mathrm{C}}^{i}}\mathbf{t}_{c}^{i}\delta\mathbf{u}^{i}\,\mathrm{d}S_{\mathrm{C}}^{i}\ . \tag{3.185}$$

The contact force induced on body 2 is equal and opposite to that induced on body 1 at the contact area

$$\mathbf{t}_{c}^{2} = -\mathbf{t}_{c}^{1}\ . \tag{3.186}$$

Therefore:

$$\delta \mathrm{W}_{\mathrm{C}}^{i}(\phi^{i},\delta\mathbf{u}^{i}) = -\int_{S_{\mathrm{C}}^{1}}\mathbf{t}_{c}^{1}\cdot(\delta\mathbf{u}^{1} - \delta\mathbf{u}^{2})\mathrm{d}S_{\mathrm{C}}^{1}\ . \tag{3.187}$$

In SPIF simulations, the forming tool is normally considered a rigid body and since that it is the body 2, the weak form of the contact on the deformable mesh is

$$\delta \mathrm{W}_{\mathrm{C}}(\phi,\delta\mathbf{u}) = \int_{S_{\mathrm{C}}^{1}}\mathbf{t}_{c}^{1}\cdot\delta\mathbf{u}^{1}\ \mathrm{d}S_{\mathrm{C}}^{1}\ . \tag{3.188}$$

At any point of the contact surface, S_{C}, a local axis frame $(\mathrm{e}_1,\ \mathrm{e}_2,\ \mathrm{e}_3)$ can be defined for each solid. The e_1 component is normal to the contact surface while the e_2 and e_3 components are tangent to the surface as it can be seen in Figure 3.12.

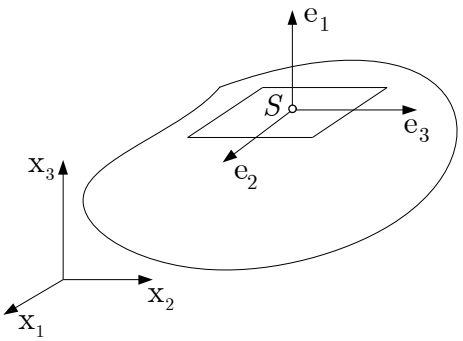

Figure 3.12: Local frame work.

In this local referential, if the contact pressure, named p, the normal component of an applied force per unit area (σ_{n}) and the contact shear stresses, τ_2, τ_3, are tangent components at S point, the surface equilibrium conditions are given as

$$\begin{aligned} \sigma_{s11} + p &= 0; \\ \sigma_{s21} + \tau_2 &= 0; \\ \sigma_{s31} + \tau_3 &= 0. \end{aligned} \tag{3.189}$$

with

$$\boldsymbol{\sigma}_S = \begin{bmatrix} \sigma_{s11} \\ \sigma_{s21} \\ \sigma_{s31} \end{bmatrix}; \boldsymbol{\sigma}_C = \begin{bmatrix} \sigma_n \\ \tau_2 \\ \tau_3 \end{bmatrix} = \begin{bmatrix} p \\ \tau_2 \\ \tau_3 \end{bmatrix}. \tag{3.190}$$

where σ_{s11}, σ_{s21}, σ_{s31} are components of stress of the solid element, σ_S, and σ_C are the contact stress vectors defined in a local referential attached, as schematically represented in Figure 3.12.

In the LAGAMINE code, the contact is discretised using a three-dimensional contact element named CFI3D, applied on the top of each hexahedral finite element. The contact stresses are computed at the contact element integration points, while displacements of the solid boundaries are computed at nodal points. The rigid body sphere is discretised as a segment in FEM model, which is defined within the subroutine named CALFON. This subroutine computes the relation between an integration point of the contact element and the foundation segment.

The contact condition is numerically enforced using the classical penalty method which allows a small penetration of the two bodies (see Figure 3.11) and a relative sliding between them. The contact condition is simply obtained locally from the geometrical computation of the distance, d_C, at contact interfaces of both Ω^1 and Ω^2, as can be seen in Figure 3.13.

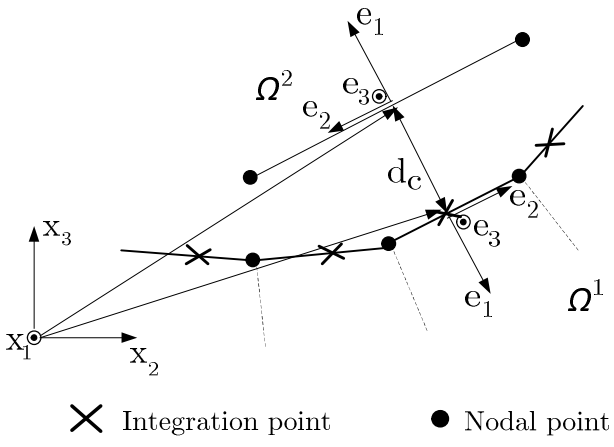

Figure 3.13: Distance between contact element GP and foundation segment (lateral view).

The computation of d_C at the integration point of contact element, from domain Ω^1, requires the coordinates of the intersection between its normal and the surface of the foundation segment, from domain Ω^2. The distance d_C is given by

$$d_C = \mathbf{u} \cdot e_1 \,. \tag{3.191}$$

where the distance vector $\mathbf{u}$ is given as

$$\mathbf{u} = \mathbf{R}\,(\mathbf{x}^1 - \mathbf{x}^2)\,. \tag{3.192}$$

in which $\mathbf{R}$ is the rotation matrix between (x_1, x_2, x_3) and $(e_1,\ e_2,\ e_3)$ axes. If $d_C < 0$ there is no contact at bodies interface and if $d_C \geq 0$, there is contact between both bodies.

The contact elements require the use of a particular constitutive relation which links the contact stress rate to the contact strain rate. The yield function, f_C, (the Coulomb's friction law) assesses the sliding and sticking conditions at the contact surface described as

$$f_C = |\tau| - \mu p = \sqrt{(\tau_2)^2 + (\tau_3)^2} - \mu p \,, \tag{3.193}$$

where μ is the friction coefficient and p is the contact pressure. In the Coulomb friction model, calculation of the tangential force follows the next conditions with both slip and stick states (Wriggers, 2002):

- $f_C < 0$ is the domain of sticking contact (the stress lies in the elastic zone);
- $f_C = 0$ is the domain of sliding contact (the stress lies in the plastic zone);
- $f_C > 0$ is impossible.

If sliding occurs, the relative displacement rate between the points in contact can be split into an elastic and plastic part

$$\dot{\boldsymbol{\varepsilon}}_C = \dot{\boldsymbol{\varepsilon}}_C^e + \dot{\boldsymbol{\varepsilon}}_C^p \,. \tag{3.194}$$

The contact stress rate, $\dot{\boldsymbol{\sigma}}_C$, is given as follows

$$\dot{\boldsymbol{\sigma}}_C = \mathbf{C}_C \dot{\boldsymbol{\varepsilon}}_C \Leftrightarrow \begin{Bmatrix} \dot{p} \\ \dot{\tau}_2 \\ \dot{\tau}_3 \end{Bmatrix} = \begin{vmatrix} K_p & 0 & 0 \\ \varphi \mu K_p \dfrac{\tau_2}{|\tau|} & K_\tau \left(1 - \dfrac{\varphi \tau_2^2}{|\tau|^2}\right) & -\varphi K_\tau \dfrac{\tau_2 \tau_3}{|\tau|^2} \\ \varphi \mu K_p \dfrac{\tau_3}{|\tau|} & -\varphi K_\tau \dfrac{\tau_2 \tau_3}{|\tau|^2} & K_\tau \left(1 - \dfrac{\varphi \tau_3^2}{|\tau|^2}\right) \end{vmatrix} \begin{Bmatrix} \dot{\varepsilon}_{C_1} \\ \dot{\varepsilon}_{C_2} \\ \dot{\varepsilon}_{C_3} \end{Bmatrix} . \tag{3.195}$$

with $\varphi = 0$, if sticking contact (elasticity occurs) and $\varphi = 1$, if sliding contact (plasticity occurs). The $\mathbf{C}_C$ is the contact matrix and K_p, K_τ are the penalty coefficients on contact pressure p and on the contact shear stresses τ_2, τ_3, respectively.

3.7 Reduced Enhanced Solid-Shell (RESS): Description

The development of Finite Element formulations for sheet metal forming using "Solid-Shell" elements, combines the main features of shell formulations with a solid topology. The RESS (Alves de Sousa *et al.*, 2005, 2006, 2007) Finite Element is a hexahedral element composed with 8 nodes, where each node has three degrees of freedom (displacements). The advantage of RESS integration scheme is the possibility to eliminate the volumetric locking phenomena, due to the reduced integration in the element plane. Besides the use of reduced integration procedures, there are other well established techniques in the literature to avoid locking phenomena. In this context, the Enhanced Assumed Strain (EAS) method was applied to increase the element deformation modes, in order to avoid locking problems. Originally EAS method was proposed by Simo and Rifai (1990). Within this approach, the strain field is enriched in order to enlarge the subspace of admissible deformation modes (Alves de Sousa *et al.*, 2003) and, therefore, to increase the flexibility of the Finite Element formulation attenuating locking effects. In the formulation adopted in this work, only one enhancing variable is needed to attenuate the volumetric locking (Alves de Sousa *et al.*, 2005). Consequently, the vector of enhanced internal variables is equivalent to a single scalar.

Volumetric locking effect is attenuated using the EAS method and the reduced integration in the element plane. However, the reduced integration in the element plane is prone to generate spurious modes of deformation, also so-called "hourglass". Consequently, a stabilization scheme is needed to eliminate the hourglass effect. The combination of EAS method and hourglass stabilization in plane, with the use of an unlimited number of integration points in the thickness direction characterizes this element.

The use of a conventional solid element requires several element layers to correctly capture bending effects, but multiple layers of finite elements along the thickness direction increases the computation time. Figure 3.14 presents the advantage of RESS Finite Element structure compared with different finite element integration schemes. For instance, all formulations below using 4 integration points through thickness directions, but the computational efficiency increases from a) to b) and from b) to c).

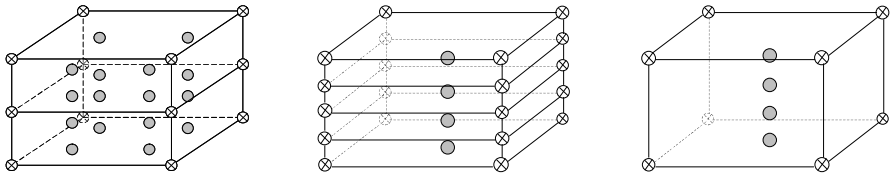

Figure 3.14 – Comparison between (a) fully integrated, (b) reduced integrated and (c) RESS formulation, regarding the number of integration points.

Notice that it is essential to know the element orientation within the mesh generation, since the EAS method and the integration schemes described below depend on the element thickness direction. These conditions are preserved taking into account the numeration of the nodes and its connectivity order.

3.7.1. Enhanced Assumed Strain Method

The virtual work principle described in Section 3.1 is not sufficient to overcome all the problems related to the locking phenomena. In this sense, the Enhanced Assumed Strain (EAS) method was employed. The Fraeijs de Veubeke-Hu-Washizu (VHW) (Fraeijs de Veubeke, 1951; Kyuichiro Washizu, 1955) variational principle is the starting basis for the EAS method, in its linear version as originally presented by Simo and Rifai (1990). The nonlinear version was presented by Vu-Quoc and Tan (2003) and it can be given as

$$\prod^{\mathrm{VHW}}(\mathbf{u},\tilde{\mathbf{E}},\mathbf{S}) = \int_{\mathrm{V}} W_S(\tilde{\mathbf{E}})\,\mathrm{d}\,V + \int_{\mathrm{V}} \mathbf{S}:\left[\frac{1}{2}\left(\mathbf{F}^{\mathrm{T}}\mathbf{F}\text{ - }\mathbf{I}\right)\text{ - }\tilde{\mathbf{E}}\right]\mathrm{d}\,V\text{ - }\prod_{\mathrm{ext}}\,, \quad (3.196)$$

where W_S is the strain energy, $\prod_{\mathrm{ext}}$ is the virtual work of the external loading, as similarly defined in Equation 3.14 and $\tilde{\mathbf{E}}$ is the enhanced strain tensor.

Following the original proposal of Simo and Rifai (1990), the essential point of the EAS method is the enrichment of the displacement-based (Green-Lagrange) strain field, $\mathbf{E}$, by means of the so-called enhancing strain field ($\mathbf{E}_\alpha$), generating the enhanced strain field, $\tilde{\mathbf{E}}$, decomposed in the form

$$\tilde{\mathbf{E}} = \mathbf{E} + \mathbf{E}_\alpha . \quad (3.197)$$

The imposition of the orthogonality condition between the stress field, $\mathbf{S}$, and the enhanced strain field, $\mathbf{E}_\alpha$, is

$$\int_V \mathbf{S}:\mathbf{E}_\alpha\,\mathrm{d}\,V = 0\,, \quad (3.198)$$

which leads to reduce the number of independent variables of Equation 3.196

$$\prod^{\mathrm{VHW}}(\mathrm{u},\mathbf{E}_{\alpha}) = \int_{V} W_{S}(\mathbf{E}+\mathbf{E}_{\alpha})\,\mathrm{d}\,V \text{ - } \prod_{\mathrm{ext}} . \tag{3.199}$$

The weak form of above modified equation, with respect to two independent variables, is obtained applying the so-called Gateaux derivatives and detailed in the work of Alves de Sousa (2006).

3.7.2. FEM approximation of the EAS method

The Finite Element kinematics is based on the displacements field without requiring rotational degree of freedom. The equations are integrated using updated Lagrangian approach, where the reference configuration is from now associated to a converged state t and the current configuration points to the unknown state $t+\Delta t$. Let us consider the natural coordinates $\Psi = (\xi,\eta,\zeta)$, representing the isoparametric cubic domain V chosen such as $\int_{\mathrm{V}} \mathrm{dV} = 8$. The corresponding position after incremental deformation (current configuration) can be defined with an analogous expression, now referred to state $(t+\Delta t)$. The displacement field of a point in the converged state can be obtained by

$$^{t+\Delta t}_{t}\mathbf{u} = {}^{t+\Delta t}\mathbf{x} - {}^{t}\mathbf{x}\,, \tag{3.200}$$

which is interpolated in each finite element domain in the form

$$\mathbf{u} \approx \mathbf{u}^{h} = \mathbf{N}(\Psi)\cdot\mathbf{d}\,, \tag{3.201}$$

$$\delta\mathbf{u} \approx \delta\mathbf{u}^{h} = \mathbf{N}(\Psi)\cdot\delta\mathbf{d}\,, \tag{3.202}$$

$$^{t+\Delta t}_{t}\mathbf{u} \approx {}^{t+\Delta t}_{t}\mathbf{u}^{h} = \mathbf{N}(\Psi)\cdot {}^{t+\Delta t}_{t}\mathbf{d}\,. \tag{3.203}$$

where $\mathbf{N}$ denotes the usual isoparametric shape functions for a low order 3D element, relating the continuum displacement field ($\mathbf{u}$) and the corresponding vector of 24 degrees-of-freedom ($\mathbf{d}$) of the 8-node finite element. Its corresponding shape functions, $\mathbf{N}$, are described by Equation 3.93 regarding hexahedral element discretization using natural coordinates of Equation 3.94. Figure 3.15 exhibited the integration scheme with multiple integration points through the thickness, in the isoparametric domain. This integration scheme presents an in-plane reduced integration and a higher integration scheme through-thickness direction.

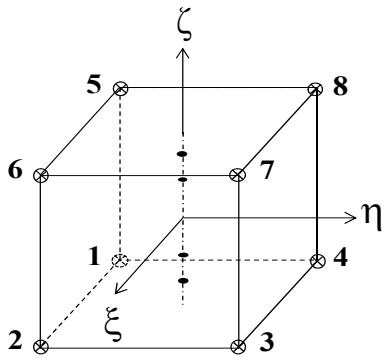

Figure 3.15: Integration scheme in isoparametric domain with n Gauss points in the thickness direction.

Using the in-plane integration scheme, the terms of strain-displacement matrix $\mathbf{B}_u$ depending on ξ and η are zero. For implementation convenience, $\mathbf{B}_u$ can be calculated using the decomposition into constant (c) and ζ dependent terms (Alves de Sousa *et al.*, 2005)

$$\mathbf{B}_{\mathrm{u}} = \mathbf{B}^{c} + \mathbf{B}^{\zeta}\zeta\,, \tag{3.204}$$

where $\mathbf{B}_{\mathrm{u}}$ definition can be found easily in the literature as expressed in Equation 3.99 (Section 3.3.1). In the context, the enhanced strain tensor can be interpolated in the element domain using the nodal displacement vector ($\mathbf{d}$) and the enhanced parameter vector is reduced to a scalar, α, as only one enhanced mode is used

$$\tilde{\mathbf{E}} = \mathbf{E} + \mathbf{E}_{\alpha} = \left[\mathbf{B}_{\mathrm{u}} \;\; \mathbf{B}_{\alpha}\right]\begin{bmatrix}\mathbf{d}\\ \alpha\end{bmatrix}. \tag{3.205}$$

Considering locking as the inability of a formulation to reproduce a deformation pattern under a given set of constraints (Alves de Sousa, 2006), in the EAS method the role of the $\mathbf{B}_{\alpha}$ operator is to supply this lack of deformation modes, increasing the space of possible solutions. To do so, the number of degrees of freedom (24, for a conventional solid element formulation) is increased by the number of internal variables present in enhanced strain modes vector. These extra-variables have no physical meaning, and given their discontinuity between element's boundaries, they can be eliminated at the element level (Simo and Rifai, 1990).

For RESS element, just one enhancing variable needs to be used to attenuate volumetric locking (Alves de Sousa *et al.,* 2005). Consequently, the vector of internal variables is equivalent to a single scalar, α. The associated strain-displacement operator $\mathbf{B}_{\alpha}$ is a vector, initially defined in the natural convective frame as

$$\left(\mathbf{B}_{\alpha}\right)^{\mathrm{T}} = \left[0 \;\; 0 \;\; \zeta \;\; 0 \;\; 0 \;\; 0\right]. \tag{3.206}$$

Typically, the enhanced part of the strain field can be transformed into the Cartesian frame, using (Simo and Rifai, 1990)

$$\hat{\mathbf{B}}_{\alpha} = \frac{\det({}^{l}_{e}\mathbf{T}_{0})}{\underbrace{\det({}^{l}_{c}\mathbf{T}_{\psi})}_{\approx 1}} \mathbf{T}_{0}\mathbf{B}_{\alpha}, \tag{3.207}$$

where $\mathbf{T}_0$ is the second order transformation tensor.

The transverse shear locking phenomenon, on the other hand, is associated to an overestimation of stiffness associated to transverse shear strain energy, which does not automatically vanish in the case of 2×2 in-plane integrated elements when applied to thin structures. In the work of Alves de Sousa (2006) it is shown, that use a suitable subspace analysis, an in-plane reduced numerical integration eliminates the transverse shear locking effects.

From the linearization procedure of the weak form terms, detailed in the work of Alves de Sousa (2006), the variations $\delta\prod_{\text{int}}$ and $\delta\prod_{\text{ext}}$ can be expressed as

$$\delta\prod\nolimits_{\text{int}}(\mathbf{d},\boldsymbol{\alpha}) = \delta\mathbf{d}^{\mathrm{T}}\int_{V}\mathbf{B}^{\mathrm{T}}\mathbf{S}\,\mathrm{d}V + \delta\boldsymbol{\alpha}^{\mathrm{T}}\int_{V}\left(\hat{\mathbf{B}}_{\alpha}\right)^{\mathrm{T}}\mathbf{S}\,\mathrm{d}V\,, \tag{3.208}$$

and

$$\delta\prod\nolimits_{\text{ext}}(\mathbf{d}) = \delta\mathbf{d}^{\mathrm{T}}\int_{V}\mathbf{N}^{\mathrm{T}}\cdot\mathbf{b}\rho\,\mathrm{d}V + \delta\mathbf{d}^{\mathrm{T}}\int_{S_{\mathrm{N}}}\mathbf{N}^{\mathrm{T}}\cdot\mathbf{t}\,\mathrm{d}S\,. \tag{3.209}$$

As a consequence of the inclusion of the enhancing parameters into the variational formulation, the coupling stiffness matrices $\mathbf{K}^{\alpha\mathrm{u}}$ and $\mathbf{K}^{\mathrm{u}\alpha}$ are obtained, as well as the enhanced stiffness operator $\mathrm{K}^{\alpha\alpha}$, a scalar within this formulation, all of them having the same structure as the linear formulation of Simo and Rifai (1990)

$$\mathbf{K}^{\mathrm{u}\alpha} = \left(\mathbf{K}^{\mathrm{u}\alpha}\right)^{\mathrm{T}} = \int_{V}\mathbf{B}^{\mathrm{T}}\mathbf{C}\cdot\hat{\mathbf{B}}_{\alpha}\,\mathrm{d}V, \tag{3.210}$$

$$\mathrm{K}^{\alpha\alpha} = \int_{V}\left(\hat{\mathbf{B}}_{\alpha}\right)^{\mathrm{T}}\mathbf{C}\cdot\hat{\mathbf{B}}_{\alpha}\,\mathrm{d}V\,. \tag{3.211}$$

The linear geometric stiffness matrix ($\mathbf{K}_{\mathrm{L}}^{\mathrm{uu}}$) is defined as in the fully displacement-based formulation as function of $\mathbf{B}_{\mathrm{u}}$, whereas the geometrically nonlinear stiffness matrix $\mathbf{K}_{\mathrm{NL}}^{\mathrm{uu}}$ is given in Section 3.6.1. The final result gives the equivalent system of equations, on matrix form

$$\begin{bmatrix} \mathbf{K}_{\mathrm{L}}^{\mathrm{uu}} + \mathbf{K}_{\mathrm{NL}}^{\mathrm{uu}} & \mathbf{K}^{\mathrm{u}\alpha} \\ \mathbf{K}^{\alpha\mathrm{u}} & \mathrm{K}^{\alpha\alpha} \end{bmatrix} \begin{Bmatrix} {}^{t+\Delta t}_{t}\mathbf{d} \\ {}^{t+\Delta t}_{t}\alpha \end{Bmatrix} = \begin{Bmatrix} \int_{V}\mathbf{N}^{\mathrm{T}}\cdot\mathbf{b}\rho\,\mathrm{d}V + \int_{S_{\mathrm{N}}}\mathbf{N}^{\mathrm{T}}\cdot\mathbf{t}\,\mathrm{d}S - \int_{V}\mathbf{B}^{\mathrm{T}}\mathbf{S}\,\mathrm{d}V \\ -\int_{\mathrm{V}}\left(\hat{\mathbf{B}}_{\alpha}\right)^{\mathrm{T}}\mathbf{S}\,\mathrm{d}V \end{Bmatrix}, \tag{3.212}$$

Simplifying the equation system above leads to

$$\begin{bmatrix} \mathbf{K}_{\mathrm{L}}^{\mathrm{uu}} + \mathbf{K}_{\mathrm{NL}}^{\mathrm{uu}} & \mathbf{K}^{\mathrm{u}\alpha} \\ \mathbf{K}^{\alpha\mathrm{u}} & \mathrm{K}^{\alpha\alpha} \end{bmatrix} \begin{Bmatrix} {}^{t+\Delta t}_{t}\mathbf{d} \\ {}^{t+\Delta t}_{t}\alpha \end{Bmatrix} = \begin{Bmatrix} \mathbf{f}_{\mathrm{ext}}^{\mathrm{u}} \\ 0 \end{Bmatrix} - \begin{Bmatrix} \mathbf{f}_{\mathrm{int}}^{\mathrm{u}} \\ \mathbf{f}_{\mathrm{int}}^{\alpha} \end{Bmatrix}. \tag{3.213}$$

The increment of the additional enhanced freedom degrees, ${}^{t+\Delta t}_{t}\alpha$, at element level, are updated using a static condensation procedure, as

$${}^{t+\Delta t}_{t}\alpha = -\left[\mathrm{K}^{\alpha\alpha}\right]^{-1}(\mathbf{f}_{\mathrm{int}}^{\alpha} + \mathbf{K}^{\alpha\mathrm{u}}\,{}^{t+\Delta t}_{t}\mathbf{d}). \tag{3.214}$$

Replacing ${}^{t+\Delta t}_{t}\alpha$ into its expression in the system of equations above, leads to the static condensation for the stiffness matrix and the internal force vector written at the element level, as

$$\left[\mathbf{K}_{\mathrm{L}}^{\mathrm{uu}} + \mathbf{K}_{\mathrm{NL}}^{\mathrm{uu}} - \frac{1}{\mathbf{K}^{\alpha\alpha}}\mathbf{K}^{\mathrm{u}\alpha}\mathbf{K}^{\alpha\mathrm{u}}\right]{}^{t+\Delta t}_{t}\mathbf{d} = \mathbf{f}_{\mathrm{ext}}^{\mathrm{u}} - \mathbf{f}_{\mathrm{int}}^{\mathrm{u}} + \frac{\mathbf{f}_{\mathrm{int}}^{\alpha}}{\mathbf{K}^{\alpha\alpha}}\mathbf{K}^{\mathrm{u}\alpha}, \tag{3.215}$$

$$\mathbf{K}^{\mathrm{u}+\alpha}\left({}^{t+\Delta t}_{t}\mathbf{d}\right) = \mathbf{f}_{\mathrm{ext}}^{\mathrm{u}} - \mathbf{f}^{\mathrm{u}+\alpha}. \tag{3.216}$$

The internal forces for the displacement ($\mathbf{f}_{\mathrm{int}}^{\mathrm{u}}$) and the residual forces from enhanced part ($\mathbf{f}_{\mathrm{int}}^{\alpha}$) can be written, under the following expressions

$$\mathbf{f}_{\mathrm{int}}^{\mathrm{u}} = \int_{V} \mathbf{B}_{\mathrm{u}}^{\mathrm{T}}\boldsymbol{\sigma}^{\mathrm{m}}\,\mathrm{d}\,V, \tag{3.217}$$

$$\mathbf{f}_{\mathrm{int}}^{\alpha} = \int_{V} \hat{\mathbf{B}}_{\alpha}^{\mathrm{T}}\boldsymbol{\sigma}^{\mathrm{m}}\,\mathrm{d}\,V, \tag{3.218}$$

Since the $\mathbf{B}_{\mathrm{u}}^{\mathrm{T}}$ and $\hat{\mathbf{B}}_{\alpha}$ matrices have been obtained from the displacement part and from enhanced part, respectively, the integrals of equations 3.217 and 3.218 can be calculated numerically as follows

$$\mathbf{f}_{\mathrm{int}}^{\mathrm{u}} = \sum_{ipi=1}^{npi} \mathbf{B}_{\mathrm{u}}^{\mathrm{T}}(\xi,\eta,\zeta)_{ipi}\boldsymbol{\sigma}^{\mathrm{m}}(\underline{x},\underline{\varepsilon})_{ipi}\left|\mathbf{J}\right|_{ipi}\mathrm{w}_{ipi}\ , \tag{3.219}$$

$$\mathbf{f}_{\mathrm{int}}^{\alpha} = \sum_{ipi=1}^{npi} \hat{\mathbf{B}}_{\alpha}^{\mathrm{T}}(\xi,\eta,\zeta)_{ipi}\boldsymbol{\sigma}^{\mathrm{m}}(\underline{x},\underline{\varepsilon})_{ipi}\left|\mathbf{J}\right|_{ipi}\mathrm{w}_{ipi}\ , \tag{3.220}$$

where $\boldsymbol{\sigma}^{\mathrm{m}}$ is the Cauchy stress which is obtained from the integration of material law, w_{ipi} is the Gauss point weight, *npi* is the total number of integration points and *ipi* is the corresponding integration point. In the equation of the variational principle, $\mathbf{f}_{\mathrm{int}}^{\alpha}$ must be equal to zero resorting to an iterative procedure in order to avoid the α effect. While $\mathbf{f}_{\mathrm{int}}^{\mathrm{u}}$ represents the forces of the element which should be in equilibrium with the external forces.

Comparing RESS approach with other well-established EAS formulations, it is possible to understand its advantages in terms of CPU efficiency, mostly due to the number of enhancing variables, which is only one. Consequently, the matrix operations (inversions and multiplications) involved in Equation 3.213 is less computationally expensive. This advantage allows for a crucial contribution in the numerical simulation of demanding industrial processes.

3.7.3. Stabilization Procedure

The integration scheme used for RESS finite element leads to the rank-deficiency of the formulation, coming exclusively from the reduced integration procedure in the element plane, as can be seen in Figure 3.15. To reduce the occurrence of hourglass problems the physical stabilization procedure, originally suggested for a shell formulation (Cardoso *et al.*, 2002), is extended to cover 3D solid elements.

The compatible strain tensor from displacement field ($\mathbf{E}$) term, included in Equation 3.205, can be rewritten into a convenient manner by the decomposed standard strain-displacement matrix, $\mathbf{B}_{\mathrm{u}}$

$$\mathbf{E} = \left(\mathbf{B}^{c} + \mathbf{B}^{\xi}\xi + \mathbf{B}^{\eta}\eta + \mathbf{B}^{\zeta}\zeta + \mathbf{B}^{\xi\eta}\xi\eta + \mathbf{B}^{\xi\zeta}\xi\zeta + \mathbf{B}^{\eta\zeta}\eta\zeta\right)\mathbf{u}\,. \tag{3.221}$$

where $\mathbf{u}$ is the nodal displacements vector and the sub-terms of Equation 3.221 are detailed in Alves de Sousa *et al.* (2005). In fact, for the special integration scheme where $\xi = 0$ and $\eta = 0$ for each integration point, the calculation of $\mathbf{B}_{\mathrm{u}}$ turns out to be simple as demonstrated in Equation 3.99.

Under the in-plane reduced integration scheme adopted in this formulation, the constant $\mathbf{B}^{\mathrm{c}}$ and $\mathbf{B}^{\zeta}\zeta$ terms for the stabilization procedure are intentionally removed, since the used integration scheme does not cancel them. The ζ term is not required due to the arbitrary number of integration points through the thickness direction. For this reason, the strain-displacement sub-matrices that contribute to element stabilization and define the stabilization matrix, $\mathbf{B}^{\mathrm{H}}$, are

$$\mathbf{B}^{\mathrm{H}} = \mathbf{B}^{\xi}\xi + \mathbf{B}^{\eta}\eta + \mathbf{B}^{\xi\eta}\xi\eta + \mathbf{B}^{\xi\zeta}\xi\zeta + \mathbf{B}^{\eta\zeta}\eta\zeta, \tag{3.222}$$

Also, it is useful to decompose $\mathbf{B}^{\mathrm{H}}$ matrix by lines and to add a parameter β in the formulation

$$
\begin{aligned}
\mathbf{B}^{\mathrm{H}}_{\xi\xi} &= \mathbf{B}^{\xi}_{\xi\xi}\xi + \mathbf{B}^{\eta}_{\xi\xi}\eta + \mathbf{B}^{\xi\eta}_{\xi\xi}\xi\eta + \mathbf{B}^{\xi\zeta}_{\xi\xi}\xi\zeta + \mathbf{B}^{\eta\zeta}_{\xi\xi}\eta\zeta \ , \\
\mathbf{B}^{\mathrm{H}}_{\eta\eta} &= \mathbf{B}^{\xi}_{\eta\eta}\xi + \mathbf{B}^{\eta}_{\eta\eta}\eta + \mathbf{B}^{\xi\eta}_{\eta\eta}\xi\eta + \mathbf{B}^{\xi\zeta}_{\eta\eta}\xi\zeta + \mathbf{B}^{\eta\zeta}_{\eta\eta}\eta\zeta \ , \\
\mathbf{B}^{\mathrm{H}}_{\zeta\zeta} &= \mathbf{B}^{\xi}_{\zeta\zeta}\xi + \mathbf{B}^{\eta}_{\zeta\zeta}\eta + \mathbf{B}^{\xi\eta}_{\zeta\zeta}\xi\eta + \mathbf{B}^{\xi\zeta}_{\zeta\zeta}\xi\zeta + \mathbf{B}^{\eta\zeta}_{\zeta\zeta}\eta\zeta \ , \\
\mathbf{B}^{\mathrm{H}}_{\xi\eta} &= \mathbf{B}^{\xi}_{\xi\eta}\xi + \mathbf{B}^{\eta}_{\xi\eta}\eta + \mathbf{B}^{\xi\eta}_{\xi\eta}\xi\eta + \mathbf{B}^{\xi\zeta}_{\xi\eta}\xi\zeta + \mathbf{B}^{\eta\zeta}_{\xi\eta}\eta\zeta \ , \\
\mathbf{B}^{\mathrm{H}}_{\xi\zeta} &= \beta\left(\mathbf{B}^{\xi}_{\xi\zeta}\xi + \mathbf{B}^{\eta}_{\xi\zeta}\eta + \mathbf{B}^{\xi\eta}_{\xi\zeta}\xi\eta + \mathbf{B}^{\xi\zeta}_{\xi\zeta}\xi\zeta + \mathbf{B}^{\eta\zeta}_{\xi\zeta}\eta\zeta\right) \ , \\
\mathbf{B}^{\mathrm{H}}_{\eta\zeta} &= \beta\left(\mathbf{B}^{\xi}_{\eta\zeta}\xi + \mathbf{B}^{\eta}_{\eta\zeta}\eta + \mathbf{B}^{\xi\eta}_{\eta\zeta}\xi\eta + \mathbf{B}^{\xi\zeta}_{\eta\zeta}\xi\zeta + \mathbf{B}^{\eta\zeta}_{\eta\zeta}\eta\zeta\right) \ .
\end{aligned}
\tag{3.223}
$$

Accordingly, when applying this formulation for thin-walled structures, the β parameter of Equation 3.223 can be set to zero, not adding transverse shear energy and avoiding transverse shear locking (Alves de Sousa *et al.*, 2005). Once the $\mathbf{B}^{\mathrm{H}}$ matrix is defined in natural frame, it is transformed to the global frame, applying the transformation matrix $\mathbf{T}_0$, similarly to Equation 3.207

$$
\hat{\mathbf{B}}^{\mathrm{H}} = \mathbf{T}_0 \mathbf{B}^{\mathrm{H}}. \tag{3.224}
$$

To avoid the volumetric locking phenomenon which occurs in solid finite elements, the B-bar approach is adopted, as introduced by Malkus and Hughes (1978). Accordingly, the hourglass counterpart of the strain-displacement operator is divided into its volumetric (dilatational) and deviatoric components, the dilatational part being computed at the element centre

$$
\hat{\mathbf{B}}^{\mathrm{H}}\left(\xi,\eta,\zeta\right) = \hat{\mathbf{B}}^{\mathrm{H}}\left(\xi,\eta,\zeta\right)\Big|_{\mathrm{dev}} + \hat{\mathbf{B}}^{\mathrm{H}}\left(0,0,0\right)\Big|_{\mathrm{dil}} \ . \tag{3.225}
$$

where $\hat{\mathbf{B}}^{\mathrm{H}}\Big|_{\mathrm{dev}}$ and $\hat{\mathbf{B}}^{\mathrm{H}}\Big|_{\mathrm{dil}}$ are further expanded according to Equation 3.223.

Following an incremental-iterative Newton-Raphson scheme, both the stiffness matrix and the internal force vector of the equilibrium Equation 3.216 must be corrected, providing the nodal increment of displacement, $\Delta\mathbf{d}$

$$
(\mathbf{K}^{\mathrm{u}+\alpha} + \mathbf{K}^{\mathrm{H}})\Delta\mathbf{d} = \mathbf{f}_{\mathrm{ext}} - (\mathbf{f}^{\mathrm{u}+\alpha} + \mathbf{f}^{\mathrm{H}}). \tag{3.226}
$$

The next decompositions are considered for the hourglass stiffness ($\mathbf{K}^{\mathrm{H}}$) and the increment of hourglass forces ($\mathbf{f}^{\mathrm{H}}$)

$$
\mathbf{K}^{\mathrm{H}} = \mathbf{K}^{\xi} + \mathbf{K}^{\eta} + \mathbf{K}^{\xi\eta} + \mathbf{K}^{\xi\zeta} + \mathbf{K}^{\eta\zeta}, \tag{3.227}
$$

$$
\mathbf{f}^{\mathrm{H}} = \mathbf{f}^{\xi} + \mathbf{f}^{\eta} + \mathbf{f}^{\xi\eta} + \mathbf{f}^{\xi\zeta} + \mathbf{f}^{\eta\zeta}. \tag{3.228}
$$

where the hourglass forces ($\mathbf{f}^{\mathrm{H}}$) is calculated at the mid-step configuration (Alves de Sousa *et al.*, 2005). Each hourglass stiffness term of Equation 3.227 is detailed below

$$
\mathbf{K}^{\xi} = \int_V \left[\left(\mathbf{B}^{\xi}\right)^{\mathrm{T}} \mathbf{C} \ \mathbf{B}^{\xi} \right] \xi^2 \left|\mathbf{J}_0\right| \mathrm{d}\, V \ , \tag{3.229}
$$

$$\mathbf{K}^{\eta} = \int_V \left[\left(\mathbf{B}^{\eta} \right)^{\mathrm{T}} \mathbf{C}\ \mathbf{B}^{\eta} \right] \eta^2 \left| \mathbf{J}_0 \right| \mathrm{d}V \,, \tag{3.230}$$

$$\mathbf{K}^{\xi\eta} = \int_V \left[\left(\mathbf{B}^{\xi\eta} \right)^{\mathrm{T}} \mathbf{C}\ \mathbf{B}^{\xi\eta} \right] \xi^2 \eta^2 \left| \mathbf{J}_0 \right| \mathrm{d}V \,, \tag{3.231}$$

$$\mathbf{K}^{\xi\zeta} = \int_V \left[\left(\mathbf{B}^{\xi\zeta} \right)^{\mathrm{T}} \mathbf{C}\ \mathbf{B}^{\xi\zeta} \right] \xi^2 \zeta^2 \left| \mathbf{J}_0 \right| \mathrm{d}V \,, \tag{3.232}$$

$$\mathbf{K}^{\eta\zeta} = \int_V \left[\left(\mathbf{B}^{\eta\zeta} \right)^{\mathrm{T}} \mathbf{C}\ \mathbf{B}^{\eta\zeta} \right] \eta^2 \zeta^2 \left| \mathbf{J}_0 \right| \mathrm{d}V \,. \tag{3.233}$$

where the isoparametric domain is chosen such as $\int_V \mathrm{d}V = 8$ and $\left|\mathrm{J}_0\right|$ is the Jacobian determinant computed at the element centre. Similarly, each hourglass force ($\mathbf{f}^{\mathrm{H}}$) component of Equation 3.228 is written as

$$\mathbf{f}^{\xi} = \int_V \left[\left(\mathbf{B}^{\xi} \right)^{\mathrm{T}} \boldsymbol{\sigma}^{\xi} \right] \xi \left| \mathbf{J}_0 \right| \mathrm{d}V, \tag{3.234}$$

$$\mathbf{f}^{\eta} = \int_V \left[\left(\mathbf{B}^{\eta} \right)^{\mathrm{T}} \boldsymbol{\sigma}^{\eta} \right] \eta \left| \mathbf{J}_0 \right| \mathrm{d}V, \tag{3.235}$$

$$\mathbf{f}^{\xi\eta} = \int_V \left[\left(\mathbf{B}^{\xi\eta} \right)^{\mathrm{T}} \boldsymbol{\sigma}^{\xi\eta} \right] \xi\eta \left| \mathbf{J}_0 \right| \mathrm{d}V, \tag{3.236}$$

$$\mathbf{f}^{\xi\zeta} = \int_V \left[\left(\mathbf{B}^{\xi\zeta} \right)^{\mathrm{T}} \boldsymbol{\sigma}^{\xi\zeta} \right] \xi\zeta \left| \mathbf{J}_0 \right| \mathrm{d}V, \tag{3.237}$$

$$\mathbf{f}^{\eta\zeta} = \int_V \left[\left(\mathbf{B}^{\eta\zeta} \right)^{\mathrm{T}} \boldsymbol{\sigma}^{\eta\zeta} \right] \eta\zeta \left| \mathbf{J}_0 \right| \mathrm{d}V. \tag{3.238}$$

The increment of the Cauchy stress ($\boldsymbol{\sigma}$) are given by

$$\boldsymbol{\sigma}^{\xi} = \xi \mathbf{C} \mathbf{B}^{\xi} \Delta\mathbf{d}, \tag{3.239}$$

$$\boldsymbol{\sigma}^{\eta} = \eta \mathbf{C} \mathbf{B}^{\eta} \Delta\mathbf{d}, \tag{3.240}$$

$$\boldsymbol{\sigma}^{\xi\eta} = \xi\eta \mathbf{C} \mathbf{B}^{\xi\eta} \Delta\mathbf{d}, \tag{3.241}$$

$$\boldsymbol{\sigma}^{\xi\zeta} = \xi\zeta \mathbf{C} \mathbf{B}^{\xi\zeta} \Delta\mathbf{d}, \tag{3.242}$$

$$\boldsymbol{\sigma}^{\eta\zeta} = \eta\zeta \mathbf{C} \mathbf{B}^{\eta\zeta} \Delta\mathbf{d}, \tag{3.243}$$

where $\mathbf{C}$ is the constitutive stress-strain law tensor (6x6). In the set of equations from 3.229 to 3.233, the non-constant terms can be analytically calculated

$$\int_V \xi^2 \mathrm{d}V = \int_V \eta^2 \mathrm{d}V = \frac{8}{3}, \tag{3.244}$$

$$\int_V \xi^2 \eta^2 \mathrm{d}V = \int_V \xi^2 \zeta^2 \mathrm{d}V = \int_V \eta^2 \zeta^2 \mathrm{d}V = \frac{8}{9}. \tag{3.245}$$

It should be noted that no numerical integration is required at this stage, which leads to save a considerable computational time.

Generally, the aspects that contribute to the computational advantages of this formulation are: i) the use of only one internal variable per element for the enhanced part of the strain field; ii) the reduced integration scheme; iii) the use of

one element layer along thickness with multiple integration points; iv) the evaluation of analytical stabilization terms instead of resorting to empirical parameters and numerical integration.

The formulation of RESS finite element described in the above sections is currently implemented within LAGAMINE in-house code, subroutine called RESS3.

3.8. Numerical Code LAGAMINE

The present section presents the nonlinear Finite Element in-house code called LAGAMINE developed in FORTRAN by MSM team of ArGEnCo department in University of Liège since 80's. This code includes different research fields, implicit and dynamic explicit integration schemes, different analysis type (2D and 3D), extensive list of finite elements and constitutive laws. Schematically, Figure 3.16 exhibits the nonlinear procedure of LAGAMINE code.

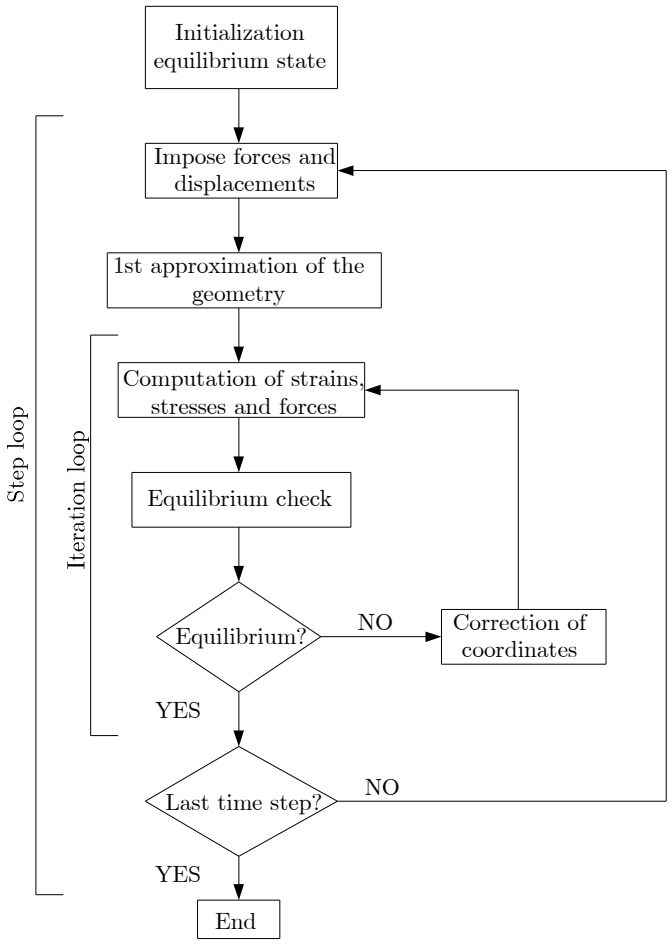

Figure 3.16: Procedure scheme of nonlinear LAGAMINE code.

3.8.1. Pre-Processor: Generation of the "reading" files

The LAGAMINE in-house code is mostly used as research tool, with a flexible open source structure, composed by two parts: the PREPRO program and the LAGAMINE program. The PREPRO program is the pre-processor responsible to read the data from the input file (*.lag) verifying also its consistency, and converting it into a group of files that can be read by the LAGAMINE processor. Figure 3.17 presents the files generated after PREPRO read the data file *lag.

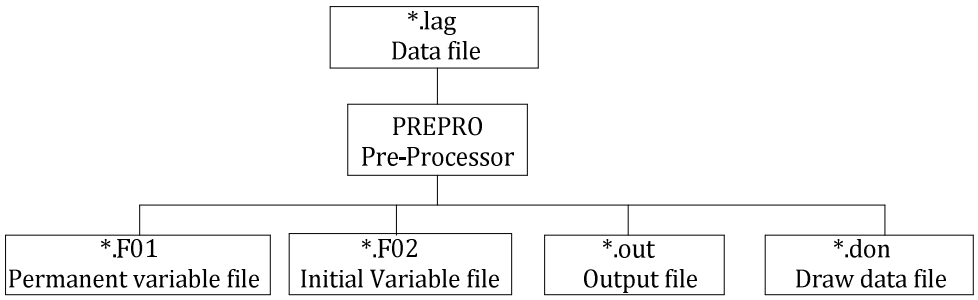

Figure 3.17: Files generated by PREPRO.

The files generated by PREPRO program provides:

- File.F01: for permanent parameter. It is a binary file which includes the list of DOF per node, list of elements, constitutive law parameters.
- File.F02: the initial variable file. It is a binary file which contains the initial position, initial reaction and initial stress.
- File.out: output file which is an ASCII file and presents the verification summary of the input/data file (*.lag).
- File.don: drawing parameter file. It is an ASCII file used to visualise the mesh on the auxiliary drawing viewer called DESFIN.

3.8.2. Processor: Simulation Processing

The program processor is responsible for the simulation runs. The LENABO subroutine is the main program which manages the LAGAMINE code and performs the analysis after reading an additional data file called strategy data file (*.dat). This data file contains the information of the simulation control parameters. The main controlled parameters are: the initial force increment size, the initial

displacement increment size, initial and maximum increment size, total time, read and print options, just a few parameters are here mentioned. The input files generated by the pre-processor PREPRO program are: the permanent variable file (*.F01) and the initial variable file (*.F02). The displacements input file (*.dep) is used when the displacement history are not radial/constant during the simulation runtime and/or when they are radial but are applied in a different orientation in each direction component. The reading of displacements data file (*.dep) is requested by an option within the strategy file (*.dat). Any non-radial stress history can be read within parameters file (*.loa) if required by the strategy file. The current variables file (*.F03) is continually updated during the simulation execution until the simulation is concluded, and it saves the information of the last increment performed.

Figure 3.18 schematically shows the input files used and the generated files by the LAGAMINE processor.

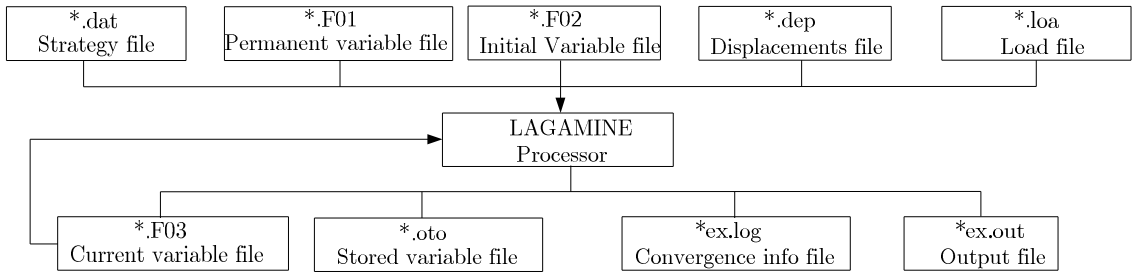

Figure 3.18: Input files and generated files by LAGAMINE code.

The files generated by LAGAMINE program are:

- File.F03: binary file with current variable information (position, reaction, stress...) updated at each step;
- File.oto: binary file with required stored variables for any requested step or all of them (package of file.f03);
- Fileex.log: ASCII file which contains advanced computation and convergence information;
- Fileex.out: output file is an ASCII file with more info (advancement, convergence, stress field, displacement field, state variables);
- Others output files not described here allowing specific generation files for results visualisation, such as File.rea.

The simulation can be restarted from the last converged increment, as well, if the simulation was divided into different execution stages. In this case different

strategy files (*.dat) are used at each simulation stage, previously planned by the user. If the simulation was stopped, due to convergence problems for instance, the user can restart the simulation again and it restarts from the last converged increment. The simulation is restarted from the information saved in the binary file (*.F03) and it becomes the initial file information to continue the simulation. Hence, the updated information of the following increments are saved in the file which was initially the variable file (*.F02).

3.8.3. Pos-Processor: Simulation Result Treatment

The pos-processor is a program called SELECT and it is responsible to exhibit the results in function of parameters chosen by the user. The file which is used in the pos-processor program generated by the processor LAGAMINE are:

- File.F02: Binary file with the initial variables values;
- File.F03: Binary file with the current variables updated;
- File.rea: ASCII file with the results of reaction forces;
- File.oto: Binary file with the variables information of all steps or requested steps saved. This request is optional and it should be defined by the user within the strategy file (*.dat).

The files generated by the pos-processor are:

- File.imp: ASCII file with the results chosen by the user;
- File.res: Binary file (input file of DESFIN) to visualise the final deformable of the mesh, stress, strain and internal variable fields.

DESFIN is the viewer program, where it is possible to display the deformable mesh. Figure 3.19 presents the general LAGAMINE work scheme and its files connection between the pre-processor, processor and pos-processor to prepare/analyse a numerical simulation.

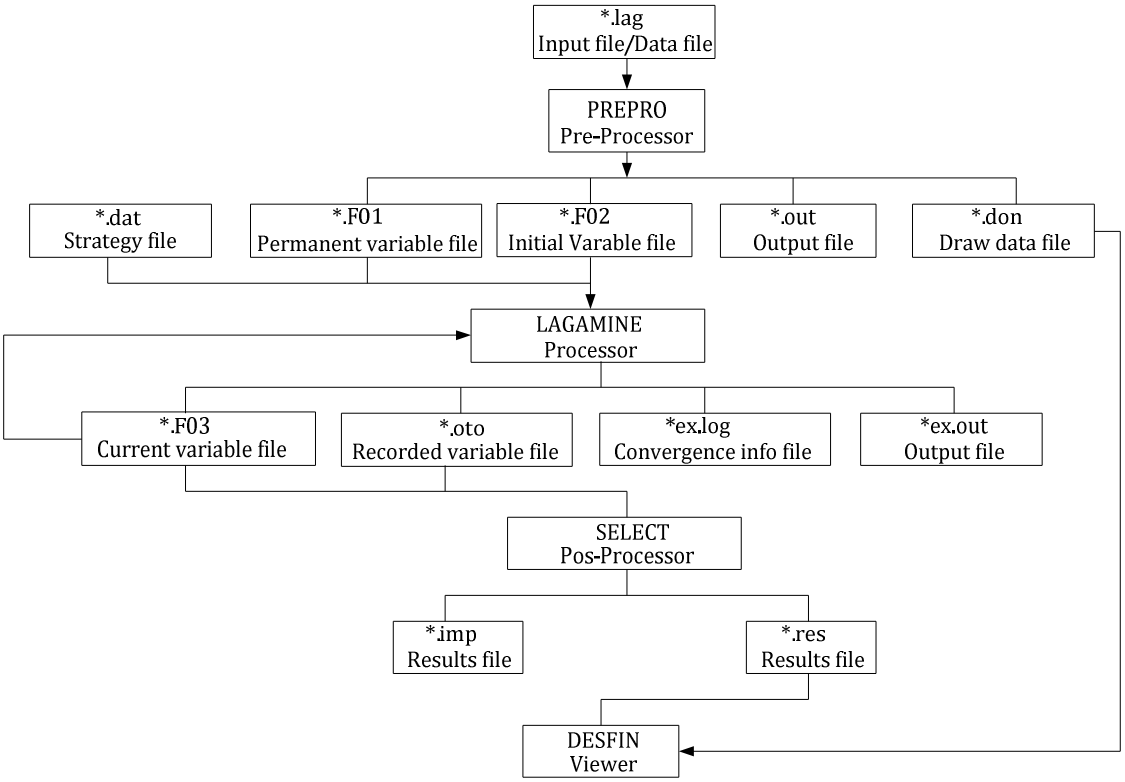

Figure 3.19: LAGAMINE code working scheme.

Chapter 4

Remeshing for SPIF: Description

The current chapter presents a mesh refinement procedure based on the Finite Element Method (FEM). Many issues appear when simulating SPIF process resorting to FEM, and it is always necessary to find a compromise between accuracy and CPU efficiency. The mesh size has a significant effect on the numerical results accuracy. It influences the convergence rate, the computational time and the contact between two surfaces. An initially refined mesh can improve the accuracy of results but the computational time required to perform the simulation is huge. On the other hand, a coarse mesh leads to inconsistent results, penetration issues and convergence problems during simulations. The alternative to obtain the advantages of fine meshes with less computational time is the use of an adaptive remeshing technique.
The following sections are focused on the description of the implemented mesh refinement technique. These features are not usually available in common commercial FEM codes, in particular for a solid-shell formulation. In this work special focus will be given to a solid-shell finite element formulation combined with an adaptive remeshing method chosen. Implicit scheme analysis was selected to perform the simulations.

4.1. Adaptive Remeshing Method

This section introduces and describes the adaptive remeshing method implemented in the in-house Finite Element code LAGAMINE. Initially, this remeshing procedure was developed by Lequesne *et al.* (2008) and it was available only for a shell element. Currently, this section presents the extension of the chosen method for an eight nodes solid-shell element, more specifically the RESS finite element (Alves de Sousa *et al.*, 2005, 2006, and 2007).

In SPIF, the blank surface area where high deformations occur is always close to the current tool location. In the presented technique only a portion of the sheet mesh is refined at the tool vicinity following its motion. Doing so, the requirement of initially refined mesh is avoided and consequently, the global CPU time can be reduced.

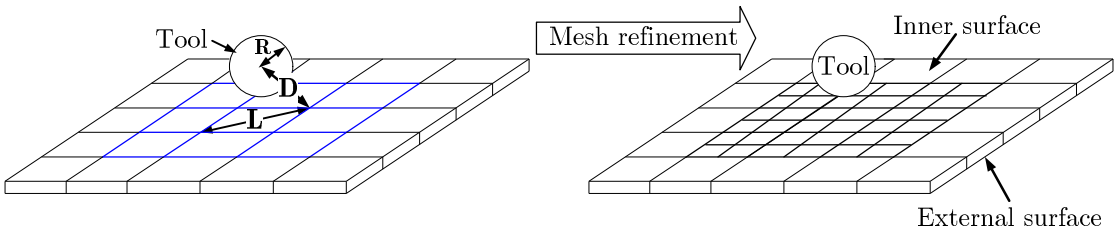

Figure 4.1: Adaptive remeshing procedure.

4.1.1. Refinement Criterion

In the adaptive remeshing procedure, the initial coarse mesh is refined based on a selected refinement criterion. The adopted remeshing criterion for both solid-shell element and its associated contact element is based on the shortest distance between the centre of the spherical tool and the contact nodes applied on the inner surface (see Figure 4.1). The used contact element is described in Habraken and Cescotto (1998). The criterion defining the size of the tool vicinity is given through the expression (Lequesne *et al.*, 2008)

$$D^2 \leq \alpha(L^2 + R^2)\,. \tag{4.1}$$

where D is the shortest distance between the centre of the spherical tool and the element nodes, L is the length of the longest diagonal of the element, R is the radius of the tool and α is the neighbourhood coefficient chosen by the user. This α coefficient defines the size of the tool vicinity. The nodes used as reference to check the criterion condition are the contact element nodes at the top layer of the mesh. The criterion and the list of coarse elements to be refined are performed in LPROXEL2 subroutine (see Appendix A.1). The recommended α value choice is studied in the present chapter and presented in Section 4.3.

4.1.2. Generation of New Nodes

The coarse element which fulfils the criterion (Equation 4.1) is deactivated and becomes a "cell" (storage name for new elements) which contains all information of the new smaller elements. The coarse element is divided into a fixed number of new smaller elements, defined through the number of nodes per edge, n, chosen by the user. Each cell has $(n+2)^2$ nodes, where $(n+2)^2-4$ is the number of new nodes generated. The new nodes are generated as shown in Figure 4.2 and the generation procedure is described below.

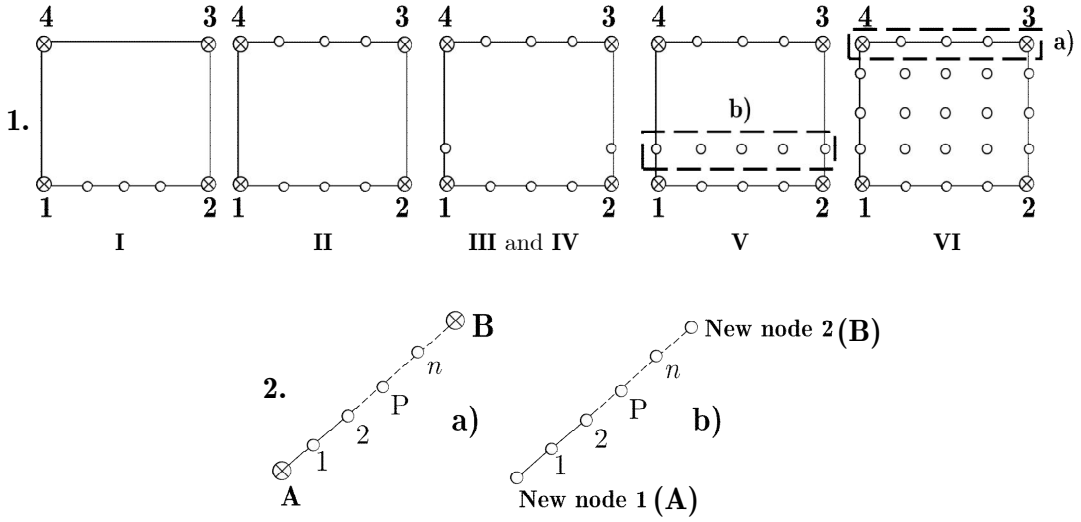

Figure 4.2: Generation of new nodes in element plane.

In the example of Figure 4.2, n was considered to be equal to 3. The steps to generate the new nodes are:

I) the new nodes (n) on the first edge are generated between nodes 1 and 2;

II) a second edge with new nodes (n) is generated between nodes 3 and 4;

III) one node is generated between 1 and 4;

IV) one node is generated between 2 and 3;

V) the new nodes (n) are generated between the last two new nodes of step III and IV;

VI) the steps III, IV and V are repeated for each new node in an equivalent manner.

This procedure is performed over the element plane and repeated for each layer of nodes through the thickness direction. For instance, with a solid-shell element as RESS, it will be always two layers. All nodes are stored in a table size of n+2 lines,

n+2 columns and number of layers, 1 layer for shell element and 2 layers for 8 node element (solid-shell or "brick"). The number of layers defines the table size in the third direction. The FORTRAN language contains 5 different intrinsic types (integer, real, complex, logical, and character) of variables. Additionally, the user can define data objects of different types, known in programming as "derived type". An object of a derived data type is called a structure. Each new node is a "data object" containing: current coordinate positions, last step coordinate position, velocity, acceleration, master list and relative position between the master nodes. The "data object" structure of derived type for each new node is defined into GEST_NEW_NODE module (Appendix A.2). The generation of all nodes within a cell is performed in CONSTRUCT_TAB_NEW_NODES subroutine (Appendix A.3). The generation of the new nodes at an edge of the cell is located between two old nodes, A and B (Figure 4.2.a). The old nodes A and B are stored as master nodes. The relative positions of the old nodes within the storage table, as shown in Figure 4.3, are: node 1) 1, 1; node 2) 1, n+2; node 3) n+1, n+2; node 4) 1, n+2.

Bottom layer

$$\begin{bmatrix} 4 & 4^{new} & 5^{new} & 6^{new} & 3 \\ 17^{new} & 19^{new} & 20^{new} & 21^{new} & 18^{new} \\ 12^{new} & 14^{new} & 15^{new} & 16^{new} & 13^{new} \\ 7^{new} & 9^{new} & 10^{new} & 11^{new} & 8^{new} \\ 1 & 1^{new} & 2^{new} & 3^{new} & 2 \end{bmatrix}$$

Top layer

$$\begin{bmatrix} 8 & 25^{new} & 26^{new} & 27^{new} & 7 \\ 38^{new} & 40^{new} & 41^{new} & 42^{new} & 39^{new} \\ 33^{new} & 35^{new} & 36^{new} & 37^{new} & 34^{new} \\ 28^{new} & 30^{new} & 31^{new} & 32^{new} & 29^{new} \\ 5 & 22^{new} & 23^{new} & 24^{new} & 6 \end{bmatrix}$$

Figure 4.3: Table of nodes with two layers corresponding to an eight node element.

The generation of new nodes in the nodes table (Figure 4.3) is performed layer by layer from the bottom to the top. The new nodes generation between two new nodes (step V) is performed using the positions between both new nodes generated in steps III and IV (see Figure 4.2.b). The global coordinates of each new node, $\mathbf{x}_P$, at each layer of the coarse element are computed by

$$\mathbf{x}_P = \left(1 - \frac{p}{n+1}\right)\mathbf{x}_A + \left(\frac{p}{n+1}\right)\mathbf{x}_B \,, \tag{4.2}$$

where n is the number of new nodes between A and B (Figure 4.2.2.a) or between two new nodes (Figure 4.2.b), p is the index of new number on the segment (see Figure 4.2.a or b), $\mathbf{x}_P$, $\mathbf{x}_A$ and $\mathbf{x}_B$ are respectively the global coordinates of new node p and old nodes A and B or free new nodes 1 and 2. The local coordinate ξ of

each new node at each edge of the coarse element is computed at the same time than Equation 4.2, using the following equation

$$\xi = -1 + \frac{2\,p}{n+1} \tag{4.3}$$

with $\xi_A = -1$ and $\xi_B = +1$. The computation of equations 4.2 and 4.3 are performed in CALCOORD subroutine. The addition of new nodes in the table of nodes is performed layer by layer in AJOUT_NEW_NODES subroutine (Appendix A.4). Figure 4.4 exhibits the schematic representation of new nodes table for 8 node element generated during refinement procedure.

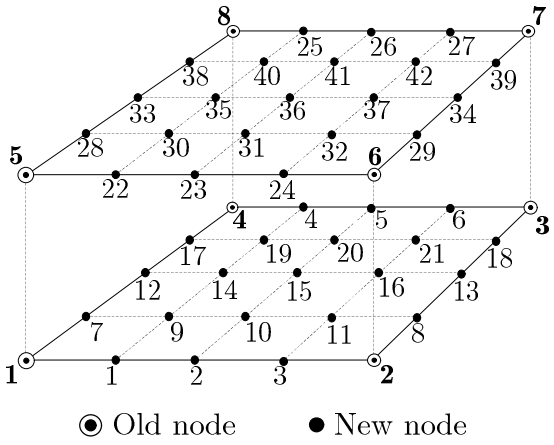

Figure 4.4: Schematic representation of new nodes table for eight node element during refinement.

4.1.3. Generation of New Elements

The element generation procedure from the table of nodes is performed as shown in Figure 4.5. The numbers of lines, columns and layers enable to know the relative position of the node and the node list for each element is generated. As the node list is generated from the table of nodes, each list has its own information associated to the element which belongs. In the module GEST_NEW_ELEM the data object structure of derived type for each new refined element is defined (Appendix A.5). The subroutine CONSTRUCT_TAB_NEW_ELEM generates the table of the new refined elements (Appendix A.6). It assigns the local indices of each new element within the table of elements and gives its global number to each new refined element.

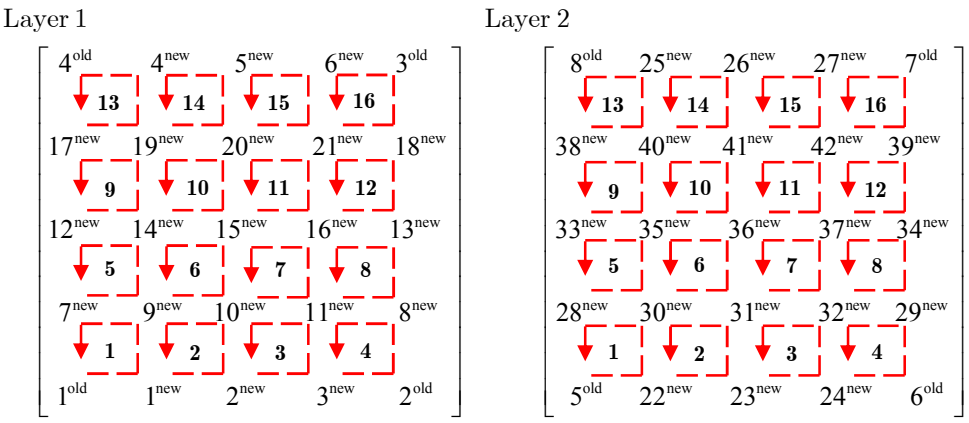

Figure 4.5: New elements list generation from nodes table for eight node elements example.

The subroutine AJOUT_NEW_ELEM adds the information from the nodes table into each corresponding refined element in the list of new elements (Appendix A.7). The first finite elements stored in the list of elements are the solid-shell elements. As the contact element is assembled on the top layer, these are stored afterward, in the following positions.

As mentioned previously the refinement criterion uses only the nodes over the top layer, which belongs to the contact elements. Doing so, the coarse contact element number becomes the future cell identity (identifier number). Based on this choice, any solid-shell element is identified using a pointer (memory allocation), which identifies its number stored in an array of the corresponding contact element. The sequential procedure which geometrically divides a coarse element starts with the coarse solid-shell partition. Subsequently, the contact element partition becomes the top layer of the solid-shell, as can be seen in Figure 4.6.

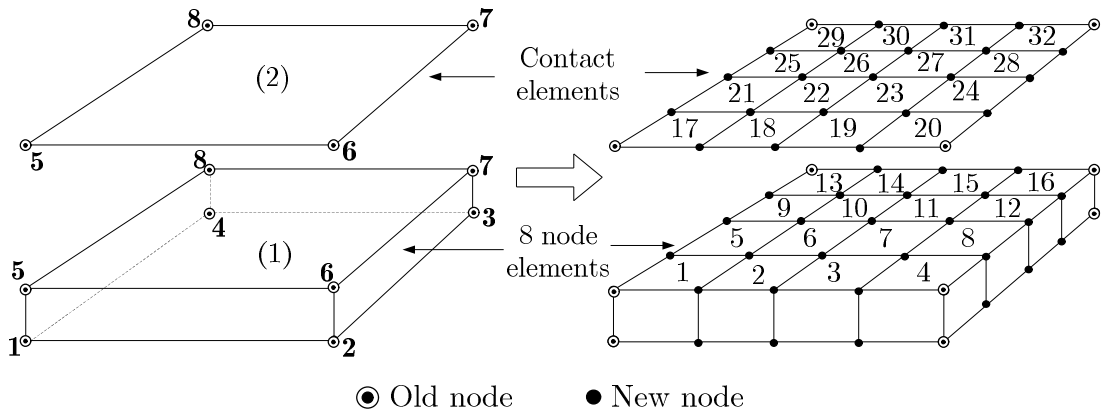

Figure 4.6: Refined elements generation of coarse elements from new nodes table.

4.1.4. Transfer of State Variables and Stress Components

The transfer of stresses and state variables from the coarse element to the new elements is performed using an interpolation method. The transfer data is performed from the integration points in the vicinity of the new integration point which belongs to the new element generated. The integration points at the vicinity can be from coarse and refined elements. The interpolation method chosen is based on a weighted-average formula from the work of Habraken (1989)

$$Z_J = \begin{cases} \dfrac{\sum_K \dfrac{Z_K}{R_{KJ}^N} + \dfrac{CZ_P}{R_{PJ}^N}}{\sum_K \dfrac{1}{R_{KJ}^N} + \dfrac{C}{R_{PJ}^N}} & \text{if} \quad R_{PJ} > R_{min} \\ Z_P \quad \text{if} \quad R_{PJ} \le R_{min} \end{cases} . \tag{4.4}$$

where K are the integration points where the variable Z_K is known, P is the closest integration point to the new integration point J, where the variable Z_P is known, R_{KJ} and R_{PJ}, are the distance between K and J, P and J, respectively, C is an user-defined constant used to amplify the influence of the closest integration point P, N is a interpolation exponent which must be an even number. The choice of this interpolation method was based on past experience, comparing it with other method tested using the line-test benchmark. Although, in Barnichon (1998) and Habraken (1989), other transfer methods have been implemented but the one presented above was the most robust. Figure 4.7 schematically represents the transfer method variables.

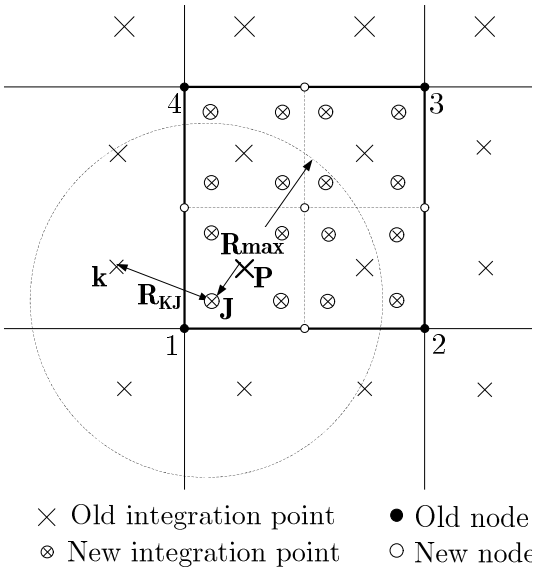

With:

$R_{max} = 1.5d$

$R_{min} = 0.001D$

Figure 4.7: Interpolation method scheme (Habraken, 1989).

All the integration points for which $R_{KJ} > R_{max}$ and the integration points of coarse elements deactivated are not taken into account in the interpolation. After a trial-and-error procedure, the best set of threshold values were found to be: C=5, N=4, $R_{max} = 1.5d$, where d is the highest length of the new element, and $R_{min} = 0.001D$, where D is the highest length of the mesh. The R_{min} value is initially calculated within INIT_ADAPT_REMESH subroutine (Appendix A.8). This transfer method is performed in the INTERPOL_IP subroutine (Appendix A.9) called within the subroutine INTERPOL_ELEM (Appendix A.10).

A similar procedure is performed to interpolate the state variables and the stress components at each integration point of the deactivated coarse element. Those integration points also belong to the set of data and later the state variables and stresses are interpolated from each integration point of the remeshing elements. The interpolation of state variables and stress of the coarse deactivated element is performed to keep it updated for any possible re-activation during the simulation runtime. This procedure is made only at the end of the increment when the convergence is achieved. It is performed using the INTERPOL_ELEM subroutine (Appendix A.10) called within the subroutine ELEMB2, which at this stage only integration points belonging to deactivated coarse elements are interpolated.

4.1.5. Linked List and Cell Management: Addition of a New Cell

During the SPIF process simulation, many elements are refined and coarsened. As a result, many cells are created and removed. A “linked list” is a storage structure of data objects of derived type that are linked together by pointers. It consists of a sequence of objects, with each one containing arbitrary data fields and a reference (“link") pointing to the next object. It allows inserting and removing cells at any point in the list. A cell is an object which has: the coarse element number, the table of edge state, the table of nodes, the table of refined elements and the following pointer. The contact coarse element number is the cell identity (ID) which allows identifying each cell during the simulation runtime. The table of edge state contains the information of the borders of the cell which enables to know if each edge is: free, in common with other cell and in common with an unrefined coarse element. If a cell has common edge with other cell, the nodes along this edge are copied to avoid duplicate. This is performed in AJOUT_ELEM_RAFFIN subroutine (Appendix A.11). The cell structure

definition is performed in the LIST_ELEMENT_RAFFIN module (Appendix A.12). Figure 4.8 exhibits a linked list based on pointers.

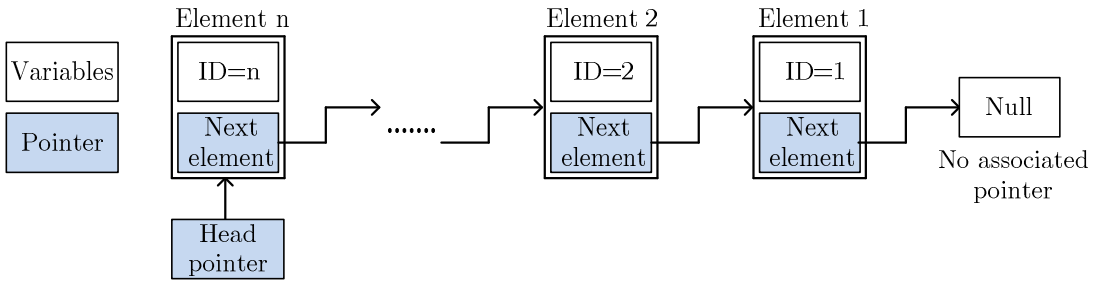

Figure 4.8: Linked list based on pointers.

The head pointer always points to the first cell of the chained list which was the last cell added in the list. The basic concept definition of a generic chained list presents the following structure:

```
MODULE list_module

    TYPE cell_name
        INTEGER                          : ID
        TYPE (cell_name), POINTER        :: next_cell =>NULL()
    END TYPE cell_name

    TYPE(cell_name), POINTER :: head_pointer =>NULL()

END MODULE
```

The head pointer is initially undefined and a special syntax, =>NULL(), is used to initialise it as a dissociated target. It is useful also when the end of the list is reached. It must be guaranteed that the head pointer does not point on a random part in the memory. The head pointer is declared outside of the list structure definition.

The head pointer points to an object inside the list, such as the ID variable:

```
head_pointer%ID
```

or it can point to the next cell:

```
head_pointer%next_cell
```

The dynamic access to a cell requires an additional new pointer. Technically it does the same as the head pointer but the additional pointer is used to dynamically change its target during the runtime. The declaration is local and its definition is analogous:

PROGRAM *list*

USE *list_module*

TYPE(*cell_name*), POINTER :: *additional_pointer*=>NULL()

!or NULLIFY(*additional_pointer*)

END PROGRAM

To start a linked list the additional pointer is referred to head pointer:

$$additional\_pointer => head\_pointer$$

Now the additional pointer can access data of the head pointer, such as the cell ID:

$$additional\_pointer\%ID$$

To access the next cell, the additional pointer is pointed on the head pointer:

$$additional\_pointer => additional\_pointer\%next\_cell$$

From now the additional pointer can access the data in the following cell pointing to the next cell until reach the end of the list. If the additional pointer is not nullified, the pointer should be deallocated to avoid a random position in the memory.

The steps to add a cell in the linked list are: a new cell is generated, the following pointer of the new cell points to the head cell and the head pointer goes to the new cell. Figure 4.9 represents the addition of a new cell into a linked list.

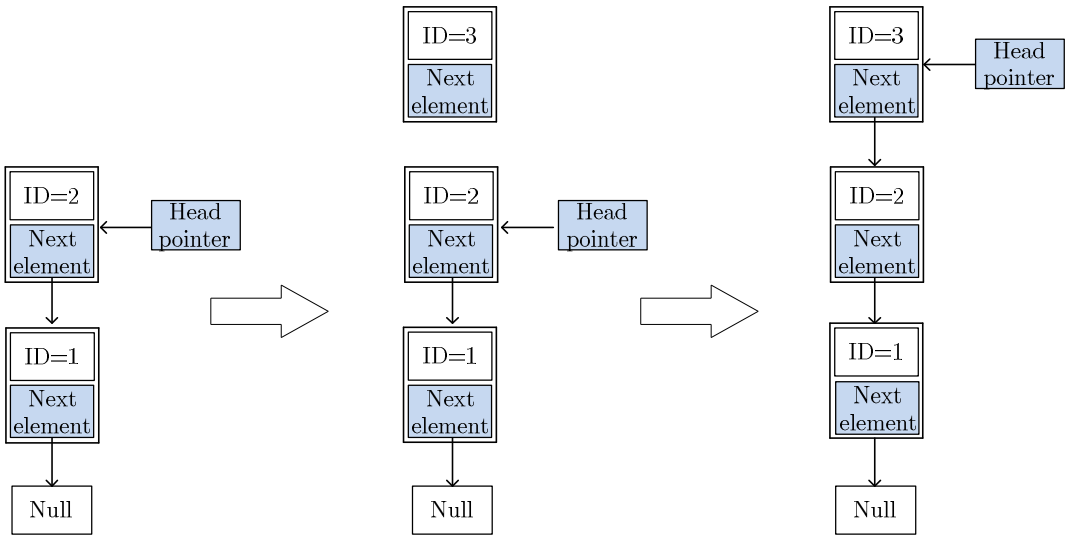

Figure 4.9: Addition of a new cell in the linked list.

The AJOUT_ELEM subroutine is responsible to add the new cell containing refined elements in the chained cell list (Appendix A.13).

4.1.6. Derefinement Indicator

When the tool is far from a refined element and the cell does not respect the neighbourhood criterion, Equation 4.1, the refined elements are removed and the coarse element is reactivated. However, the shape prediction may be less accurate if the new elements are simply removed. Consequently, an additional criterion is used to avoid losing accuracy. This condition is based on the distance, d, between the current position of each new node, $\mathbf{X}_{\mathrm{C}}$, and a virtual position, $\mathbf{X}_{\mathrm{V}}$, as illustrated in Figure 4.10.

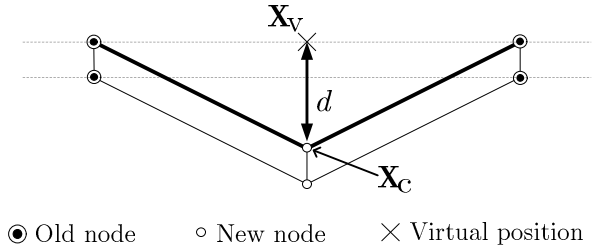

Figure 4.10: Distortion criterion, lateral view.

The virtual position is the coordinates of the new node when it has the same relative position in the plane described by the coarse element. This position is computed by interpolation between the four nodes positions in the element plane, $\mathbf{X}_i$, of the coarse element (see Figure 4.10)

$$\mathbf{X}_{\mathrm{V}} = \sum_{i=1,4} \mathrm{H}_i(\xi,\eta)\mathbf{X}_i \ , \tag{4.5}$$

where H is the interpolation function, ξ and η are the initial relative positions of each new node within the cell, determined by

$$\xi = 2\times\frac{(l\text{-}1)}{(n+1)\text{-}1} \quad \text{and} \quad \eta = 2\times\frac{(c\text{-}1)}{(n+1)\text{-}1} \tag{4.6}$$

where l and c are the new node position within the cell in line and in column, respectively. The criterion for reactivating a coarse element or unrefinement is given by (Lequesne *et al.*, 2008)

$$d \le d_{\max} \quad \text{with} \quad d = \left\| \mathbf{X}_{\mathrm{C}} - \mathbf{X}_{\mathrm{V}} \right\| , \tag{4.7}$$

where $d_{\max}$ is the maximum distance value chosen by the user. If the criterion is not respected for a single node ($d > d_{\max}$), it means that the mesh distortion is

significant and the refinement remains on the location of the coarse element. Then, the coarse element is not reactivated and remains the cell with refined elements. The element nodes used as reference to verify the distortion criterion are the new nodes of the refined contact element over the top layer of the mesh. As some nodes are removed, to avoid gaps in the mesh numbering, all nodes inside the cells are renumbered from the removed nodes. This is performed at the subroutine named RENUM_CELL_NOD (Appendix A.14).

4.1.7. Removing a Cell

Assuming that a cell of elements is deleted from the chained linked list and the coarse finite element is activated, the common edges with the removed cell are marked. The nodes not common are stored in a linked list of nodes to be removed. The steps to remove a cell are: firstly, the pointer which indicates the target cell (head pointer or a previous cell pointer) is searched. Secondly, the pointer which refers to the target cell also points to the following cell and finally, the target cell is removed by deallocation of the memory. This is performed in RETRAIT_ELEM_RAFFIN subroutine (Appendix A.15) and the subroutine RETRAIT_ELEM is responsible for the cell deallocation procedure (Appendix A.16). Figure 4.11 illustrates the removal procedure of an arbitrary cell from a chained linked list.

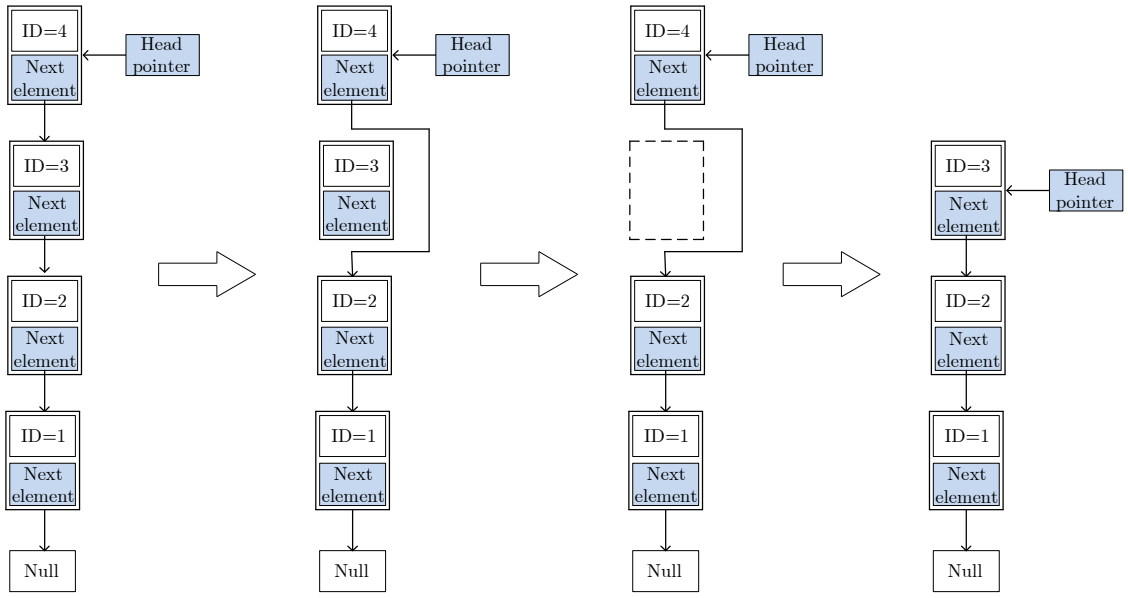

Figure 4.11: Removing a cell from the chained linked list.

4.1.8. Constrained Nodes: Master-Slave Method

During the simulation, selected cells of refined elements are removed (step 1 of Figure 4.12) in case of mesh unrefinement. This remeshing method creates selected nodes that are incompatible with the coarse (non-refined) finite element with common edges. As the current approach does not take into account any transition zone between coarse and fine elements, there are four types of nodes: old nodes, master nodes, free new nodes and constrained new nodes. The nodes which belong to a cell edge in common with a removed cell or with an unrefined coarse element become constrained nodes (step 2 of Figure 4.12), also called as slaves nodes. The constrained nodes are used to allow the structural compatibility of the mesh. The degrees of freedom and positions of the slave nodes on a "cell" edge depend on the two old master-nodes, which are extremities of this edge. The new slave-nodes can have a different position from the initial relative position between the two old nodes (masters) because they were free before. Doing so, new relative positions are computed based on the intersection of the segment between the two master nodes, 1) and 2) (see Figure 4.12). Figure 4.12 schematically represents the slave node generation during unrefinement occurrence.

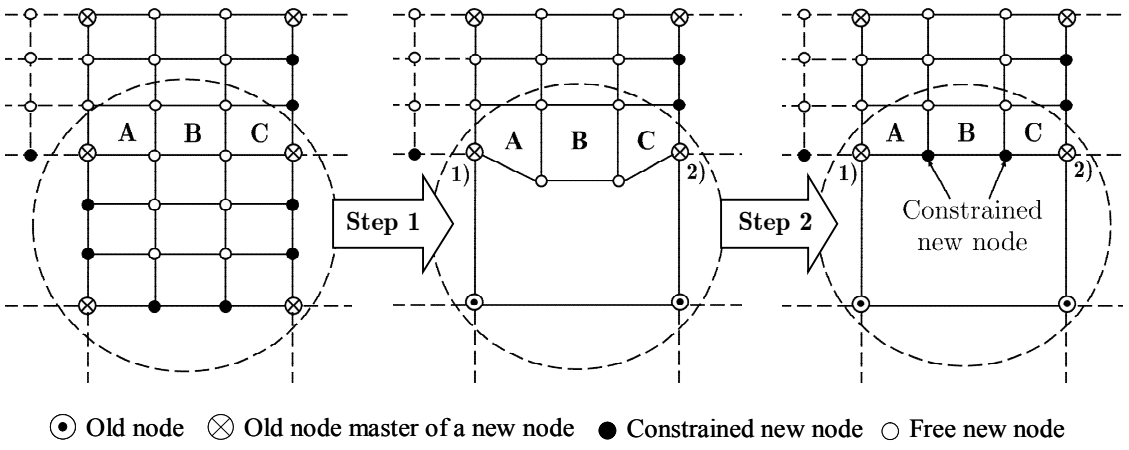

Figure 4.12: Constrained new nodes generation during the mesh unrefinement.

The constrained nodes must remain at the same relative positions between the two master nodes and the elements A, B and C have a new shape (step 2 of Figure 4.12). Consequently, the global list of degrees of freedom (DOF) is modified. The DOF of the slave nodes are replaced with the master DOF which belongs to a common edge. If the master nodes have fixed DOF and the new node belongs to a

common edge, its DOF becomes fixed. There are two types of DOF $\mathbf{q}$, either unconstrained, $\mathbf{q}_\mathrm{f}$ (free), or constrained, $\mathbf{q}_\mathrm{s}$ (slave)

$$\mathbf{q} = \begin{bmatrix} \mathbf{q}_\mathrm{f} \\ \mathbf{q}_\mathrm{s} \end{bmatrix}. \tag{4.8}$$

The constrained DOF which belong to the slave nodes are computed in function of unconstrained DOF

$$\mathbf{q}_\mathrm{s} = N\mathbf{q}_\mathrm{f} \quad \text{with} \quad N = 0.5\times(1\pm x)\,, \tag{4.9}$$

where N is an interpolation function. Based on master-slave method used (Driessen, 2000), Equation 4.8 can be rewritten without $\mathbf{q}_\mathrm{s}$

$$\mathbf{q} = \mathbf{A}\mathbf{q}_\mathrm{f} \quad \text{with} \quad \mathbf{A} = \begin{bmatrix} \mathbf{I} \\ \mathbf{N} \end{bmatrix}\,, \tag{4.10}$$

where $\mathbf{I}$ is an identity matrix applied to unconstrained nodes and $\mathbf{N}$ matrix contains the interpolation function, N, applied to each constrained DOF of the slave nodes.

The virtual power principle combining slave and free DOF is

$$\tilde{\mathbf{q}}^\mathrm{T}\mathbf{K}\mathbf{q} = \tilde{\mathbf{q}}^\mathrm{T}\mathbf{f}\,, \tag{4.11}$$

where $\mathbf{K}$ is the stiffness matrix and $\mathbf{f}$ is the equilibrium forces array, $\tilde{\mathbf{q}}$ is a virtual DOF. As the free virtual degrees of freedom follow the same relationship as Equation 4.10, Equation 4.11 becomes

$$\mathbf{q}_\mathrm{f}^\mathrm{T}\mathbf{A}^\mathrm{T}\mathbf{K}\mathbf{A}\mathbf{q}_\mathrm{f} = \tilde{\mathbf{q}}_\mathrm{f}^\mathrm{T}\mathbf{f}\,, \tag{4.12}$$

The variable number of DOF induces a modification in the force equilibrium and in the stiffness matrix

$$\tilde{\mathbf{q}}_\mathrm{f}^\mathrm{T}\mathbf{K}_\mathrm{f}\mathbf{q}_\mathrm{f} = \tilde{\mathbf{q}}_\mathrm{f}^\mathrm{T}\mathbf{f}_\mathrm{f} \quad \text{with} \quad \begin{cases} \mathbf{f}_\mathrm{f} = \mathbf{A}^\mathrm{T}\mathbf{f} \\ \mathbf{K}_\mathrm{f} = \mathbf{A}^\mathrm{T}\mathbf{K}\,\mathbf{A} \end{cases}. \tag{4.13}$$

where $\mathbf{f}_\mathrm{f}$ is the forces equilibrium array and $\mathbf{K}_\mathrm{f}$ is the stiffness matrix of the unconstrained DOF. This computation is performed in ADD_F_AK_MASTERS subroutine (Appendix A.17) called within the element loop (subroutine ELEMB) to compute stress, nodal forces and stiffness matrix.

4.1.9. Boundary Conditions

A constrained node is an object stored into a nodes master list defined into the module named GEST_SLAVE (Appendix A.18). The table of constrained nodes is constructed in NEWCONEC subroutine (Appendix A.19). All new nodes which belong to the edges in common with a non-refined (coarse) element become slave being its master list and relative position saved in the data object of each refined cell.

In the subroutine named NEWELEM (Appendix A.20), the list of DOF is modified, in which the slave degrees of freedom are replaced by the master DOF. The matrix **A** (see Equation 4.10) is computed in this subroutine according to the master list and the relative position of the master nodes. The imposition of the constrained DOF is performed in the subroutine IMPSLAV (Appendix A.21). It is called after the imposition of the displacement at the step beginning and updated at each iteration after the resolution of the equation system, before the next iteration until achieve the convergence of the step.

Just the main subroutines were mentioned in the sections description above. All subroutines directly involved in the adaptive remeshing procedure combining RESS coupled with contact element CFI3D within LAGAMINE in-house code are schematically presented in Appendix A. It includes the link between subroutines and a small description for each subroutine.

4.1.10. Storage Array Update of LAGAMINE

At each equilibrium state (end of the increment when convergence of forces and displacements are reached), the linked list input variables is updated. It is performed in the subroutine called UPDATE_ELEMENT_RAFFIN (Appendix A.22). The principal advantage of a linked list compared to a conventional array is that the order of the linked items can be different from the order used to store the information in the memory. This property allows reading in a different order the list of cells.

The arrays which depend on the number of nodes identification, elements and DOF are modified or updated due to the adaptive remeshing procedure during the simulation runtime. This procedure is performed through the module called GEST_DYNAMICS_STORAGE_STRUCTURES which enables the dynamic

allocation update of variables within the code in runtime. If there are some modifications, addition or removing, of a cell in the chained linked list, the arrays of LAGAMINE code are reallocated and modified according to the linked list. One of the main storage arrays of LAGAMINE code is called SIGVA. It stores all the state variables and stress components of each element of the mesh during the simulation runtime.

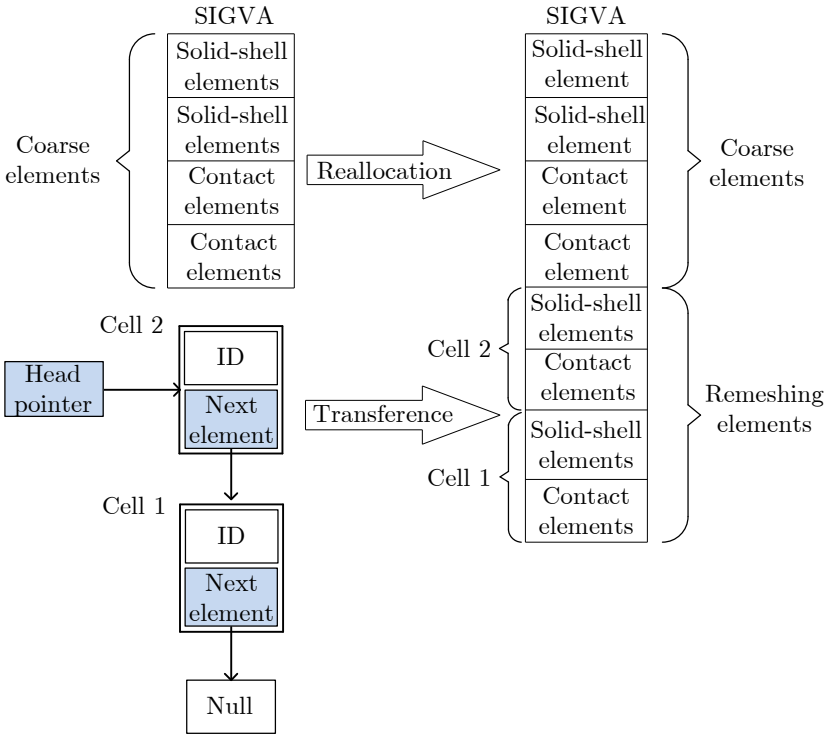

Figure 4.13: Storage array (SIGVA) update of LAGAMINE code.

The storage sequence within SIGVA array is exhibited in Figure 4.13. Firstly the solid-shell coarse elements data are stored (stresses, state variables, coordinates) then the contact coarse elements data from the initial mesh follow. Subsequently, the refined elements of each cell are stored. The transfer from each cell of refined elements to the SIGVA array starts with the last cell added in the chained linked list. Similarly, the sequence of stored elements begins with the refined solid-shell elements and then the refined contact elements. This storage sequence of elements is repeated for each cell of the chained linked list until they became not associated.

The reallocation involves resizing the initial storage arrays. The subroutines employed are:

- REDIM_STRUCTURE_NUMNP for arrays which depend on number of nodes;

- REDIM_STRUCTURES_NELEM for arrays which depend on number of elements. It updates the structure dimension and computes the new number of state variables to update SIGVA array dimension for the new finite element addition from remeshing procedure;
- REDIM_STRUCTURES_NEQUA for arrays which depend on number of degrees of freedom.

The transfers from the cells linked list to the LAGAMINE array are performed by the subroutines:

- NEWCONEC for arrays which depend on number of nodes;
- NEWELEM for arrays which depend on number of elements;
- NEW_STRUCTURE_NEQUA for arrays which depends on number of degrees of freedom.

4.1.11. Mesh Renumbering

The new nodes addition can significantly increase the global stiffness matrix size. Consequently, number of DOF computation can strongly increase. The node renumbering can tackle this problem. The renumbering is performed in RENUMB module. Two renumbering methods are available: seed method and directional method. The method chosen for remeshing elements was the directional method.

4.1.11.1. Seed Method or oil spot

The identification of the connection table between nodes is performed by CONECT_NODE subroutine. The first node is chosen to be the first node of the renumbering. The connected nodes are the next ones in the renumbering. Then the nodes connected to these nodes are added. The effect on the bandwidth depends on the choice of the first node. It is more efficient to choose the node where the mesh is refined. Usually, the closest node to the tool is chosen as the first node.

4.1.11.2. Directional Method

Nodes are ranked according to the direction in which the mesh has the greatest number of nodes. If some nodes have the same position in this direction, they are ranked according to the second direction in which the mesh has the greatest number of nodes. The ranks of the directions are an input chosen by the user from the adaptive remeshing input file (*.ari).

4.2. Working Procedure in LAGAMINE Code

In general, the adaptive remeshing parameters controlled by the user are: α coefficient, number of nodes division per edge (n) and $d_{\max}$ value. Their influences in the numerical simulation results are analysed in Section 4.3. Figure 4.14 shows the schematic flow chart of adaptive remeshing procedure inside LAGAMINE code.

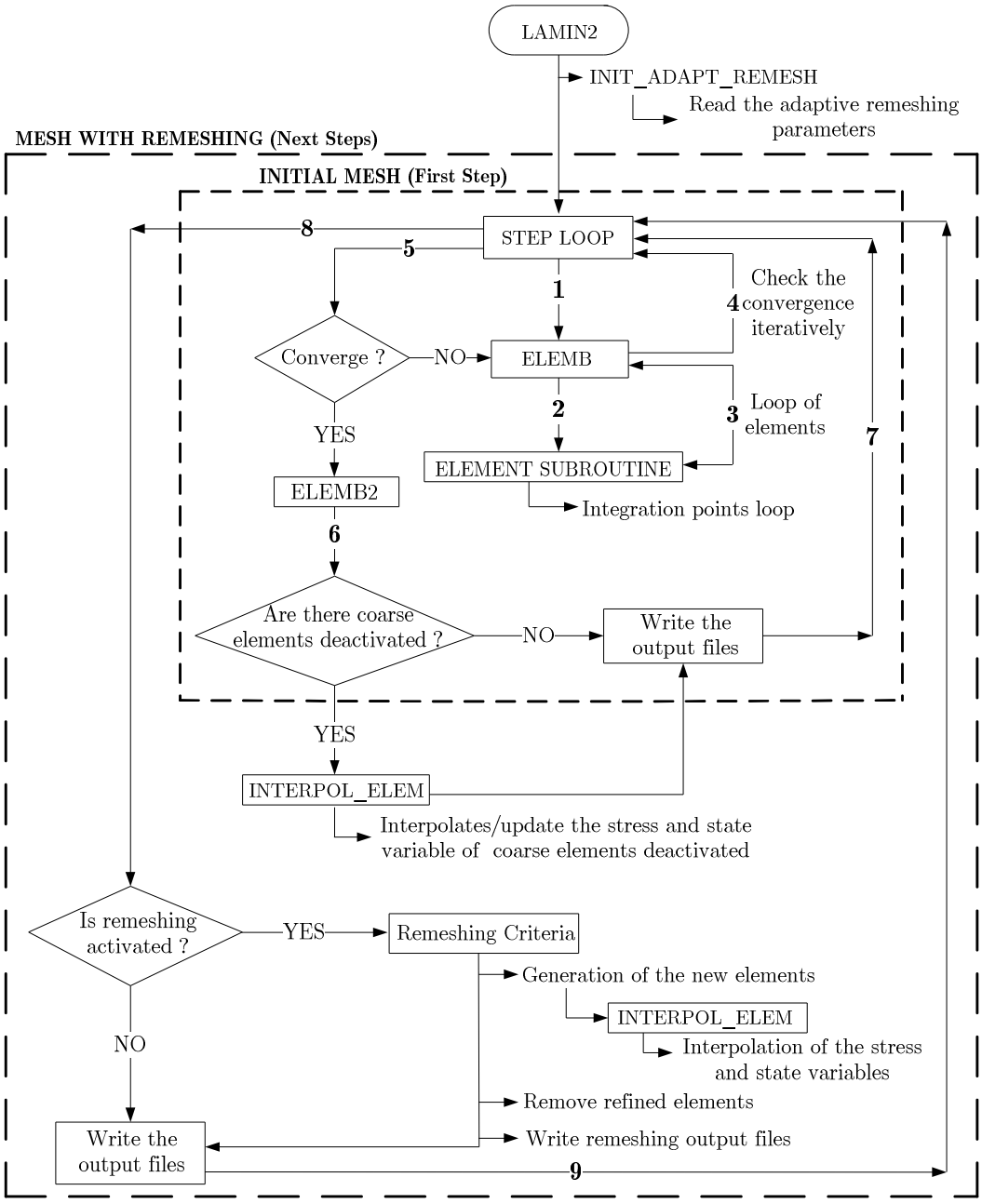

Figure 4.14: Flow chart of adaptive remeshing procedure in LAGAMINE in-house code.

Notice that at the first step all coarse elements are activated. The mesh is updated at the end of a converged step (which means beginning of next step), performing all the methodology previously described in Section 4.1. Afterward, iteratively the new mesh equilibrium is assessed until achieve the step convergence.

4.3. Line Test Benchmark: Numerical Simulation

In this section, a simple test is used to assess the adaptive remeshing parameters combined with RESS formulation described in the previous sections.

The test is based on the work of Bouffioux *et al.* (2008a). It consists of a line test using a SPIF machine where a square metallic sheet, with an initial thickness of 1.2 mm and clamped along its edges, is plastically deformed. The spherical tool radius is 5 mm. The friction coefficient between the tool and the sheet is assumed to be equal to 0.05, and penalty coefficients, K_P, K_τ, are 1000. The different stages of the experimental test are schematically illustrated in Figure 4.15.

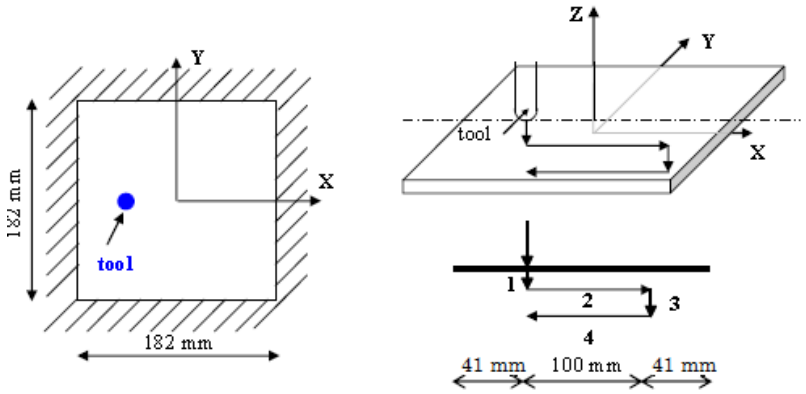

Figure 4.15: Schematic description of the experimental setup (Bouffioux *et al.*, 2008a).

The complete tool path is composed by five steps with an initial tool position tangent to the sheet surface: starting with an indentation of 5 mm (step 1), a linear motion at the same (constant) depth along the X axis occurs (step 2). After that, a second indentation takes place, down to the depth of 10 mm, relatively to the initial position (step 3). Then, a new linear motion (now backwards along the X axis) is imposed, again at a constant depth (step 4), and finally an unloading stage (step 5, not shown in the picture) occurs and brings the tool to its initial position.

The material chosen for the sheet is an AA3003-O. The material behaviour is elastically described by E = 72600 MPa and $\nu = 0.36$. The hardening parameters

for the plastic range are described by Swift's law. The material parameters set and the constitutive law used in the present work were selected as optimal ones from the work of Henrard *et al.* (2010), for 3D solid finite elements (see Table 4.1).

Table 4.1: Constitutive parameters for an AA3003-O (Henrard *et al.*, 2010).

Hardening type	Hill parameters	Swift parameters
Isotropic	F=1.224; G=1.193; H=0.8067;	K=183; n=0.229;
hardening	N=L=M=4.06	ε_0=0.00057

The relevance of this test resides in the fact that it generates a stress history and a strain path similar as the ones present in incremental forming. However, a step down of 5 mm is strongly higher than in typically incrementally formed components.

The purpose of the next section is to search the optimal adaptive remeshing parameter values, in order to use them in future SPIF numerical simulations with the proposed adaptive remeshing technique.

4.3.1. Sensitivity Analysis of Remeshing Parameters

The present section provides the analysis of adaptive remeshing parameters which allow the best approximation of the experimental measurements. The main numerical outputs presented in this section are related with the final shape of the sheet, the cross-section along the symmetry axis and the evolution of the tool force. The forming forces (reaction force on the spherical tool) and the deformed shape come from the experimental analysis of Bouffioux *et al.* (2008a). These results will be considered as the reference data in the following sections, to be compared against the numerical results of FE simulations

To assess the influence of the number of integration points along the thickness direction, numerical simulations were carried out with RESS finite element, as similarly presented in the work of Sena *et al.* (2011). The obtained results showed no variation concerning the different number of integration points adopted (for a range from 3 to 10 points). This is possibly due to the deformation mechanism present, dominated by membrane components even if bending is present. The number of integration points through the thickness chosen for the current work is 5 Gauss points (GP).

Figure 4.16 illustrates two distinct mesh refinements and only half of the sheet model is considered applying symmetry boundary conditions. The initial refined mesh is composed by 806 solid-shell elements disposed in one layer in the thickness direction. The coarse mesh used with adaptive remeshing method is composed by 72 elements on the sheet plane with one layer of solid-shell elements in the thickness direction. The nodes at the top layer of both meshes define the contact element layer at the surface. The contact modelling is based on a penalty approach at each integration point and on a Coulomb's law (Habraken and Cescotto, 1998). Finally, the initially refined (reference mesh) and the coarse meshes have two layers of elements (the solid-shell and the contact elements) in the thickness direction, i.e., the total number of elements is 1612 and 144 elements, respectively.

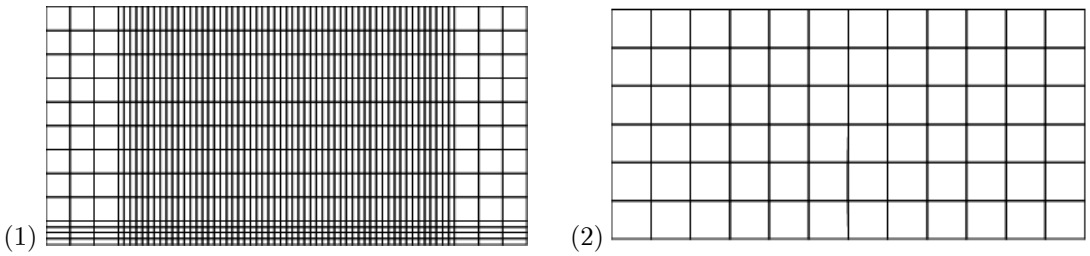

Figure 4.16: Reference mesh (1) and coarse mesh (2) used with adaptive remeshing.

The following results are based on the computation of the errors between the experimental measurements and the numerical predictions. The influences of adaptive remeshing parameters are evaluated for the final shape, the CPU time and the reaction force of the tool. The force error is determined during the tool loading stages of the forming, as shown in Figure 4.15.

Numerous simulations were performed to verify the parameter influence in the numerical results. Different values for each parameter were tested such as derefinement distance ($d_{\max}$) as well the vicinity size (α): $d_{\max}$ values were 0.005 mm, 0.05 mm, 0.1 mm and 0.2 mm and α coefficient values were 0.1, 0.6, 0.8 1.0 and 1.6. The value of n (number of nodes inserted in one edge) adopted was 3, from preliminary tests using the line-test benchmark compared with reference mesh.

The final choices are based on the parameter values which allow less accuracy error for each combination of adaptive remeshing parameters. The relative error average is computed using the following expression:

$$Error(\%) = \left[\left(\sum_{i=1}^{N} \left(\sqrt{(Num. - Exp.)^2 / Exp.^2} \right) \right) / N \right] \times 100 \tag{4.14}$$

where *Num.* is the numerical value of a chosen variable, *Exp.* is the corresponding experimental value and N is the number of comparison points in X axis (Figure 4.15). The difference between the numerical value and the experimental one is computed for the common abscise values, X axis presented in Figure 4.15. The numerical values in the X axis were linearly interpolated to match the corresponding X values of experimental measurements.

The following graphs exhibit the sensitivity of the results for different combination values between α coefficient and $d_{\max}$ parameter using the line test benchmark.

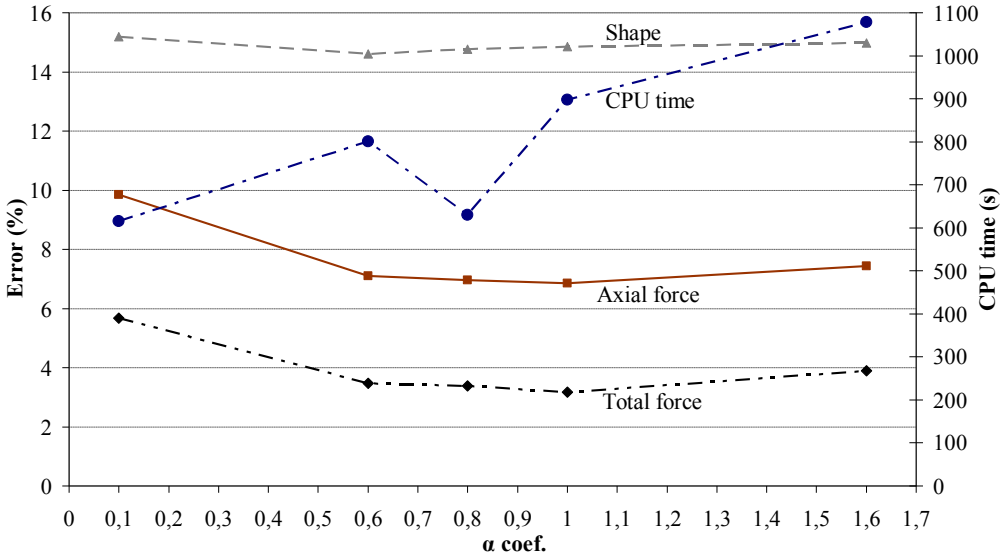

Figure 4.17: CPU time and error sensitivity of forces and shape prediction for $d_{\max}$ equal to 0.2 mm.

Increasing the value of α coefficient with $d_{\max}$ equal to 0.2 mm (Figure 4.17), the error of force prediction tends to decrease with more significance than the shape error. In terms of CPU performance, generally the time increases but there is an exception when the α coefficient is equal to 0.8. Increasing the value of the α parameter, the number of generated new elements increases during the remeshing procedure, and consequently, the CPU time increases. However, the adaptive remeshing parameters affect also the convergence performance during the simulation. This is due to the fact that the number of iterations performed decreases when the mesh is refined and it directly reduces the simulation time. For instance, α equal to 0.8, which allows more accurate force or shape prediction, has similar CPU time compared with α equal to 0.1, which allows the generation of a smaller number of elements during the adaptive remeshing method.

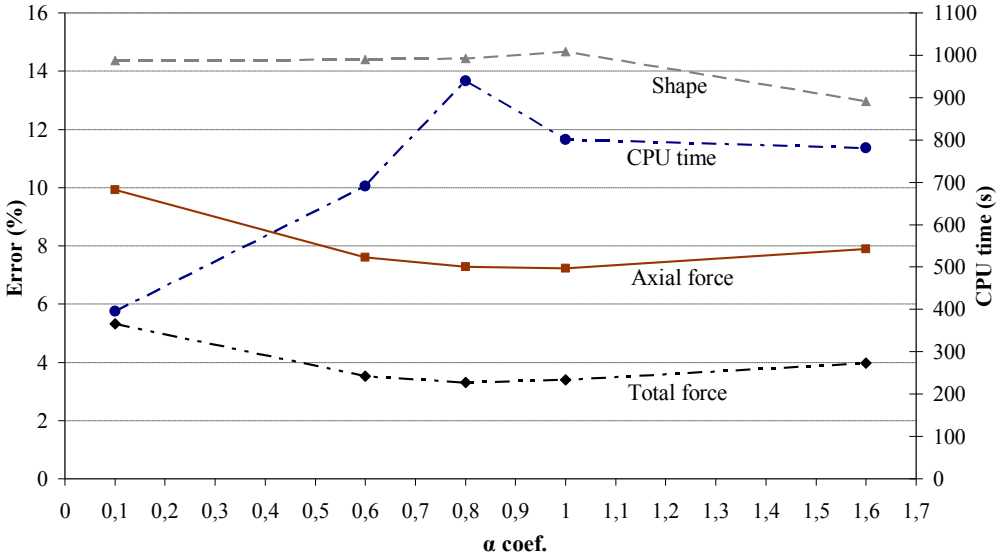

Figure 4.18: CPU time and error sensitivity of forces and shape prediction for d_{max} equal to 0.1 mm.

When $d_{\max}$ parameter is equal to 0.1 mm (Figure 4.18), the force error decreases when the value of α coefficient increases until α value equal to 1 which enables the lowest error. The error concerning the shape prediction decreases with α parameter higher than 1.0. In terms of CPU time, generally the time increases for increased α values. In Figure 4.18, the combination of α value equal to 0.8 and $d_{\max}$ equal to 0.1 mm, the CPU time has an opposite behaviour in comparison with previous results of $d_{\max}$ equal to 0.2 presented in Figure 4.17. However, the error of the numerical results are being influenced by experimental data, in terms of the opposite behaviour of shape prediction in comparison with force prediction.

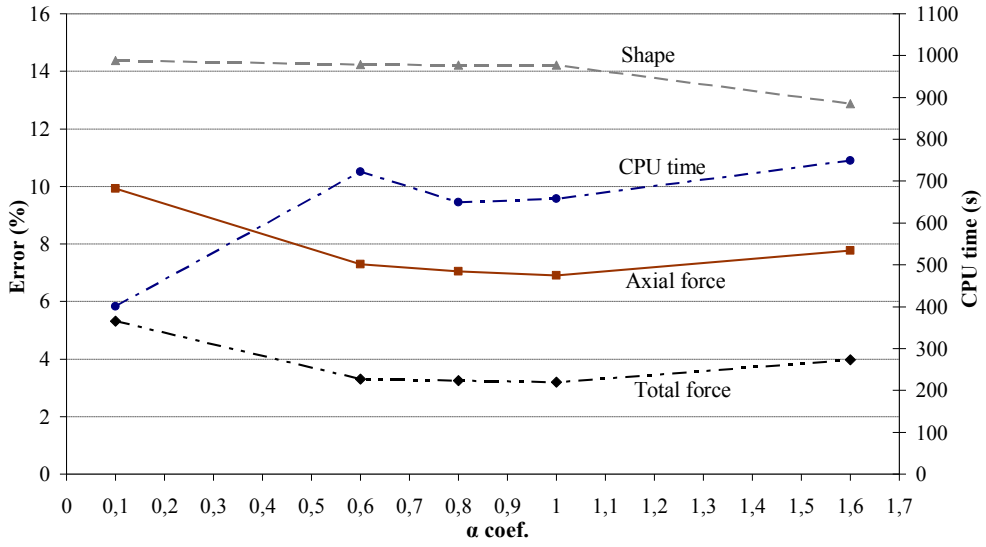

Figure 4.19: CPU time and error sensitivity of forces and shape prediction for d_{max} equal to 0.05 mm.

When d_{max} is equal to 0.05 mm (Figure 4.19), the values of the α parameter which gives the lowest error, in terms of force prediction, are between 0.6 and 1.0. The error determination for the shape prediction decreases for α value higher than 1. The CPU time has the tendency to increase with the α coefficient. However, at the intermediate values of the α parameter (0.8 and 1.0), the CPU time is lower than with α value equal to 0.6, showing again an effect of convergence efficiency related to specific values of remeshing parameters.

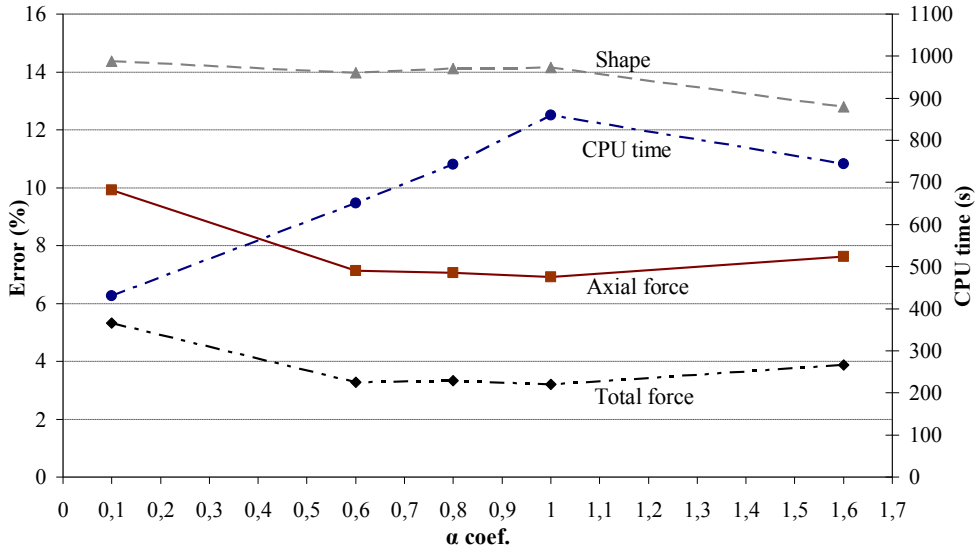

Figure 4.20: CPU time and error sensitivity of forces and shape prediction for d_{max} equal to 0.005 mm.

Figure 4.20 demonstrates similar results as the previous ones using d_{max} equal to 0.005 mm, which nearly prevents any derefinement. These simulations should be the most accurate for shape, however they demonstrate that the shape error value stabilizes for all values of d_{max} lower than 0.2 mm, as similar shape errors were reached. The CPU time seems to be quite stable (d_{max} = 0.05 mm) or to decrease (d_{max} =0.1 mm; 0.005 mm) when α value is higher than 1.0 combined with d_{max} values lower than 0.2 mm. The common aspect in all results is that the average error for total force prediction is lower than the average error of axial force. The load in axial direction (Z axis) can be influenced by high accuracy of tangential forces, in X and Y directions (Figure 4.15), and its values remain stabilized for the same values of α parameter.

The following figures exhibit the adaptive remeshing parameters sensitivity on the CPU time, the error on the force and shape predictions in a different perception manner. The error is exhibited in the following figures in function of d_{max} values for different α coefficients.

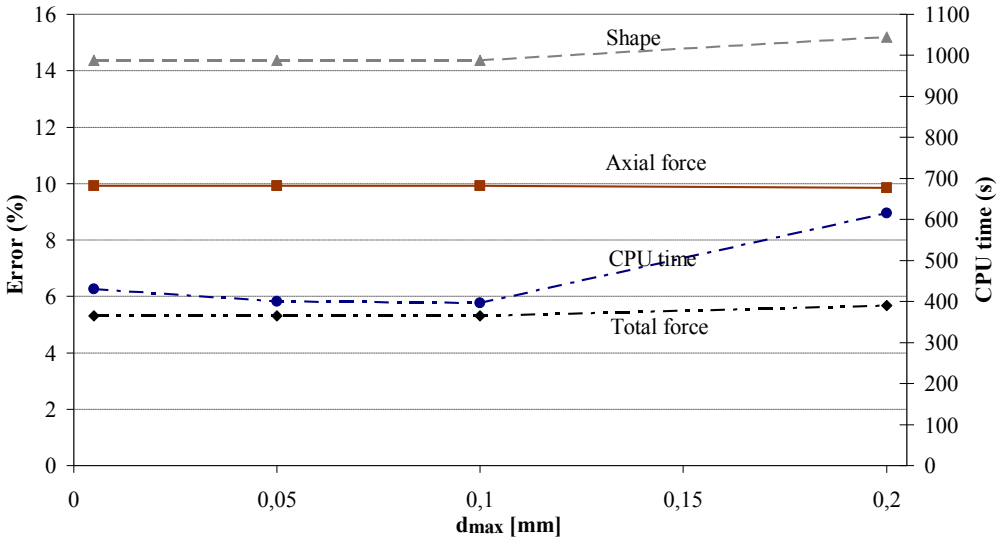

Figure 4.21: CPU time and error sensitivity of forces and shape prediction for α coefficient equal to 0.1.

The combination of α coefficient equal to 0.1 with different $d_{\max}$ values (Figure 4.21) induces higher error than the previous values chosen in the prediction of axial force and total force. In contrast, CPU time needed to perform the simulation decreased. With low value of α coefficient, the mesh area of refinement is small. Consequently, the number of coarse elements included in the refinement is minimal, as the total number of elements.

Analysing Figure 4.22, Figure 4.23 and Figure 4.24 for α values ranging from 0.6 to 1.0, it is verified that the error prediction of shape, axial force and total force are analogous with negligible difference between each parameters set. The only differentiation is the CPU time spent to perform each simulation.

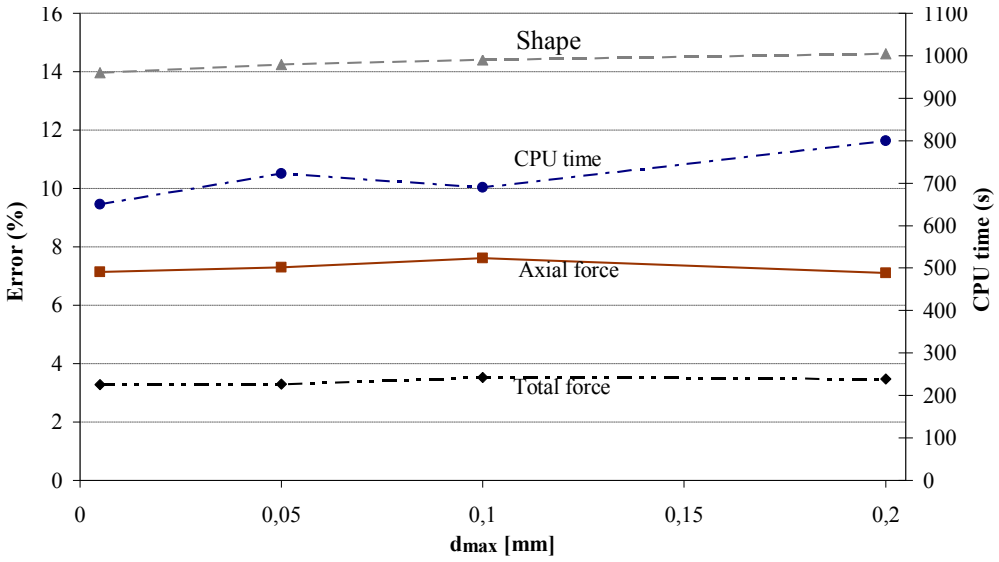

Figure 4.22: CPU time and error sensitivity of forces and shape prediction for α coefficient equal to 0.6.

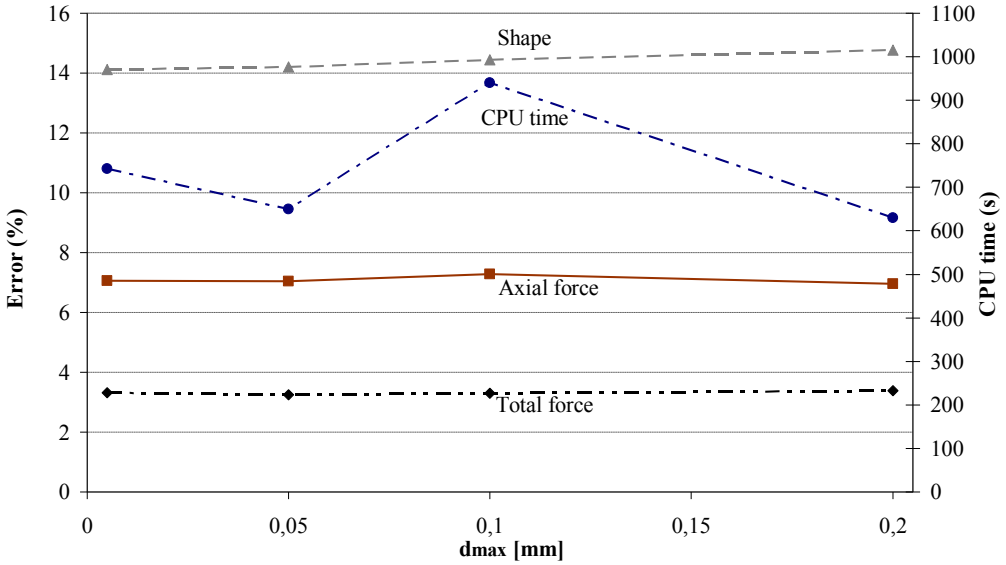

Figure 4.23: CPU time and error sensitivity of forces and shape prediction for α coefficient equal to 0.8.

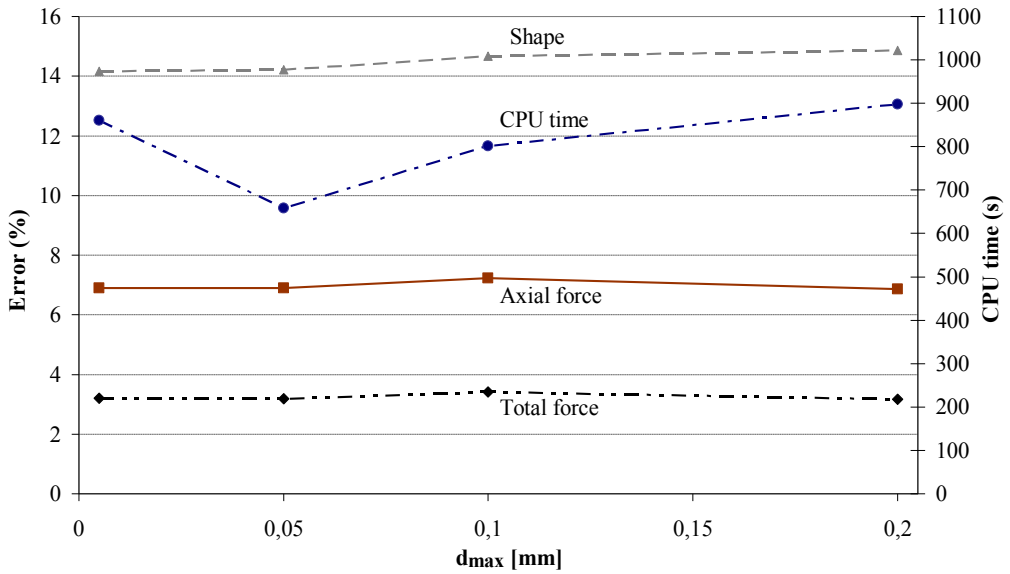

Figure 4.24: CPU time and error sensitivity of forces and shape prediction for α coefficient equal to 1.0.

Figure 4.25 presents distinct values of error prediction for shape, axial force and total force in comparison with the combination sets exhibited above, Figure 4.21 to Figure 4.24. The error of shape prediction is lower than with the previous parameters combination. The adaptive remeshing parameters which present the lowest shape prediction error is α coefficient equal to 1.6 combined with $d_{\max}$ value lower or equal to 0.1mm. Using α coefficient equal to 1.6 combined with $d_{\max}$ value equal to 0.2mm, the shape error is comparable as the previous results. However, the axial force prediction and total force prediction show higher error in relation to numerical results obtained previously.

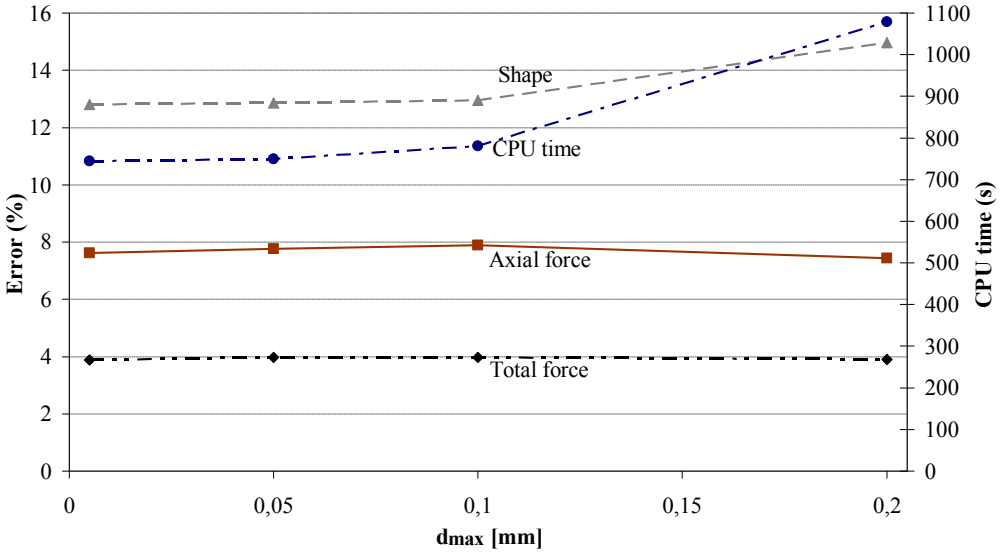

Figure 4.25: CPU time and error sensitivity of forces and shape prediction for α coefficient equal to 1.6.

In general, the choice of adaptive remeshing parameters values for α coefficient has more effect on the force prediction than the $d_{\max}$ parameter. Analysing the shape prediction error of all figures in function of $d_{\max}$ parameter, it is verified that this result is more sensitive to $d_{\max}$ than to α coefficient. The simulation performance is affected by the adaptive remeshing parameters using different combination values for $d_{\max}$ and α parameters. A combination of a high α coefficient with small value of $d_{\max}$ parameter allows a huge number of new remeshing elements at the end of the simulation. However, in the particular case of line-test benchmark it does not mean that the simulation is slower due to the better convergence and the decrease of number of iterations per step (increment) in the FE analysis.

Figure 4.26 illustrates the number of elements and nodes evolution during the adaptive remeshing procedure. The adaptive remeshing parameters chosen were: α coefficient is equal to 1.6, $d_{\max}$ parameters equal to 0.2mm and n equal to 3 nodes per edge.

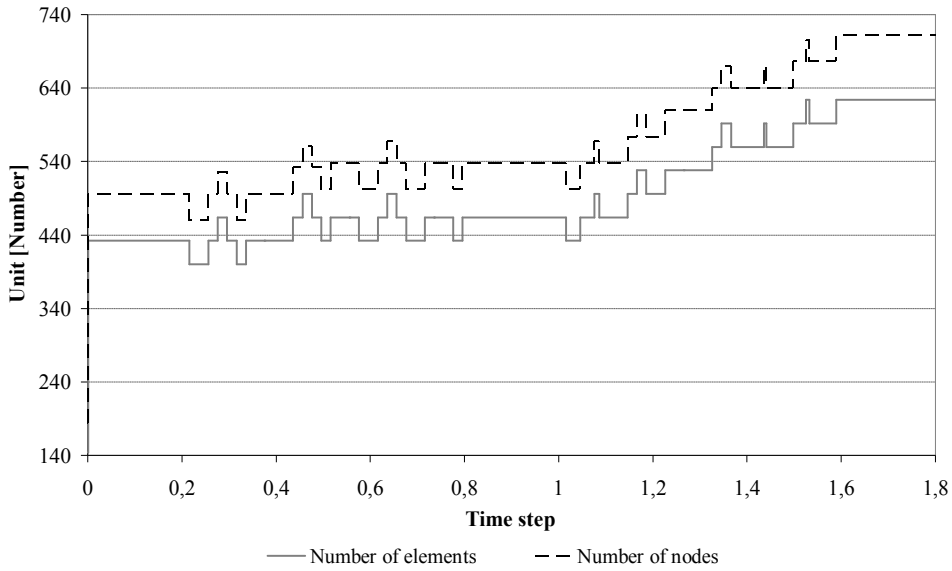

Figure 4.26: Evolution of number of elements and nodes during the adaptive remeshing procedure.

The minimum number of elements and nodes are 144 elements and 189 nodes, respectively (only at the beginning of the simulation). The number of elements and nodes varies during the tool motion. When the step 4 (see Figure 4.15), between time steps 1.0 and 1.6, the number of elements increase due to the higher level of mesh distortion ($d_{\max}$). Figure 4.27 presents the final number of elements for each combination of α with $d_{\max}$ parameters for a constant number of nodes divisions per edge (n) equal to 3.

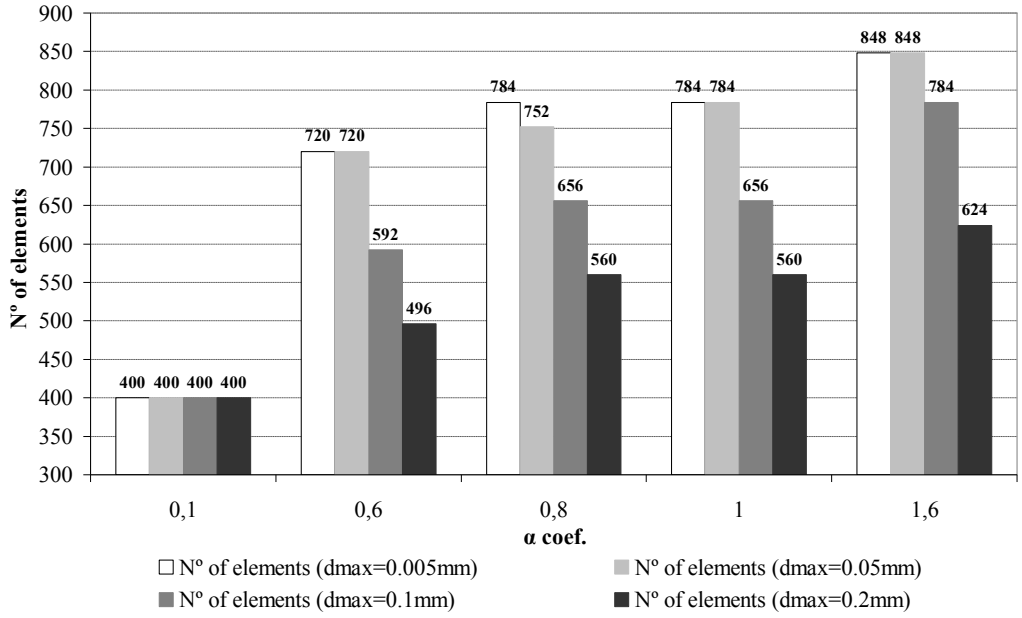

Figure 4.27: Final number of elements for different pair combination of remeshing parameters.

As mentioned, $d_{\max}$ equal to 0.05 mm or equal to 0.005 mm presents similar results even for the final number of elements. Exceptionally with α equal to 0.8 the final number of elements is different for both values chosen for $d_{\max}$ parameter. However, Figure 4.27 demonstrates that the $d_{\max}$ parameter has an influence on the final number of elements.

Table 4.2 shows the performance for different adaptive remeshing parameters selected from the previous results and reference mesh (initial mesh refinement without remeshing).

Table 4.2: Average error of shape and force prediction.

Adaptive remeshing	Total force error (%)	Axial force error (%)	Shape error (%)	CPU time (s)
$\alpha = 1.0$; $d_{\max} = 0.05$mm	3.192	6.899	14.218	658.176
$\alpha = 1.0$; $d_{\max} = 0.1$mm	3.406	7.232	14.672	801.513
Reference mesh	5.347	3.078	13.557	2300.819

A relative good correlation was obtained between the simulation results and the experimental measurement using either refined mesh or coarse mesh with remeshing. The comparisons between the numerical results obtained with adaptive remeshing method and with the reference mesh are similar. However, the remeshing procedure presents better accuracy for the total force achieved. The initial refinement mesh has better accuracy (less error) in the axial force and shape predictions. Even for such small SPIF simulation, the computation time is reasonably large using an initial refined mesh. These preliminary results evidence the advantage of adaptive remeshing technique, taking into account the combination of different parameters values.

4.3.2. Remarks

The main interest of the previous section was the assessment of an adequate set of adaptive remeshing parameters in order to support future SPIF simulations.

Analysing the results sets provided by the sensitivity analysis, some intermediate values were chosen. In terms of force prediction, α parameter exposes better accuracy using the intermediate values [0.6, 0.8 and 1.0] for each combination with $d_{\max}$ parameter. However, the intermediate values attributed to

α parameter show less accuracy in terms of shape prediction. The shape prediction has better accuracy when the value of α coefficient is 1.6 and $d_{\max}$ parameter is smaller than 1.0 mm. Globally, the error of shape prediction presents a smaller difference between each combination of parameters than the error obtained for the force prediction. In this sense, the final choice should be an intermediate value for α coefficient. The values of adaptive remeshing parameters selected are: α coefficient equal to 1.0 and for $d_{\max}$ parameter two different values were selected, which are 0.05 mm and 0.1 mm. These two values will be analysed in the following section in the forming of a conical geometry. The number of nodes division per element edges (n) will also be analysed in details in the next Chapter.

Chapter 5

Numerical tests

In this chapter, the performance of RESS finite element described in Chapter 3 combined with the adaptive remeshing technique proposed in Chapter 4 is validated using well known benchmark problems. The reduction of computational time is a vital request to perform numerical simulations of SPIF.
The numerical examples chosen and presented in the following sections, are the usual shapes selected to study the SPIF process: cones and pyramids. All the simulations are performed using the Finite Element in-house code LAGAMINE. The adaptive remeshing parameters influence are assessed and the numerical results are compared with the experimental measurements.

5.1 Simulation of incrementally formed conical shape

This section updates the results of Sena *et al.* (2013). The numerical simulation of SPIF addressed in the current section consists into a conical aluminium part from the NUMISHEET 2014 benchmark proposal. It has a 45° wall angle with a depth of 45 mm (Figure 5.1). The sheet material is an AA7075-O with an initial thickness of 1.6 mm. The backing plate maximum and minimum diameters are 148 mm and 140 mm, respectively. The tool tip diameter is 12.66 mm and the toolpath is based on successive circles with a vertical step size of 0.5 mm per contour, consisting in 90 vertical steps. The initial gap between the tool and sheet is 0.5 mm. The numerical toolpath is based on the experimental toolpath available in the conference proceedings (Yoon *et al.*, 2013). The dimensions of ideal shape and backing plate geometry are schematically shown in Figure 5.1.

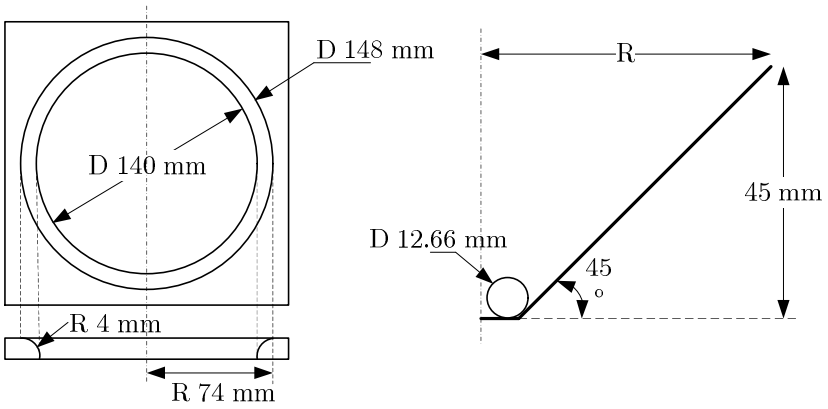

Figure 5.1: Forming of a conical shape: geometric dimensions.

The elastic material behaviour is described by the Hooke's law (E = 72000 MPa and $\nu = 0.33$). The adopted hardening type is isotropic and its parameters for the plastic domain are described by Swift and Voce laws. According to the benchmark proposal data, isotropic yield behaviour (von Mises) was assumed. The chosen material parameters are listed in Table 5.1, from the benchmark proposal.

Table 5.1: Material parameters of AA7075-O.

Test type	Test direction	Hardening type	Parameters
Biaxial tension	-	Swift law	K=335.1MPa; n=0.157; ε_0=0.004
Uniaxial tension	0°	Voce law	K=129,17MPa; n=30.55; σ_0=97.4MPa
Uniaxial tension	0°	Swift law	K=386.93MPa; n=0.229; ε_0=0.004

In order to reduce the computation time, a 45° pie model of the sheet is modelled and displacement boundary conditions are imposed by displacements on the edges (Bouffioux *et al.*, 2007, Henrard *et al.*, 2010; Bouffioux *et al.*, 2010). For isotropic material, the pie mesh with 45° can predict as accurately as the full 360° mesh the experimental results in terms of shape, thickness and force (Henrard, 2008). The numerical shape prediction is extracted from the cross-section along the middle line (see Figure 5.2 and Figure 5.3) of the 45° pie model used within the FE model to avoid inaccuracy due to boundary conditions and taking the radius as the horizontal axis. No distinction was made between X and Y, since the numerical results are considered equal in all directions. Two meshes with 74 mm of radius were tested: an initially refined mesh (reference mesh) with 5828 elements (solid-shell, contact and boundary condition elements (BINDS)) without the remeshing

method, Figure 5.2, and a coarse mesh initially with 347 elements combined with the adaptive remeshing technique, Figure 5.3.

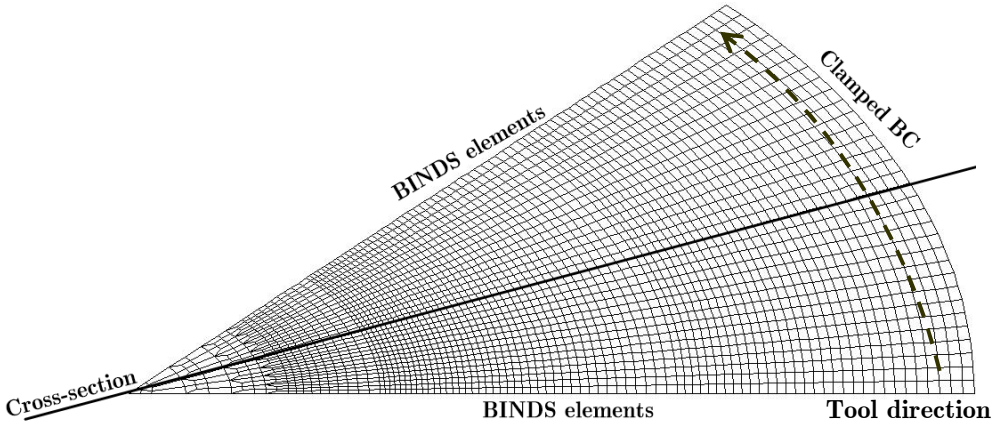

Figure 5.2: Reference mesh with 5828 finite elements used to perform a 45° wall angle cone simulation.

The values used for each remeshing parameter were chosen based on the line test benchmark from the Section 4.3. However, the parameter $d_{\max}$ is tested with two different values (0.05 mm and 0.1 mm). The number of nodes per edge is also additionally tested for different values (from 1 to 4 nodes). The results generated by these adaptive remeshing parameters are analysed for different values in order to verify their influence, to find the compromise between the CPU time and numerical accuracy, while the value of the α coefficient is fixed and equal to 1.0. Figure 5.3 presents the coarse mesh used with different numbers of nodes per edge (n), from 1 to 4 nodes.

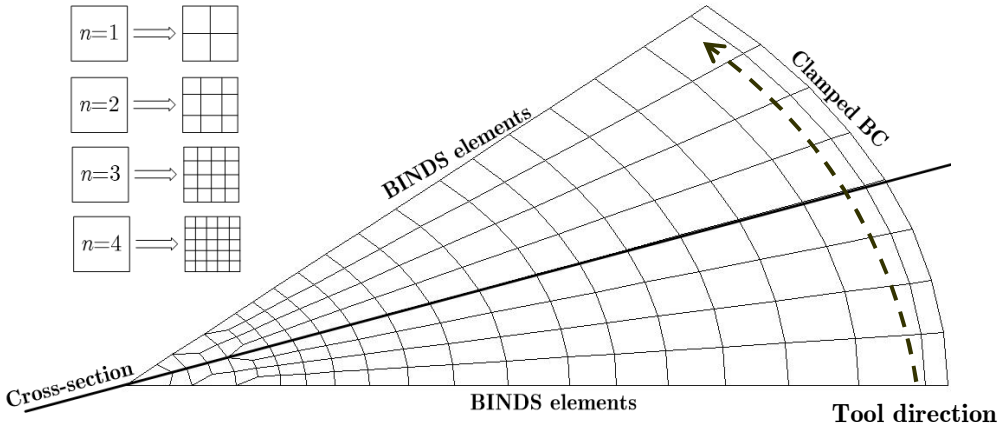

Figure 5.3: Coarse mesh of 347 finite elements used with adaptive remeshing to perform a 45° wall angle cone simulation.

The displacement boundary condition, by using BINDS element, was imposed in order to minimize the effect of missing material at both edges of the pie model. This type of Boundary Condition (BC) is a link between the displacements of both edges. The main purpose to use the displacement BC is due to the tool motion which always moves in the same direction. The material in the tool vicinity is forced to move inducing the twist effect of the shape around its rotational symmetric axis. The tendency to twist can be simulated using the BINDS element applied at the edges of the pie model. The twist effect cannot be predicted using symmetric BC. The contact model interface between the rigid tool model and the sheet metal discretization is taken into account by a contact element named CFI3D based on penalty method. Its penalty coefficients, K_P and K_τ, were set to 1000. This value was chosen due to the good compromise between accuracy and convergence for implicit simulations based on the work of Henrard (2008). Finally, Coulomb's friction coefficient, μ, between the tool and sheet is set to 0.01, value suggested in the benchmark proposal. Both meshes concern one layer of RESS finite element in sheet thickness direction with 5 Gauss Points (GP) through the thickness and CFI3D contact element with 4 GP on plane.

Table 5.2 shows the results obtained with RESS finite element, concerning the final number of elements at the end of the numerical simulation for different levels of refinement combined with different values of $d_{\max}$ parameter.

Table 5.2: Final number of elements for different levels of refinement.

N° of nodes per edge (n)	**Initial n° of elements**	**Final n° of elements for $d_{\max}$=0.05 mm**	**Final n° of elements for $d_{\max}$=0.1 mm**
1	347	1004	884
2	347	1698	1176
3	347	3068	1852
4	347	4548	2998
Reference	5828	5828	5828

The main numerical outputs presented in the following sections are the final shape, final thickness, minor and major strains, and the evolution of the tool force in the tool axial direction predicted during the simulation.

5.1.1. Shape and thickness prediction

Figure 5.4 presents the comparison between the numerical results obtained using the adaptive remeshing method for different refinement levels and the reference mesh. The exhibited numerical results are the thickness prediction and final shape of bottom layer, and top layer. The results of adaptive remeshing procedure chosen to exhibit below were achieved using $d_{\max}$ equal to 0.05 mm.

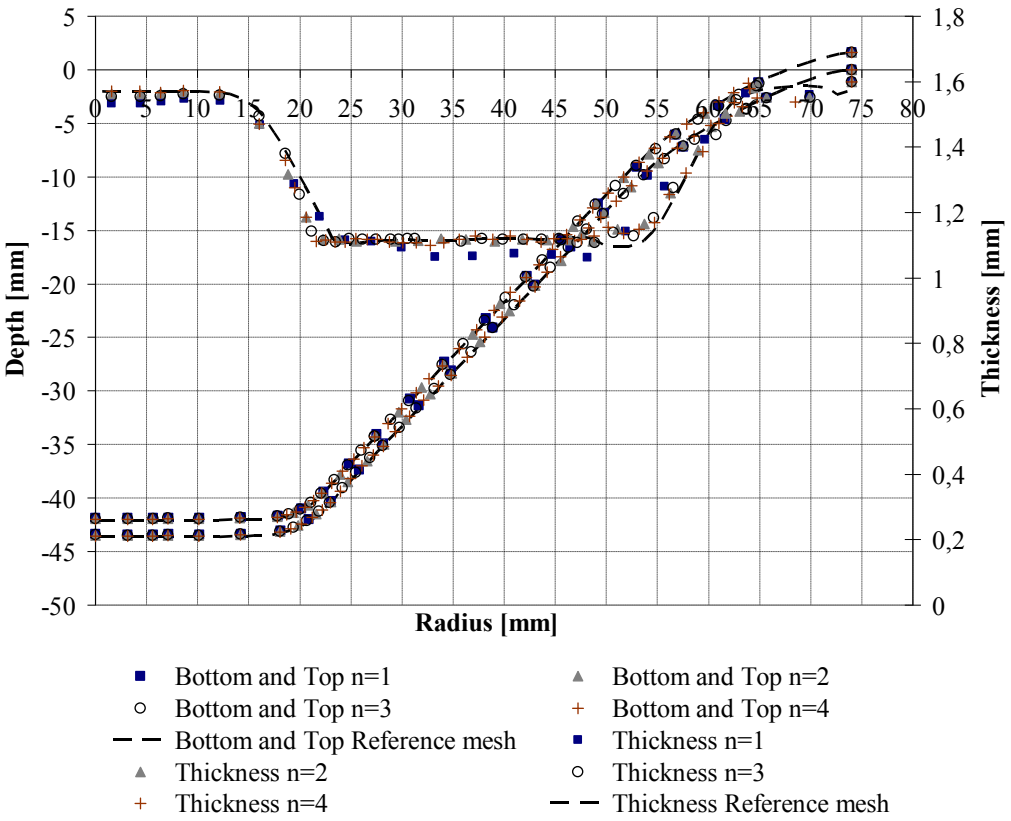

Figure 5.4: Final shape and thickness prediction using adaptive remeshing with α coefficient equal to 1.0 and $d_{\max}$ equal to 0.05 mm.

Globally, shape predictions with different refinement levels have similar results when compared with the reference mesh. The thickness prediction has analogous results compared to the reference thickness. However, the thickness prediction using one node per edge presents lower values in the wall region than the other refinement levels.

Figure 5.5 presents the absolute error of shape prediction for different levels of refinement (n) and reference mesh. The average shape error is presented as the absolute value computed using the following equation

$$\text{Shape}_{\text{Error}}[\text{mm}] = \left(\sum_{i=1}^{N} \text{Abs.} \left| \textit{Num.} - \textit{Exp.} \right| \right) \Big/ N \tag{5.1}$$

where *Num.* is the numerical value, *Exp.* is the experimental value and N is the number of points in the radius direction. The difference between the numerical values along the cross section and the experimental ones (value of X and Y measurements) is computed for the common values in radius direction. The numerical values along middle cross section in the radius axis were linearly interpolated for the corresponding radius values of experimental measurements.

The results accuracy using two different $d_{\max}$ values from the adaptive remeshing procedure are compared with experimental data in Rolling Direction (RD) and Transverse Direction (TD). The reference mesh is represented in the following figure with the parameter n as equal to zero (n=0).

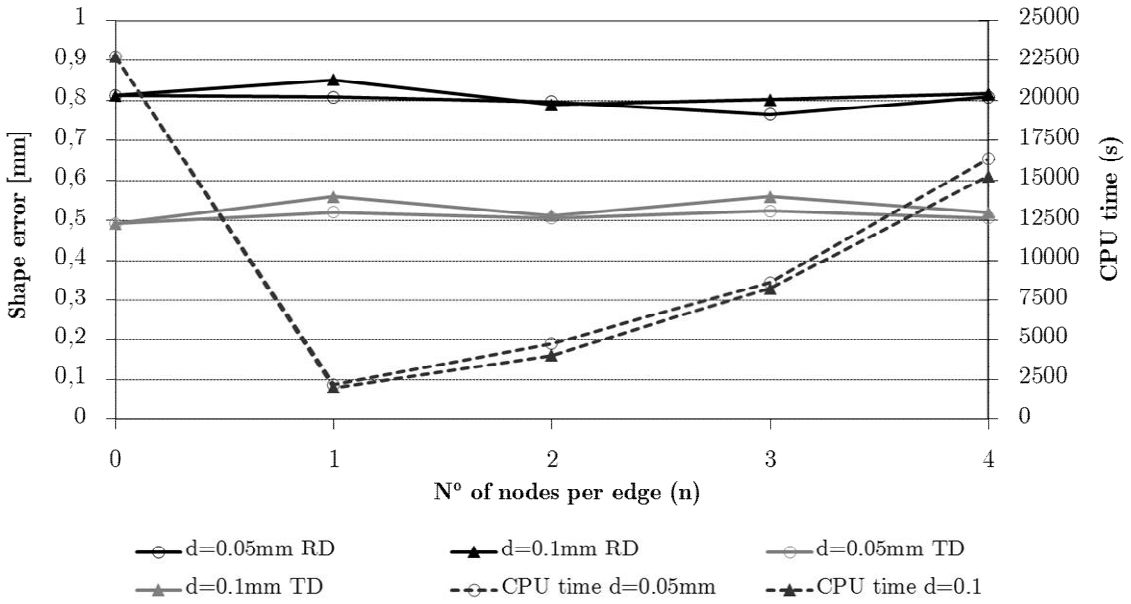

Figure 5.5: Shape prediction error and CPU time for different levels of remeshing refinement and reference mesh (corresponding to n=0).

The shape error was computed for different refinement levels combined with two different values of $d_{\max}$ parameter. In general, the average shape error is less than 1 mm for all numerical results obtained with different refinement levels, as well as with the reference mesh. The shape prediction with highest level of refinement does not mean that it will provide the best shape accuracy, as observed in Figure 5.5. It shows the influence of $d_{\max}$ value in the accuracy of adaptive remeshing results for n values equal to 1 and 3 nodes division per edge.

However, the cases of n values equal to 2 and 4 nodes combined with $d_{\max}$ equal to 0.1 mm or $d_{\max}$ equal to 0.05 mm provide similar results in terms of shape accuracy. Their average errors in transverse direction (TD) and in rolling direction (RD) can be considered similar for an equivalent $d_{\max}$ value.

The CPU time increases from n equal to 1 node until n equal to 4 nodes, as expected, and its CPU time is lower than using the reference mesh. The CPU time differences between both values of d_{max} parameter present a small difference for all refinement levels. A small value of d_{max} keep the remeshed elements, which can influence the CPU time as well as the shape accuracy.

The following sections present the numerical results of adaptive remeshing with "2 nodes" division per edge combined with $d_{\max}$ equal to 0.05 mm and α coefficient is equal to 1.0. The adaptive remeshing parameters were chosen based on the number of nodes per edge (n) which allows an acceptable average error in both directions with a good reduction of CPU time. The comparison with experimental measurements and reference mesh is made.

Figure 5.6 and Figure 5.7 exhibit shape and thickness predictions using adaptive remeshing method, regarding 2 nodes division per edge combined with $d_{\max}$ equal to 0.05 mm. The comparison was performed for different experimental measurement directions, rolling direction (RD) and transverse direction (TD).

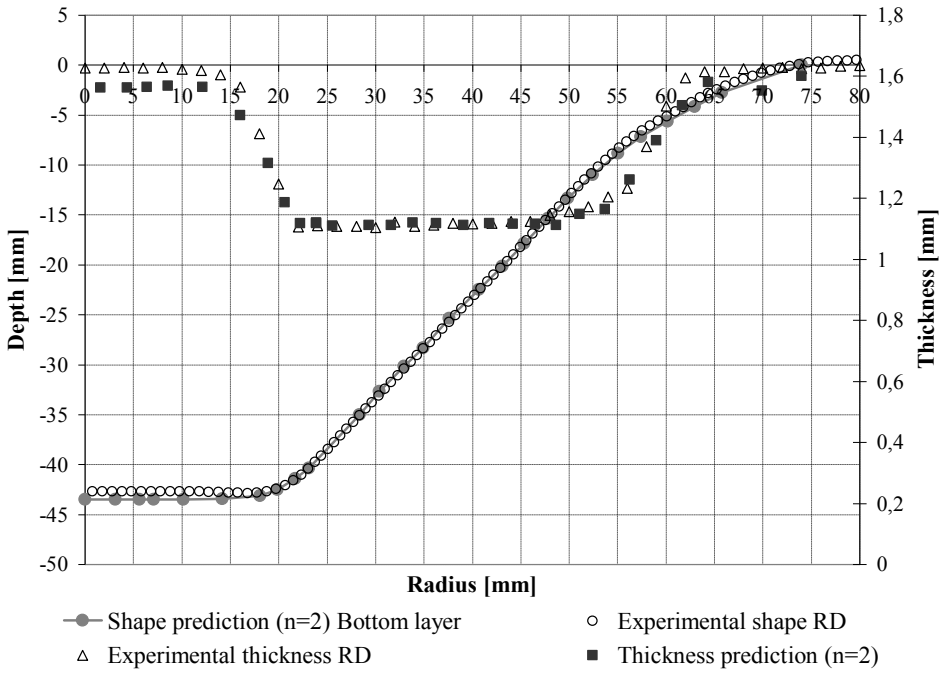

Figure 5.6: Shape and thickness predictions in the rolling direction (RD) with adaptive remeshing refinement (n=2).

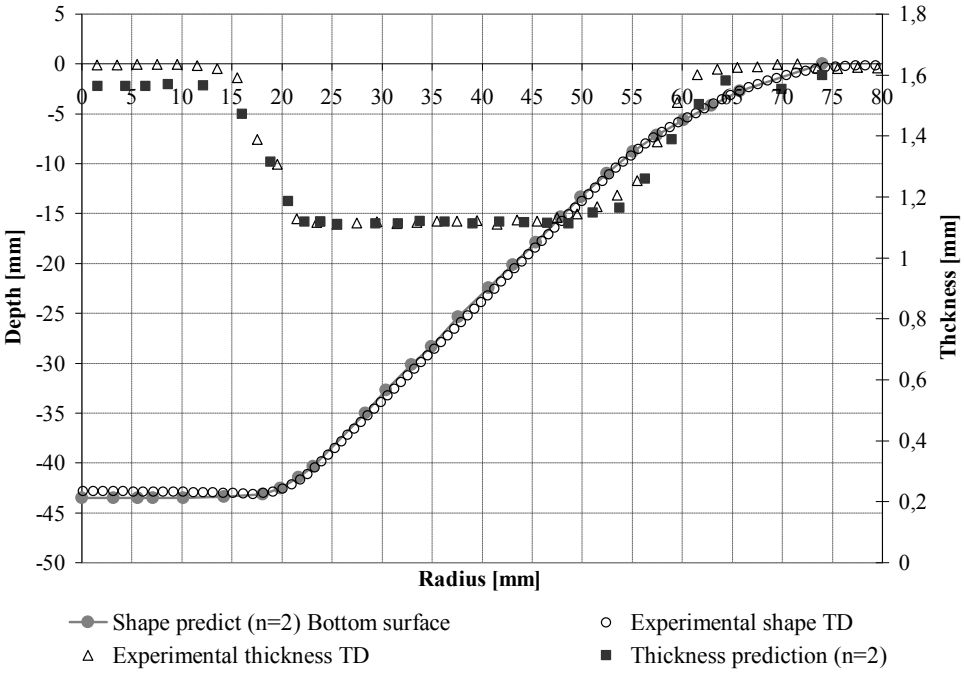

Figure 5.7: Shape and thickness predictions in the transverse direction (TD) with adaptive remeshing refinement (n=2).

Figure 5.6 and Figure 5.7 exhibit a suitable accuracy on the numerical shape prediction in comparison with the experimental measurements. The symmetry assumption of the numerical results in both directions is validated. The differences between the measurements in the transverse direction (TD) and rolling direction (RD) are negligible for this material and this symmetric conical shape.

An analogous analysis was performed for the thickness prediction. The numerical thickness prediction has an acceptable accuracy compared with the experimental results in both measured directions. However, the final thickness experimentally measured is higher than the initial thickness in the central area of the sheet and in the area near the clamped zone of the backing plate. This effect is not predicted in the numerical model, which can be due to the blank sliding effect not considered: the clamped boundary condition is applied in the mesh limits (see figures 5.2 and 5.3). The main comparison is the final thickness value along the final wall angle shape, where the higher deformations occur and in that sense the numerical results obtained have reasonable accuracy.

5.1.2. Major and minor strains prediction

The current section presents the minor and major strains in rolling and transverse directions. The obtained numerical results are considered equal for both directions due to von Mises isotropic yield locus. The comparison of numerical results are performed between the reference mesh and adaptive remeshing procedure using 2 nodes per edge (n=2) in relation to the experimental measurements. Figure 5.8 and Figure 5.9 exhibit the results comparison in rolling and transverse directions.

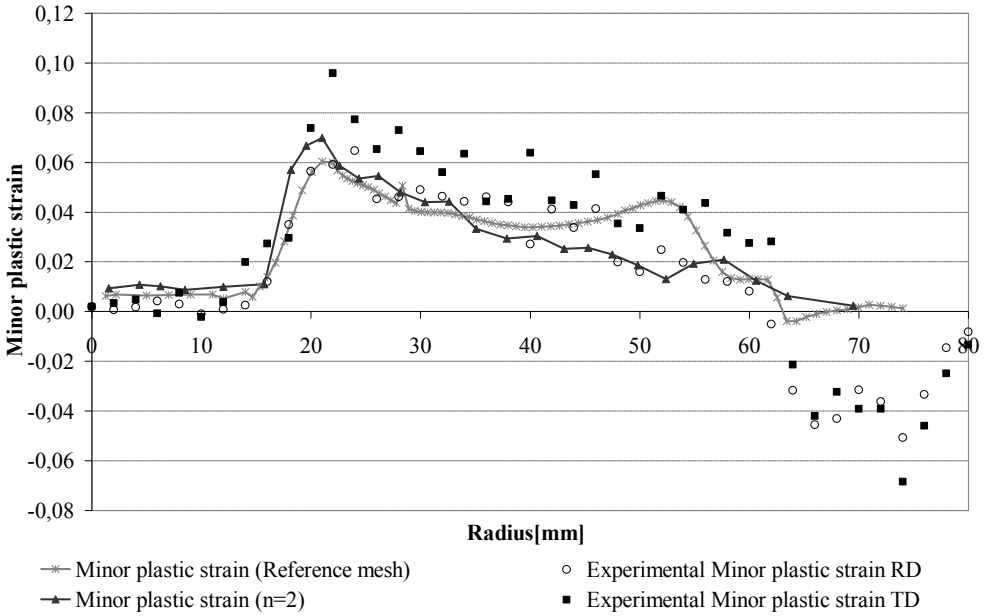

Figure 5.8: Minor plastic strain prediction.

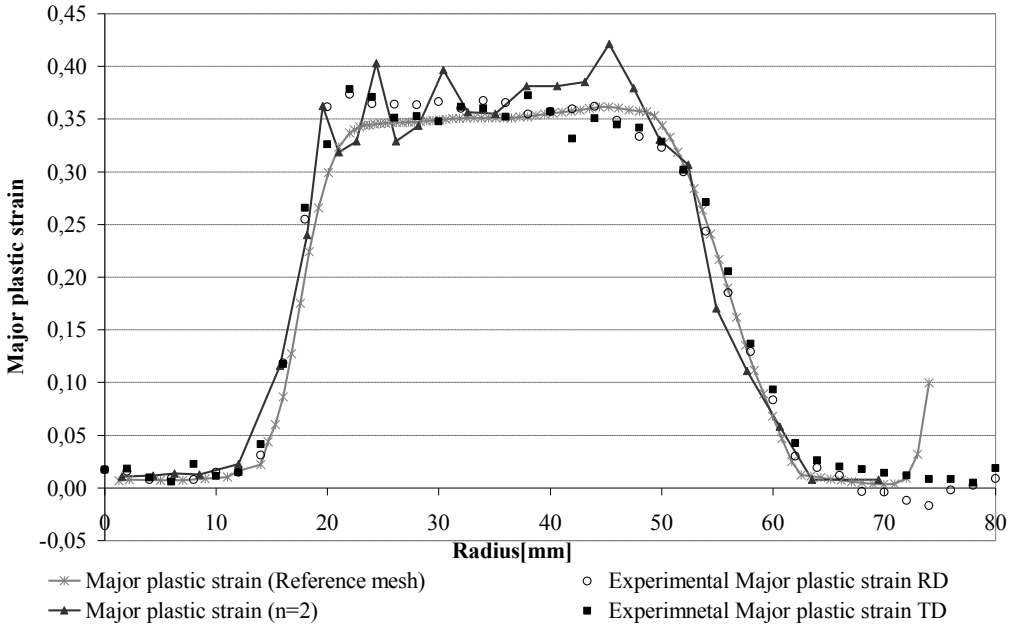

Figure 5.9: Major plastic strain prediction.

The numerical prediction of minor plastic strain in rolling direction presents acceptable approximation using adaptive remeshing method in comparison with experimental measurements. The main difference between both numerical predictions is at the end of the wall (radius around 50 mm), where the reference mesh provides higher values than the use of the adaptive remeshing prediction. In terms of major strain the reference mesh has better approximation to the experimental measurement. The numerical results using adaptive remeshing present higher values of major plastic strain in the wall region. The results using adaptive remeshing are sparser than the use of reference mesh which presents dense results. This difference between both mesh topologies is related with the mesh density at the wall region, as confirmed through the final number of elements in Table 5.2. In the transitions areas, as the mesh centre and the region near the clamped boundary conditions, the numerical predictions are similar.

The experimental measurement of the minor plastic strain in transverse direction is higher than the numerical results obtained with both mesh topologies. The numerical predictions in comparison with the experimental measurements for the major plastic strain are similar in the transition areas. However, the values prediction in the wall region is better predicted with the uses of reference mesh while the values obtained with adaptive remeshing are higher.

5.1.3. Axial force prediction

Figure 5.10 and Figure 5.11 present the prediction of numerical axial tool force (Fz) with different levels of refinement using adaptive remeshing method. The simulations were performed using Swift and Voce hardening laws with material parameters of Table 5.1. To simplify the comparison, the numerical force evolution is replaced by the average calculation when the tool is at the central positions of each contour (Henrard *et al.*, 2010), to avoid inaccuracy from boundary conditions.

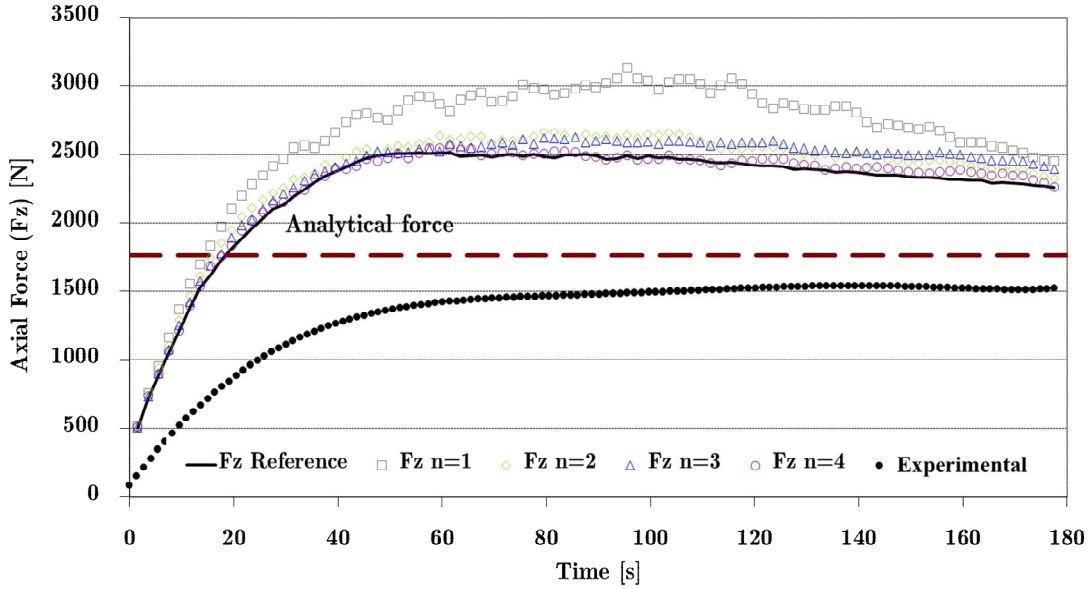

Figure 5.10: Force prediction for different levels of adaptive remeshing refinement and reference mesh using the Swift hardening law with biaxial material parameters.

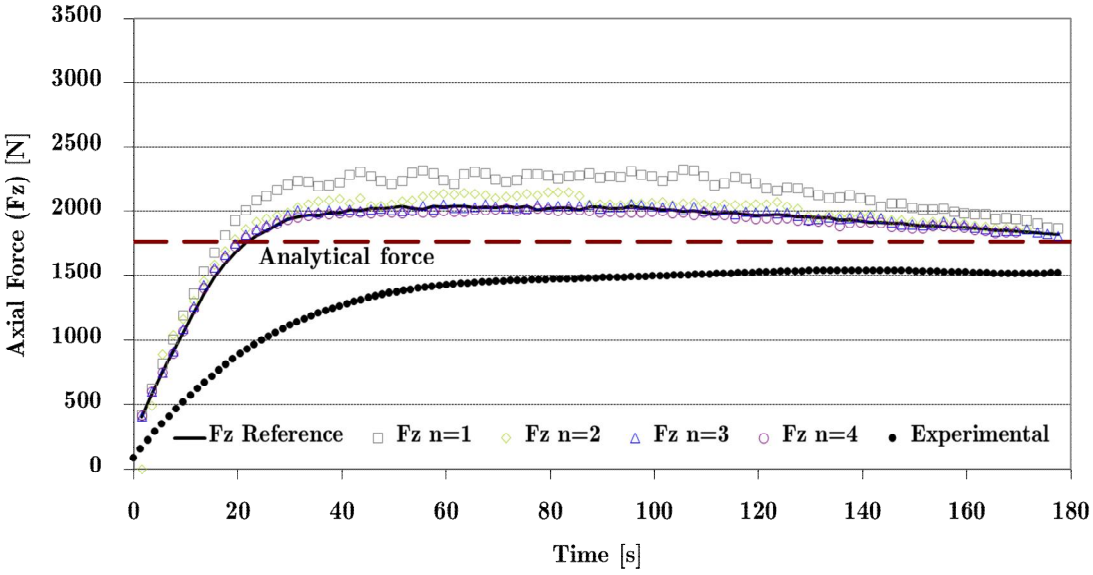

Figure 5.11: Force prediction for different levels of adaptive remeshing refinement and reference mesh using the Voce hardening law with uniaxial material parameters.

The results are similar between the reference case and the remeshing procedure using 3 and 4 nodes per each edge in the element plane. It is noticeable that the axial force results are sensitive to the variation of the number of new smaller elements per coarse element. The oscillations of the force are due to the penalty method used to model contact. They are higher using a low refinement (n=1) for the reason that the mesh used is coarser than the reference one. In addition, increasing the value of remeshing parameter $d_{\max}$ could increase the oscillation effect, as being a consequence of mesh derefinement.

As expected, the axial force level using Voce hardening law is smaller than using Swift, due to the well-known saturation behaviour of Voce's law. However, Swift hardening law provides a more realistic behaviour of the material than the use of Voce hardening law.

Figure 5.12 demonstrates the comparison between different material parameters, with different hardening laws, to predict the axial force in comparison with experimental measurements. An analytical force prediction was performed to compare its approximation to the numerical results and experimental measurements. The main interest of the analytical formula is to provide a first estimation of the axial force prediction before knowing the experimental results. The analytical force is computed using the following formula (Aerens *et al.*, 2009; 2013):

$$F_{Z\_S} = 0.0716 R_m t^{1.57} d_t^{0.41} \Delta h^{0.09} (\phi - \Delta\theta) \cos(\alpha - \Delta\theta)\,, \tag{5.2}$$

where R_m is the tensile strength, also known as Ultimate tensile Strength (UTS), t is the sheet thickness, d_t is the tool diameter, ϕ is the wall angle in degrees and Δh is the scallop height. The empirical correction value, $\Delta\theta = 0.05$ rad or 2.86°, was from Aerens *et al.* (2013).

Table 5.3: Material parameters used to compute the analytical force and its resulting values.

Material property	Units	Uniaxial tension at 0° direction test
R_m (UTS)	N/mm²	202.1
t	mm	1.6
d_t	mm	12.66
Δh	mm	0.0099
ϕ	Degrees	45°
Force	N	1767.1

Figure 5.12 exhibits the comparison between the numerical simulations with the material parameters from Table 5.3 with the use of different application of boundary conditions. Initially in Figure 5.10, the clamped boundary conditions were considered as shown in Figures 5.2 and 5.3.

From the benchmark proposal, the die plate and holder plate dimensions are given. Similarly, as the blank mesh, a 45° pie model of die plate and holder plate was assumed. The contact properties between the sheet and holder plate and die plate force are not given. The contact parameters and holder plate force were based on values found in literature related to deep drawing examples. The contact

parameters used between the sheet and the components consist of penalty coefficients (K_P, K_τ) and friction value (μ) of 1000 and 0.05, respectively. The applied force in the 45° pie model of holder plate was 1250N.

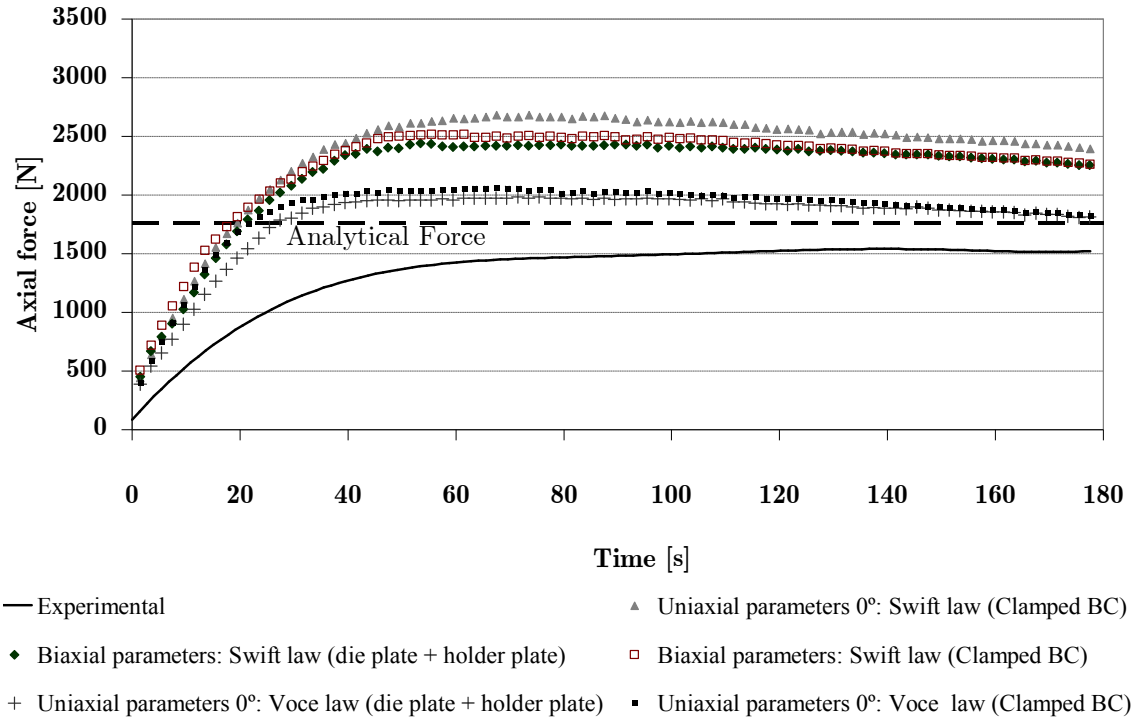

Figure 5.12: Axial force prediction using the reference mesh with Swift hardening law.

The absence of die plate and holder plate in the numerical model was substituted by the clamped boundary conditions in the limits of the mesh, in order to decrease the CPU time. On the other hand to understand the difference between the numerical results and the experimental results presented in Figure 5.10 and Figure 5.11, the approximation to the real boundary conditions was tested in Figure 5.12. The addition of die plate and holder plate in the numerical model was necessary to assess their influence on the numerical prediction of the axial force.

The use of uniaxial parameters combined with Swift hardening law using clamped boundary conditions presents the highest level of axial force. However, the biaxial parameters exhibit lower axial force than the uniaxial values, but without significant difference. The use of blank holder and die plate decreases the axial force prediction and presents a better agreement with the analytical force prediction using the biaxial material parameters. However, it was necessary to adapt the contact parameters values and blank holder force to achieve the approximation of axial force prediction to the analytical force obtained with Aerens *et al.* formula.

The contact interaction between the sheet mesh and the modelling of clamped devices in the numerical simulation increases the CPU time.

The obtained analytical force of Equation 5.2, using the material parameters of uniaxial tension test, is still distant from the experimental result. However, the difference is acceptable. The use of Voce's hardening law combined with the modelling of clamped devices (die plate and blank holder), allows the approximation of the axial force prediction to the analytical force using the uniaxial parameters.

According to the numerical results, the values are still far from the experimental reference using Voce hardening law but closer than the one using Swift hardening law. The use of Voce hardening equation allows the saturation of stress values and the axial force level is maintained low. However, tensile test is not the suitable test to provide the correct material data to simulate the SPIF process (Bouffioux *et al.*, 2010).

Figure 5.13 presents the comparison of axial force prediction between several Finite Element codes. These results were proposed by different authors and evaluated in NUMISHEET 2014 benchmark (n°3).

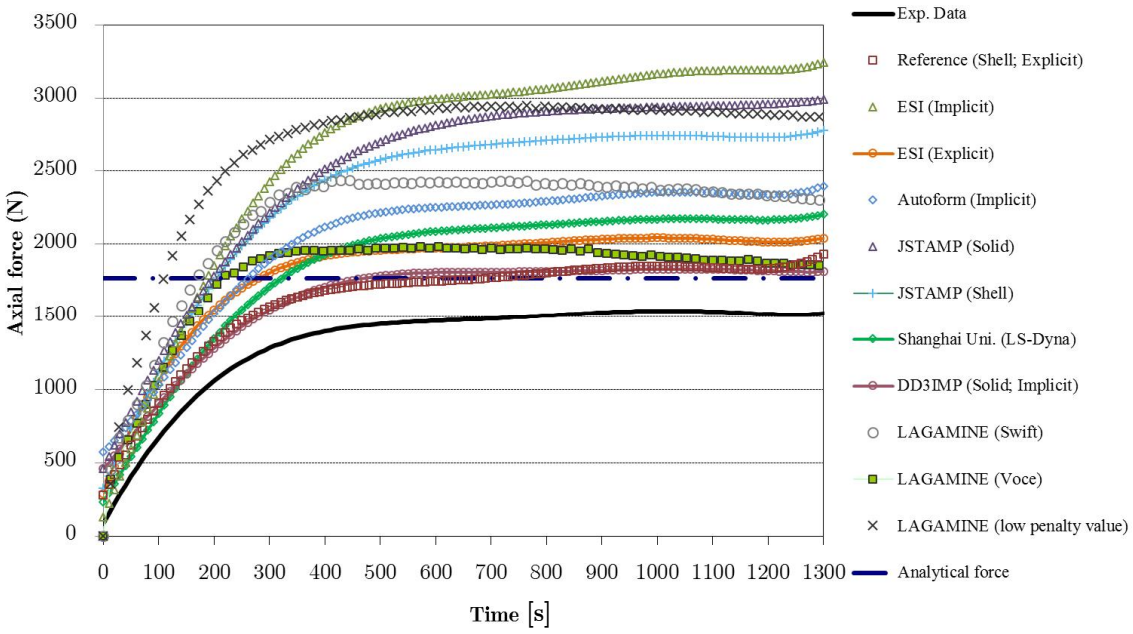

Figure 5.13: Comparison of axial force prediction obtained from different Finite Elements codes.

Except from DD3MP and the reference numerical results, all the numerical results from different Finite Elements codes overestimate the axial force prediction. However, the result from LAGAMINE code using Voce hardening law also presents an approximate force prediction to the reference solution. In addition, it is worth to

notice the influence of a low penalty coefficient in the axial force prediction, which revealed an evident overestimation of force, as a consequence of tool penetration effect.

5.1.4. Remarks of cone shape simulations

In general, the numerical results exhibit good accuracy using RESS finite element combined with adaptive remeshing technique. The Swift hardening law allows a better agreement in relation to the uniaxial test curve performed experimentally than the use of Voce hardening law. Figure 5.14 exhibits the uniaxial tensile curve with material data in 0° direction using different hardening laws from Table 5.1.

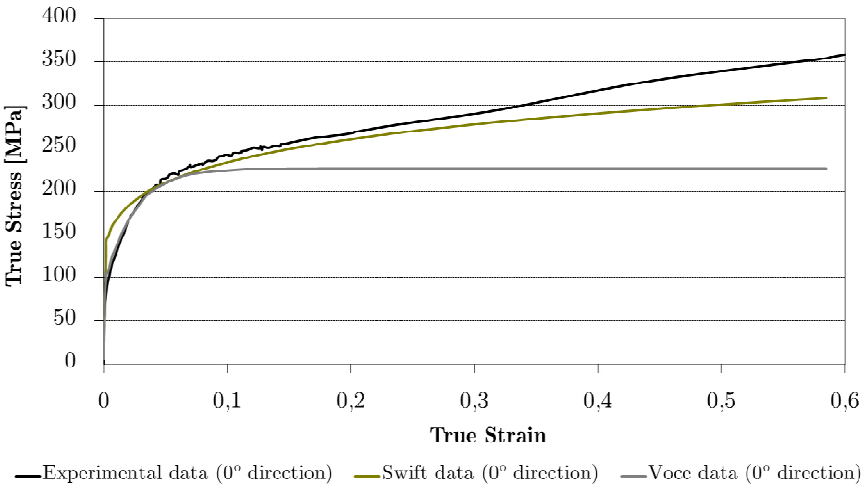

Figure 5.14: Uniaxial tensile test (extrapolated).

As shown in the comparison, the Swift hardening model does not provide the most accurate results in the present SPIF numerical simulations. Indeed, the force predictions by RESS with Swift law for the incrementally formed conical shape is farther from experimental measurements than the results generated by Voce law. This fact confirms that extrapolating tensile test curves to identify the hardening parameters used in SPIF simulations is not an efficient method to identify the actual behaviour law in SPIF process. Note that the best Finite Element force predictions using different hardening laws, different codes converges to the analytical prediction of force and not to the experimental measurement. This obtained analytical force prediction using Equation 5.2 and the available material parameters allowed an acceptable approximate value in comparison to the

experimental force measured. However, this formula showed to be more accurate in many cases, so it generates some doubts on all the exact conditions of the experiments.

The numerical results achieved using the addition of die plate and blank holder in the numerical model decreased the values of axial force prediction. However, the contact properties and force applied on the holder plate were assumed ones as their experimental values are unknown. Probably, if the experimental contact properties and force applied on the blank holder were known the axial force prediction could have similar level as the axial force achieved with clamped boundary conditions. The friction value (μ=0.05) used between the aluminium sheet and the blank holder is questionable, as well as the blank holder force. These parameters mentioned were adjusted in order to improve the approximation of the numerical axial force, regarding the experimental axial force.

Finally, in order to use acceptable adaptive remeshing parameters in further simulations, the best adaptive remeshing parameters found are: the number of nodes division per edge (n) equal to 3 nodes combined with $d_{\max}$ equal to 0.05 mm. These parameters are chosen regarding the results obtained in previous sections, in terms of shape error, CPU time and force prediction. The α coefficient value equal to 1.0 was chosen from the line test benchmark analysis performed in Section 4.3.

5.2 Simulation of a two slope pyramid

The numerical simulation of SPIF addressed in the current section consists in a two slope pyramid benchmark with different wall angles at different depths. The sheet material is low carbon steel alloy, DC01, with an initial thickness of 1.0 mm, being clamped on its border by means of a 182 mm x 182 mm blank holder plate. The tool tip diameter is 10 mm and the toolpath is based on successive quadrangular paths with a vertical step size of 1.0 mm per contour. The number of contours for the first slope of the pyramid is 60 and 30 contours are present in the second slope. The experimental toolpath points were given in order to use it in the numerical simulations. These SPIF experiments as well as the shape measurements were performed by Joost Duflou's team at KU Leuven (Duchêne *et al.*, 2013) who provided all the required data for the numerical simulations and their validation. The dimensions of an ideal design are schematically shown in Figure 5.15.

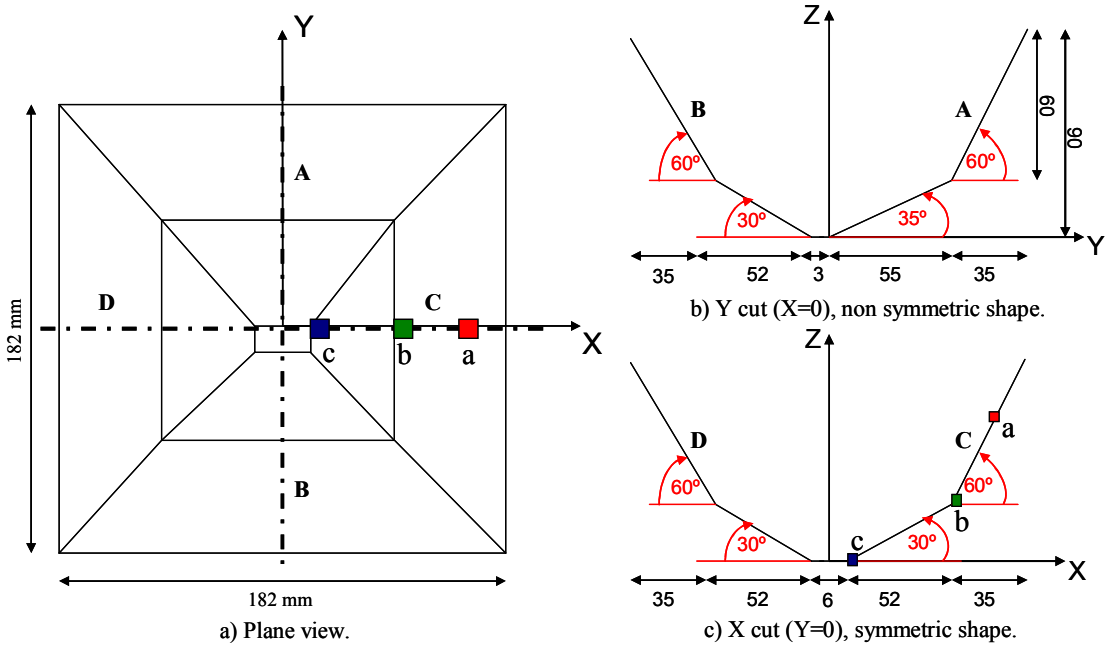

Figure 5.15: Component nominal target dimensions.

The shape analysis is divided in four sections (A, B, C, D), in order to analyse them separately in the middle section of the mesh model (see Figure 5.16), to avoid the influence of boundary conditions. The material behaviour is elastically described by E = 142800 MPa and ν = 0.33. The plastic domain is described by a von Mises yield surface with mixed hardening model, which combines isotropic and kinematic hardening. The isotropic hardening behaviour is defined by means of a Swift's law and the evolution of the back-stress is governed by Armstrong-Frederick definition. The material parameters are listed in Table 5.4. The initial yield stress (σ_0) is 144.916 MPa.

Table 5.4: Material parameters of DC01 steel.

Name and hardening type	Parameters	Back-stress
Swift Isotropic hardening	K=472.19MPa; n=0.171; ε_0 =0.001	C_X =51.65; X_{sat} =5.3

Figure 5.16 illustrates two distinct mesh refinements. Due to the square geometry in XY plane (see Figure 5.15.a) and to benefit the computation time reduction, only half of the sheet is modelled. This simplification also can provide a similar result as a full mesh (Henrard, 2008). The initial refined mesh (reference mesh) is composed by 2048 elements disposed in one layer of RESS finite element in the thickness direction. The coarse mesh used with adaptive remeshing method is modelled by 128 elements on the sheet plane, with one layer of RESS finite element

in the thickness direction. However, the nodes at the top layer of both meshes define the contact element layer at the surface. The contact modelling is based on a penalty approach and on a Coulomb law (Habraken and Cescotto, 1998). So, both meshes have two layers of elements (solid-shell + contact elements) in thickness direction, and the spherical tool was modelled as a rigid body. Finally, Coulomb friction coefficient (μ) between the tool and sheet is set to 0.05 and the penalty coefficients (K_P and K_τ) are equal to 1000.

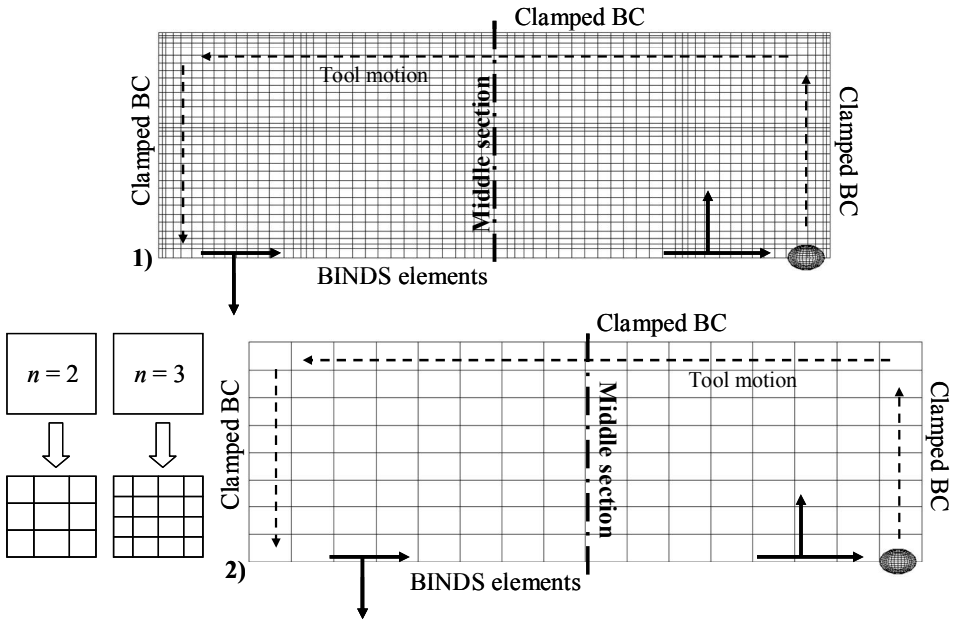

Figure 5.16: Reference mesh (1) and coarse mesh used with adaptive remeshing (2).

The numerical shape prediction is extracted from the middle section of the half mesh used within the FE model. To avoid inaccuracy due to BC effect, each pyramid wall section is analysed separately.

Displacement BC were imposed (see Figure 5.16) in order to minimize the effect of missing material along the symmetric axis. This type of BC is introduced by a finite element called BINDS and it is a link between the node displacements of both edges (Bouffioux *et al.*, 2010; Henrard *et al.*, 2010). The absence of backing plate and blank holder in the numerical model was replaced by the clamped BC at the borders of both meshes. The absence of modelling of the clamping devices avoids additional contact elements in the model.

Different values for each parameter were tested for derefinement distance (d_{max}) as well for the number of nodes per edge (n): d_{max} values were 0.1 mm and 0.2 mm; n values were 2 and 3 nodes. The value used for α coefficient is equal to 1.0. These values used for each remeshing parameters were chosen based on a

previous sensitivity analysis using the line-test benchmark simulation (Bouffioux *et al.*, 2008). The total number of elements in both meshes includes the number of all finite elements of the model (RESS+CFI3D+BINDS). The number of integration points through the thickness used in RESS finite element is 5 GP.

Table 5.5 presents the performance of both refinement strategies assessed at equivalent section analysis. It is possible to confirm the adaptive remeshing advantages even when the final number of elements is higher than the reference mesh.

Table 5.5: Simulation performance.

Mesh type		CPU time	CPU time Reduction (%)	Initial nº of elements	Final nº of elements
n=2	d_{max}=0.1mm	6h:28m:25s	76.67	298	2602
n=3	d_{max}=0.1mm	13h:38m:43s	50.8		4394
	d_{max}=0.2mm	13h:18m:2s	52.1		4394
Reference		27h:44m:27s	-------	4282	4282

The application of the adaptive remeshing with n equal to 3 delivers an average CPU time reduction of 50% while negligible difference for different values of $d_{\max}$ parameter is observed. The CPU time reduction using n equal to 2 is considerably larger than for n equal to 3. However, the shape accuracy obtained with different refinement levels is analysed in the following section.

The main numerical outputs presented in the next sections are the final shape of the sheet, in a middle-section along the symmetric axis in different directions (see Figure 5.15.b and Figure 5.15.c) and stress state behaviour. The deformed shape evolution is also analysed for different tool depths.

5.2.1. Shape prediction

In the current section, the deformed shape predictions from the bottom nodes are compared to the available experimental results. The experimental shape measurements were extracted using Digital Image Correlation (DIC) throughout the SPIF process (Guzmán *et al.*, 2012). Figure 5.17 exhibits the shape prediction in Y direction using the adaptive remeshing procedure and provides a simultaneous comparison with the reference mesh and experimental measurements. Different

adaptive remeshing parameters are tested in order to assess their influence in the numerical shape accuracy.

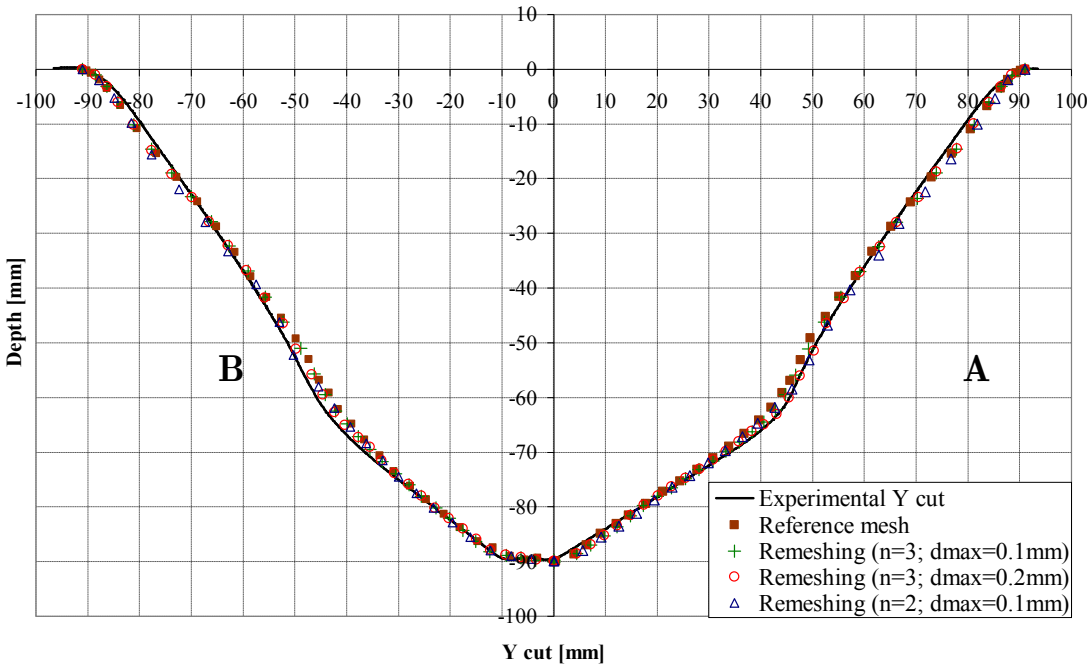

Figure 5.17: Final shape prediction in Y cut for different refinement levels after the tool unload.

It can be observed in Figure 5.17 that an acceptable accuracy is achieved between the numerical results and the experimental measurements. The derefinement criterion occurs with more frequency using d_{max} equal to 0.2 mm than for d_{max} equal to 0.1 mm. A low value of d_{max} parameter means that the refinement is kept increasing the mesh flexibility. In this case, at the transition region of wall angle on section A, the adaptive remeshing using n equal to 3 combined with d_{max} equal to 0.2 mm seems more accurate than the others numerical simulations results. Figure 5.18 exhibits a zoom at wall angle change of section A, which evidences a better shape prediction using n equal to 3 combined with d_{max} equal to 0.2 mm.

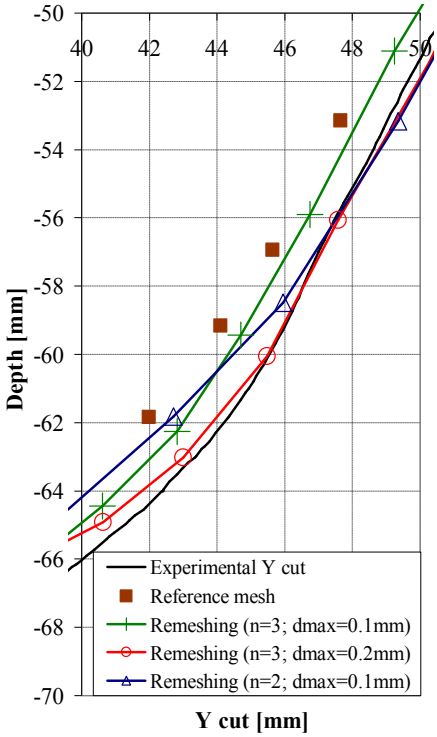

Figure 5.18: Zoom of shape prediction at wall angle change on section A in Y cut for different refinement levels.

Hereafter, the average relative and absolute errors are computed and presented in Table 5.6 for each refinement level. The difference between the numerical results along the middle section of the mesh and the experimental measurements is computed for common values in the corresponding axis. Previously, the numerical values along of middle cross section were linearly interpolated for the corresponding values of experimental measurements.

The average relative error is computed using the following expression:

$$\text{Error}(\%) = \left[\left(\sum_{i=1}^{N}\left(\sqrt{(Num. - Exp.)^2 / Exp.^2}\right)\right) / N\right] * 100 \qquad (5.3)$$

where *Num.* is the numerical value, *Exp.* is the experimental value and N is the number of points in X axis.

Table 5.6: Average error for Y cut section A.

Y cut (A)	**Remeshing mesh**	**Reference mesh**
Error	**Relative (%)**	
n=3; d_{max}=0.1mm	5.95	6,37
n=3; d_{max}=0.2mm	5.32	
n=2; d_{max}=0.1mm	9,22	

In general, the refinement level using adaptive remeshing method with n equal to 3 nodes per edge provides results closer to the experimental ones, than the reference mesh or adaptive mesh with n equal to 2 nodes per edge. However, an improvement was obtained for the case using n equal to 3 combined with d_{max} equal to 0.2 mm at the wall angle transition region. Its absolute error at wall angle change is equal to 0.12 mm while using n equal to 3 and d_{max} equal to 0.1 mm the absolute error at wall angle change is 2 mm.

Section B of Y cut presents a similar behavior as section A, as can be seen in Table 5.7. However, the absolute error at the wall angle change is more noticeable on section B for n equal to 3 nodes per edge with different values of d_{max}. It presents an absolute error of 3.53 mm using d_{max} equal to 0.1 mm and the error decrease to 2.49 mm using d_{max} equal to 0.2 mm.

Table 5.7: Average error for Y cut section B.

Y cut (B)	**Remeshing mesh**	**Reference mesh**
Error	**Relative (%)**	
n=3; d_{max}=0.1mm	6.63	6.94
n=3; d_{max}=0.2mm	6.37	
n=2; d_{max}=0.1mm	9.93	

In this first cut analysis, the section A has better shape accuracy than the cut B. However, for both sections a better shape accuracy was achieved using a d_{max} value equal to 0.2 mm. Probably, this improvement occurred due to a derefinement at some regions of the wall angle mesh during the simulation forming, which leads to a stiff wall zone and an improvement at the wall angle transition area.

Figure 5.19 exhibits the shape predictions in X direction using the adaptive remeshing procedure after tool unload. The following numerical results were obtained using the adaptive remeshing parameters n equal to 3 nodes per edge combined with different d_{max} values of 0.1 mm and 0.2 mm.

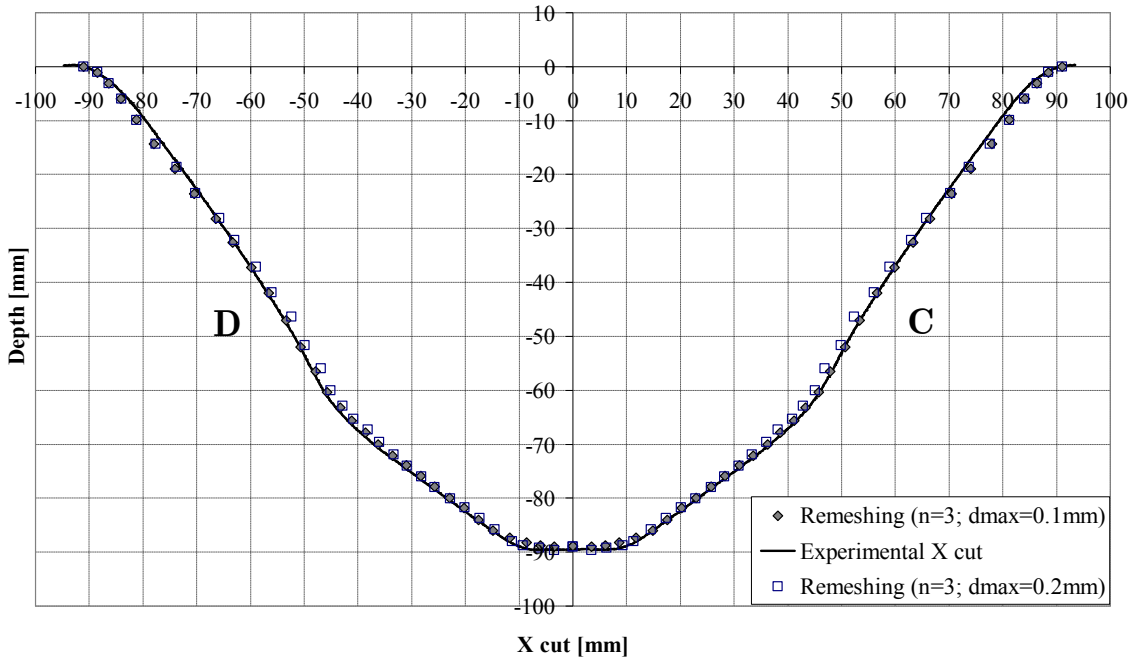

Figure 5.19: Final shape prediction in X cut for refinement n equal to 3 nodes per edge, after tool unload.

The numerical results on the X cut are considered symmetric, as the wall angle of sections C and D are similar. Table 5.8 presents the average error in X direction, at the middle section.

Table 5.8: Average error for Y cut section C or D.

X cut (C and D)	**Remeshing mesh**
Error	**Relative (%)**
n=3; d_{max}=0.1mm	4.72
n=3; d_{max}=0.2mm	4.77

The average relative error analysis of X cut using d_{max} equal to 0.1 mm is negligibly smaller than the use of d_{max} equal to 0.2 mm. However, at transition region of wall angle change, it is observable that for d_{max} equal to 0.1 mm the shape accuracy is better than for d_{max} equal to 0.2 mm.

Figure 5.20 exhibits the comparison between the experimental measurements and the numerical results of four different contours. The numerical curves are intentionally shifted to coincide with experimental at similar depth value. This method is justified as there are missing data in the experimental measurements near the backing plate. Near X equal 0 mm, data are difficult to extract from the results of DIC measurements (Guzmán *et al.*, 2012). The numerical results were

obtained using the adaptive remeshing method with n equal to 3 nodes per edge and d_{max} equal to 0.1 mm.

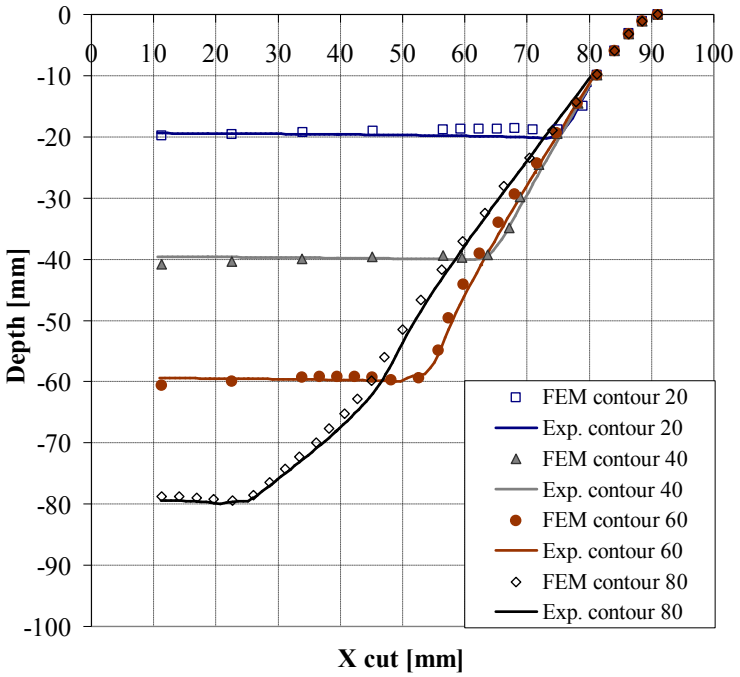

Figure 5.20: Shape prediction for X cut at different depth steps using the adaptive remeshing method.

The numerical results follow the overall shape of the experimental measurements for the contours 20 mm to 60 mm. However, there is a difference at the central region of the mesh due to non-refined area of contours 40 mm and 60 mm. This difference occurs when the refinement and derefinement criteria were not achieved in the finite elements near the central area of the mesh. Firstly, due to distance between the tool and the nodes in the tool vicinity (see Figure 5.22.1 describing the 60 mm contour). Secondly, due to no significant deformation happening in the mesh plane according to the derefinement indicator (see Figure 4.8). To understand the deviation occurrence at the central region of the mesh for contours 40 mm and 60 mm using the adaptive remeshing method, a new analysis was carried out. Thanks to a simulation using the reference mesh of Figure 5.16.1 and another one with adaptive remeshing method, as well as using a new value of α coefficient equal to 3 combined with d_{max} equal to 0.1 mm, the accuracy at the central area of the meshes has been further analysed.

Figure 5.21 presents the obtained results with both refinement topologies.

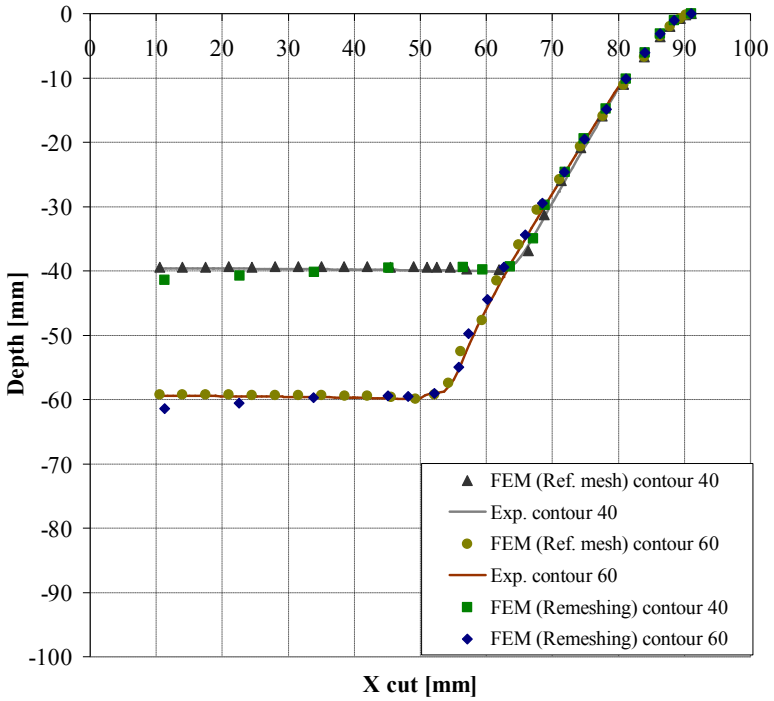

Figure 5.21: Shape prediction for X cut at 40 mm and 60 mm of depth.

The obtained results using the reference mesh proves that the refinement at the central region avoids the numerical deviation error. However, using the adaptive remeshing even with a high value of α coefficient, the deviation is kept, due to the fulfilment of the derefinement criterion. The refinement at the central area remains if a significant distortion occurs and if the d_{max} value is higher than the value chosen by the user. Once the forming tool does not move on the referred region, the refinement due to a high value of α coefficient is deleted and the coarse elements are reactivated. The zone with poor degrees of freedom is very sensitive to very small error of slope in refined region as elements are very coarse.

At 80 mm depth, Figure 5.20 presents a visible error in the transition zone of the wall angle. This shape error was mentioned by Guzmán *et al.* (2012) (see Figure 12 in Guzmán *et al.*, 2012) as the "tent" effect. In order to understand the origin of this shape inaccuracy after wall angle transition, the following section will present a stress analysis in the thickness direction.

5.2.2. Through thickness stress analysis

The main interest of the current section is the analysis of stress state in thickness direction in different wall regions of the mesh at the middle section. The stress state is obtained using the adaptive remeshing technique at the end of two

different forming stages. Figure 5.22 exhibits the mesh plane view and the elements selected for stress extraction.

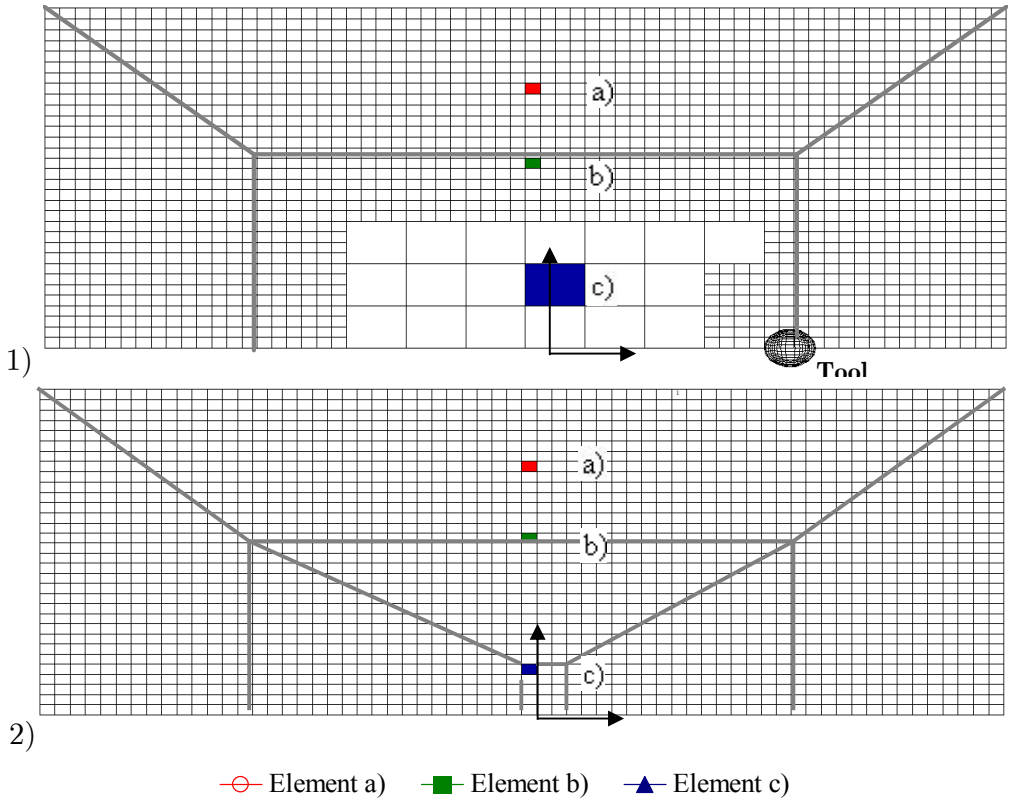

Figure 5.22: Position of three selected elements after contour 60 mm (1) and after contour 90 mm unloading step (2).

The stress analysis behaviour of each Gauss Point (GP) through thickness is performed at different forming depths for three selected elements. The GP positions are such that GP1 is near the sheet external surface (the one not in contact with the tool) and GP5 near the internal surface. The orientation of the local stress in plane components (σ_{11} and σ_{22}) can be recovered by their projections in Figure 5.22. The component σ_{33} is the stress component in thickness direction.

Figure 5.23 presents the relative stress (σ / σ_0) values (σ_0 being the initial yield stress 144.916 MPa) at the 60^{th} contour (at the beginning of the forming of the second slope pyramid when the tool has already had contact with the sheet and is going deeper). The associated mesh and the tool position are shown in Figure 5.22.1.

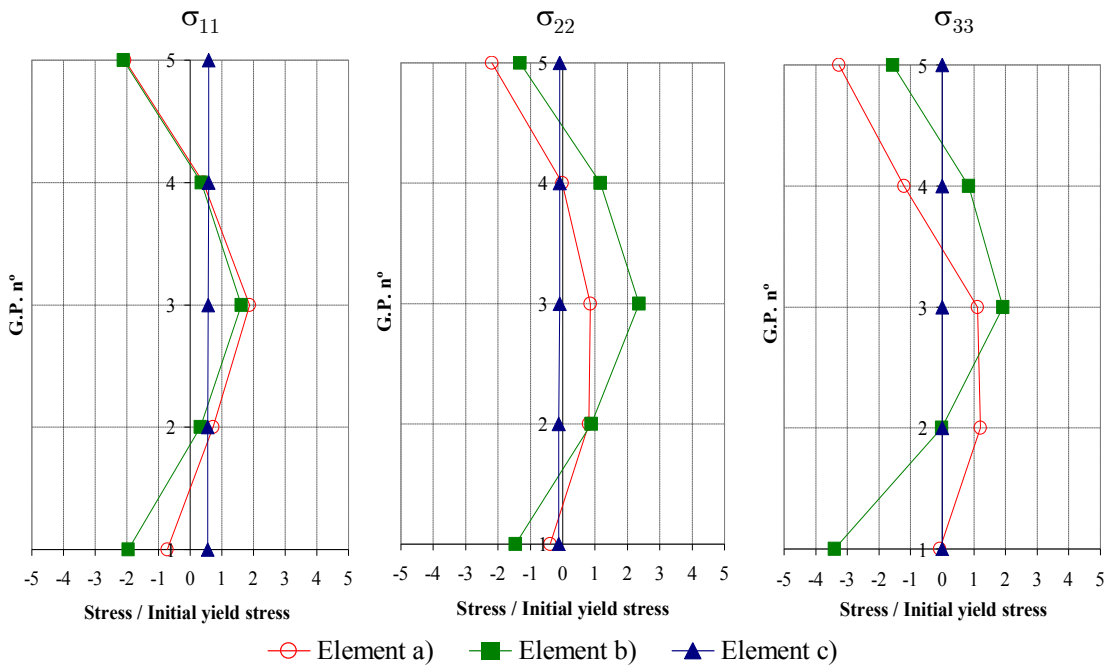

Figure 5.23: Stress components through the thickness for the three elements at depth stage 60 mm.

The cyclic strain path associated to SPIF, checked by He *et al.* (2006), confirms the bending/unbending type of load associated to a stretch forming. The σ_{11} and σ_{22} stress components (Figure 5.23) of the element a) at middle position on the 60° wall has a typical scheme resulting from such stress state.

Guzmán *et al.* (2012) used a shell finite element to analyse a two slope pyramid made in Aluminium AA3003, similar to the DC01 pyramid studied in the present work. As expected, the stress states computed by shell and solid-shell approaches present both similarities and discrepancies. The results from Guzmán *et al.* 2012 were based on the shallow shell theory, thus they assumed that the mid-plane coincides with the neutral plane. The solid-shell element formulation allows a greater flexibility and takes into account through thickness shear stresses and normal stress in thickness direction in addition to the membrane stresses. The deformation characteristics of SPIF during the tool contact could induce a strong element deflection (as probed by the choice of $d_{\max}$ equal to 0.2 mm in the previous section). Hence, the shell hypothesis of the mid/neutral plane could be considered as somewhat severe. The membrane stress distribution in Figure 5.23 for element (a) and (b) could be considered as the sum of bending/unbending plus stretching, as previously observed by Eyckens *et al.* 2010.

The typical stress distribution is depicted schematically in Figure 5.24 assuming for simplicity elastic behaviour. Indeed true behaviour is more complex as plasticity occurs in both bending and unbending processes (see equivalent plastic

strain values in Table 5.9). Note that the local contact, generating σ_{33} stress as well as through thickness shear stress justify a slightly higher plastic strain near the internal surface. The stress profile of σ_{33} related to element a) in the wall middle section presents the typical gradient expected due to tool contact. The GP near the internal surface (GP 5) is associated to the tool compression effect during the forming path and zero stress on the external surface (GP 1). For element b) at change of slope, a more complex pattern of σ_{33} is observed due to further plasticity increase at this location during the forming of the second pyramid, however higher number of GP computation confirms a null stress at external surface.

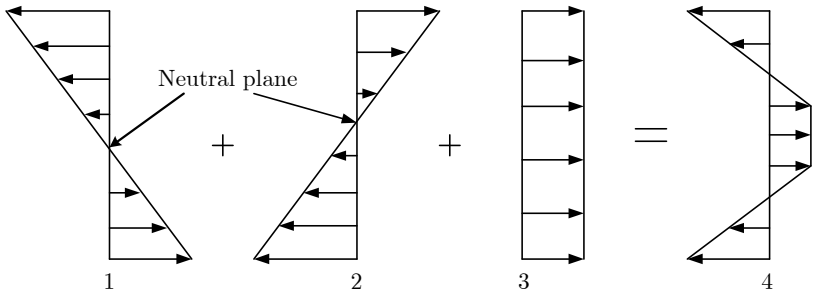

Figure 5.24: Simple elastic schematic representation of bending/unbending plus stretching associated to elements a) and b).

Figure 5.25 presents the relative stress (σ/σ_0) values at 90 mm depth for each GP through the sheet thickness. Figure 5.22.2 is its corresponding mesh, note that the tool has been removed, it is an unloaded configuration.

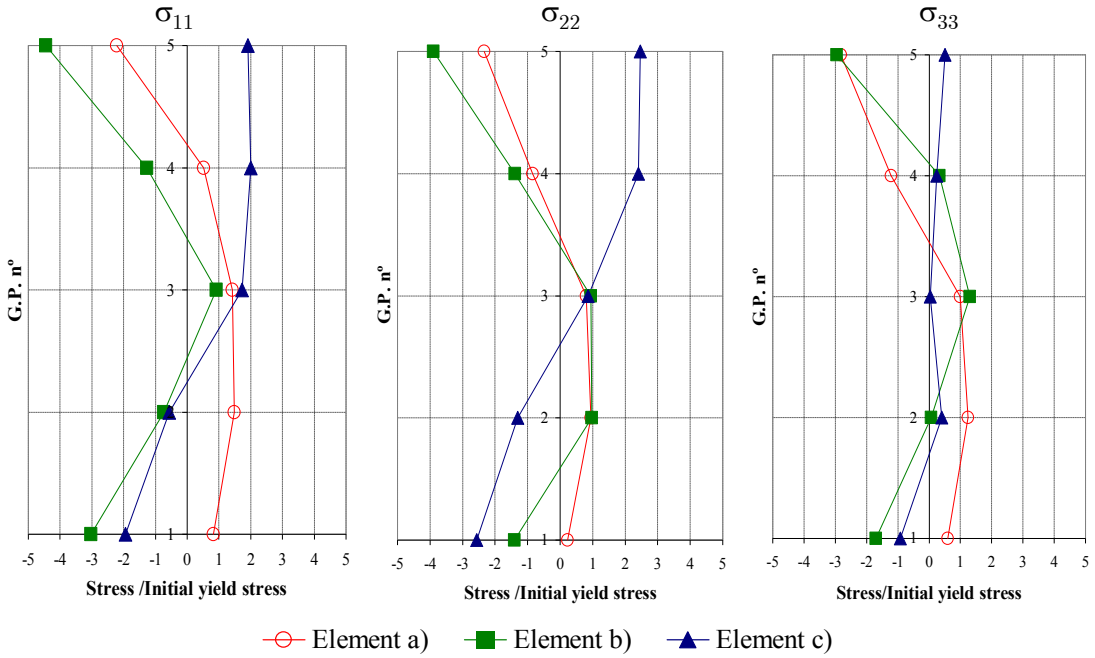

Figure 5.25: Relative stress components in thickness direction for the three elements at the end of 90 mm, after tool unloaded.

The elements a) and b) at the end of contour 90 have a similar stress profile to the pattern of contour 60, however, they present identical or higher values stress values. The strong increase of membrane stresses of GP 5 compared to Figure 5.23 as well as the values of equivalent plastic strain in Table 5.9 confirm that additional plastic deformation appeared at depth 60 (change of pyramid slope) during further forming (increased value from 0.599 to 0.855). Already mentioned in the work of Guzmán *et al.* (2012), the "tent" effect (Behera *et al.* 2011, 2012, 2013, 2014) is the name given to the displacement of the material at depth 60 mm during second pyramid forming (see Figure 5.20). As explained in Figure 12 of Guzmán *et al.* (2012), structural bending effect far from the tool location induces this displacement as the smaller slope angle increases the lever arm of the tool force and generates high moment in this transition zone. Guzmán *et al.* 2012 showed that it occurs only as an elastic effect for their case, however in the present work a different material is used and plastic strain in element b) clearly increases between contour at 60 and 90 mm depth. Comparing element b) at contour depth 60 mm (Figure 5.23) and element c) at contour depth 90mm in Figure 5.25 and in Table 5.9, one can observed typical differences of stress states in SPIF formed shapes with high and low slopes respectively. Plastic strain levels in all GP as well as the normal stress and shear stress components in thickness direction of element c) decreased at the second wall angle slope. The thickness profile of σ_{11} and σ_{22} stress components of element c) in Figure 5.25 is associated to one moment and a stretching stress suggesting that plasticity did not occurred in both bending and unbending events.

Table 5.9: Relative values of σ_{13}/σ_0 and σ_{23}/σ_0, ε^p_{eq}, yield strength and σ_{eq} at contours 60 and 90.

Stress		Contour 60 mm			Contour 90 mm		
	Element	a	b	c	a	b	c
σ_{13}/σ_0	GP 5	-0.379	-0.146	0.006	-0.344	-0.096	-0.160
	GP 3	0.112	-0.271	-0.002	-0.026	0.158	0.181
	GP 1	0.668	0.270	-0.002	0.538	0.3273	0.495
σ_{23}/σ_0	GP 5	-1.145	0.080	-0.000	-1.027	-1.585	0.005
	GP 3	0.554	0.076	0.001	0.429	0.658	0.031
	GP 1	0.598	-0.136	0.001	0.593	1.264	0.193
ε^p_{eq}	GP 5	1.251	0.599	0.000	1.251	0.855	0.483
	GP 3	0.873	0.356	0.000	0.873	0.571	0.283

	GP 1	1.077	0.581	0.000	1.077	0.869	0.491
Yield strength [MPa]	GP 5	490.677	432.721	144.916	490.719	459.828	417.064
	GP 3	461.408	395.898	144.916	461.408	429.186	380.753
	GP 1	478.321	430.460	144.9161	478.321	461.061	418.199
σ_{eq} [MPa] von Mises	GP 5	464.132	398.134	20.720	462.506	425.074	329.010
	GP 3	262.035	382.365	11.043	223.949	93.438	270.531
	GP 1	232.149	425.234	34.809	256.896	458.994	305.779

5.2.3. Remarks of two-slope pyramid simulations

In general, the shape prediction and the stress analysis in thickness direction are the main contributions of this work. An acceptable accuracy was obtained when comparing the numerical results in different stages with experimental DIC measurements. Most of numerical shape error are from transitions areas, as near the backing plate edge and at the wall angle change. However, the error near the backing plate is only noticeable at the end of the simulation. The adaptive remeshing parameter $d_{\max}$ showed negligible influence on CPU time. The increase of $d_{\max}$ value improved the shape accuracy at the wall angle change on section A and B but the same improvement was not verified for sections C and D. However, concerning the relative shape error found for different $d_{\max}$ values used, the error difference between both shape sections can be considered negligible. The adaptive remeshing parameter which has exhibited a significant influence in the shape accuracy was the number of nodes per edge (n).

The stress analysis through the thickness of the sheet exhibited a bending/unbending plus stretching, already documented in previous publications, while the shear stresses remain very small. The combination of membrane under tension with bending behaviour was also found at different levels of depth. The elastic stress state affects the geometrical shape accuracy, mainly, after the wall angle transition. For the studied case (DC01 steel material and a 2 slopes, non-symmetrical pyramid with angles 60/30° and 60/35° and respective depths 60/90 mm), one can confirm that at the wall angle slope transition, it is plastically affected by the second pyramid forming process.

5.3 Second analysis of a two-slope pyramid

The present section concerns a detailed analysis of two-slope pyramid geometry described in Section 5.2 by Figure 5.15. The geometry is kept the same, but the material used is a different steel alloy elastically described by E = 210000 MPa and ν = 0.3, named HC660XD steel (Volkswagen VW 50060 Hot Dipped Galvanised Dual Phase steel). The plastic domain is described by a von Mises yield surface and an isotropic hardening behaviour defined by means of a Swift law. Table 5.10 describes the material hardening parameters obtained from uniaxial tensile test in 0° direction. The initial yield stress (σ_0) is 784.0 MPa.

Table 5.10: Material parameters of HC660XD steel.

Name and hardening type	Parameters
Swift Isotropic hardening	K=1586.17 MPa; n=0.128; $\varepsilon_0 = 0.02$

The geometry described in Figure 5.15 has been experimentally repeated resorting to an innovative SPIF machine developed at University of Aveiro, Department of Mechanical Engineering, named SPIF-A (Alves de Sousa *et al.*, 2014). Previously, on the external surface of the material sheet with 1 mm thick a small circular grid was printed, in order to measure sheet deformation by DIC procedure with ARGUS software. Figure 5.26 exhibits the shape forming process and the experimental measurement of the deformed shape through ARGUS software and its hardware equipment, which uses only one camera.

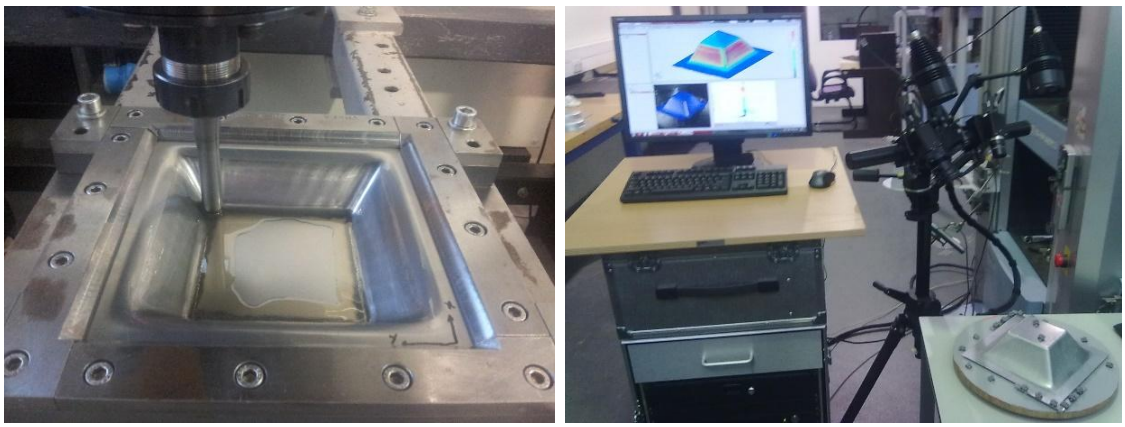

Figure 5.26: Experimental measurements resorting to DIC from ARGUS software.

Figure 5.27 exhibits the measurement of the cross sections on the external surface (opposite face with respect to the tool contact) of the final deformed shape. In both figures the reference points of each section set to zero are shown, in order to match with the similar points of the numerical results.

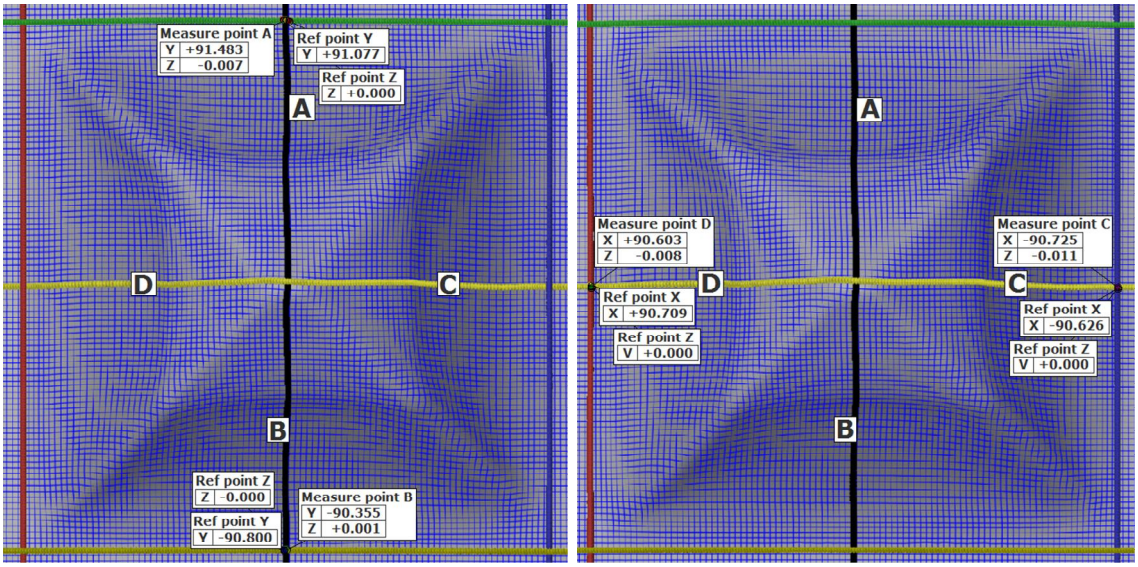

Figure 5.27: Sections measurement on the external surface of the shape.

Afterwards, the comparison is made between the measurements obtained from DIC and the numerical results from the implicit analysis, combined with adaptive remeshing method.

The simulations were carried out with a 180° coarse mesh for the adaptive remeshing procedure, as shown in Figure 5.16 2), with 5 GP through the thickness. The adaptive remeshing strategy is applied with the following refinement parameters: 3 nodes per edge (n=3), α equal to 1.0 and $d_{\max}$ equal to 0.1 mm.

The penalty coefficient (K_P and K_τ) of the contact elements between the tool and the metal sheet mesh was chosen as 1000. Concerning the friction coefficient, μ, given the absence of experimental data, it was assumed to be 0.05.

Table 5.11 presents the average CPU time using adaptive remeshing procedure with the steel chosen.

Table 5.11: Adaptive remeshing technique performance.

Mesh type	CPU time	Initial nº of elements	Final nº of elements
n=3 d_{max}=0.1mm	15h:11m:13s	298	4394

5.3.1. Prediction of the shape and thickness

This section focuses on the prediction of the shape and thickness of the pyramid for sections AB (Y cut) and CD (X cut). As the experimental measurements were measured on the external surface of the shape, the numerical shape prediction is extracted for the bottom nodes of the mesh. Figure 5.28 and Figure 5.29 present the shape and thickness prediction.

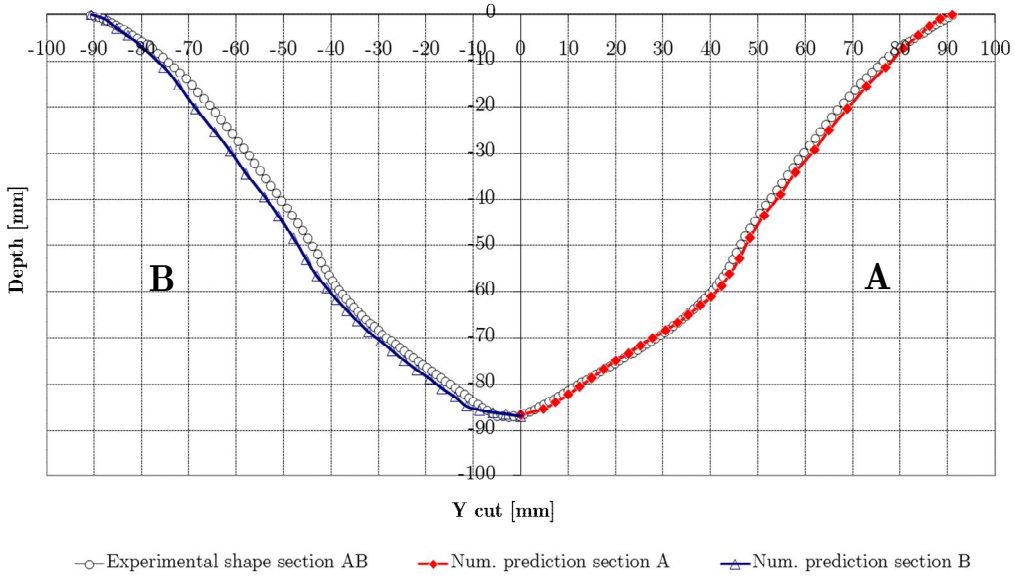

Figure 5.28: Final shape prediction of section AB corresponding to Y cut.

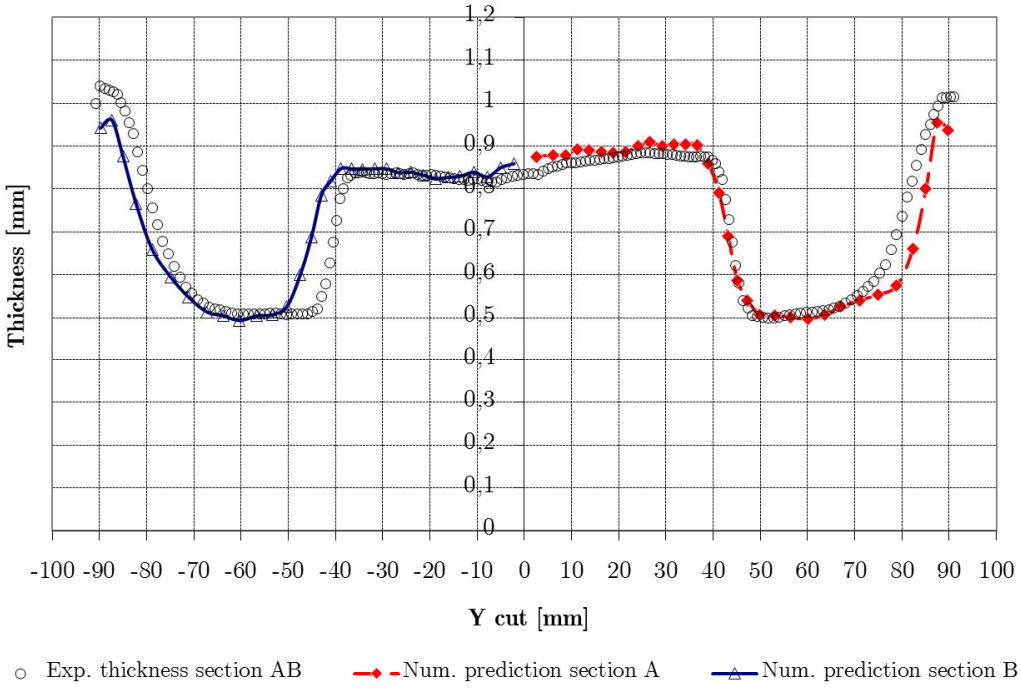

Figure 5.29: Thickness prediction of section AB corresponding to Y cut.

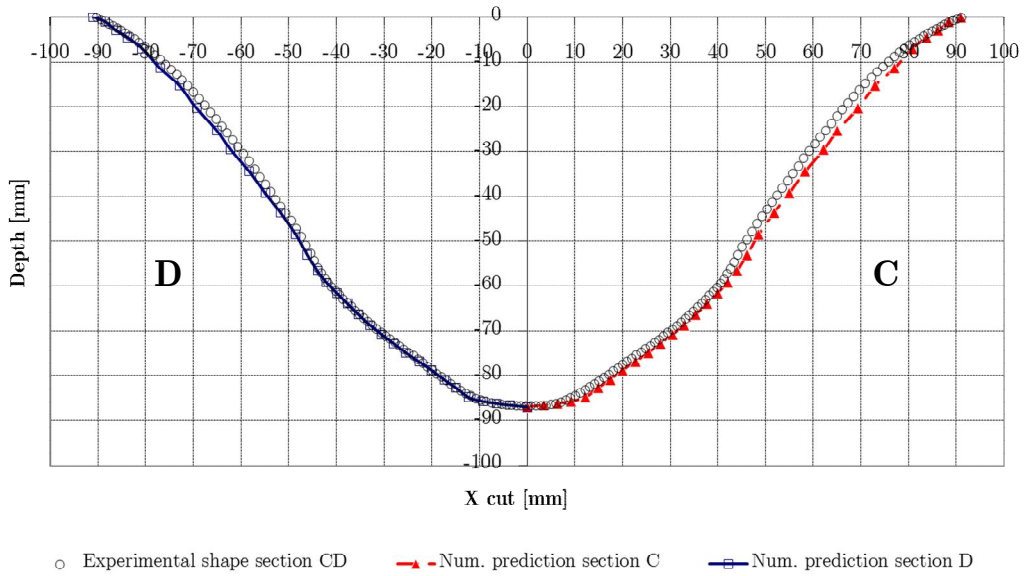

Figure 5.30: Final shape prediction of section CD corresponding to X cut.

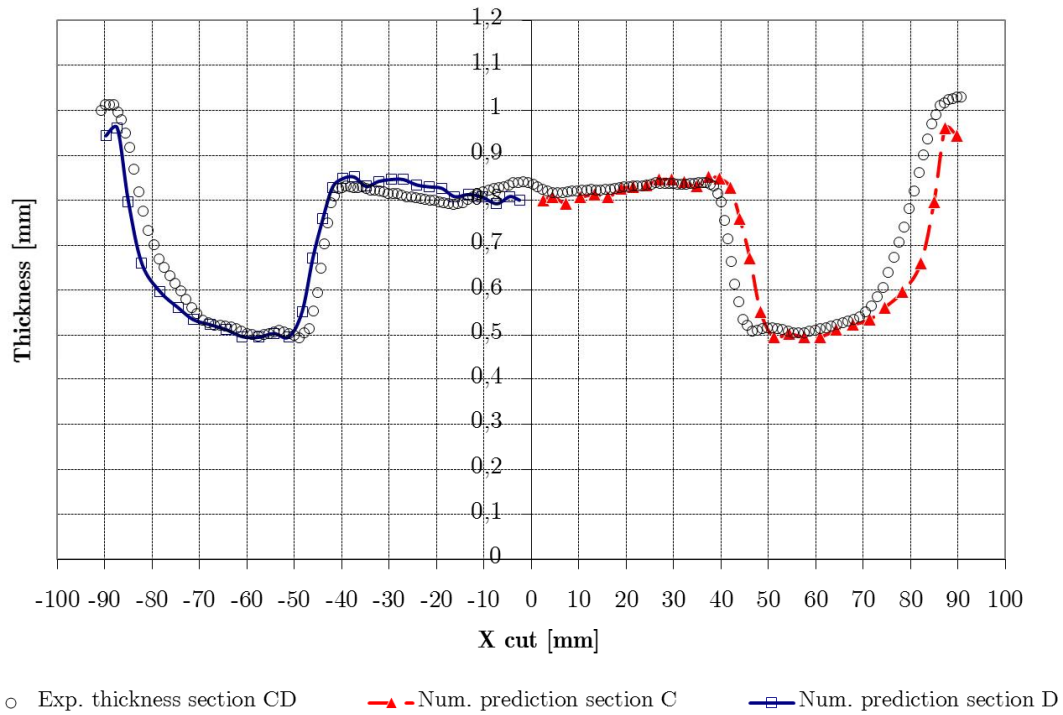

Figure 5.31: Thickness prediction of section CD corresponding to X cut.

As shown above, an acceptable correlation was found between the simulation results and the experimental measurements. The shape error is limited to a small deviation of millimetre, but not uniform for all sections, with evident error at the first wall angle slope of section B of Y cut, Figure 5.28. The wall angle transition is well predicted in particular for sections A (Y cut) and D (X cut).

In terms of thickness prediction, the largest error can be found near the clamping boundary conditions, which exhibits a thinner prediction than the experimental data. The deviation of the horizontal axis in the thickness comparison figures is proportional to the deviation of the shape prediction. Concerning the wall angle transition effect, it is visible that the thickness reduction is higher at the first wall angle than for the second slope wall angle.

Additionally, from the comparison of both shape predictions using two different steels to build the same geometry, it reveals better accuracy for the results using DC01 (see Section 5.2.1). As possible explanation for less shape accuracy prediction in the second attempt using the material described in Table 5.10 can be the occurrence of springback effect during the forming and after the unclamping. This means that the isotropic hardening is not adequate to take into account the springback effect, as well as the influence of the GP number through sheet thickness, as reported by Alves de Sousa *et al.* (2007).

5.3.2. Major strain prediction

The current section is focused on the analysis of the major strain prediction along both sections, schematically shown in Figure 5.15, in comparison with the experimental data. The major strains of the numerical model are computed at the integration points. This means that the numerical major strains presented below are obtained from the integration point near to the bottom layer of the mesh. The minor strains are negligible in comparison with major strains.

Figure 5.32 and Figure 5.33 exhibit the major strain comparison between the experimental data and the simulation prediction.

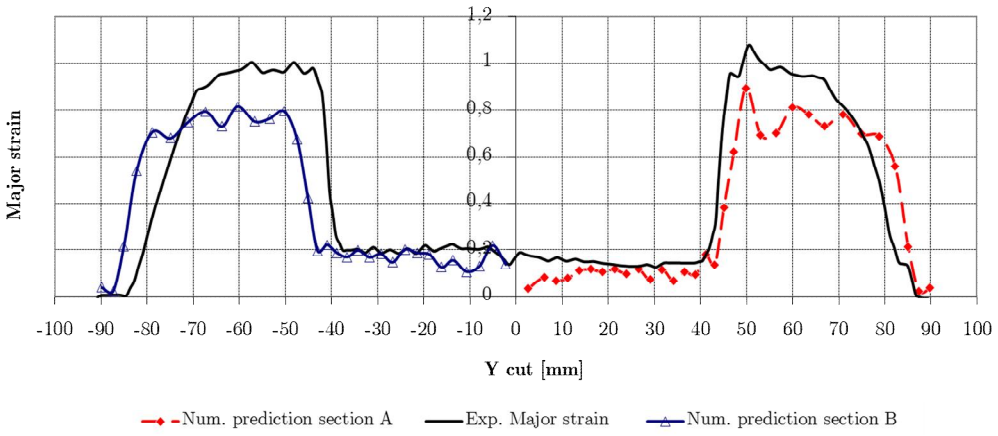

Figure 5.32: Final major strain prediction of section AB corresponding to Y cut

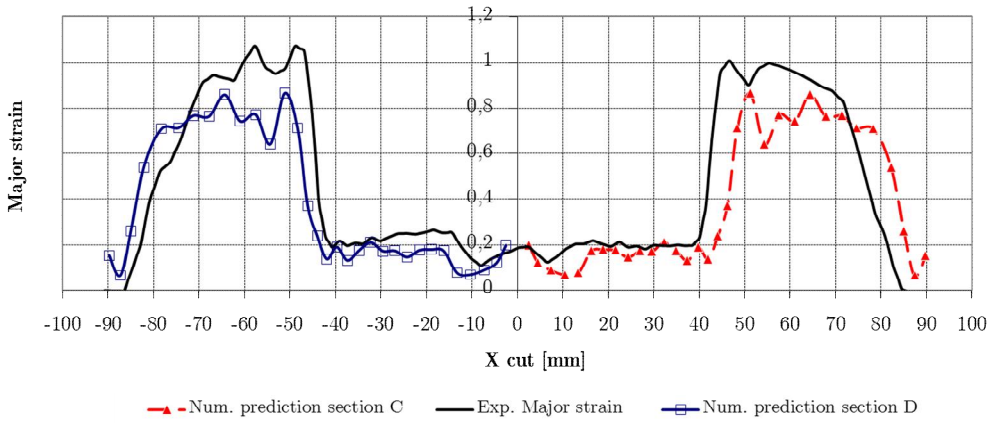

Figure 5.33: Final major strain prediction of section CD corresponding to X cut.

Both results, experimental and numerical ones, follow a similar pattern with a pronounced large level of major strain at the first wall angle slope. The experimental measurements present a higher level of major strain than the simulation results. A possible explanation for this difference can be measurement effects of the deformed sheet surface from DIC due to the occurrence of out-of-plane motion introducing strain errors. Figure 5.34 schematically presents the physical meaning of out-of-plane motion (Lava *et al.*, 2014) and the strain error, ε_{error}, occurrence due to the surface bent originating a concave surface. This bent effect of sheet surface is well visible in the pyramidal shapes walls.

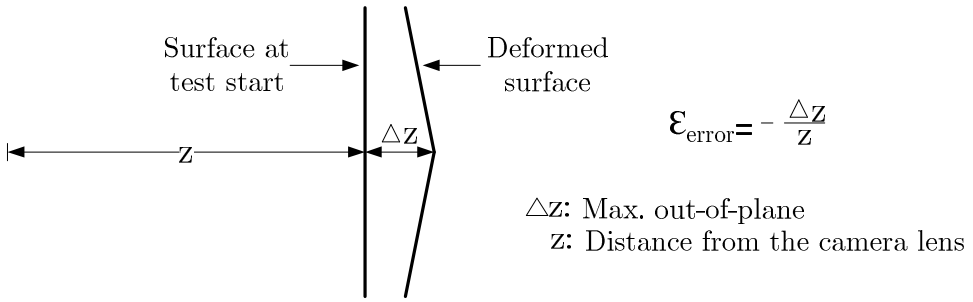

Figure 5.34: Physical meaning of out-of-plane motion.

5.3.3. Through thickness stress analysis

As final analysis point, in terms of average CPU time, the simulations performed with DC01 material (Table 5.4) presents better performance compared to the simulation with HC660XD material (Table 5.10), for equivalent adaptive remeshing parameters (n=3; α=1.0; d_{max}=0.1 mm). This means that the material parameters and hardening law influence the performance of the numerical

simulation. For identical geometry and sheet thickness, the mixed hardening applied to DC01 steel achieved better CPU performance and shape accuracy than the isotropic hardening by means of the material parameters of Table 5.10. The CPU for HC660XD material simulation time increases in 15% in comparison with DC01 steel simulation. In order to understand the origin behind the performance difference between both steel alloys, the equivalent plastic strain, yield strength and equivalent von Mises stress are analysed. Table 5.12 presents the values of equivalent plastic strain, ε_{eq}^{p}, and equivalent von Mises stress, σ_{eq}, computed in different GP in thickness direction at contours 60 and 90. Those values were obtained from similar GP at equivalent elements location in the mesh, as schematically exhibited in Figure 5.15 a).

Table 5.12: Values of ε_{eq}^{p}, yield strength and σ_{eq} at contours 60 and 90.

Stress		**Contour 60 mm**			**Contour 90 mm**		
	Element	**a**	**b**	**c**	**a**	**b**	**c**
ε_{eq}^{p}	GP 5	1.442	0.584	6.64E-04	1.440	0.925	0.395
	GP 3	1.025	0.438	0.000	1.025	0.623	0.254
	GP 1	1.396	0.662	1.80E-03	1.400	0.814	0.441
Yield strength [MPa]	GP 5	1662.52	1481.20	742.724	1662.52	1570.80	1409.17
	GP 3	1591.56	1428.12	715.948	1591.56	1493.49	1332.25
	GP 1	1655.91	1505.27	777.266	1655.91	1545.42	1429.04
σ_{eq} [MPa] von Mises	GP 5	643.419	853.987	149.329	835.900	1011.99	745.230
	GP 3	483.366	469.657	48.887	361.012	915.812	471.949
	GP 1	376.296	1432.33	61.438	452.996	1240.66	599.851

From Table 5.12 is noticeable higher yield strength and equivalent von Mises stress values than in Table 5.9. Besides the hardening effect, another possible reason for the performance different between both materials is related with the plasticity level achieved. On the other hand, let us remind that the material parameters of steel HC660XD was obtained resorting to uniaxial tensile test which gives a limited parameterization of a proper material behaviour. Additionally, the increments/iterations number, using the steel HC660XD increased 33% in comparison with steel DC01. In terms of equivalent plastic strain both tables exhibit insignificant difference between the values of similar GP.

5.4 Simulation of multistage incremental sheet forming

The purpose of this section is to analyse the multistage forming to obtain a cone with vertical wall performed in five different stages. Instead of forming a 90° wall-angle cone directly, the forming starts with a 50° cone, followed by a 60, 70, 80 and 90° cone. Figure 5.35 schematically presents the strategy of five stages adopted to obtain a vertical wall angle shape.

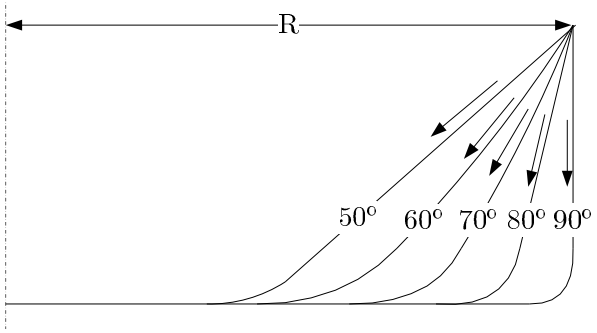

Figure 5.35: Strategy to form a vertical wall shape.

The global toolpath is composed of five times 30 contours, with a vertical step of 1 mm between two successive contours. The forming tool is a hemispherical tip with a diameter of 10 mm and the initial thickness of the sheet is 1.0 mm of AA1050-H111. Table 5.13 describes the material hardening parameters obtained from uniaxial tensile test.

Table 5.13: Material parameters of AA1050-H111.

Name and hardening type	Parameters
Swift Isotropic hardening	K=206.57 MPa; n=0.091; $\varepsilon_0 = 0.002$

Figure 5.36 exhibits a schematic view profile with the dimensions of the cone with vertical wall (a cylinder).

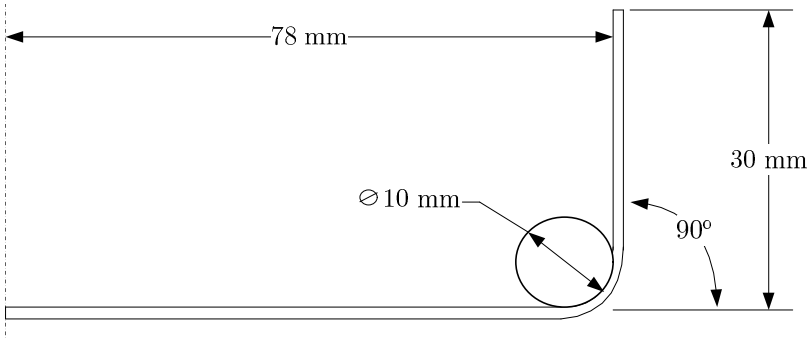

Figure 5.36: Dimensions of the cone with vertical wall angle.

The experimental tests were similarly carried out in University of Aveiro resorting to the concept SPIF machine, named SPIF-A. The procedure to measure the obtained deformed shape was similarly performed as mentioned in Section 5.3.

Figure 5.37 shows the final shape obtained and its measurement. The reference points are used by ARGUS software for assembling the photos in order to build the DIC of the shape.

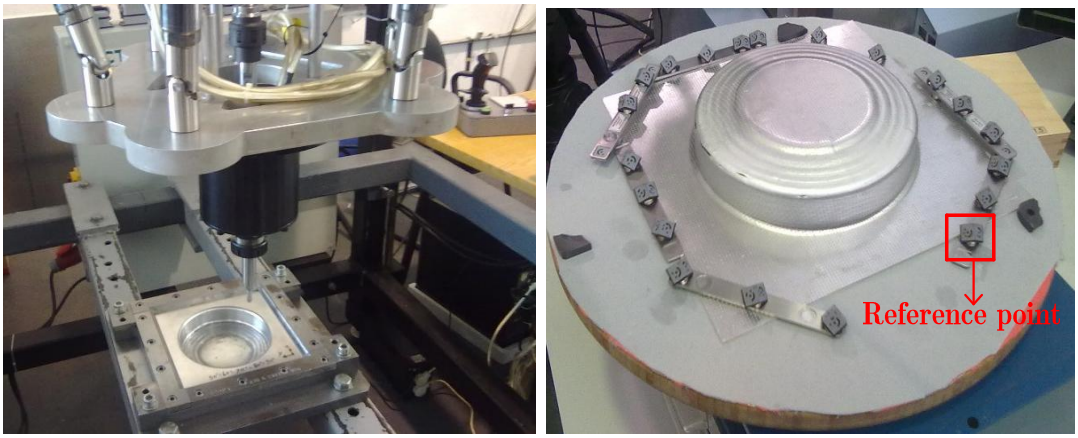

Figure 5.37: The final vertical wall angle shape.

Figure 5.38 shows all the deformed shapes at each forming stage. Afterwards, each shape was measured in order to be compared with the numerical predictions. The shapes measurement were obtained from the circular grid printed on the opposite surface with respect to the tool working surface.

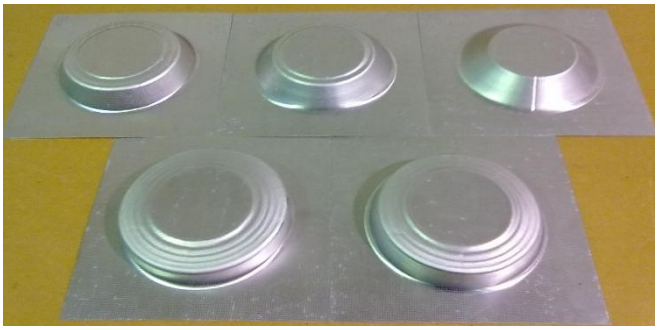

Figure 5.38: Shapes obtained after each forming stage.

The failure occurrence was observed at the last contour of the 90° wall angle stage, as shown in Figure 5.39.

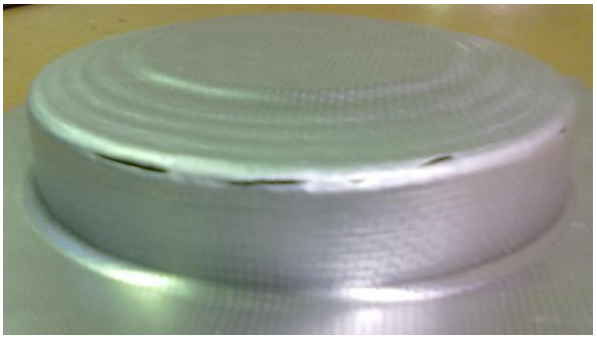

Figure 5.39: Occurrence of fracture in the last contours of the last stage.

In order to reduce the CPU time, a solution was to simulate only a 45° pie of the mesh with BINDS elements, on both edges of the pie to replace and minimize the effect of missing material. In terms of mesh density, an initial refined mesh (reference case) and a coarse mesh with an adaptive remeshing strategy are applied with the following refinement parameters: 3 nodes per edge (n=3), α equal to 1.0 and $d_{\max}$ equal to 0.05 mm. Both meshes concern one layer of RESS finite element in thickness direction with reduced integration in plane and 5 GP through the thickness. The contact interface between the tool and the sheet is performed taken into account a contact element, named CFI3D applied on the top layer of the RESS element. The penalty coefficients, K_P and K_τ, chosen are 1000 and the absence of experimental data concerning the friction coefficient, μ, it is assumed to be 0.01. Figure 5.40 and Figure 5.41 present both meshes used for the simulations of the multistage cone with vertical wall.

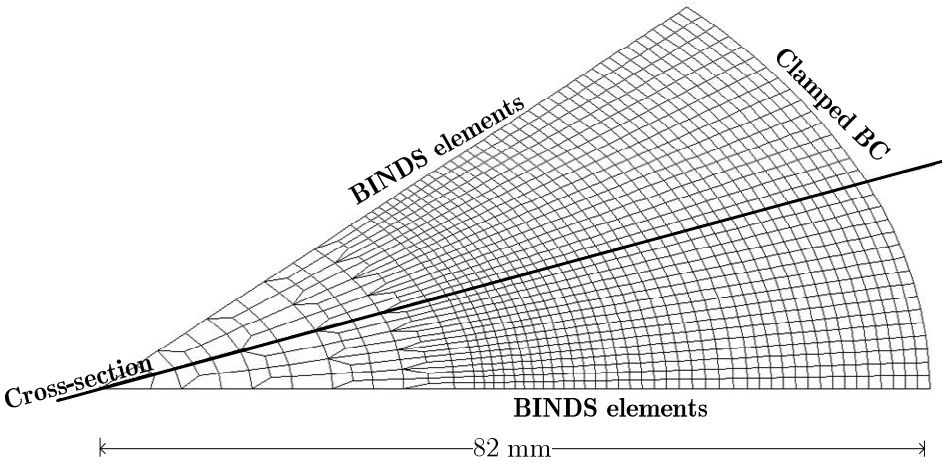

Figure 5.40: Reference mesh with 3325 finite elements.

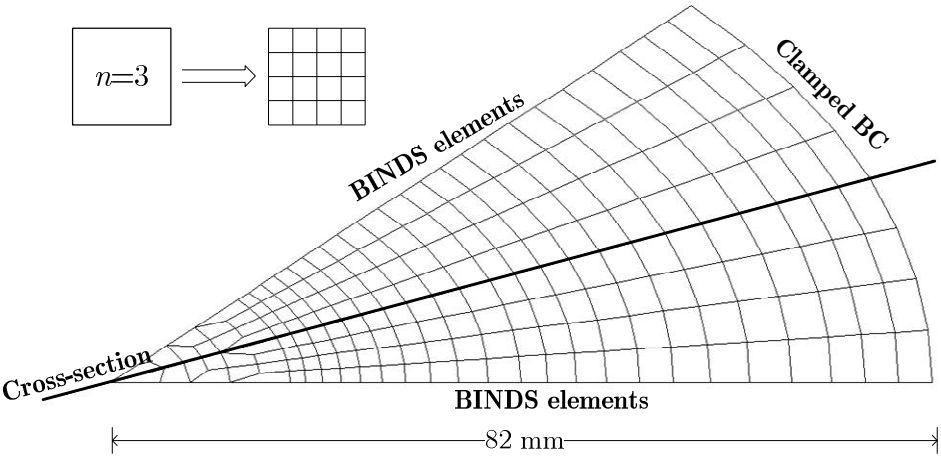

Figure 5.41: Coarse mesh of 523 finite elements used with adaptive remeshing method.

The simulation results are retrieved from the cross section at the middle of the 45° pie mesh, as exhibited in the previous figures. All numerical results in the following sections are obtained after unloading of the forming tool.

5.4.1. Shape and thickness prediction

This section presents the results related to the shape and thickness prediction at the end of each stage of the multistage forming procedure to generate a cone with a vertical wall. In addition, a large area of the current shape is never touched by the forming tool, so the accuracy of shape prediction is highly dependent of the quality of the finite element chosen and the transition zone description between flat bottom and wall. Figure 5.42 and Figure 5.43 exhibit the shape and thickness predictions at the end of the first stage, when the toolpath has produced a cone with a wall angle of 50°.

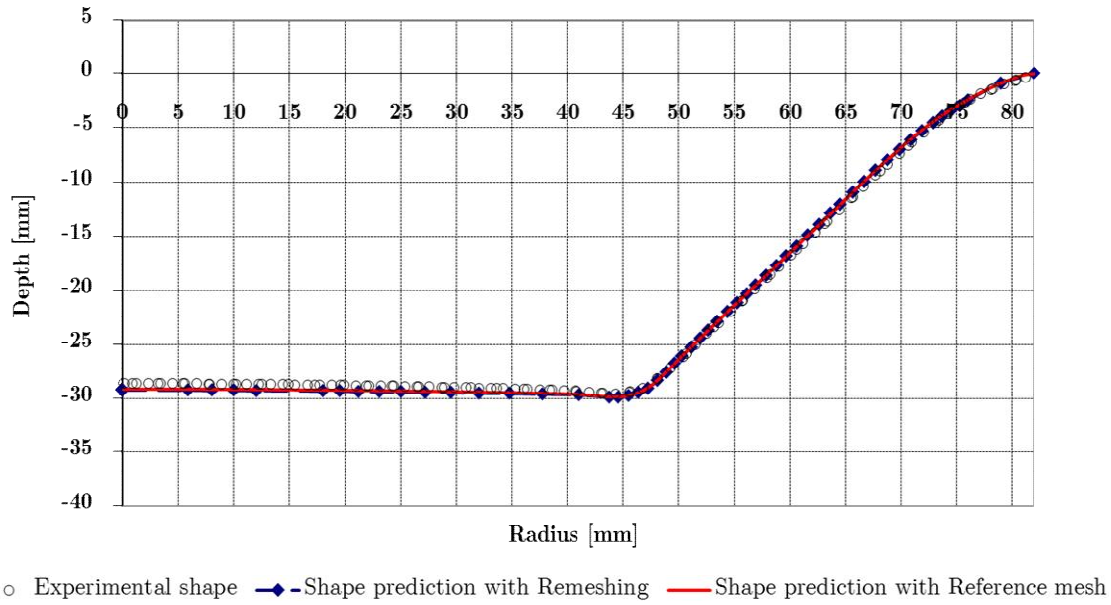

Figure 5.42: Shape after first stage of 50° wall angle.

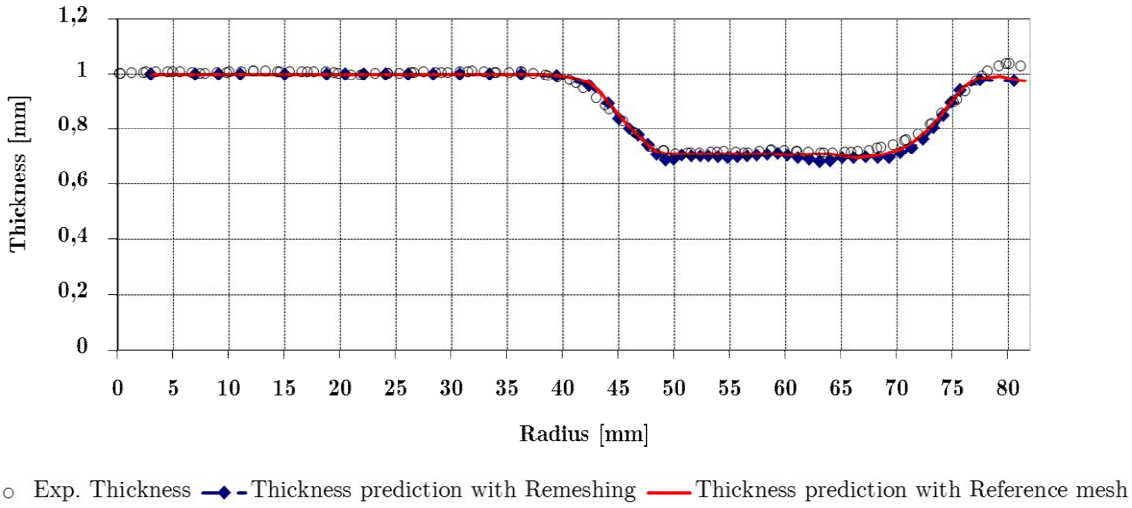

Figure 5.43: Thickness of the shape after the first stage of 50° wall angle.

The accuracy of the first cone with 50° wall angle, in particular the shape prediction of the final cone, it achieves a high level of precision for both mesh types. The thickness prediction also presents a good accuracy in the wall region with a slightly thinning near to the backing plate region, modelled by clamping boundary conditions.

Similarly, Figure 5.44 and Figure 5.45 show the result comparison at the second stage corresponding to a wall angle cone of 60°.

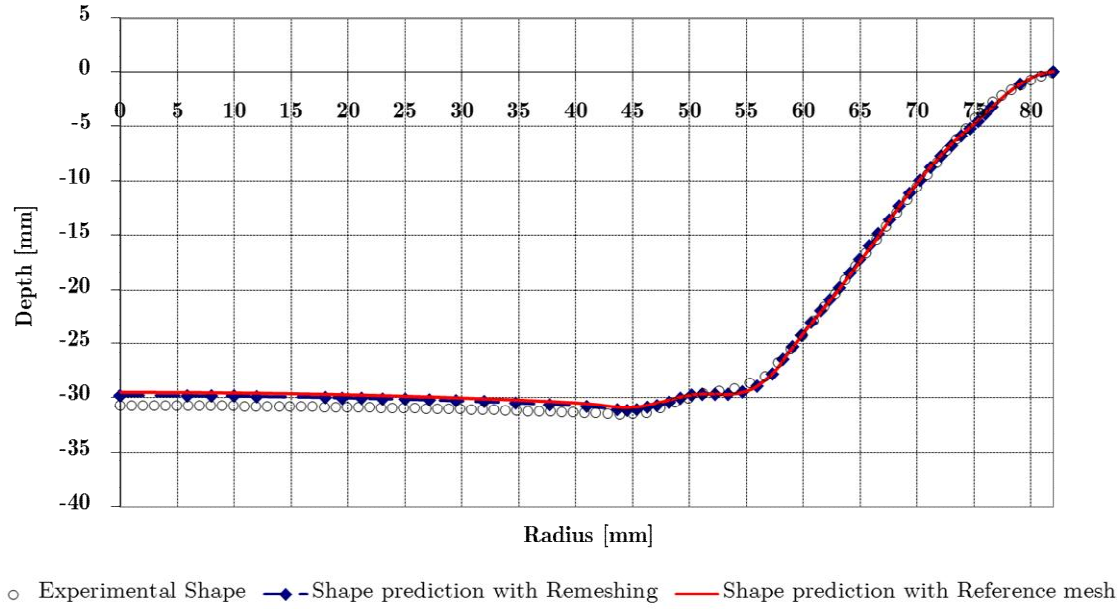

Figure 5.44: Shape after first stage of 60° wall angle.

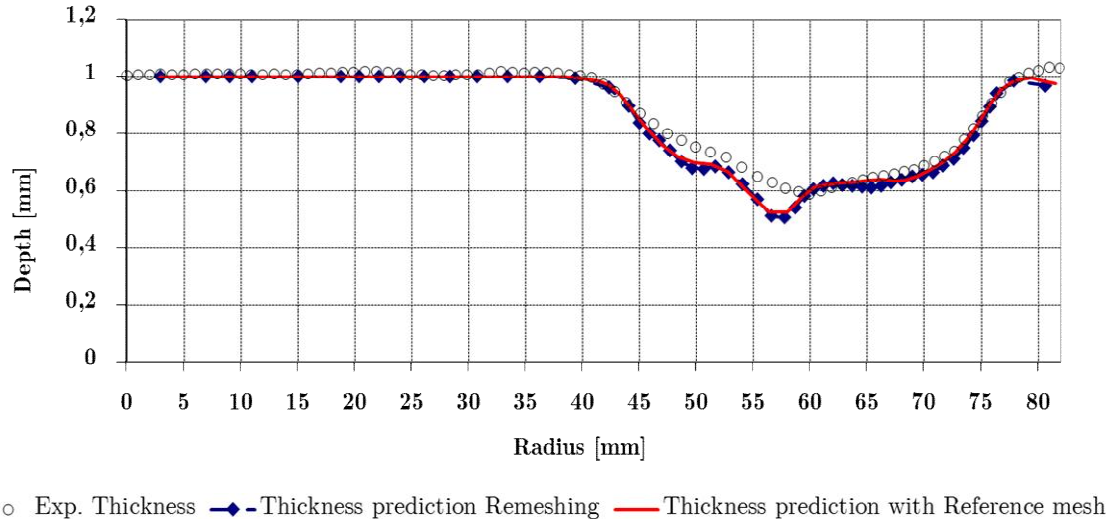

Figure 5.45: Thickness of the shape after the first stage of 60° wall angle.

From the second stage of the toolpath for 60° wall angle cone, the experimental measurement begins to show that the shape at the central region of the bottom surface is deeper and flatter than Finite Element predictions. The bottom of the shape numerically predicted did not follow the same trend at the same depth, the bottom shape prediction is slightly moved upwards. In terms of thickness prediction, besides the visible thinning occurrence near the clamping region, there is a second thinning effect, consequence of the corner shape from the previous stage, remaining noticeable for the following stage. A strain localisation appears in the zone with thinning effect from stage one. This experimental effect is

reproduced and evidenced in the numerical prediction, as can be seen on the external bottom surface of the experimental specimens in Figure 5.38.

Analogous observations can be associated to the further stages, showing that the prediction of the bottom of the cones becoming less and less accurate during the simulation progresses. Concerning the measured experimental thickness, it is not able to correctly exhibit the thinning effect of the corner effect left by previous stages. However, this thinning effect is not present (it can be seen by eyes and yields to fracture at the last stage) in the measurements due to technical issues. As the tool travels several times on the same local during the multistage forming, consequently the printed grids on the external surface becomes less visible especially at the transition region. This leads to measurement difficulties and to overcome this problem the DIC software allows the interpolation of missing regions, in particular corners. However, this strategy introduces measurement errors, as it can be seen in Figure 5.46. Notice that the marks left by the previous stages visible in Figure 5.38 are not observable on the surface of mesh generated for measuring thinning within the software. Thinning is extracted from a false geometrical shape, confirming accuracy problems within measurements.

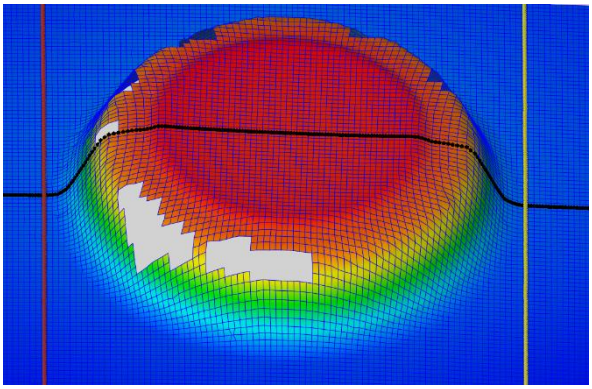

Figure 5.46: Measurement of cross section of 70° wall angle cone (colour lines of depth).

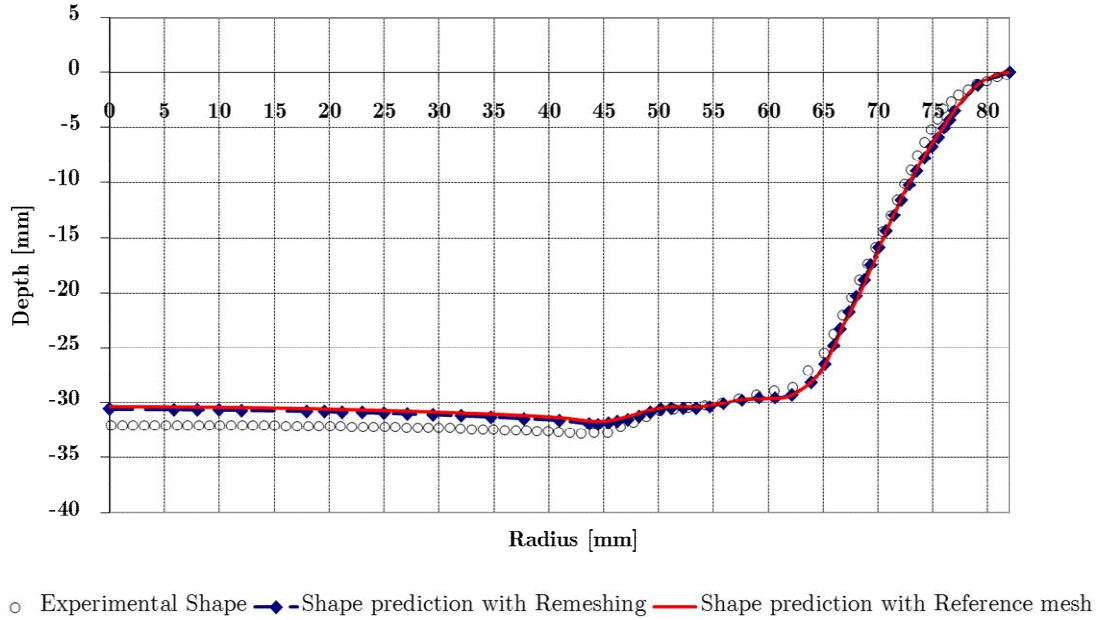

Figure 5.47: Shape after first stage of 70° wall angle.

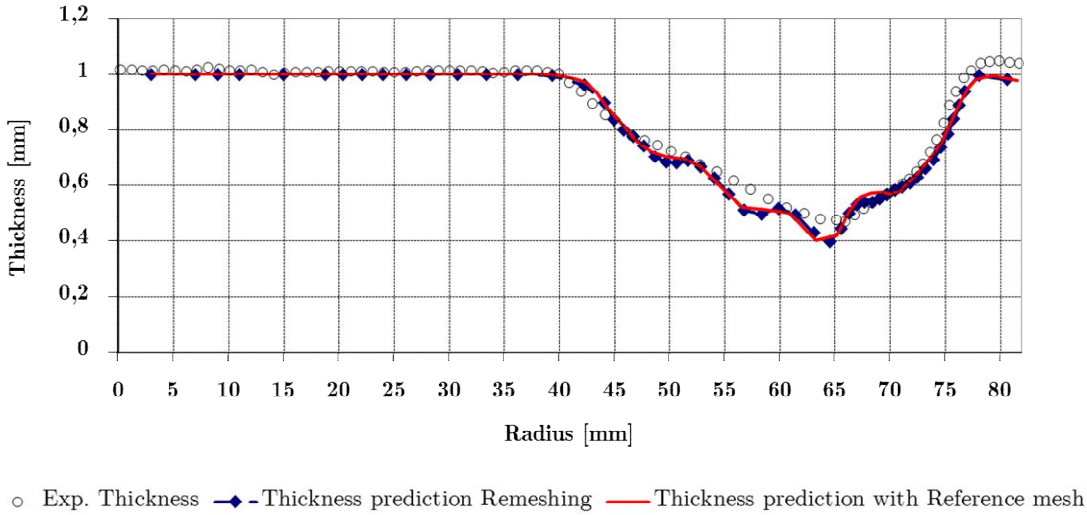

Figure 5.48: Thickness of the shape after the first stage of 70° wall angle.

Notice that the peak at the transition zone due to previous wall angle stages disappears from the DIC measurement and it is negligible in predicted shapes, but not in the actual piece (see Figure 5.38). On the other hand, the thickness profile maintain thinning peaks as consequence of previous stages, as well as the thinning effect of the corner at the current stage. Similar observations can be seen in the next forming stages.

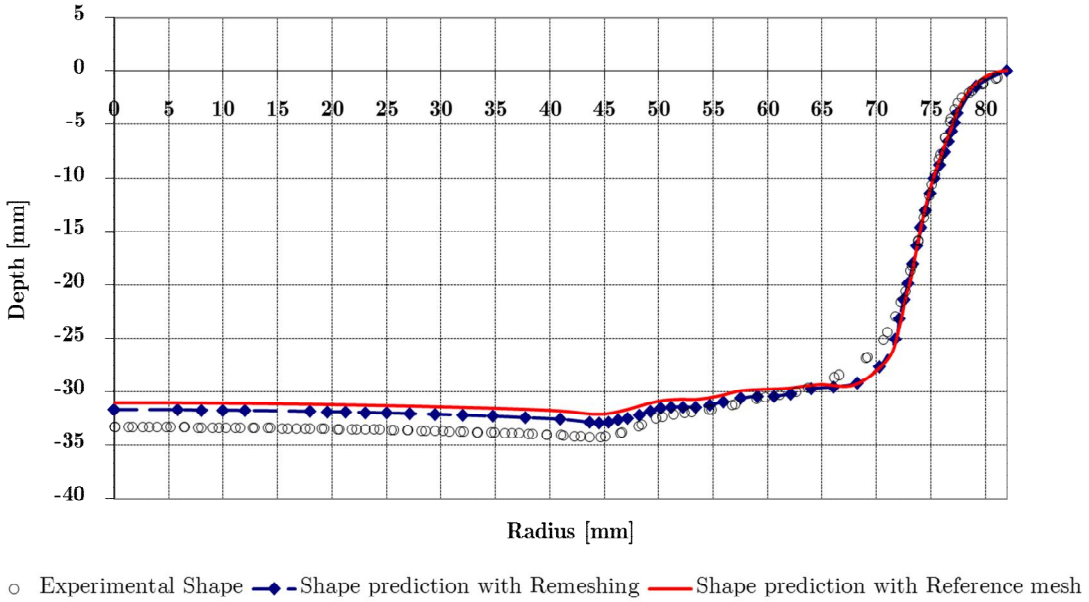

Figure 5.49: Shape after first stage of 80° wall angle.

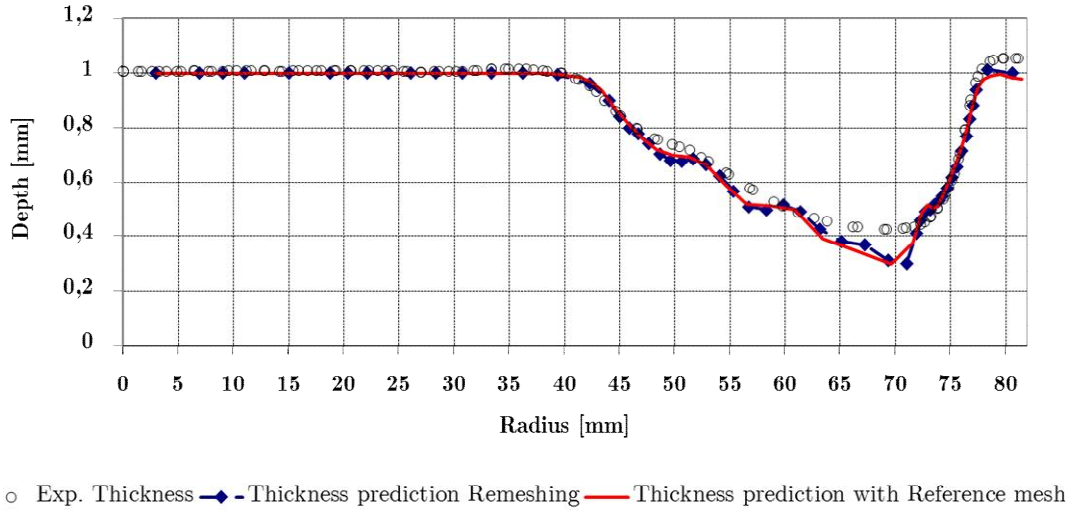

Figure 5.50: Thickness of the shape after the first stage of 80° wall angle.

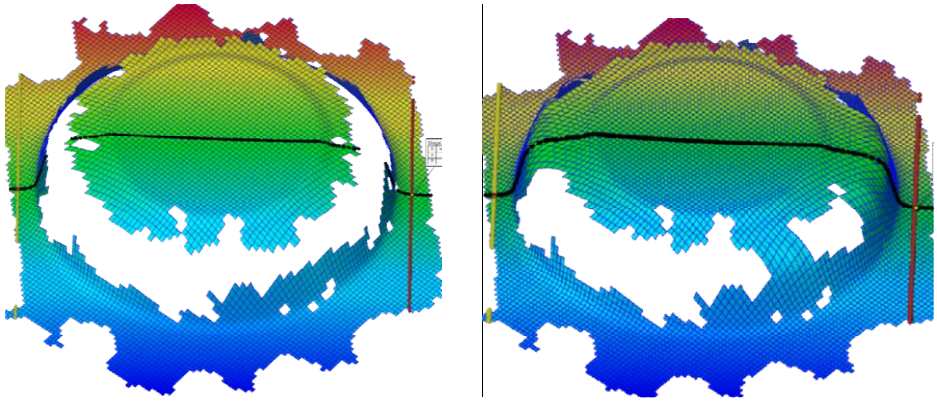

Figure 5.51: Application of interpolation procedure from ARGUS software in 80° wall angle cone.

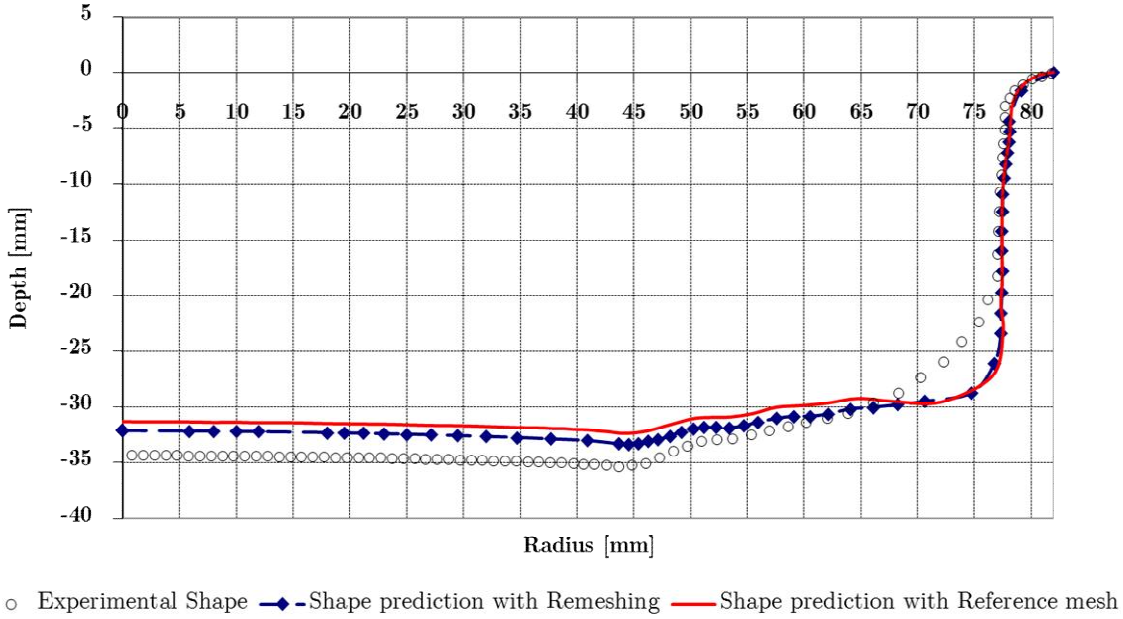

Figure 5.52: Shape after first stage of 90° wall angle.

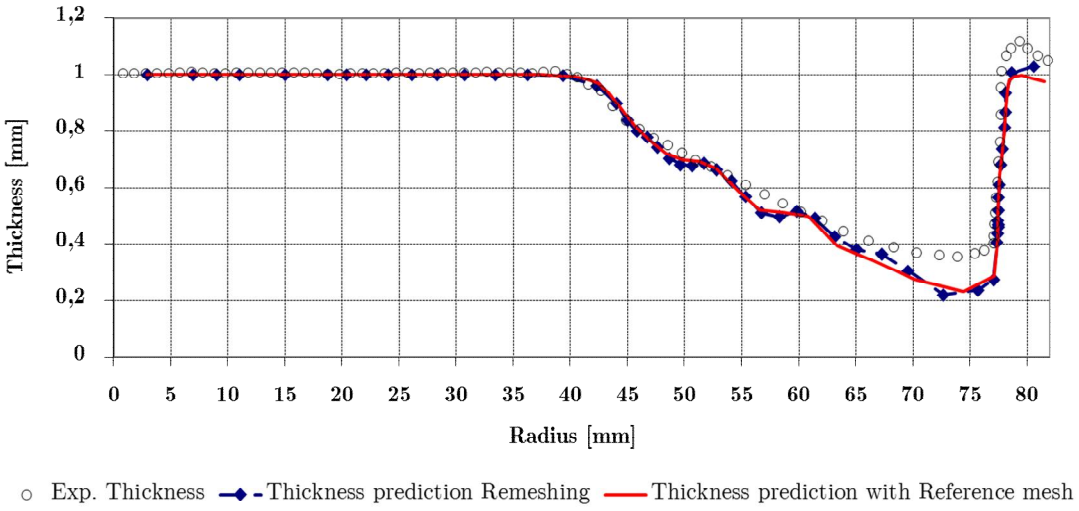

Figure 5.53: Thickness of the shape after the first stage of 90° wall angle.

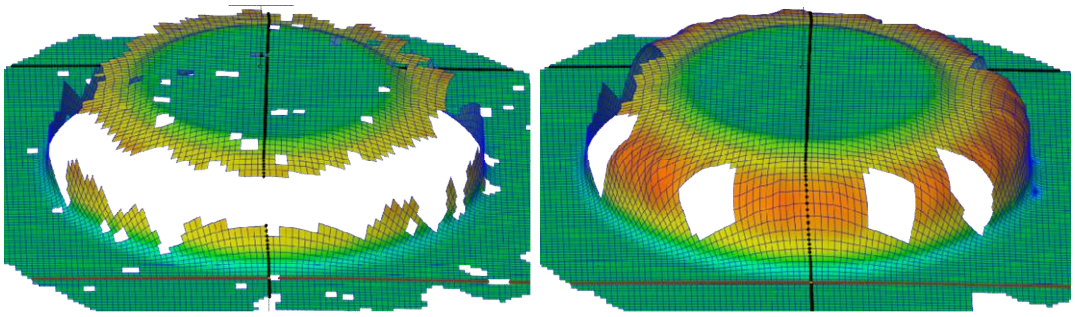

Figure 5.54: Application of interpolation procedure from ARGUS software in 90° wall angle cone.

Both meshes predict similar geometry at the transition between the bottom and the wall. However, at the centre mesh region in the last two stages, 80° and 90° wall angles, an evident deviation between both meshes is observed.

The difference between the experimental thickness measurement and the numerical thickness is more pronounced at the transition region, showing overestimation of numerical thickness reduction compared to DIC measurements. However, the accuracy of Finite Element prediction compared to our measurements is confirmed by the fact the fracture occurred at the last stage forming of wall angle with 90°, as shown in Figure 5.39, means that the numerical model presents a realistic thinning.

Figure 5.55 presents the nodal displacement in the centre of both meshes in comparison with the experimental measurement, where the tool never touched. This region is dependent of the elements stiffness and not constrained by the tool displacement, as in the wall region.

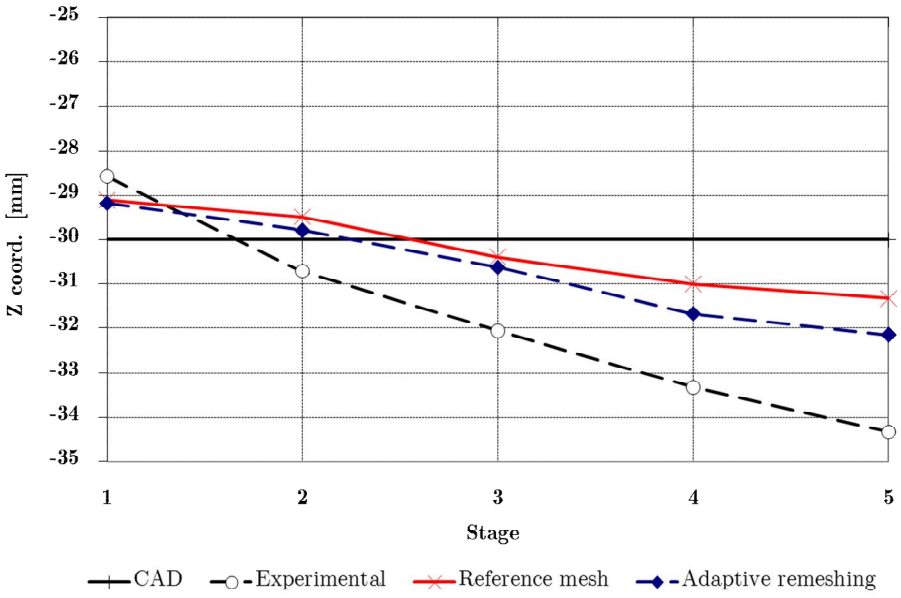

Figure 5.55: Depth in the centre of the cone mesh at the end of the 5 stages.

Similar analysis using shell elements was presented by Henrard (2008), which uses a plane stress law. The RESS element uses a 3D stress law and it allows computing the stress distribution across the thickness. It improves the approximation of the experimental results. The error between the experimental data and the numerical prediction increases at each stage and for adaptive remeshing method, the maximum deviation is 6.33% (slightly less than the

reference mesh). However, the error between the experimental shape and numerical prediction is subjected to an errors of the measurements as previously described.

5.4.1.1. Second analysis of multistage sheet forming

In order to confirm the numerical results accuracy of shape and thickness predictions, the multistage forming simulation presented in the work of Henrard (2008) was carried out with RESS and adaptive remeshing. The shapes were measured with laser scanner after each of the five stages in this research. All the numerical results are reported in Appendix B. Regarding the numerical results obtained, they have demonstrated the ability to achieve a high level of accuracy in the simulation of multistage forming. In addition, the existence of thinning peak due to transition zone of previous wall angle stages numerically predicted are accurately confirmed with experimental data. Furthermore, different yield surface definitions were tested using the material parameter from Henrard (2008) in order to analyse their influence in the shape and thickness predictions. Globally, all yield surface definitions showed similar thickness predictions without significant differences between them, achieving a very good accuracy in comparison with the experimental data. The shape prediction using isotropic and anisotropic yield surfaces exhibited similar level of accuracy regarding the experiments. The kinematic hardening law presents similar accuracy level at the wall region and transition corner, but higher deviation at the centre region of the shape bottom, as shown in all simulations of Appendix B.

5.4.2. Major strain prediction

The following results present the numerical major strain prediction computed at integration point level. The chosen results correspond to the integration point close to the external surface, as similarly the experimental data are obtained from the external sheet surface.

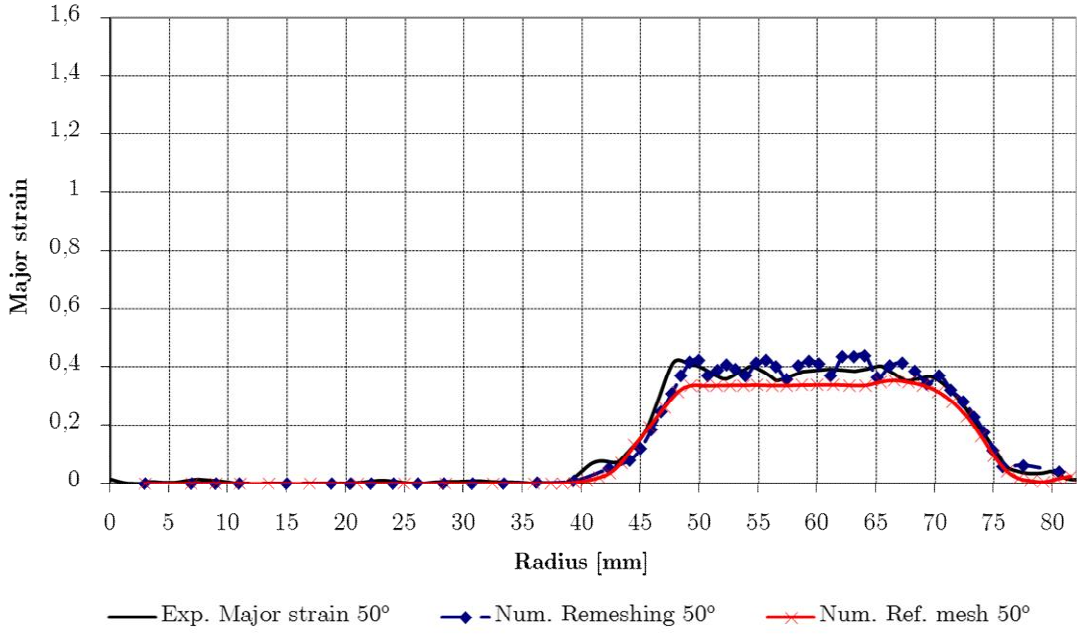

Figure 5.56: Final major strain prediction of 50° wall angle shape.

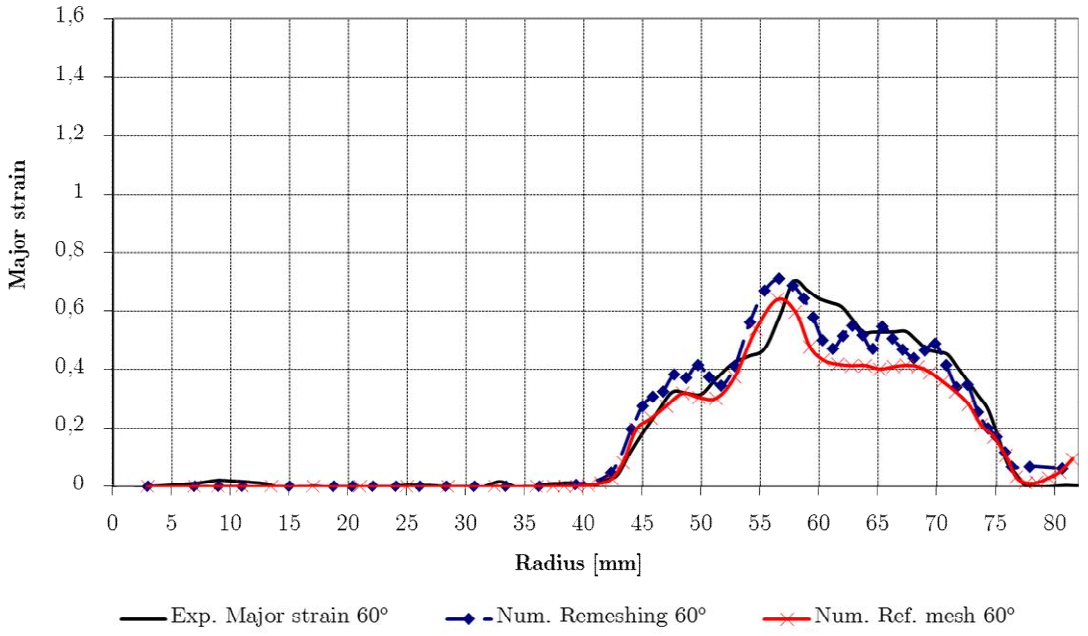

Figure 5.57: Final major strain prediction of 60° wall angle shape.

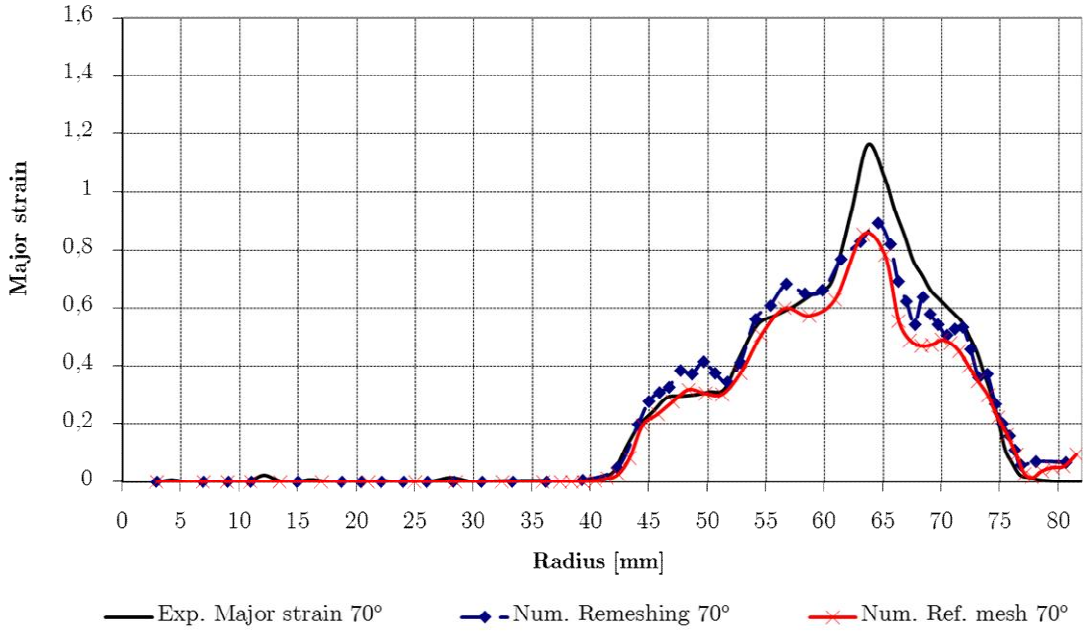

Figure 5.58: Final major strain prediction of 70° wall angle shape.

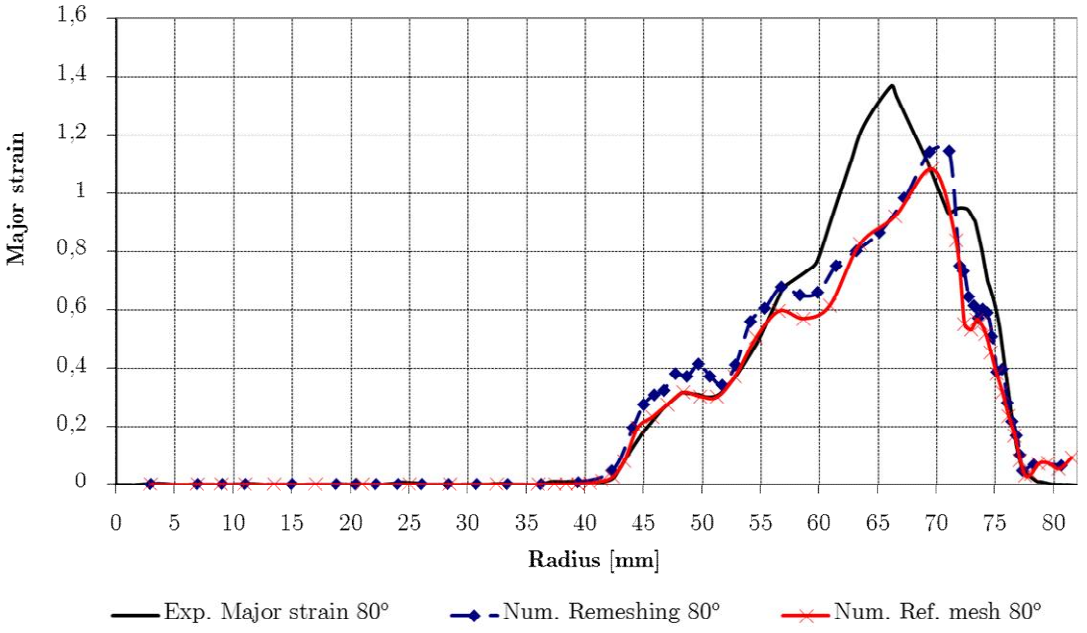

Figure 5.59: Final major strain prediction of 80° wall angle shape.

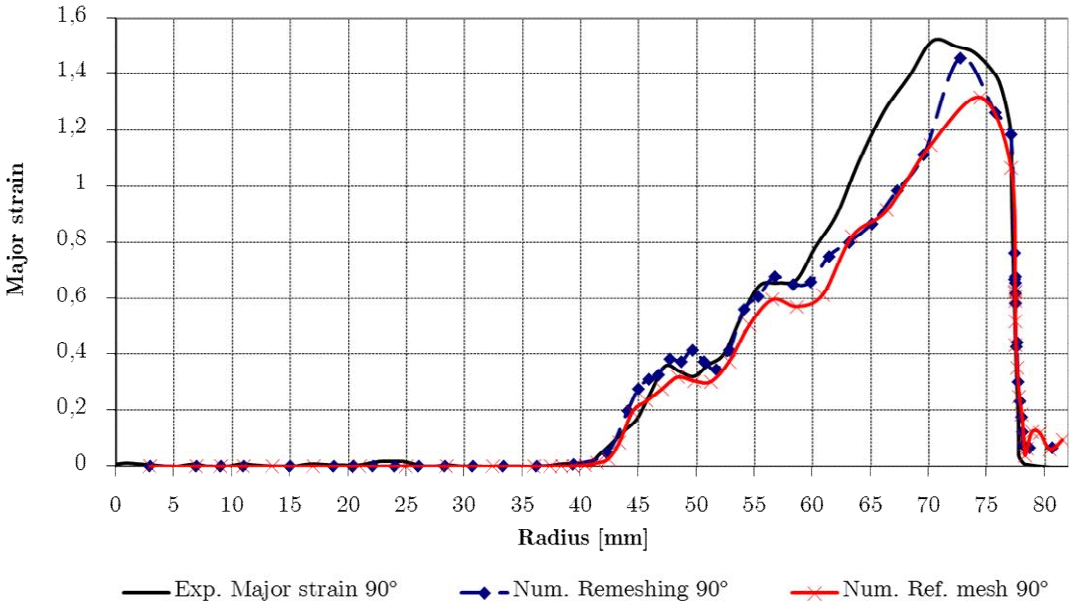

Figure 5.60: Final major strain prediction of 90° wall angle shape.

All previous results exhibit the increase of major strain for each forming stage, from 50° wall angle until the final target shape with a wall angle of 90°. The numerical prediction using remeshing procedure follows a similar pattern and achieve similar levels of major strain with a good accuracy for the curve strain pattern of 50° and 60° wall angles. However, the curve patterns from 70° to 90° present an acceptable accuracy prediction in the regions corresponding to the wall and flat bottom. Concerning transition region between wall and the flat bottom, the interpolation of the missing surfaces does not present a significant accuracy error as occurred for the shape and thickness predictions.

In general, the numerical results of major strain using the reference mesh exhibit similar patterns in all forming stages. However, it is noticeable a slight difference between both mesh refinement types regarding the major strain values at the transition regions. In terms of accuracy, the reference mesh achieves a good approximation level in comparison with the experimental data.

The out-of-plane motion effect occurred resorting to DIC measurement method, as previously suggested (see Figure 5.34), is not noticeable for round shapes. In terms of the interpolation of missing areas performed using ARGUS software, an acceptable approximation between the experiments and numerical predictions is obtained.

5.5 Final remarks

In summary, this chapter demonstrates the interest, reliability and efficiency of the proposed adaptive remeshing method combined with RESS finite element. Regarding the chosen element, the numerical results validate its ability to accurately analyse sheet metal forming using only one element layer.

The first benchmark test concerns the analysis of a cone shape. It identifies the key remeshing parameter for accurate numerical results, as the number of nodes per edge (n). The use of 45° pie mesh for low refinement level, provides a CPU time that is smaller than the CPU time of the reference mesh, as expected. However, the CPU value becomes close to the reference one for high refining level (n=4).

In the two-slope pyramid shape simulation in DC01 steel grade, the CPU reduction achieved with adaptive remeshing application reavealed to be more efficient for larger meshes. As shown for different initial density meshes, the adaptive remeshing which generated higher final number of elements than the reference mesh, still allowed a pronounced CPU time reduction of 50%. Regarding the repetition of the pyramid shape with a different steel in Aveiro (SPIF-A), the CPU time increases in 15% in comparison with DC01 steel simulation. So the influence of the material parameters in the CPU performance is observed. Let us remind that for identical geometry is compared DC01 behaviour modelled by mixed hardening with steel HC660XD modelled by von Mises yield locus and isotropic hardening. Furthermore, the increase of CPU time demonstrated to be non-proportional to the increase of the increments/iterations number, responsible for CPU time increase.

The deep analysis of the shape prediction of two-slope pyramid using DC01 showed an accurate prediction of overall shapes at different depths and wall angle transition using a kinematic hardening model. From the analysis of the second two slope pyramid from Aveiro (simulated only with isotropic hardening), one can see a less global accurate shape prediction. Clearly some asymmetric accuracy is present (see Figure 5.28 and Figure 5.30) suggesting a type of twist effect or mode probably an asymmetric springback as the pyramid is not totally symmetric. A possible explanation is that the simulation using an isotropic hardening is not enough correct to take into account this springback effect. Indeed the available material tests did not allow identifying of more complex hardening law than the isotropic one.

The CPU time using adaptive remeshing procedure in the multistage simulation revealed insignificant decrease. The CPU time advantage is only obtained in the first stage of 50° wall angle due to the initial mesh density. In further stages the refined elements remains and consequently the addition and removal procedures decrease.

The effects of different refinement levels in the shape prediction exhibited an irrelevant influence in the accuracy of the results. In terms of thickness prediction all the numerical results showed similar thinning effect close to the clamping boundary conditions. However, for the lowest level of refinement (n=1), it is observed an underestimate thickness prediction, as it can be seen in Figure 5.4.

The multistage forming prediction in terms of shape and thickness presented a good agreement at the wall angle region in comparison with experimental measurements. As previously mentioned, the centre region of the bottom shape exhibits a deviation tendency, increasing from the first stage until the final target shape. The transition area between the flat bottom and the wall angle showed a good prediction from 50° to 70° wall angles. As previously described, the missing accuracy of experimental data for 80° and 90° wall angles leads to a deviation of numerical results. On the other hand, the numerical validation resorting to a similar example from Henrard (2008) confirmed the ability of adaptive remeshing method to accurately predict the shape and thickness of multistage forming, as shown in Appendix B.

The information retrieved from integration points allowed to understand stress state components at different zone of the sheet as previously demonstrate in Section 5.2.2. The analysis of DC01 pyramid simulated by RESS element confirms that plasticity occurs within the slope transition zone during the forming of the second pyramid. In the contrary, the analyses of aluminium pyramid simulated by shell (Guzmán *et al.*, 2012) confirms that no plasticity occurs in this case. This confirms that geometry and material are important to take into consideration before identifying the strain mechanism in SPIF process.

Also, the major strain prediction computed from the integration points for all shapes present an acceptable level of accuracy compared to strain surface measurements when they are reliable. In the simulation of multistage forming accuracy issues were reported due to DIC measurements at the transition region. In contrast, the major strain prediction at the bottom and wall region demonstrated an acceptable accuracy.

Finally, the geometries chosen validate the application of adaptive remeshing procedure for symmetric and asymmetric shapes. In addition, Table 5.14 shows the characteristics of the computer used to perform all the simulations previously discussed.

Table 5.14: Computational characteristics used for all simulations.

CPU type	
CPU clock speed	Intel L5420 2.50 GHz
Number of cores per CPU	2 (2 CPU - 4 cores)
Main memory	4*1024 MB
Operating system	Cluster Vision OS, kernel 2.6.18-128.1.10el5

Chapter 6

Conclusion

In this thesis an efficient adaptive refinement method was applied using a solid-shell finite element in order to accelerate the standard implicit FEM simulation of the SPIF process. The method and the element formulation were explained focusing the fundamental concepts and implementation procedure. Their performance was demonstrated through numerical simulation examples.
The main conclusions and suggestions for future developments are presented in the following sections.

6.1 Final considerations

The numerical simulation carried out by nonlinear analysis of SPIF using static implicit scheme has shown its inefficiency. In this context, the present research work was mainly devoted to the application of an adaptive remeshing method combined with a specific solid-shell finite element. Both developments were implemented into an in-house Finite Element implicit code called LAGAMINE. Moreover, Chapter 2 reviewed different approaches on the automatic refinement mesh topic. However, the common aspect found between similar research works was always the use of shell elements, both in in-house codes or commercial codes. As it is well-known, generally shell elements formulations are based on plane stress assumptions and the thickness is obtained through mathematic artifices. In this sense, the use of a hexahedral finite element allows the possibility to use general 3D constitutive laws. Additionally, a direct consideration of thickness variations, double-sided contact conditions and evaluation of all components of the stress field are available with solid-shell and not with shell elements.

From the finite element developments of high-order solid elements, it is required additional formulation to solve locking pathologies. The Enhanced Assumed Strains (EAS) method allows enhancing the solid finite element deformation modes. Consequently, a high number of enhancing modes to solve the locking phenomena inevitably leads to high computational time. The choice of RESS finite element, presented earlier, has advantages due to its integration scheme to eliminate locking phenomena using reduced integration in the element plane. In this formulation, only one enhancing variable is needed to attenuate the volumetric locking. As a result, the vector of enhanced internal variables is equivalent to a single scalar. The arbitrary number of integration points through thickness in one single layer avoids the addition of elements in thickness direction. This characteristic decreases the total number of nodes and elements, and as a result reduces the computation time.

A number of researchers have been interested in studying the deformation mechanisms and its peculiarities in order to understand the high formability achieved by SPIF process. These mechanisms were presented and described individually in the stat-of-art chapter (Chapter 2). However, there was not a general agreement due to the fact that each author has claimed and demonstrated his mechanism proposal. The main aspect found in the state-of-art research topic of deformation understanding on SPIF process was that all proposed mechanisms are directly or indirectly related with cyclic bending occurrence.

Initially, the influence of adaptive remeshing parameters, more properly the α coefficient and the $d_{\max}$ value, was analysed in the prediction of final shape and tool forces. These preliminary tests were used to select a set of parameters to be applied in further simulations. The line test was chosen due to its simplicity and high deformation imposed during the vertical step, larger than the value used during a complex shape forming. The best value of α coefficient and two values of $d_{\max}$ were chosen. Afterwards, the obtained parameter sets were tested into a conical shape forming simulation combined with different number of nodal division per edge. These parameters sets were studied in the prediction of the major and minor plastic strains, shape, thickness and tool forces.

A second simulation was performed in order to assess an incrementally formed component based on a pyramidal shape with two slopes. For this example, the shape accuracy was focused at transition region between both wall angle slopes. In particular, a special emphasis was given to the stress behaviour through the thickness in order to understand the shape evolution at transition wall angle zone.

The stress analysis through the sheet thickness exhibited a bending/unbending plus stretching, already documented in previous chapter, while the shear stresses remain very small. The combination of membrane under tension with bending behaviour was also found at different levels of depth.

These numerical results were compared with experimental measurements along the middle section of the sheet resorting to displacement boundary conditions (BC) instead of symmetric BC. From these comparisons, a good accuracy agreement was obtained between experimental measurements, adaptive remeshing procedure and initially refined mesh. They also clearly confirmed that the combination of a trilinear hexahedral finite element and a remeshing strategy become appropriate to perform future SPIF simulations. Besides the drastic CPU time reduction while keeping accuracy, the use of the presented framework into further studies will allow for a deeper understanding of SPIF mechanisms, as could be shown in the present thesis.

In conclusion, it has been shown that it is possible to perform accurate and efficient finite element simulations of SPIF process, resorting to implicit analysis and continuum elements. This is definitively a step-forward on the state-of-art in this field.

6.2 Future works

The author of this thesis suggests for further studies the following aspects:

- Find the origin of memory leaks due to the use dynamic allocation and pointer (already identified within LAGAMINE code);
- Adaptive remeshing using non-structured mesh;
- Application of damage model coupled with adaptive remeshing procedure;
- Implementation of different alternatives to Jauman rate;
- Test different return mapping algorithms;
- Correct prediction of springback phenomenon;
- Numerical analysis of different toolpath strategies;
- Experimental tests to find an adequate friction coefficient to be used into the numerical simulations.

Appendix A

Adaptive Remeshing subroutines: Flowchart description

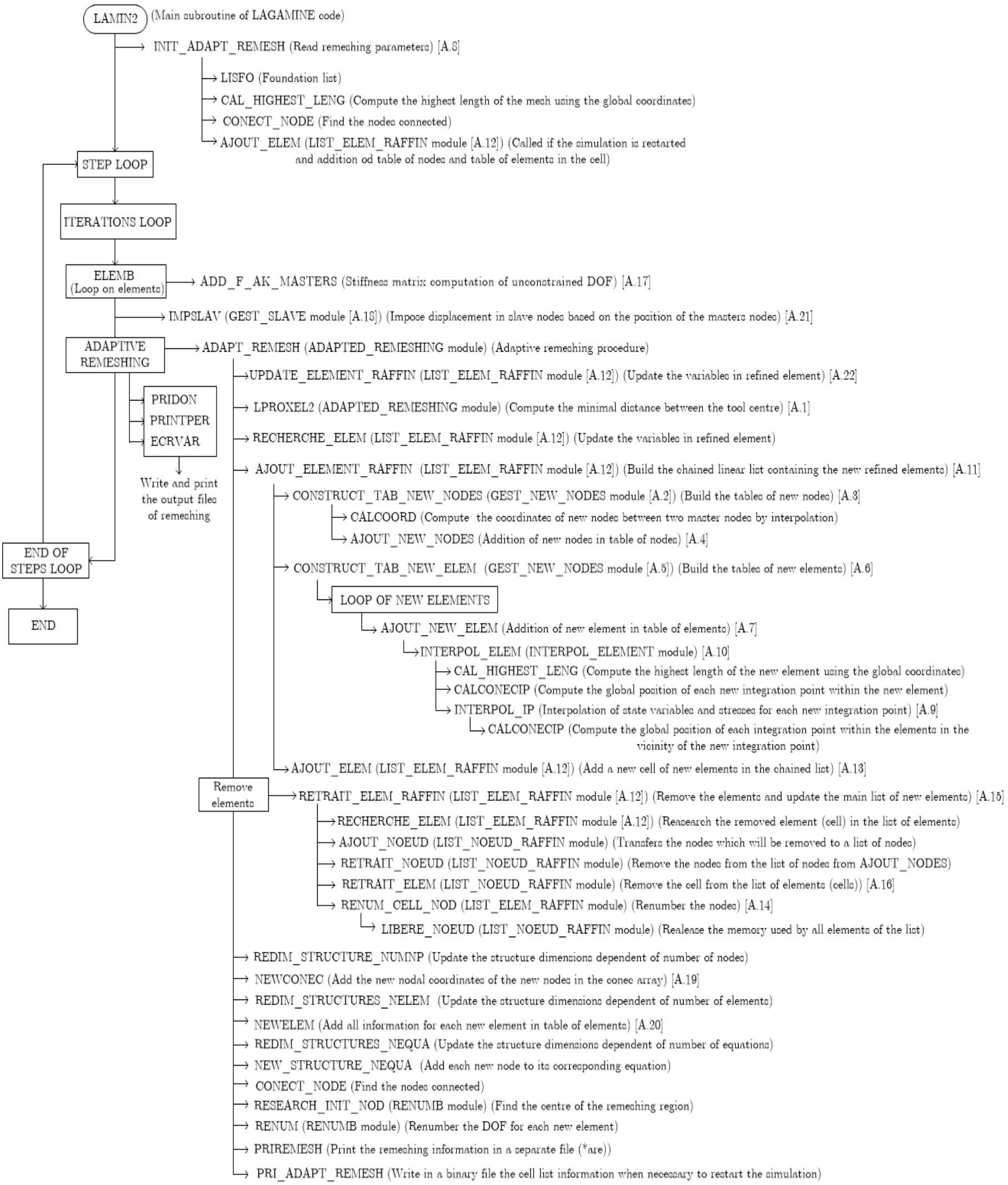

Figure A.1: Flowchart of all adaptive remeshing subroutines within LAGAMINE in-house code.

Appendix B

Yield surface influence

The purpose of this section is to analyse the influence of different yield surface definitions in the prediction of shape and thickness of a cone with vertical wall resorting to multi-stage forming. Besides, this section is also used to complement and overcome the missing accuracy between the numerical results and the experiments, especially in the 70°, 80° and 90° wall angles cones, described in Section 5.4. The problems faced were related with the experimental measurements and, consequently, the errors introduced due to the interpolation procedure from ARGUS software used to replace the missing region of the measured DIC mesh.

The experimental measurements and geometry dimensions used in these Appendix simulations are based on the work of Henrard (2008), schematically described in Figure B.1. The final shape forming is achieved by 5 stages performed through the SPIF process using circular contours separated by a vertical step of 1 mm, as similarly detailed in Section 5.4.

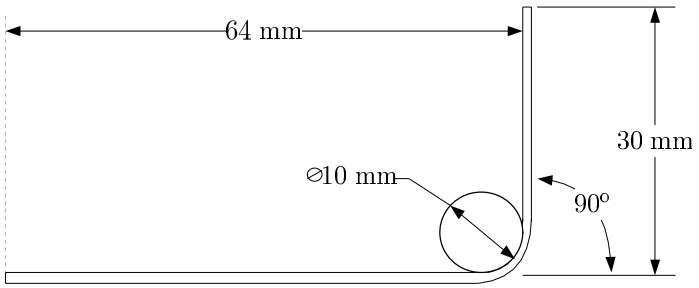

Figure B.1: Dimensions of the cone with vertical wall (Henrard, 2008).

The material used is an AA3003-O sheet with initial thickness of 1.5 mm. The material parameters presented in the following table are well detailed in the work of Henrard (2008). The elastic domain is described by E = 72600 MPa and a

Poisson coefficient (ν) equal to 0.36. The following tables detail the material parameters used for each yield surface. The hardening behaviour of all yield surfaces are defined by means of Swift's law.

Table B.1 presents the material parameters for von Mises yield locus coupled with isotropic Swift hardening.

Table B.1: Hardening parameters for isotropic yield locus.

Swift's law parameters
$\sigma_F^0 = 42.97$ MPa
K=180.0 MPa
$\varepsilon_0 = 0.00109$
n=0.21

Table B.2 gives the parameters for anisotropic Hill yield locus coupled with isotropic Swift hardening.

Table B.2: Hill 48 yield locus parameters.

Yield surface coefficients	**Swift's law parameters**
F=1.224	K=180.0 MPa
G=1.193	$\varepsilon_0 = 0.00109$
H=0.807	n=0.21
N=L=M=4.06	

Table B.3 describes the parameters for isotropic von Mises yield locus coupled with mixed isotropic, kinematic hardening.

Table B.3: Kinematic yield locus using Ziegler's parameters combined with isotropic surface expansion.

Yield surface coefficients	**Swift's law parameters**	**Back-stress data**
F=G=H=1	K=175.0	$C_A = 800$
N=L=M=3	$\varepsilon_0 = 1.5\,10^{-4}$	$G_A = 45.9$
	n=0.328	

More detailed information regarding the identification procedures used to obtain the material parameters can be found in the work of Henrard (2008).

In order to reduce the CPU time, only a 45° pie mesh with applied rotational boundary conditions to replace the missing material on the edges is

chosen, as similarly performed for circular meshes used in Chapter 5. Figure B.2 presents the coarse mesh for the application of adaptive remeshing. The adaptive remeshing parameters chosen were: 3 nodes per edge (n=3), α equal to 1.0 and $d_{\max}$ equal to 0.05 mm. Figure B.2 exhibits the coarse mesh used with adaptive remeshing method modelled with 435 elements on the sheet plane using one layer of RESS finite element coupled with CFI3D contact element in thickness direction. The mesh concerns one layer of RESS finite element in sheet thickness direction with 5 GP through the thickness and CFI3D contact element (4 GP on plane).

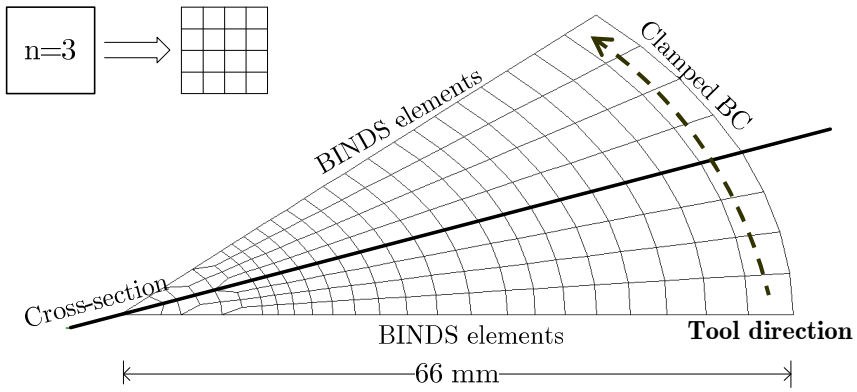

Figure B.2: Coarse mesh with 435 finite elements used with adaptive remeshing.

Finally, Coulomb friction coefficient, μ, between the tool and sheet is set to 0.05 and the penalty coefficients, K_P and K_τ, are equal to 1000 (Henrard, 2008). The following results are obtained at the end of each stage.

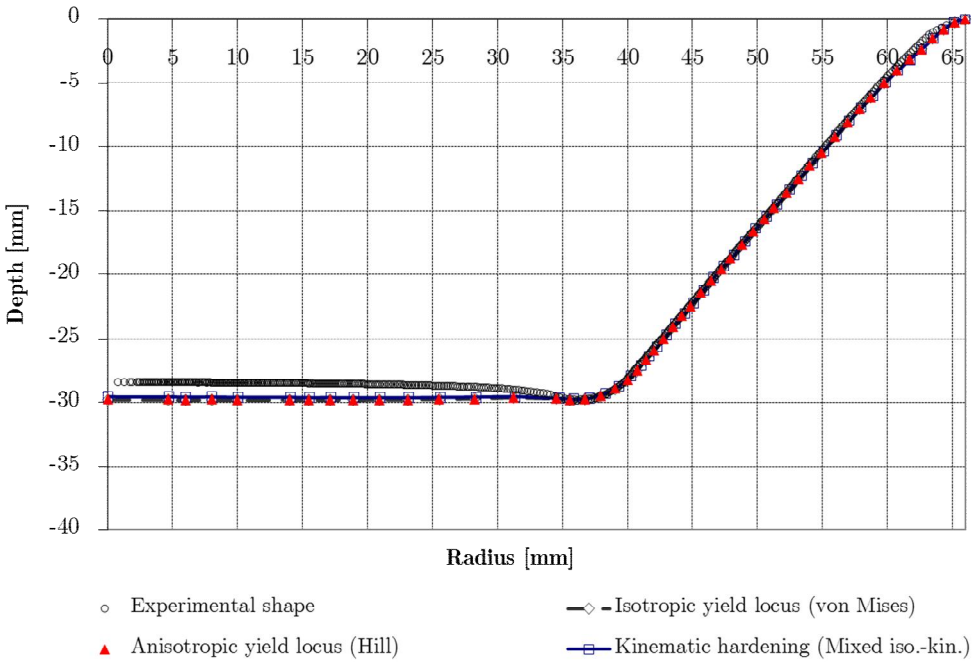

Figure B.3: Shape at the stage of 50° wall angle.

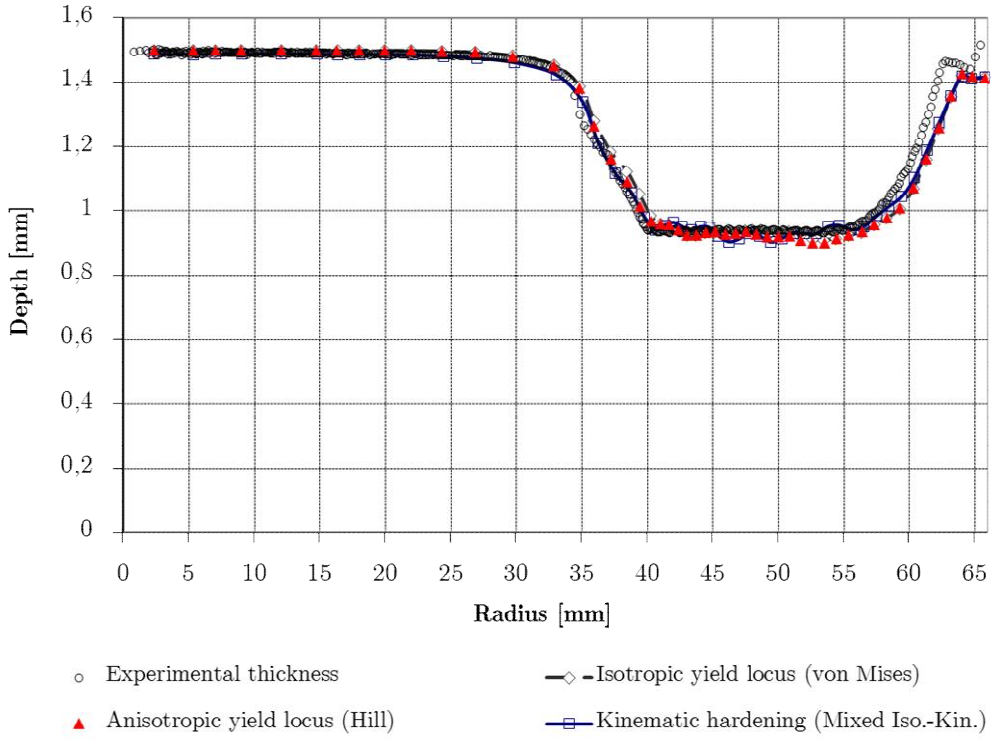

Figure B.4: Thickness at the stage of 50° wall angle.

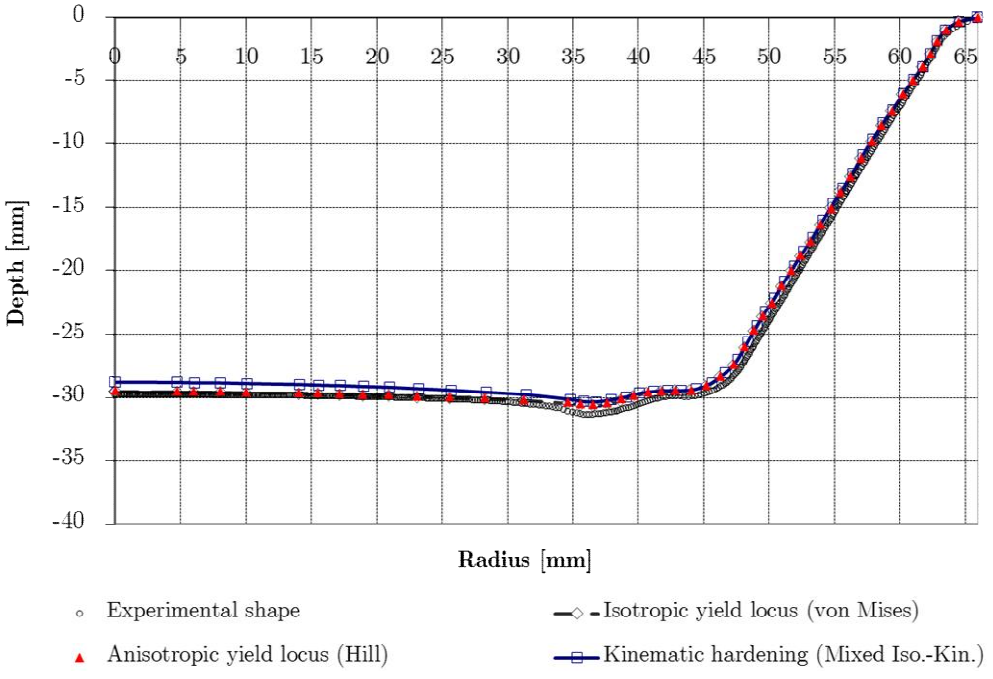

Figure B.5: Shape at the stage of 60° wall angle.

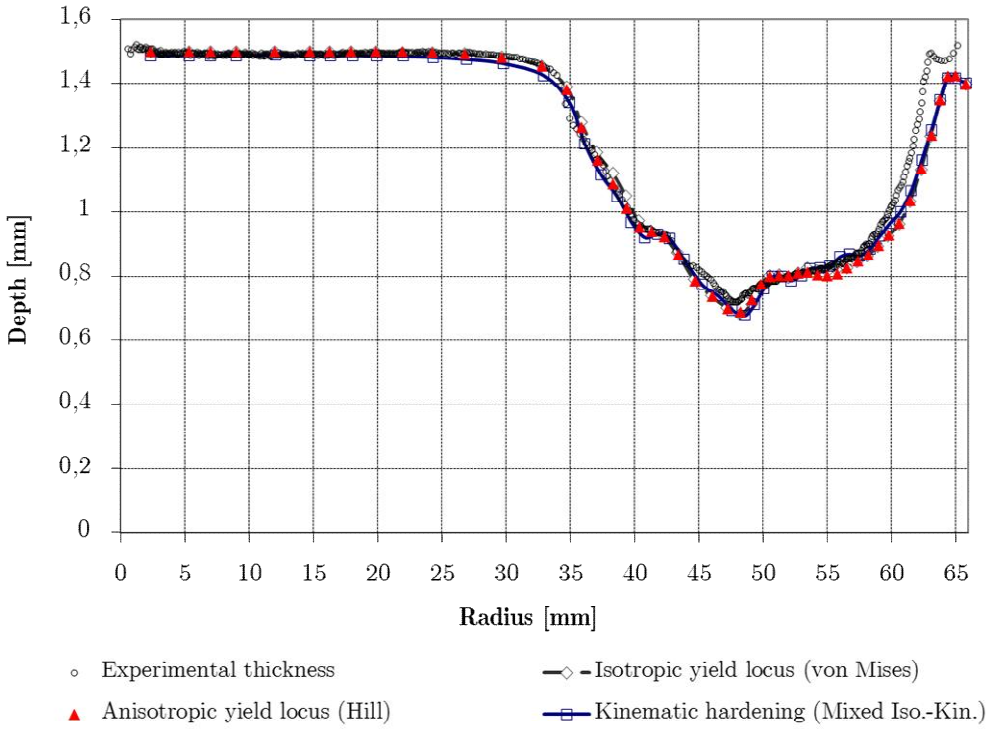

Figure B.6: Thickness at the stage of 60° wall angle.

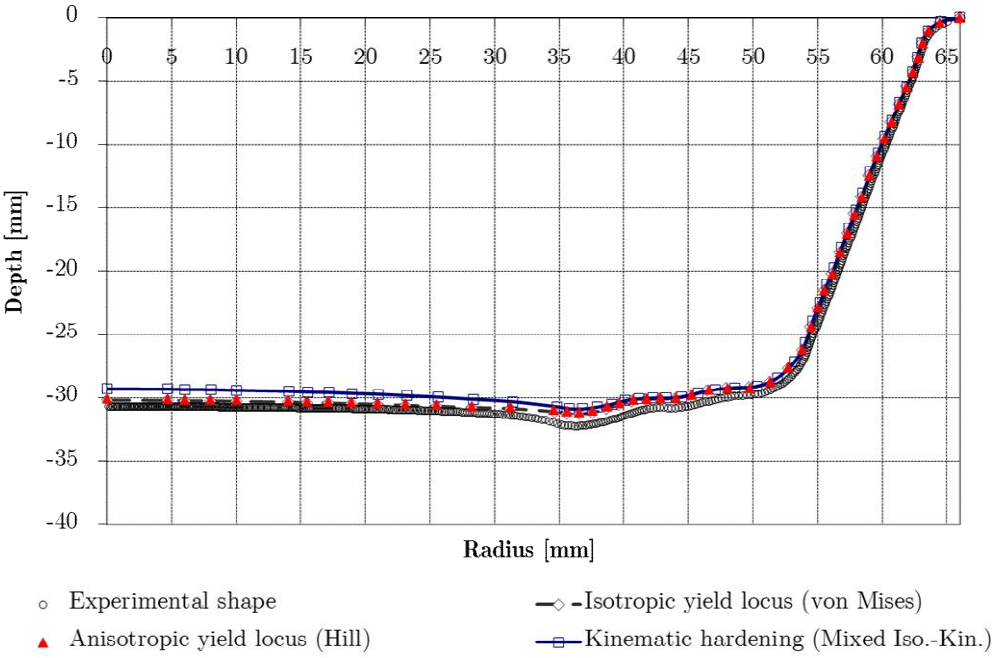

Figure B.7: Shape at the stage of 70° wall angle.

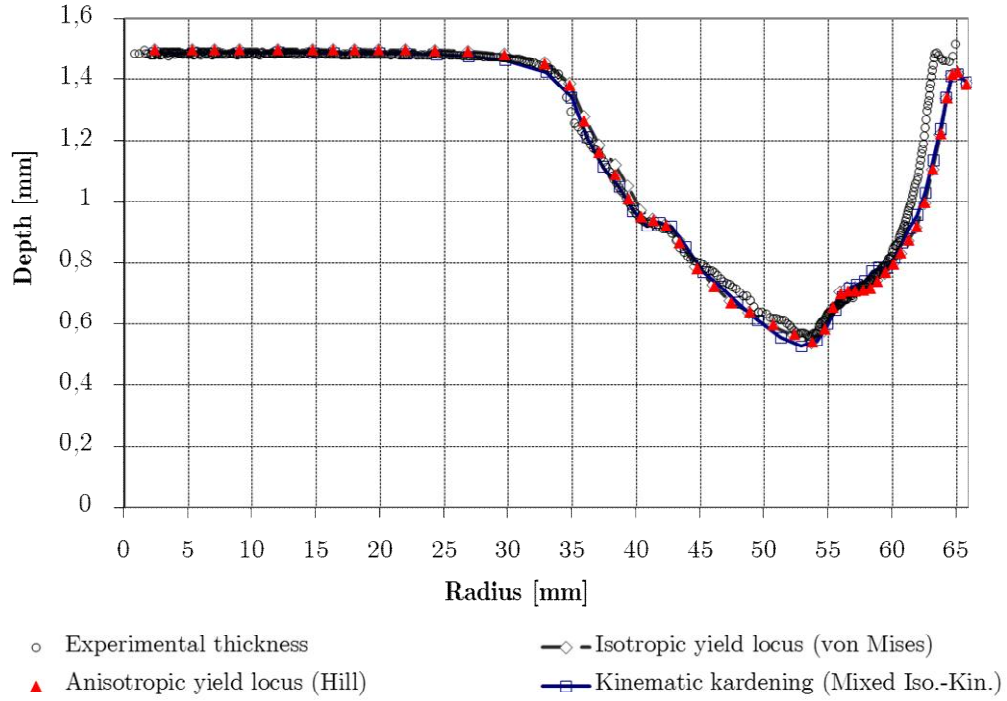

Figure B.8: Thickness at the stage of 70° wall angle.

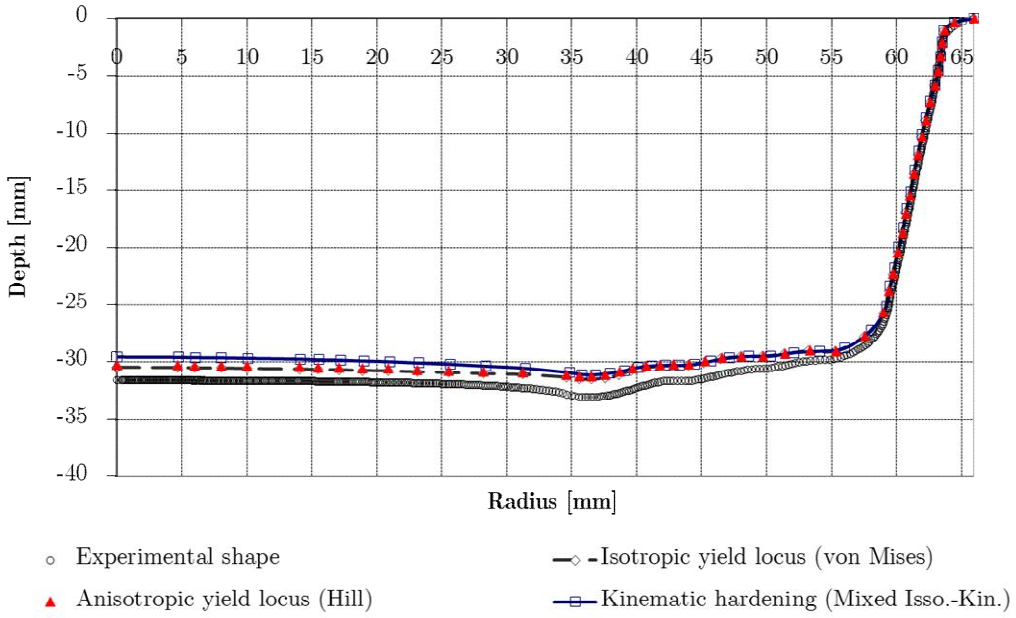

Figure B.9: Shape at the stage of 80° wall angle.

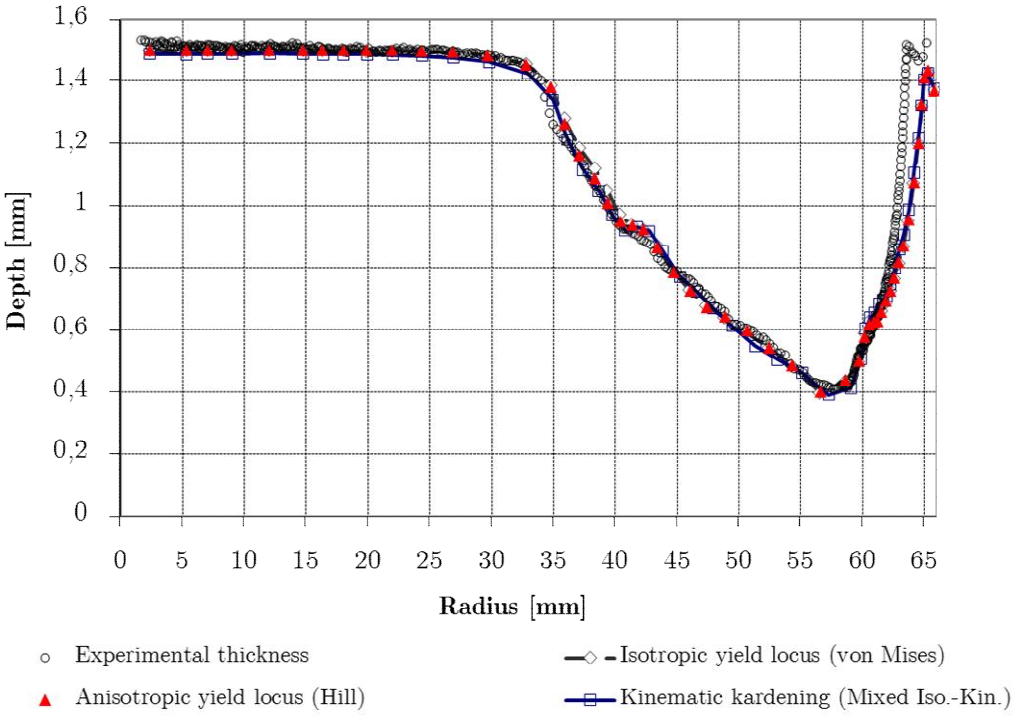

Figure B.10: Thickness at the stage of 80° wall angle.

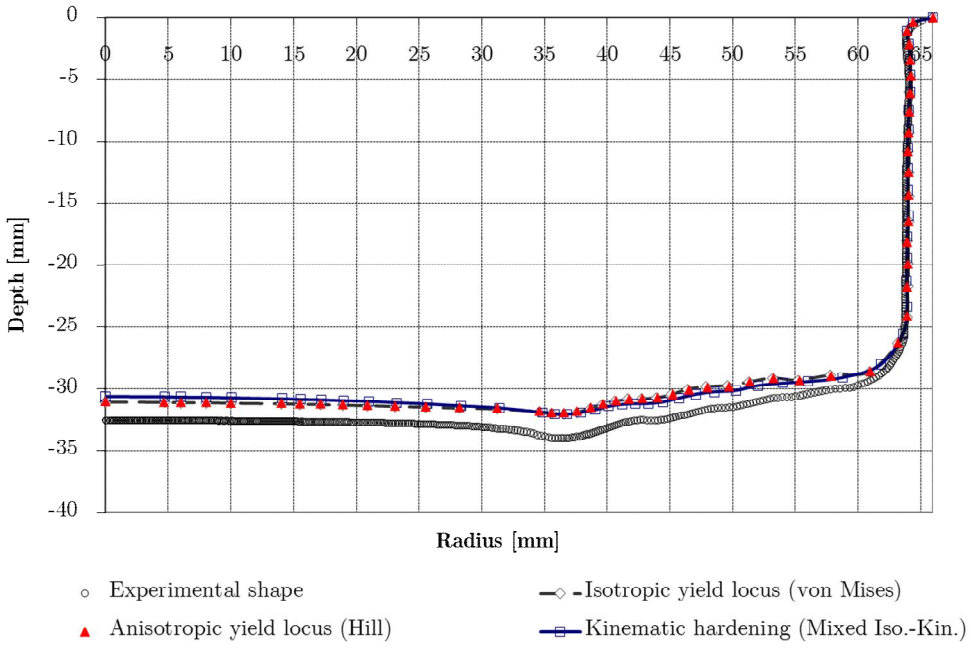

Figure B.11: Shape at the stage of 90° wall angle.

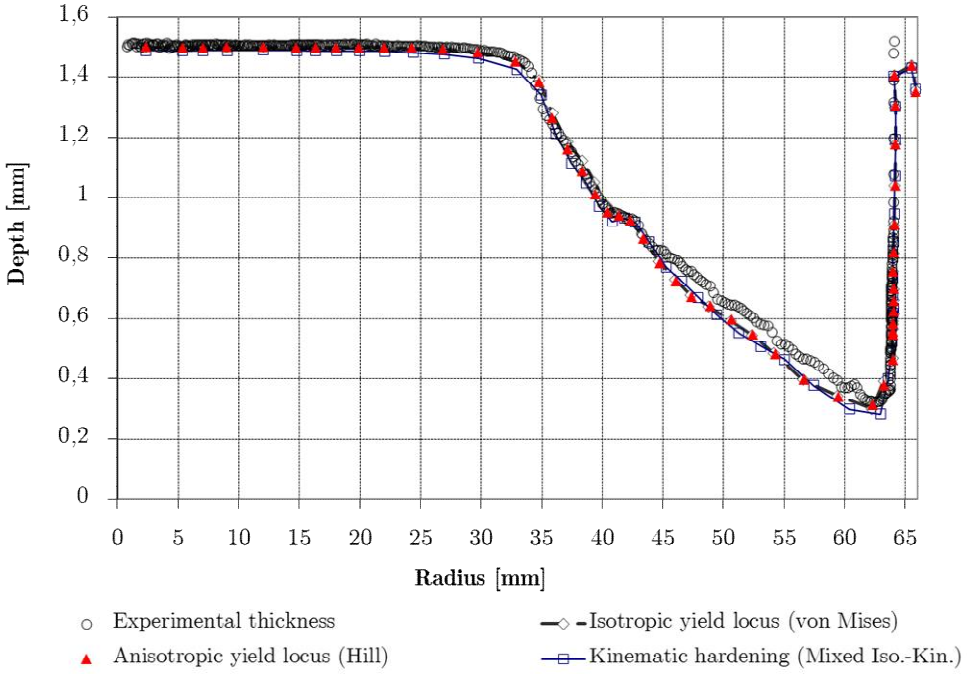

Figure B.12: Thickness at the stage of 90° wall angle.

All the simulations performed resorting to adaptive remeshing achieved an equivalent final number of 2772 elements. These results generated by different constitutive laws for AA3003-O confirm for this shape the following statements:

- no effect of anisotropy of the yield surface on the shape and thinning;
- the error in the predicted depth of the bottom cannot be solved with a better description of the material behaviour as more advanced law, such as kinematic hardening does not improve the Finite Element predictions;
- the experimental measurement accuracy seems better as it shows profile oscillation due to the multistep stages as the piece show them;
- the Finite Element measured strains are in close agreement, Figure B.6 exhibits a strong thinning localization reported by both approaches.

This additional work confirms the idea that the Finite Element predictions are accurate from point of view of strains. The shift of bottom in numerical predictions with real state cannot be solved by material law.

In order to analyse the refinement effect at the flat bottom area where the tool does not touch the sheet, a high density refinement mesh all over the sheet mesh is used. Figure B.13 describes the initial mesh density modelled with 6119 elements on the sheet plane. Similarly, in the thickness direction the mesh is composed by one layer of RESS finite element coupled with CFI3D contact. The number of integration points for both elements are similar as previously described for the coarse mesh (see Figure B.2).

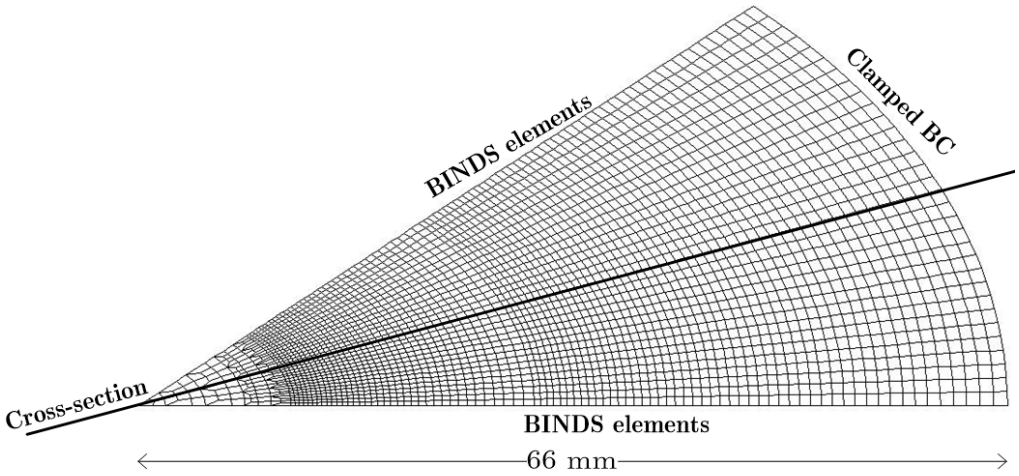

Figure B.13: Initial refined mesh modelled with 6119 finite elements (RESS+CFI3D).

The following results present the comparison between different mesh densities at the final stage of 90° wall-angle using the material parameters described in Table B.1. Figure B.14 and Figure B.15 exhibit the shape and thickness predictions using a high refined mesh in centre region of the flat bottom.

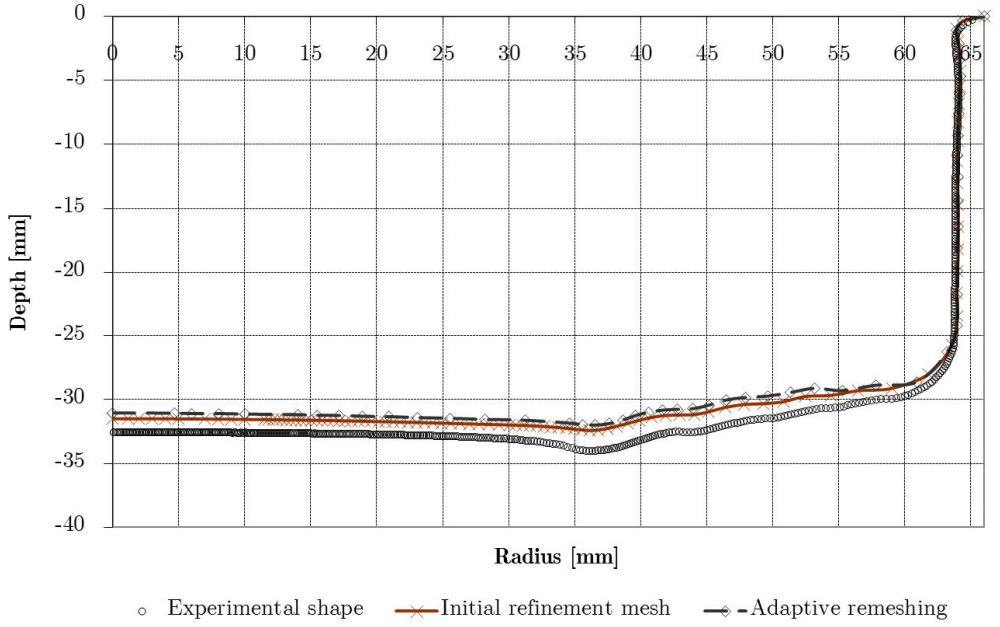

Figure B.14: Shape comparison between different densities meshes at the stage of 90° wall angle.

As observed in Figure B.14, there is a slight improvement using a high refined mesh on the centre region of the shape prediction. However, the refinement of the centre region of the mesh is not the solution to improve the approximation of the numerical prediction. The wall and transition regions show similar predictions

for both meshes refinement strategies. Additionally, increasing the value of the vicinity size parameter (α) from adaptive remeshing procedure does not improves the numerical shape prediction.

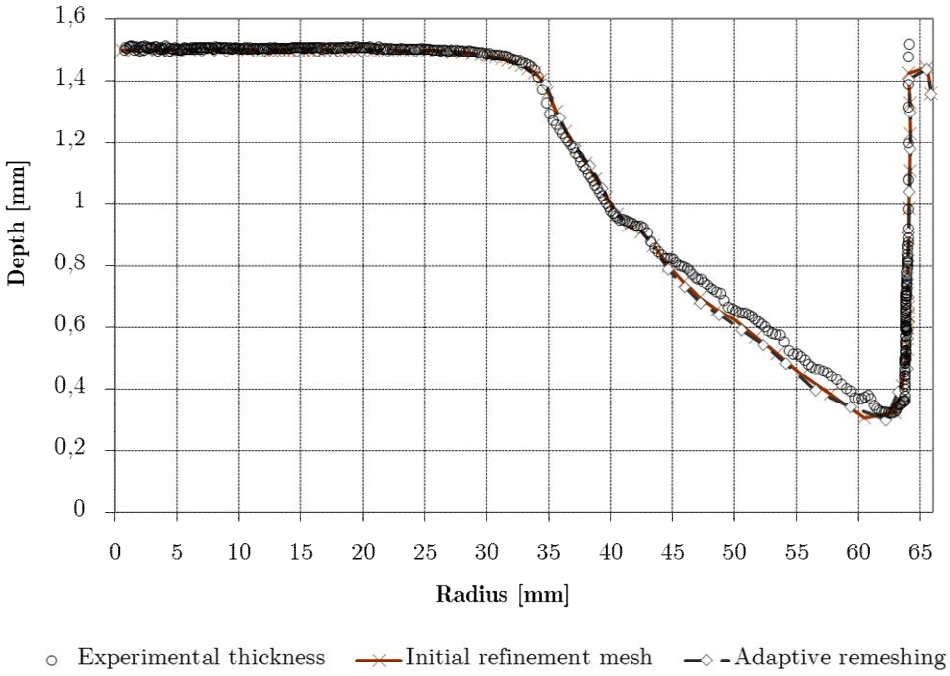

Figure B.15: Thickness comparison between different densities meshes at the stage of 90° wall angle.

Figure B.15 shows identical thickness prediction for both meshes, there is no difference between the numerical results resorting to different strategies of mesh refinement. The initial refinement mesh density at the centre region of the mesh significantly increased the CPU time in 68%.

References

ABAQUS (2008), ABAQUS, Theory Manual, Version 6.8, Simulia, Providence, RI.

ABAQUS (2005), Theory Manual, Version 6.5, Hibbitt, Karlsson & Sorensen Inc., USA.

Aerens, R., Eyckens, P., Bael, a. and Duflou, J.R. (2009), "Force prediction for single point incremental forming deduced from experimental and FEM observations", *The International Journal of Advanced Manufacturing Technology*, Vol. 46 No. 9-12, pp. 969–982.

Allwood, J.M., Houghton, N.E. and Jackson, K.P. (2005), "The design of an incremental forming machine", *Proceedings of the 11th Conference on Sheet Metal*, pp. 471-478.

Allwood, J.M., Braun, D. and Music, O. (2010), "The effect of partially cut-out blanks on geometric accuracy in incremental sheet forming", *Journal of Materials Processing Technology*, Elsevier B.V., Vol. 210 No. 11, pp. 1501–1510.

Alves de Sousa, R.J., Natal Jorge, R.M., Fontes Valente, R.A. and César de Sá, J.M.A. (2003), "A new volumetric and shear locking-free EAS element", *Engineering Computations*, Vol. 20, pp. 896-925.

Alves de Sousa, R.J., Cardoso, R.P.R., Fontes Valente, R.A., Yoon, J.-W., Gracio, J.J. and Natal Jorge, R.M. (2005), "A new one-point quadrature enhanced assumed strain (EAS) solid-shell element with multiple integration points along thickness: Part I: geometrically linear applications", *International Journal for Numerical Methods in Engineering*, Vol. 62 No. 7, pp. 952–977.

Alves de Sousa, R.J., Cardoso, R.P.R., Fontes Valente, R. a., Yoon, J.-W., Grácio, J.J. and Natal Jorge, R.M. (2006), "A new one-point quadrature enhanced assumed strain (EAS) solid-shell element with multiple integration points along thickness part II: nonlinear applications", *International Journal for Numerical Methods in Engineering*, Vol. 67 No. 2, pp. 160–188.

Alves de Sousa, R.J. (2006), *Development of a General Purpose Nonlinear Solid-Shell Element and its Application to Anisotropic Sheet Forming Simulation*, University of Aveiro, Portugal.

Alves de Sousa, R.J., Yoon, J., Cardoso, R., Fontes Valente, R. and Gracio, J. (2007), "On the use of a reduced enhanced solid-shell (RESS) element for sheet forming simulations", *International Journal of Plasticity*, Vol. 23 No. 3, pp. 490–515.

Alves de Sousa, R.J., Ferreira, J.A.F., Sá de Farias, J.B., Torrão, J.N.D., Afonso, D.G. and Martins, M.A.B.E. (2014), "SPIF-A : on the development of a new concept of incremental forming machine", *Structural Engineering and Mechanics*, Vol. 49 No. 5, pp. 645–660.

Ambrogio, G., Filice, L., Gagliardi, F. and Micari, F. (2005), "Three-dimensional FE simulation of single point incremental forming: experimental evidences and process design improving", *VIII International Conference on Computational Plasticity COMPLAS VIII*, Barcelona, Spain, pp. 3–6.

Ambrogio, G., Duflou, J.R., Filice, L. and Aerens, R. (2007), "Some considerations on force trends in Incremental Forming of different materials", *AIP Conference Proceedings*, Vol. 907 No. 2007, pp. 193–198.

Ambrogio, G., Filice, L. and Manco, G.L. (2008), "Warm incremental forming of magnesium alloy AZ31", *CIRP Annals - Manufacturing Technology*, Vol. 57 No. 1, pp. 257–260.

Ambrogio, G., Filice, L., Guerriero, F., Guido, R. and Umbrello, D. (2010a), "Prediction of incremental sheet forming process performance by using a neural network approach", *The International Journal of Advanced Manufacturing Technology*, Vol. 54 No. 9-12, pp. 921–930.

Ambrogio, G., Filice, L. and Manco, G.L. (2010b), "Improving process performance in incremental sheet forming (ISF)", *AIP Conference Proceedings*, Vol. 1315, pp. 613–618.

Amino, H., Lu, Y., Maki, T., Osawa, S., Fukuda, K. and Maki, T. (2002), "Dieless NC Forming, prototype of automotive service parts", *Proceedings of the 2nd International Conference on Rapid Prototyping and Manufacturing (ICRPM)*, Beijing.

Araghi, B.T., Manco, G.L., Bambach, M. and Hirt, G. (2009), "Investigation into a new hybrid forming process: Incremental sheet forming combined with stretch forming", *CIRP Annals - Manufacturing Technology*, Vol. 58 No. 1, pp. 225–228.

Arfa, H., Bahloul, R. and BelHadjSalah, H. (2012), "Finite element modelling and experimental investigation of single point incremental forming process of aluminum sheets: influence of process parameters on punch force monitoring and on mechanical and geometrical quality of parts", *International Journal of Material Forming*, Vol. 6 No. 4, pp. 483–510.

Attanasio, A., Ceretti, E. and Giardini, C. (2006), "Optimization of tool path in two points incremental forming", *Journal of Materials Processing Technology*, Vol. 177 No. 1-3, pp. 409–412.

Attanasio, a., Ceretti, E., Giardini, C. and Mazzoni, L. (2008), "Asymmetric two points incremental forming: Improving surface quality and geometric accuracy by tool path optimization", *Journal of Materials Processing Technology*, Vol. 197 No. 1-3, pp. 59–67.

Azaouzi, M. and Lebaal, N. (2012), "Tool path optimization for single point incremental sheet forming using response surface method", *Simulation Modelling Practice and Theory*, Vol. 24, pp. 49–58.

Asghar, J., Shibin, E., Bhattacharya, A. and Reddy, N.V. (2012), "Twist in single point incremental forming", *Proceedings of the international manufacturing science and engineering conference*, University of Norte Dame, Norte Dame.

Azevedo, N.G., Farias, J.S., Bastos, R.P., Teixeira, P., Davim, J.P., Jose, R. and Sousa, A. De. (2015), "Lubrication Aspects during Single Point Incremental Forming for Steel and Aluminum Materials", *International Journal of precision engineering and manufacturing*, Vol. 16 No. 3, pp. 1–7.

Bagudanch, I., Centeno, G., Vallellano, C. and Garcia-Romeu, M.L. (2013), "Forming Force in Single Point Incremental Forming under Different Bending Conditions", *Procedia Engineering*, Vol. 63, pp. 354–360.

Bambach, M. and Hirt, G. (2005), "Performance assessment of element formulations and constitutive laws for the simulation of incremental sheet forming (ISF)", *COMPLAS. CIMNE, Barcelona*, pp. 1–4.

Bambach, M. Cannamela, M., Azaouzi, M., Hirt, G. and Batoz, J.L. (2007), "Computer-Aided Tool Path Optimization for Single Point Incremental Sheet Forming", *Advanced Methods in Material Forming*, Springer Berlin Heidelberg, pp. 233–250.

Bambach, M. (2014), "Fast simulation of asymmetric incremental sheet metal forming by adaptive remeshing and subcycling", *International Journal of Material Forming*, Vol. 847, pp. 844–847.

Bathe, K.J. and Bolourchi, S. (1979), "Large displacement analysis of three-dimensional beam structures", *International Journal for numerical engineering*, Vol. 14 No. April 1978, pp. 961–986.

Bathe, K.J. (1996), *Finite element procedure*, 1st Edition, Prentice Hall.

Behera, A.K., Lauwers, B. and Duflou, J.R. (2014), "Tool path generation framework for accurate manufacture of complex 3D sheet metal parts using single point incremental forming", *Computers in Industry*, Vol. 65 No. 4, pp. 563–584.

Belchior, J., Guines, D., Leotoing, L. and Ragneau, E. (2013), "Force Prediction for Correction of Robot Tool Path in Single Point Incremental Forming", *Key Engineering Materials*, Vol. 554-557, pp. 1282–1289.

Belchior, J., Leotoing, L., Guines, D., Courteille, E. and Maurine, P. (2014), "A Process/Machine coupling approach: Application to Robotized Incremental Sheet Forming", *Journal of Materials Processing Technology*, Vol. 214 No. 8, pp. 1605–1616.

Ben Ayed, L., Robert, C., Delamézière, A., Nouari, M. and Batoz, J.L. (2014), "Simplified numerical approach for incremental sheet metal forming process", *Engineering Structures*, Vol. 62-63, pp. 75–86.

Bhattacharya, A., Maneesh, K., Venkata Reddy, N. and Cao, J. (2011), "Formability and Surface Finish Studies in Single Point Incremental Forming", *Journal of Manufacturing Science and Engineering*, ASME, Vol. 133 No. 6.

Blaga, A., Bologa, O., Oleksik, V. and Breaz, R. (2011), "Influence of tool path on main strains, thickness reduction and forces in single point incremental forming process", *Proceedings in Manufacturing Systems*, Vol. 6 No. 4, pp. 2–7.

Bonet, J. and Wood, R. (2008), *Non-linear Continuum Mechanics for Finite Element Analysis*, Cambridge University Press.

Borst R., Crisfield, M.A., Remmers J.J.C. and Verhoosel C.V. (2012), *Non-linear Finite Element Analysis of Solids and Structures*, 2nd Edition, Wiley.

Bouffioux, C., Eyckens, P., Henrard, C., Aerens, R., Bael, A. Van, Sol, H., Duflou, J.R. and Habraken, A.M. (2008a), "Identification of material parameters to predict Single Point Incremental Forming forces", *International Journal of Material Forming*, pp. 1147–1150.

Bouffioux, C., Henrard, C., Eyckens, P., Aerens, R., Bael, A. Van, Sol, H., Duflou, J.R., et al. (2008b), "Comparison of the tests chosen for material parameter identification to predict single point incremental forming forces", *International Deep Drawing Research Group-IDDRG 2008 International Conference*, Olofström, Sweden.

Bouffioux, C., Pouteau, P., Duchêne, L., Vanhove, H., Duflou, J.R. and Habraken, a. M. (2010), "Material data identification to model the single point incremental forming process", *International Journal of Material Forming*, Vol. 3 No. S1, pp. 979–982.

Callegari, M., Amodio, D., Ceretti, E. and Giardini, C. (2006), "Sheet Incremental Forming : Advantages of Robotised Cells vs . CNC Machines", in Low Kin Huat (Ed.), *Industrial Robotics: Programming, Simulation and Applicationl*, Germany, pp. 493–514.

Cardoso, R.P.R., Yoon, J.W., Grácio, J.J., Barlat, F. and César De Sá, J.M.A. (2002), "Development of a one point quadrature shell element for nonlinear applications with contact and anisotropy", *Computer Methods in Applied Mechanics and Engineering*, Vol. 191 No. 45, pp. 5177–5206.

Ceretti, E., Giardini, C. and Attanasio, A. (2004), "Experimental and simulative results in sheet incremental forming on CNC machines", *Journal Material Proceeding Technology*, Vol. 152, pp. 176-184.

Cerro, I., E. Maidagan, et al. (2006). "Theoretical and experimental analysis of the dieless incremental sheet forming process", *Journal of Materials Processing Technology*, Vol. 177(1-3), pp. 404-408.

Cescotto, S. and Grober, H. (1985), "Calibration and application of an elastic viscoplastic constitutive equation for steels in hot-rolling conditions", *Engineering Computations*, Emerald, Vol. 2 No. 2, pp. 101–106.

Crowson, R. and Walker, J. (2015), *Handbook of Manufacturing Engineering*, London, doi:10.1007/978-1-4471-4670-4.

Cui, Z., Cedric Xia, Z., Ren, F., Kiridena, V. and Gao, L. (2013), "Modeling and validation of deformation process for incremental sheet forming", *Journal of Manufacturing Processes*, Vol. 15 No. 2, pp. 236–241.

Dejardin, S., Thibaud, S., Gelin, J.C. and Michel, G. (2010), "Experimental investigations and numerical analysis for improving knowledge of incremental sheet forming process for sheet metal parts", *Journal of Materials Processing Technology*, Vol. 210 No. 2, pp. 363–369.

Delamézière, A., Yu, Y., Robert, C., Ben Ayed, L. and Nouari, M. (2011), "Numerical Simulation of Incremental Sheet Forming by Simplified Approach", *AIP Conference Proceedings*, *AMPT2010*, pp. 619–624.

Doghri, I. (2000), *Mechanics of Deformable solids-linear, nonlinear, analytical and computational aspects*, Springer.

Driessen, B. (2002), "Direct Stiffness-Modification Route to Linear Consistency Between Incompatible Finite Element Meshes", in Constanda, C., Schiavone, P. and Mioduchowski, A. (Eds.),*Integral Methods in Science and Engineering SE - 12*, Birkhäuser Boston, pp. 75–80.

Duchêne, L., El Houdaigui, F. and Habraken, A.M. (2007), "Length changes and texture prediction during free end torsion test of copper bars with FEM and remeshing techniques", *International Journal of Plasticity*, Vol. 23 No. 8, pp. 1417–1438.

Duchêne, L., Lelotte, T., Flores, P., Bouvier, S. and Habraken, A.M. (2008), "Rotation of axes for anisotropic metal in FEM simulations", *International Journal of Plasticity*, Vol. 24 No. 3, pp. 397–427.

Duchêne, L., Guzmán, C.F., Behera, A.K., Duflou, J.R. and Habraken, A.M. (2013), "Numerical Simulation of a Pyramid Steel Sheet Formed by Single Point Incremental Forming using Solid-Shell Finite Elements", in Clarke, R.B., Leacock, A.G., Duflou, J.R., Merklein, M. and Micari, F. (Eds.), *Key Engineering Materials*, Trans Tech Publications, Belfast, United Kingdom, Vol. 549, pp. 180–188.

Duflou, J.R., Szekeres, A. and VanHerck, A. (2005), "Force measurements for single point incremental forming and experimental study", J*ournal Advanced Material Resistance*, Vol. 6-8, pp. 441-448.

Duflou, J.R., Callebaut, B., Verbert, J. and De Baerdemaeker, H. (2007a), "Laser Assisted Incremental Forming: Formability and Accuracy Improvement", *CIRP Annals - Manufacturing Technology*, Vol. 56 No. 1, pp. 273–276.

Duflou, J.R., Tunçkol, Y., Szekeres, A. and Vanherck, P. (2007b), "Experimental study on force measurements for single point incremental forming", *Journal of Materials Processing Technology*, Vol. 189 No. 1-3, pp. 65–72.

Duflou, J.R., Vanhove, H., Verbert, J., Gu, J., Vasilakos, I. and Eyckens, P. (2010), "Twist revisited: Twist phenomena in single point incremental forming", *CIRP Annals - Manufacturing Technology*, CIRP, Vol. 59 No. 1, pp. 307–310.

Durante, M., Formisano, a., Langella, a. and Capece Minutolo, F.M. (2009), "The influence of tool rotation on an incremental forming process", *Journal of Materials Processing Technology*, Vol. 209 No. 9, pp. 4621–4626.

Echrif, S.B.M. and Hrairi, M. (2011), "Research and Progress in Incremental Sheet Forming Processes", *Materials and Manufacturing Processes*, Vol. 26 No. 11, pp. 1404–1414.

Emmens, W.C. and Boogaard, A.H. Van Den. (2007), "Strain in Shear , and Material Behaviour in Incremental Forming", *Key Engineering Materials*, Vol. 344, pp. 519–526.

Emmens, W.C. and Boogaard, A.H. Van Den. (2008), "Tensile tests with bending : a mechanism for incremental forming .", *11th ESAFORM Conference, Lyon, France, 23-25 april 2008 Tensile*, pp. 23–25.

Emmens, W.C. and van den Boogaard, a. H. (2009), "An overview of stabilizing deformation mechanisms in incremental sheet forming", *Journal of Materials Processing Technology*, Vol. 209 No. 8, pp. 3688–3695.

Emmens, W.C., Sebastiani, G. and Boogaard, A.H. Van Den. (2010), "Technology The technology of Incremental Sheet Forming — A brief review of the history", *Journal of Materials Processing Tech.*, Elsevier B.V., Vol. 210 No. 8, pp. 981–997.

Essa, K. and Hartley, P. (2010), "An assessment of various process strategies for improving precision in single point incremental forming", *International Journal of Material Forming*, Vol. 4 No. 4, pp. 401–412.

Eyckens, P., He, S., Van Bael, a., Van Houtte, P. and Duflou, J. (2007), "Forming Limit Predictions for the Serrated Strain Paths in Single Point Incremental Sheet Forming", *AIP Conference Proceedings*, Vol. 908 No. 2007, pp. 141–146.

Eyckens, P., Bael, A. Van, Aerens, R., Duflou, J. and Houtte, P. Van. (2008), "Small-scale Finite Element Modelling of the Plastic Deformation Zone in the Incremental Forming Process", *International Journal of Material Forming*, pp. 1159–1162.

Eyckens, P., Van Bael, A. and Van Houtte, P. (2009a), "Marciniak–Kuczynski type modelling of the effect of Through-Thickness Shear on the forming limits of sheet metal", *International Journal of Plasticity*, Vol. 25 No. 12, pp. 2249–2268.

Eyckens, P., Del-lero Moreau, J., Duflou, J.R., Bael, A. and Houtte, P. (2009b), "MK modelling of sheet formability in the incremental sheet forming process, taking into account through-thickness shear", *International Journal of Material Forming*, Vol. 2 No. S1, pp. 379–382.

Eyckens, P. (2010), *Formability in incremental sheet forming: Generalization of the Marciniak-Kuczynski model*, Katholieke Universiteit Leuven, Belgium.

Eyckens, P., Belkassem, B., Henrard, C., Gu, J., Sol, H., Habraken, A.M., Duflou, J.R., Bael, A. and Houtte, P. (2010), "Strain evolution in the single point incremental forming process: digital image correlation measurement and finite element prediction", *International Journal of Material Forming*, Vol. 4 No. 1, pp. 55–71.

Eyckens, P., Van Bael, A. and Van Houtte, P. (2011), "An extended Marciniak–Kuczynski model for anisotropic sheet subjected to monotonic strain paths with through-thickness shear", *International Journal of Plasticity*, Vol. 27 No. 10, pp. 1577–1597.

Fang, Y., Lu, B., Chen, J., Xu, D.K. and Ou, H. (2014), "Analytical and experimental investigations on deformation mechanism and fracture behavior in single point incremental forming", *Journal of Materials Processing Technology*, Vol. 214 No. 8, pp. 1503–1515.

Filice, L., Fratini, L., Micari, F. (2002), "Analysis of material formability in incremental forming", Annals of CIRP, 51, 199-202.

Filice, L., Ambrogio, G. and Micari, F. (2006), "On-Line Control of Single Point Incremental Forming Operations through Punch Force Monitoring", *CIRP Annals - Manufacturing Technology*, Vol. 55 No. 1, pp. 245–248.

Fish, J. and Belytschko, T. (2007), *A First Course in Finite Elements*, John Wiley & Sons, Ltd.

Fratini, L., Ambrogio, G., Di Lorenzo, R., Filice, L. and Micari, F. (2004), "Influence of mechanical properties of the sheet material on formability in single point incremental forming", *CIRP Annals - Manufacturing Technology*, Vol. 53 No. 1, pp. 207–210.

Fraeiji de Voubeke, B.M. (1951), "Diffusion des inconnues hyperstaques dans les voilures à longeron couples", Bull. Serv. *Technique de L' Aéronautique n^0 24*, Imprimeríe Marcel Hayez, Bruxelles.

Fu, Z., Mo, J., Han, F. and Gong, P. (2013), "Tool path correction algorithm for single-point incremental forming of sheet metal", *International Journal of Advanced Manufacturing Technology*, Vol. 64 No. 9-12, pp. 1239–1248.

Giraud-Moreau, L., Cherouat, A., Zhang, J., Borouchaki, H. (2013), "Comparison between an advanced numerical simulations of sheet incremental forming using adaptive remeshing and experimental results", *Key Enginneering Materials*, Vol. 554–557, pp. 1375–1381.

Guzmán, C.F., Gu, J., Duflou, J., Vanhove, H., Flores, P. and Habraken, A.M. (2012), "Study of the geometrical inaccuracy on a SPIF two-slope pyramid by finite element simulations", *International Journal of Solids and Structures*, Vol. 49 No. 25, pp. 3594–3604.

Habraken, A.M. (1989), *Contribution to the modelling of metal forming by finite element model*, Université de Liège, Belgium.

Habraken, A.M. and Cescotto, S. (1998), "Contact between deformable solids: The fully coupled approach", *Mathematical and Computer Modelling*, Vol. 28 No. 4-8, pp. 153–169.

Hadoush, A. and Boogaard, A.H. Van Den. (2008), "Time reduction in implicit single point incremental sheet forming simulation by Refinement / Derefinement", pp. 1167–1170.

Hadoush, a. and Boogaard, a. H. (2009), "Substructuring in the implicit simulation of single point incremental sheet forming", *International Journal of Material Forming*, Vol. 2 No. 3, pp. 181–189.

Hadoush, A.M.H. (2010), *Efficient simulation and process mechanics of incremental sheet forming*, University of Twente, Netherland.

Hadoush, A. and Boogaard, A.H. Van Den. (2012), "Efficient implicit simulation of incremental sheet forming", *International Journal for Numerical Methods in Engineering*, doi:10.1002/nme.

Ham, M. and Jeswiet, J. (2006), "Single Point Incremental Forming and the Forming Criteria for AA3003", *CIRP Annals - Manufacturing Technology*, Vol. 55 No. 1, pp. 241–244.

Hamilton, K. and Jeswiet, J. (2010), "Single point incremental forming at high feed rates and rotational speeds: Surface and structural consequences", *CIRP Annals - Manufacturing Technology*, CIRP, Vol. 59 No. 1, pp. 311–314.

He, S., Bael, A. Van, Houtte, P. Van, Tunckol, Y., Duflou, J., Henrard, C., Bouffioux, C. and Habraken, A.M. (2005), "Effect of FEM choices in the modelling of incremental forming of aluminium sheets", *8th ESAFORM conference*, Cluj-Napoca, Romania, pp. 1–4.

Henrard, C. (2008), *Numerical Simulations of the Single Point Incremental Forming Process*, University of Liège, Belgium.

Henrard, C., Bouffioux, C., Eyckens, P., Sol, H., Duflou, J.R., Van Houtte, P., Van Bael, A., et al. (2010), "Forming forces in single point incremental forming: prediction by finite element simulations, validation and sensitivity", *Computational Mechanics*, Vol. 47 No. 5, pp. 573–590.

Hirt G., Ames J., Bambach M. (2006), "Basic Investigation into the Characteristics of dies and suppot tools used in CNC-Incremental Sheet Forming", *Proceedings of the International Deep Drawing Research Group Conference, IDDRG 2006*, Porto, Portugal, pp. 341–348.

Jackson, K. and Allwood, J. (2009), "The mechanics of incremental sheet forming", *Journal of Materials Processing Technology*, Vol. 209 No. 3, pp. 1158–1174.

Jadhav, S. (2004), *Basic investigation of the incremental sheet metal forming process on a CNC milling machine*, University of Dortmund, Germany.

Jeswiet, J., Hagan, E. and Szekeres, A. (2002), "Forming parameters for incremental forming of aluminium alloy sheet metal", *Proceedings of the IMechE 216*, Part B, No. 10, pp. 1367-71.

Jeswiet, J., Micari, F., Hirt, G., Bramley, A., Duflou, J. and Allwood, J. (2005), "Asymmetric Single Point Incremental Forming of Sheet Metal", *CIRP Annals - Manufacturing Technology*, Vol. 54 No. 2, pp. 88–114.

Jetteur, P. and Cescotto, S. (1991), "A mixed finite element for the analysis of large inelastic strains", *International Journal for Numerical Methods in Engineering*, John Wiley & Sons, Ltd, Vol. 31 No. 2, pp. 229–239.

Jurisevic, B., Kuzman, K. and Junkar, M. (2005), "Water jetting technology: an alternative in incremental sheet metal forming", *The International Journal of Advanced Manufacturing Technology*, Vol. 31 No. 1-2, pp. 18–23.

Kim, Y.. and Park, J.. (2002), "Effect of process parameters on formability in incremental forming of sheet metal", *Journal of Materials Processing Technology*, Vol. 130-131, pp. 42–46.

Kopac, J. and Kampus, Z. (2005), "Incremental sheet metal forming on CNC milling machine-tool", *Journal of Materials Processing Technology*, Vol. 162-163, pp. 622–628.

Lamminen, L., Wadman, B., Küttner, R.T.S. (2003), *Research report, Simulation.*

Lamminen, L., Tuominen, T. and Kivivuori, S. (2005), "Incremental sheet forming with an industrial robot- forming limits and their effects on component design", *Proceedings of 3rd International Conference on Advanced Materials Processing (ICAMP-3)*, Finland.

Lequesne, C., Henrard, C., Bouffioux, C., Duflou, J.R. and Habraken, A.M. (2008), "Adaptive remeshing for incremental forming simulation", *Numisheet 2008*, Interlaken, Switzerland, Vol. 32, pp. 4–8.

Leszak, E. (1967), "Apparatus and Process for Incremental Dieless Forming", Patent US3342051A1.

Li, K. (1995), *Contribution to the finite element simulation of three-dimensional sheet metal forming*, Université de Liège, Belgium.

Lu, B., Fang, Y., Xu, D.K., Chen, J., Ou, H., Moser, N.H. and Cao, J. (2014), "Mechanism investigation of friction-related effects in single point incremental forming using a developed oblique roller-ball tool", *International Journal of Machine Tools and Manufacture*, Vol. 85, pp. 14–29.

Malhotra, R., Cao, J., Beltran, M., Xu, D., Magargee, J., Kiridena, V. and Xia, Z.C. (2012a), "Accumulative-DSIF strategy for enhancing process capabilities in incremental forming", *CIRP Annals - Manufacturing Technology*, Vol. 61 No. 1, pp. 251–254.

Malhotra, R., Xue, L., Belytschko, T. and Cao, J. (2012b), "Mechanics of fracture in single point incremental forming", *Journal of Materials Processing Technology*, Vol. 212 No. 7, pp. 1573–1590.

Malkus, D.S. and Hughes, T.J.R. (1978), "Mixed finite element method-reduced and selective integration techniques: a unification of concepts", *Computer Methods in Applied Mechanics and Engineering*, Vol. 15, pp. 63-81.

Malwad, D.S. and Nandedkar, V.M. (2014), "Deformation Mechanism Analysis of Single Point Incremental Sheet Metal Forming", *Procedia Materials Science*, Vol. 6, pp. 1505–1510.

Martins, P. a. F., Bay, N., Skjoedt, M. and Silva, M.B. (2008), "Theory of single point incremental forming", *CIRP Annals - Manufacturing Technology*, Vol. 57 No. 1, pp. 247–252.

Meier, H.; Dewald, O. and Zhang, J. (2005), "A New Robot-Based Sheet Metal Forming Process", *Proceedings of Shemet 2005*, pp. 465-470, April 5-8, Erlangen, Germany.

Meier, H., Buff, B., Laurischkat, R. and Smukala, V. (2009), "Increasing the part accuracy in dieless robot-based incremental sheet metal forming", *CIRP Annals - Manufacturing Technology*, Vol. 58 No. 1, pp. 233–238.

Mirnia, M.J., Mollaei Dariani, B., Vanhove, H. and Duflou, J.R. (2014), "An investigation into thickness distribution in single point incremental forming using sequential limit analysis", *International Journal of Advanced Manufacturing Technology*, Vol. 70 No. 9-12, pp. 2029–2041.

Mohammadi, A., Vanhove, H., Van Bael, A. and Duflou, J.R. (2014), "Towards accuracy improvement in single point incremental forming of shallow parts formed under laser assisted conditions", *International Journal of Material Forming*, doi:10.1063/1.4850107.

Montleau, P. de, Habraken, A.M. and Duchêne, L. (2008), "A new finite element integration scheme. Application to a simple shear test of anisotropic material", *International Journal for Numerical Methods in Engineering*, Vol. 73 No. July 2007, pp. 1395–1412.

Ndip-Agbor, E., Smith, J., Ren, H., Jiang, Z., Xu, J., Moser, N., Chen, W., et al. (2015), "Optimization of relative tool position in accumulative double sided incremental forming using finite element analysis and model bias correction", *International Journal of Material Forming*, Vol. 8 No. 34, doi:10.1007/s12289-014-1209-4.

Nimbalkar, D.H. and Nandedkar, V.M. (2013), "Review of Incremental Forming of Sheet Metal Components", *International Journal of Engineering Research and Applications*, Vol. 3 No. 5, pp. 39–51.

Park, J.-J. and Kim, Y.-H. (2003), "Fundamental studies on the incremental sheet metal forming technique", *Journal of Materials Processing Technology*, Vol. 140 No. 1-3, pp. 447–453.

Pascon, F. (2003), *2D½ Thermal-Mechanical Model of Countinuous Casting of steel using Finite Element Method*, University of Liège, Belgium.

Pérez-Santiago, R., Bagudanch Frigolé, I. and García-Romeu de Luna, M.L. (2011), "Force Modeling in Single Point Incremental Forming of Variable Wall Angle Components", *Key Engineering Materials*, Vol. 473, pp. 833–840.

Petek, A., Jurisevic, B., Kuzman, K. and Junkar, M. (2009a), "Comparison of alternative approaches of single point incremental forming processes", *Journal of Materials Processing Technology*, Vol. 209 No. 4, pp. 1810–1815.

Petek, A., Kuzman, K. and Kopac, J. (2009b), "Deformations and forces analysis of single point incremental sheet metal forming", Vol. 35 No. 2, pp. 107–116.

Rauch, M., Hascoet, J.Y., Hamann, J.C. and Plennel, Y. (2008), "A new approach for toolpath programming in Incremental Sheet Forming", *International Journal of Material Forming*, Vol. 1 No. S1, pp. 1191–1194.

Reddy, N.V. and Cao, J. (2014), "Incremental Sheet Metal Forming : A Review", *Research report*.

Riadh, B., Henia, A. and Hedi, B. (2013), "Application of Response Surface Analysis and Genetic Algorithm for the Optimization of Single Point Incremental Forming Process", Vol. 557, pp. 1265–1272.

Robert, C., Delamézière, A., Dal Santo, P. and Batoz, J.L. (2012), "Comparison between incremental deformation theory and flow rule to simulate sheet-metal forming processes", *Journal of Materials Processing Technology*, Vol. 212 No. 5, pp. 1123–1131.

Schafer, T. and Schraft, R.D. (2005), "Incremental sheet metal forming by industrial robots", *Rapid Prototyping Journal*, Vol. 11, pp. 278–286.

Sebastiani, G., Brosius, a., Tekkaya, a. E., Homberg, W. and Kleiner, M. (2007), "Decoupled simulation method for incremental sheet metal forming", *AIP Conference Proceedings*, Vol. 908, pp. 1501–1506.

Sena, J.I.V., Sousa, R.J.A. De and Valente, R.A.F. (2011), "On the use of EAS solid-shell formulations in the numerical simulation of incremental forming processes", *Engineering Computations*, Vol. 28 No. 3, pp. 287–313.

Sena JIV, Guzmán CF, Duchêne L, Habraken AM, Valente RAF, Alves de Sousa RJ. (2013), "Numerical simulation of a conical shape made by single point incremental", *AIP Conference Proceedings, NUMISHEET 2014*, J-W Yoon, T B Stoughton, B Rolfe, JH Beynon, and P Hodgson, editors, 2013; pp. 852-855, Melbourne, Australia.

Sena, J.I.V., Guzmán, C.F., Duchêne, L., Habraken, a. M., Behera, a. K., Duflou, J., Valente, R. a. F., et al. (2015), "Simulation of a two-slope pyramid made by SPIF using an adaptive remeshing method with solid-shell finite element", *International Journal of Material Forming*, doi:10.1007/s12289-014-1213-8.

Seong, D.Y., Haque, M.Z., Kim, J.B., Stoughton, T.B. and Yoon, J.W. (2014), "Suppression of necking in incremental sheet forming", *International Journal of Solids and Structures*, Vol. 51 No. 15-16, pp. 2840–2849.

Shanmuganatan, S.P. and Senthil Kumar, V.S. (2012), "Experimental investigation and finite element modeling on profile forming of conical component using AA 3003(O) alloy", *Materials and Design*, Elsevier Ltd, Vol. 36, pp. 564–569.

Shim, M.S. and Park, J.J. (2001), "The formability of aluminum sheet in incremental forming", *Journal of Materials Processing Technology*, Vol. 113 No. 1-3, pp. 654–658.

Silva, M.B., Skjoedt, M., Martins, P.A.F. and Bay, N. (2008), "Revisiting the fundamentals of single point incremental forming by means of membrane analysis", *International Journal of Machine Tools and Manufacture*, Vol. 48 No. 1, pp. 73–83.

Silva, M.B., Skjoedt, M., Bay, N. and Martins, P.A.F. (2009), "Formability in multistage single point incremental forming", *7th EUROMECH Solid Mechanics Conference*.

Simo, J.C. and Rifai, M.S. (1990), "A class of mixed assumed strain methods and the method of incompatible modes", *Internatial Journal for Numerical Methods in Engineering*, Vol. 29. pp 1595-1638.

Suresh, K. and Regalla, S.P. (2014), "Effect of Mesh Parameters in Finite Element Simulation of Single Point Incremental Sheet Forming Process", *Procedia Materials Science*, Vol. 6, pp. 376–382.

Teixeira-Dias, F., Pinho-da-Cruz, J., Fontes Valente, R.A., Alves de Sousa, R. J. (2010), *Método dos Elementos Finitos - Técnicas de Simulação Numérica em Engenharia*, Lidel.

Tekkaya, A.E. (2000), "State-of-the-art of simulation of sheet metal forming", *Journal of Materials Processing Technology*, Vol. 103 No. 1, pp. 14–22.

Vanhove, H., Verbert, J., Gu, J., Vasilakos, I. and Duflou, J.R. (2010), "An experimental study of twist phenomena in single point incremental forming", *International Journal of Material Forming*, Vol. 3 No. S1, pp. 975–978.

Verbert J. (2010), *Computer Aided Process Planning for Rapid Prototyping with Incremental Sheet Forming Techniques*, Katholieke Universiteit Leuven, Belgium.

Vu-Quoc, L. and Tan, X.G. (2003), "Optimal solid shells for non-linear analyses of multilayer composites. I. Statics", *Computational Method Applied Mechanics*, Vol. 192, pp. 975-1016.

Wang, J. (2004), "A New Hexahedral Solid Element for 3D FEM Simulation of Sheet Metal Forming", *AIP Conference Proceedings*, Vol. 712, pp. 2181–2186.

Washizu, K., (1955), "On the variational principles of elasticity and plasticity", *Aeroelastic and Structures Research Laboratory*, Technical Report 25-18, MIT, Cambridge.

Wriggers, P. (2002), *Computational contact mechanics*, John Wiley & Sons, Ltd.

Wong, C.., Dean, T.. and Lin, J. (2003), "A review of spinning, shear forming and flow forming processes", *International Journal of Machine Tools and Manufacture*, Vol. 43 No. 14, pp. 1419–1435.

Wu, S.H., Reis, A., Andrade Pires, F.M., Santos, A.D. and Barata da Rocha, a. (2012), "Study of Tool Trajectory in Incremental Forming", *Advanced Materials Research*, Vol. 472-475, pp. 1586–1591.

Yamashita, M., Gotoh, M. and Atsumi, S.-Y. (2008), "Numerical simulation of incremental forming of sheet metal", *Journal of Materials Processing Technology*, Vol. 199 No. 1-3, pp. 163–172.

Yau, C.L. (2001), "Triangular gimbal", Patents US6240799.

Yoon, J.W., Rolfe, B., Beynon, J.H. and Hodgson, P. (2013), "NUMISHEET 2014 : The 9th International Conference and Workshop on Numerical Simulation of 3D Sheet Metal Forming Processes : Part A Benchmark Problems and Results and Part B General Papers", Melbourne, Australia, Vol. 1567.

Zienkiewicz O. C., Taylor R. L. (2005), *The finite element method for solid and structural mechanics.*, Elsevier Butterworth Heinemann.